UNIVERSITY OF SOUTHAMPTON

FACULTY OF NATURAL AND ENVIRONMENTAL SCIENCES

Ocean and Earth Science

Sea Surface Salinity in the Atlantic Ocean from the SMOS Mission and its Relation to Freshwater Fluxes

by

Eleni Tzortzi

Thesis for the degree of Doctor of Philosophy

April 2015

UNIVERSITY OF SOUTHAMPTON

ABSTRACT

FACULTY OF NATURAL AND ENVIRONMENTAL SCIENCES
Ocean and Earth Science

Doctor of Philosophy

SEA SURFACE SALINITY IN THE ATLANTIC OCEAN FROM THE SMOS MISSION AND ITS RELATION TO FRESHWATER FLUXES

by Eleni Tzortzi

Spatially dense sea surface salinity (SSS) measurements have recently begun to be made from space through the ESA SMOS mission. In this PhD, the sub-annual to interannual SSS distribution and variability is characterized, and its relationship with surface freshwater fluxes, i.e. Evaporation minus Precipitation (E-P) and river outflow (R) is investigated. Given its link to the Meridional Overturning Circulation, the focus is on the Tropical/ Subtropical Atlantic, which encompasses the dynamically different E-dominated Subtropics and P-dominated Tropics. The global and Atlantic SSS variability on different time scales and controlling processes are reviewed, including a description of how SSS is remotely sensed by satellites. The research initially examines the Tropical Atlantic SSS variability using the first year (2010) of SMOS data. This reveals that the variability in 2010 is dominated by eastern/western basin SSS regions ("poles") close to the major Amazon/Orinoco and Congo/Niger rivers. The poles show seasonal ranges up to 6.5 pss and out-of-phase by 6 months seasonal cycles that largely compensate each other, playing a key role in the Tropical Atlantic salinity budget. The growing SMOS record also reveals new aspects of the interannual variability of the SSS seasonal cycle during 2010-2012 and its phase-relationship with E, P, and R. It also shows that the E/W poles' seasonal compensation holds at multi-annual time scales. Next, a novel analysis of the spatio-temporal characteristic scales of SSS from SMOS over the Tropical/Subtropical Atlantic basin is presented. By examining how quickly consistent SSS changes evolve, regions with time persistent and, likewise, spatially homogeneous SSS variations, on sub-annual to interannual time scales, are identified. The spatial scales of SSS in the region are anisotropic, and persist for up to 3-4 months over most of the basin. Determination of SSS time and space scales of variability also provides insights into the controlling mechanisms of SSS. Finally, focusing on the freshwater forcing term of the salt budget equation, E-P is estimated from satellite SSS variations to explore whether and where SMOS can capture the main characteristics of E-P distribution in the region.

Contents

List of Figures

List of Tables

Declaration of Authorship

I, Eleni Tzortzi , declare that the thesis entitled *Sea Surface Salinity in the Atlantic Ocean from the SMOS Mission and its Relation to Freshwater Fluxes* and the work presented in the thesis are both my own, and have been generated by me as the result of my own original research. I confirm that:

- this work was done wholly or mainly while in candidature for a research degree at this University;
- where any part of this thesis has previously been submitted for a degree or any other qualification at this University or any other institution, this has been clearly stated;
- where I have consulted the published work of others, this is always clearly attributed;
- where I have quoted from the work of others, the source is always given. With the exception of such quotations, this thesis is entirely my own work;
- I have acknowledged all main sources of help;
- where the thesis is based on work done by myself jointly with others, I have made clear exactly what was done by others and what I have contributed myself;
- parts of this work have been published as: (*Tzortzi et al.*, 2013)

Signed:.....

Date:.....

Quote page

" "Do you know a cure for me?"
"Why yes," he said, "I know a cure for everything. Salt water."
"Salt water?" I asked him.
"Yes," he said, "in one way or the other. Sweat, or tears, or the salt sea." "

Karen von Blixen-Finecke/Isak Dinesen (pen name), Seven Gothic Tales, 1934.

Acknowledgements

Pursuit of the doctoral degree must be one of the most challenging journeys one takes in life. It requires intelligence, creativity, perseverance, patience and an overall determination to succeed in the face of setbacks. In this sense, it really does teach us a lot about life and even ourselvesI wouldnt wish it any other way. And I would be remiss if I didnt acknowledge the considerable effort and lovely support from the following individuals. Many thanks to you all!

First and foremost, I would like to thank my supervisors, Dr Christine Gommenginger, Prof Simon Josey and Prof Meric Srokosz, for their guidance, feedback, vast scientific knowledge and stimulating discussions throughout my doctoral degree program. They generously transferred to me their knowledge in the field of satellite physical oceanography and taught me several methods of approaching a scientific problem.

I thank Christine for reminding me to find the Zen in my PhD, and helping me to improve my prioritization and be a good juggler when working on multiple tasks. I am also truly grateful for her practical and emotional support during the last delicate months of my PhD and afterwards. I thank Simon for his guidance in approaching my PhD topic when I first started, his help from the basics up to coding, and his valuable guidance, stimulating feedback and interaction while writing the papers. I thank Meric for often reminding me to stop for a while and think in order to reflect on the wider picture, and for challenging me to recall my personal motivation and desire to complete this PhD. They all helped me to develop not only as a researcher in the field of oceanography but also as an individual, pushing me to discover further my abilities and overcome limitations.

I also wish to thank other panel members, Dr Joel Hirschi and Prof Neil Wells, as well as my two examiners Dr Penny Holiday and Dr Jacqueline Boutin, for their useful comments.

This work was made possible by support from the National Environmental Research Council (NERC), National Oceanography Centre Southampton (NOCS), and the Ocean and Earth Science Graduate School of the University of Southampton. I also acknowledge the European Space Agency SMOS-SOS project for helping me financially during the last few months of my PhD.

My gratitude goes to the scientists I have interacted with during this thesis and whose insights were of great help. These include the staff and scientists of the School of Ocean and Earth Science and the Marine Physics and Ocean Climate (MPOC) and Marine System Modelling (MSM) Groups at NOCS, who provided fruitful discussions and a very stimulating environment for my MSc and PhD studies. I also thank the IT support team at NOCS.

I would like to extend my thanks to the people working for the Ifremer CATDS SMOS, GPCP precipitation and ORE-HYBAM river discharge data, who were eager to provide detailed information on the data products, in particular Nicolas Reul from Ifremer for our stimulating discussions and guidance on the CATDS and river data. I am also thankful to Nicolas and Craig Donlon for their encouragement over the final months of my studies.

I was fortunate to have had the opportunity to take part in the JC064 RAPID research cruise on board the James Cook at 26°N and experience for 4 weeks the life at sea, together with my fellow oceanographers. For this I am particularly grateful to Prof Stuart Cunningham and Dr Gerald McCarthy.

A special thanks goes to Prof Ian Robinson, who played an important role in my decision to continue studying oceanography, completing my MRes degree and pursuing my PhD studies. Ian has been more than just a tutor to me all these years, providing me with support and advice whenever I needed some guidance.

A very special thanks goes to Chris Hughes for the long scientific discussions on my subject, his precious help in coding, and moral support, particularly during the last challenging months of my thesis. My thanks also to Adrien Martin and Christian Buckingham for helping me with the final format and appearance of this thesis.

Last but not least, this work was made possible thanks to the active moral support of my family and friends. Therefore I would really like to thank all those people that for a while or longer were next to me in this long journey, including Yiannis and Sen in the early times, my fellow PhD students and friends for making this journey interesting and fun, in particular Konstantina, Alanoud and Chris H.. I also thank Matti* for his psychological and emotional support. Finally, I am grateful to Johanne, Damien, Aurélie, Hannah and Yvonne, who were next to me during the last period of this PhD and helped me go through this delicate moment of my life.

And before this life chapter is over, I need to plant at least 5 trees to compensate for all that printing..!

Southampton, March 2015

List of abbreviations

AF-FOV	Alias-free Field of View
AMOC	Atlantic Meridional Overturning Circulation
Argo	Array for Real-Time Geostrophic Oceanography
BC	Boundary Current
BCC	Benguela Coastal Current
BEC	Barcelona Expert Centre
BL	Barrier layer
CATDS	Centre Aval de Traitement des Donnèes
CDOM	Coloured dissolved organic matter
CECOS	Ocean Salinity Expertise Center
CLIVAR	Climate Variability and Predictability
CNES	Centre national d'études spatiales (National Centre for Space Studies)
COARE	Coupled Ocean-Atmosphere Response Experiment
CONAE	Comisión Nacional de Actividades Espaciales (National Space Activities Commission)
CTD	Conductivity-temperature-depth
DOM	Dissolved organic matter
E	Evaporation
ECMWF	European Centre for Medium-Range Weather Forecasts
ENSO	El Niño Southern Oscillation
E-P	Evaporation minus Precipitation
ERA-40	European Reanalysis-40
ESA	European Space Agency
EUC	Equatorial Undercurrent
FOV	Field of View
GCM	General Circulation Model
GDAC	Global Data Assembly Centre
GO	Geometric Optics
GODAE	Global Ocean Data Assimilation Experiment
GPCC	Global Precipitation Climatology Centre
GPCP	Global Precipitation Climatology Project
GRACE	Gravity Recovery and Climate Experiment
GRL	Geophysical Research Letters
GRSS	Geoscience Remote Sensing Society

IPCC	Intergovernmental Panel on Climate Change
IPSL	Institut Pierre Simon Laplace
IR	Infrared
ITCZ	InterTropical Convergence Zone
LOCEAN	Laboratoire d' Océanographie et du Climat-Expérimentation et Approches Numériques
MIRAS	Microwave Imaging Radiometer using Aperture Synthesis
MLD	Mixed layer depth
MLS	Mixed layer salinity
MOC	Meridional Overturning Circulation
NAO	North Atlantic Oscillation
NASA	National Aeronautics and Space Administration
NBC	North Brazil Current
NCAR	National Center for Atmospheric Research
NCEP	National Center for Environmental Prediction
NEC	North Equatorial Current
NECC	North Equatorial Counter Current
N.H.	Northern Hemisphere
NPO	North Pacific Oscillation
NODC	National Oceanographic Data Center
OAFlux	Objectively Analyzed air-sea Fluxes
ORE-HYBAM	Environmental Research Observatory-Hydrogeodynamics of the Amazon Basin Observatory
OSCAR	Ocean Surface Current Analysis Real Time
OSTIA	Operational Sea Surface Temperature and Sea Ice Analysis
OTT	Ocean Target transformation
P	Precipitation
PDO	see NPO
PIRATA	Prediction and Research Moored Array in the Atlantic
PSG	Precipitation satellite-gauge
pss	Practical salinity scale
psu	Practical salinity unit
R	River outflow
RFI	Radio Frequency Interference
RMS	Root mean square
ROMS	Regional Ocean Modelling System
SEC	South Equatorial Current
S.H.	Southern Hemisphere
ShallMOC	Shallow Meridional Overturning Circulation
SMOS	Soil Moisture and Ocean Salinity
SPCZ	South Pacific Convergence Zone
SPURS	Salinity Processes in the Upper Ocean Regional Study
SSMIS	Special Sensor Microwave Image/Sounder

SSS	Sea surface salinity
SST	Sea surface temperature
STS	Surface temperature salinity
TACE	Tropical Atlantic Climate Experiment
Tb	Brightness temperature
THC	Thermohaline Circulation
TRMM	Tropical Rainfall Measuring Mission
TSG	Thermo-salinograph
UOS	Upper ocean salinity
VOS	Voluntary observing ship
WBC	Western boundary current
WOD	World Ocean Database
WOA	World Ocean Atlas
WOCE	World Ocean Circulation Experiment
WHOI	Woods Hole Oceanographic Institution

Chapter 1

Introduction

1.1 Motivation

A strengthening of the hydrological cycle in response to global warming will have a significant impact on Earth's climate, and consequently on society. Within the ocean, changes in the hydrological cycle modify the stratification, having an impact on oceans' capacity to transport heat, carbon and freshwater (e.g. *US CLIVAR Group*, 2007). However, our knowledge on this crucial component of climate system remains limited, as its greatest part occurs over the vast and unmonitored ocean (*Gordon and Giulivi*, 2008; *Schanze et al.*, 2010). There are few, scarce ocean rain gauges and no long-term network of meteorological stations which would provide century-long records for study of past climate variability (e.g. *Lagerloef et al.*, 2010), in addition to the poor quality of historical marine meteorological ship reports (e.g. *Durack and Wijffels*, 2010). Thus, lack of accurate measurements of freshwater fluxes over both land and ocean, hinders attempts to close the freshwater budget, and limits our understanding and ability to predict changes in the global water cycle in the context of climate change. Yet, intensification of the hydrological cycle over the last 50 years is suggested in coupled global climate models (e.g. *Allen and Ingram*, 2002; *Held and Soden*, 2006; *Meehl et al.*, 2007). Observational evidence of an intensified water cycle over land has been less compelling, since most variables such as river flows, Evaporation (E), or Precipitation (P) estimates show little trend (*Zhang et al.*, 2007; *Dai et al.*, 2009).

Changes in the water cycle will influence the ocean-atmosphere freshwater exchange, leaving consequently a fingerprint in ocean salinity (e.g. *Stark et al.*, 2006; *Gordon and Giulivi*, 2008). The ocean surface salinity (SSS) field (i.e. defined here in the top $\sim$5 m), resembling the global mean distribution of the E-P budget (e.g. *Boyer and Levitus*, 2002), exhibits the large-scale, long-term balance between E-P and terrestrial runoff, as well as the ocean's advective and mixing processes (e.g. *Durack and Wijffels*, 2010; *Helm et al.*, 2010). Hence, SSS offers the potential to serve as a rain gauge for E-P over the ocean (e.g. *Schmitt*, 2008;

Yu, 2011; *Pierce et al.*, 2012; *Terray et al.*, 2012) and salinity variations in recent decades can provide additional constraints on the freshwater fluxes (e.g. *Lagerloef et al.*, 2010; *Helm et al.*, 2010; *Yu*, 2011; *Bingham et al.*, 2011; *Durack et al.*, 2012). The relationship between the water cycle and ocean salinity is recognized in the Intergovernmental Panel on Climate Change (IPCC) 2007 (*Bindoff et al.*, 2007; IPCC, 2007) and 2013 reports (IPCC, 2013), highlighting the potential of salinity changes to act as a robust indicator of the strength of the hydrological cycle and its trends, in addition to providing a key index for monitoring future climate variability (e.g. *Schmitt*, 1995; *US CLIVAR Group*, 2007; *Yashayaev and Clarke*, 2008). Moreover, by influencing ocean density, salinity is directly linked to key ocean circulation processes such as the dense water formation at high latitudes (*Font et al.*, 2010a), and accordingly to the strength of the Atlantic Meridional Overturning Circulation (AMOC), playing a major role in the density-driven thermohaline circulation (THC) (e.g. *Manabe and Stouffer*, 1995). At lower latitudes, salinity-induced stratification can control the mixed-layer depth, and therefore, potentially regulate the heat and momentum exchanges between the ocean and the atmosphere through barrier layer effects (e.g. *Lukas and Lindstrom*, 1991).

During the last ∼50 years, widely reported trends of ocean salinity have been linked to a large-scale freshening in P-dominated and high-latitude regions, such as the Subpolar N. Atlantic and Nordic Seas (e.g. *Antonov*, 2002; *Curry et al.*, 2003; *Curry and Mauritzen*, 2005; *Boyer et al.*, 2007; *Bindoff et al.*, 2007; *Durack and Wijffels*, 2010; *Durack et al.*, 2012), and concurrent salinity increases at lower latitudes and E-dominated Subtropical Gyres in all oceans, particularly in the Southern Hemisphere (S.H) and the N. Subtropical Atlantic (e.g. *Antonov*, 2002; *Curry et al.*, 2003; *Boyer et al.*, 2005; *Wang et al.*, 2010; *Durack and Wijffels*, 2010). Accordingly, salinity inter-basin contrasts have been enhanced, with the Atlantic appearing increasingly salty, while the Pacific showing marked freshening (e.g. *Delcroix et al.*, 2007). Such changes have been mainly attributed to an anthropogenically intensified water cycle (e.g. *Curry et al.*, 2003; *Stott et al.*, 2008) and global warming conditions (*Cubasch et al.*, 2001), with increases in net P (including runoff) favouring freshening at high latitudes, and P decreases enhancing salinification in the Tropics and Subtropics (e.g. *Held and Soden*, 2006; *Zhang et al.*, 2007; *Wu et al.*, 2005; *Helm et al.*, 2010). In addition, larger water transport in the atmosphere from low to high latitudes and from the Atlantic to the Pacific (*Bindoff et al.*, 2007; *Gordon and Giulivi*, 2008), and additional freshwater into the ocean from land and ice melting (e.g. *Antonov*, 2002; *Dickson et al.*, 2007) further contribute to these salinity trends.

Some of this recently freshened water in the N. Atlantic Subpolar Gyre is expected to advect into the higher-latitude convection regions, and modify the rate of deep water formation and the N-S density gradient. Thus, it may have potential consequences for the strength of the THC (e.g. *Manabe and Stouffer*, 1995; *Josey and Marsh*, 2005), by slowing down or halting the AMOC (e.g. *Thorpe et al.*, 2001).

Meanwhile, model simulations show that, northward transport of increased salinity from lower latitudes could balance the freshwater accumulation at high latitudes and reverse the N. Atlantic freshening trend in the middle of the century (*Pardaens et al.*, 2008), enabling the MOC to recover after several decades (*Vellinga et al.*, 2002; *Vellinga and Wu*, 2004). Therefore, the Tropical-Subtropical ocean-atmosphere freshwater exchanges play a crucial role in the recovery of salinity in the N. Atlantic and MOC variability.

Given the above, and also the belief that the human fingerprint in salinity is likely to become more distinct over the next few years (e.g. *Schanze et al.*, 2010), it is essential to determine the causes of salinity changes on different time scales, in order to understand whether local changes represent trends or natural variability. The seasonal cycle represents the strongest source of salinity variability in the Tropical Atlantic (e.g. *Foltz and McPhaden*, 2008), thus an improved understanding of SSS variability on short time scales is of primary importance for a more comprehensive insight into the observed longer-term salinity changes. In addition, the link of the Tropical/Subtropical Atlantic basin to the mid-latitude climate at seasonal to decadal time scales (e.g. *Van den Dool et al.*, 2006), further highlights the need to better understand and describe the variability in the region, given its impacts on the sustenance of a large rural population which strongly depends on precipitation (*Polo et al.*, 2008).

The Tropical Atlantic encompasses two dynamic regions dominated by large freshwater discharge from the major Amazon/Orinoco and Congo/Niger river systems on either side of the basin. The Amazon/Orinoco plume, playing a major role in determining the SSS variability in the Western Equatorial basin, has attracted most of the scientific attention primarily due to the formation of barrier layers, which influence the heat exchange between the ocean and the atmosphere (e.g. *Hu et al.*, 2004; *Foltz and McPhaden*, 2008; *Romanova et al.*, 2011; *Grodsky et al.*, 2012; *Grodsky et al.*, 2014a). On the other hand, our knowledge on the role of the Congo/Niger plume in the Gulf of Guinea is still very limited despite its importance over the Eastern Tropical Atlantic. For instance, SSS variations in the Gulf of Guinea are linked to sea surface temperature (SST) anomalies and the cold tongue in the Eastern Equatorial Atlantic, coastal upwelling, the ocean circulation, P patterns and atmospheric modes (e.g. *Materia et al.*, 2012). However, there has been substantial uncertainty on the principles of the SSS seasonal cycle and its interannual (and longer-term) variability in the region, and the role of the Congo plume on it (e.g. *Denamiel et al.*, 2013). In addition, there is no information (to the author's knowledge) on the influence of other main rivers in the Gulf of Guinea, such as the Niger river outflow, and equally important, on the combined impact of these two large rivers on the regional SSS variability. As fresh anomalies from the Amazon/Orinoco region may propagate as far as the westernmost Gulf of Guinea (e.g. *Coles et al.*, 2013), this indicates the potential connectivity of the two riverine regions. Therefore, better knowledge on the salinity variability, and

in relation to the relative impact of variations in freshwater fluxes and river runoff in these dynamical regions, will also provide a more realistic view of the salinity field and its role over the wider Tropical/Subtropical Atlantic basin.

Nevertheless, the scarcity and uncertainties of SSS and upper ocean salinity (UOS, i.e. defined here between ∼5-10 m depth, typically measured by Argo profiles) observations lead to inadequate depiction of the spatio-temporal features of the salinity distribution and variability. In addition, uncertainties in freshwater datasets, particularly P records which are characterized by noisy, high-frequency spatio-temporal variations, further prevent us from closing the global water budget with confidence and fully interpreting the observed salinity long-term trends (e.g. *Schanze et al.*, 2010). Models contain long-term drifts in ocean data that could degrade any climate change signal (*Stott et al.*, 2008), and their relative inability to reproduce the observed SSS changes is largely due to the poor accuracy of air-sea fluxes. For instance, coupled general circulation models (GCMs) often display several biases in the representation of the Tropical Atlantic main features, including the generally overestimated spring P south of the equator which leads to erroneous position of the InterTropical Convergence Zone (ITCZ), (e.g. *Stockdale et al.*, 2006; *Breugem et al.*, 2007). Likewise, reanalysis data are characterized by large biases in the freshwater fluxes, and often result in unrealistic trends and incorrect seasonal cycles. On the other hand, there are also still significant gaps of knowledge of what information on the oceanic freshwater transport can be derived from atmospheric E-P climatologies and oceanographic data, respectively (*Lagerloef et al.*, 2010). Thus, each product has in general its own advantages and disadvantages, and the choice rather depends on the desired application, although one based on satellite data should display the geographical locations of P correctly (*Quartly et al.*, 2007). Satellite P estimates are of better quality in Tropical/Subtropical regions, while uncertainties increase towards higher latitudes (*Schanze et al.*, 2010). Further information on the freshwater fluxes and their uncertainties are provided in Chapter 3.

Recently, a new opportunity for studying SSS has arisen with the advent of SSS maps from the ESA Soil Moisture and Ocean Salinity (SMOS, e.g. *Kerr et al.*, 2010), and the NASA/Argentina Aquarius/SAC-D (*Lagerloef et al.*, 2008) missions. The two satellites measure salinity at the first 1 cm of the sea surface, which may differ from the top 5 m depth level typically measured by Argo as a result of vertical salinity stratifications, especially in rainy and river outflow regions and to sharp oceanic fronts (e.g. *Henocq et al.*, 2010; *Boutin et al.*, 2013). Further information on the representativeness of SMOS SSS and variations between satellite and in situ salinity are provided in Chapter 3. Thus, satellite-derived SSS observations will complement in situ measurements, contributing significantly to globally increased sampling and resolution of SSS observations and thus, to a better understanding of the spatio-temporal SSS distribution and variability. Together with improved in situ salinity sensors on drifting and profiling platforms, such as Argo

floats and gliders, this should provide an unprecedented three-dimensional view of ocean salinity patterns, and a more comprehensive monitoring of SSS variations in dynamical regions, such as close to the major river systems. In turn, this should improve our understanding of the upper ocean processes, and the estimation of the upper ocean salinity budget and global marine freshwater balance, and thus of the marine hydrological system and ocean dynamics (e.g. *Gordon and Giulivi*, 2008). This information will benefit other oceanographic fields, such as improved ENSO forecasting and better ocean-atmosphere and climate models.

1.2 Aims and objectives- Approach of this project

The rationale behind this work is to take advantage of the availability of spatially dense SSS observations from SMOS in order to obtain more detailed oceanographic information on the SSS distribution and variability. Due to the short record of satellite SSS observations, particularly as this PhD project commenced only a few months after the SMOS launch, the focus of this research is on relatively short time-scales, i.e. seasonal to interannual. The region of interest is the Tropical/-Subtropical Atlantic 30°N-30°S, which, as highlighted above, plays an important role on the MOC and the density-driven THC due to the transport of freshwater and salt to higher latitude dense-water formation regions. Encompassing the E-dominated Subtropics and P-dominated Tropics, the Atlantic basin 30°N-30°S also offers the opportunity to investigate the role of surface freshwater fluxes, i.e. E-P and river outflow (R), on SSS in these dynamically different regimes.

Using the first complete year of SMOS observations (2010), the present thesis initially examines the seasonal cycle of SSS in the Tropical Atlantic, in conjunction with the ITCZ movement and the influence of the two major river systems of the Amazon/Orinoco and Congo/Niger on the western and eastern side of the basin, respectively. Subsequently, this work is extended over the first 3 years of SMOS observations (2010-2012) to obtain a first insight into the interannual variability of the SSS seasonal cycle, and the relative impact of E, P, E-P and R variability over the Tropical Atlantic basin as a whole and in the two river-dominated regions.

Next, the research focuses on the description of the spatial and temporal characteristic scales of SSS variability from SMOS over the whole Tropical/Subtropical Atlantic basin 30°N-30°S, considering both the E- and P-dominated regimes. The aim is to identify potential regions where homogeneous SSS variations occur over large distances on seasonal to interannual time scales, and/or where SSS changes show the longest persistence in time. This helps further the definition of the SSS variability over the different regimes, while increasing our understanding of the most dominant processes influencing the SSS changes in each region. Finally, in an attempt to examine the salinity budget, this work explores the retrieval of the E-P field from satellite SSS variations. The goal is to determine the extent to

which the SMOS salinity field reflects: the main characteristics of the E-P distribution in the Evaporative Subtropics, and the presence of strong, ITCZ-driven P patterns in the Tropics, on monthly to seasonal time scales.

1.3 Structure of this thesis

The structure of this thesis has as follows: Chapter 2 presents a review of previous studies about the most significant mechanisms controlling the SSS and UOS and its global distribution and variability on different time scales, with a particular focus on the Tropical/Subtropical Atlantic basin 30°N-30°S. The description of the different datasets used in the present thesis and issues regarding their uncertainties are presented in Chapter 3, while the research results are included in Chapters 4-7. The study of the seasonal variability of SSS in the Tropical Atlantic is presented in Chapter 4, followed by the examination of the interannual variability of SSS seasonal cycle over the same region in Chapter 5. Chapter 6 presents the analysis of the space and time scales of SSS variations over the Tropical/Subtropical Atlantic. The exploratory examination of the SSS budget and the reconstruction of the E-P field from SMOS SSS changes takes place in Chapter 7. Finally, the main results are summarized and discussed in Chapter 8, which presents the achievements of this PhD thesis, and makes suggestions for future research.

Chapter 2

Background

2.1 Controlling mechanisms of salinity

2.1.1 Salinity and freshwater fluxes

Salinity is a dimensionless oceanographic parameter which serves as a measure for the concentration of the total salt content in seawater (*Schmitt*, 1995; *Yashayaev and Clarke*, 2008), including chlorine (55%), sodium (31%), and sulphate (8%), with ratios that are nearly constant from place to place (e.g. *US CLIVAR Group*, 2007). Traditionally, salinity was expressed in parts per thousand, while in recent decades it was defined using the Practical Salinity Scale of 1978 (PSS-78) based on conductivity measurements for seawater from the N. Atlantic (*Lewis and Perkin*, 1978). This non-dimensional measure of salinity is often denoted without units or by the practical salinity unit (psu) or scale (pss), (*Dauphinee*, 1980).

The salinity properties of surface waters are set by air-sea, ice-sea and land-sea exchanges of water. Salinity is remarkably uniform on a global scale. The mean salinity of ocean's waters is 34.7 pss, with a small distribution about the mean, i.e. 50% of seawater is within the range of ∼34.6-34.8 pss (*Stewart*, 2007), and 99% between ∼33.1-37.2 pss (*Worthington*, 1981). Nevertheless, although the salt content of the world ocean is approximately conserved, its local or regional signatures are influenced by the ocean circulation induced freshwater and salt fluxes (e.g. *Yashayaev and Clarke*, 2008), in response to the highly spatially variable sea-air freshwater exchange (*Gordon and Giulivi*, 2008). Thus, the distribution of sea surface salinity (SSS, i.e. defined here in the top ∼5 m) and near-surface or upper ocean salinity (UOS, i.e. defined here between ∼5-10 m depth, typically measured by Argo profiles) in the global ocean tends to be zonal (*Stewart*, 2007), reflecting the climate belts associated with the general atmospheric circulation. This is seen, for instance, in Figure 2.1, which depicts the climatological annual mean field of the objectively analyzed SSS from the World Ocean Atlas 2009 (WOA09, *Antonov*

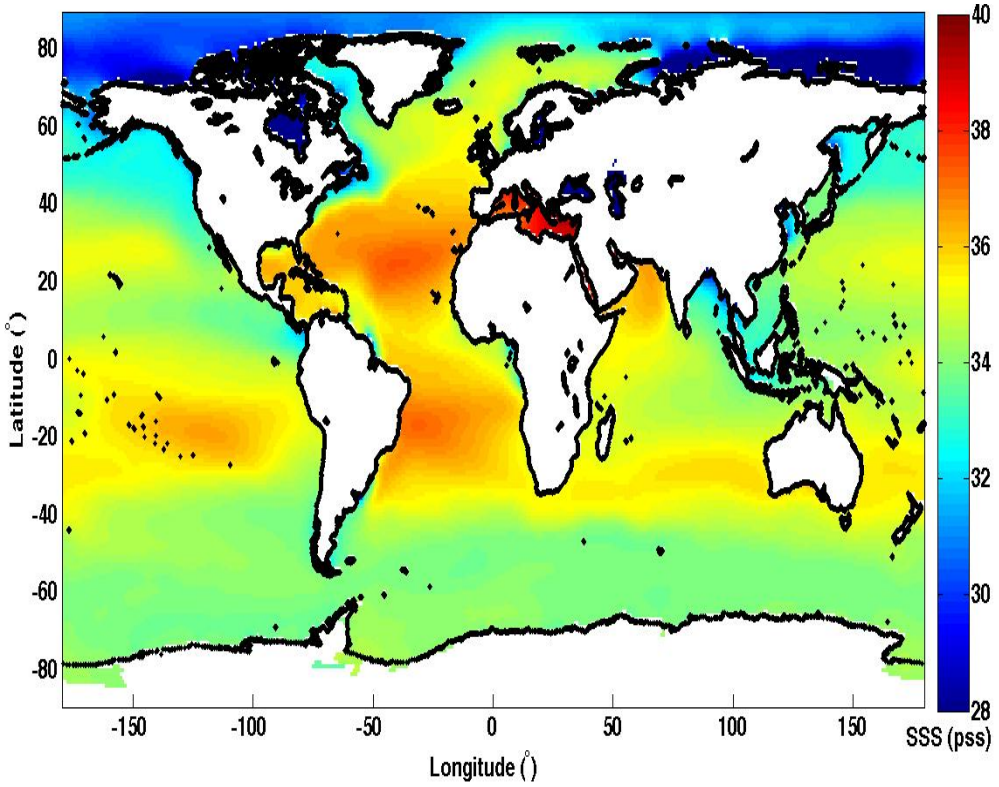

Figure 2.1: Climatological annual mean field of objectively analyzed SSS from the WOA09 (1955-2006).

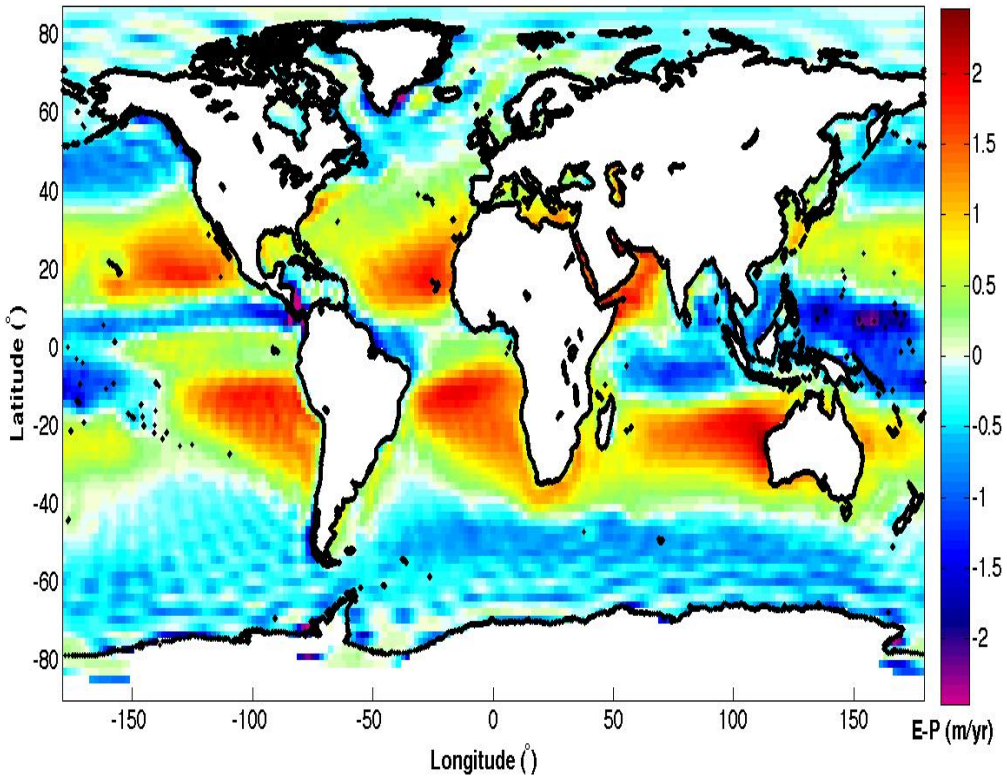

Figure 2.2: The (unsmoothed) climatological annual mean field of E-P from NCEP-1 (1955-2006).

et al., 2010). Comparison of the spatial patterns between mean SSS and net sea-air freshwater fluxes (Figure 2.2) reveals remarkable similarities, with the former

being first-order reminiscent of the mean distribution of the Evaporation minus Precipitation (E-P) budget (e.g. *Boyer and Levitus*, 2002; *Schmitt*, 2008). This is evident when comparing the WOA09 SSS in Figure 2.1 with the climatological annual E-P mean field from NCEP-1 seen in Figure 2.2 over the same period (1955-2006).

E and P have opposite effects on sea surface water, with P making it fresher and reducing the surface salinity and density, while E leads to salt enrichment of the ocean surface and increase in density (e.g. *Cronin and McPhaden*, 1999). P also differs from E in terms of intensity, duration, and spatial extent. As long as the air is unsaturated, E takes place at all times and over all regions, while P occurs sporadically, over confined areas and its duration varies (*Yu*, 2010). Typically, dominance of E, and thus, loss of freshwater, occurs over the eastern parts of the Subtropical Gyres, with similar patterns and extreme freshwater loss between ∼10°-20° N-S in both the Atlantic, Pacific and Indian Oceans (Figure 2.2). Interestingly, there is a characteristic asymmetry in freshwater loss between the two Hemispheres, with the Southern Hemisphere having a larger E-dominated area compared to the Northern Hemisphere (*Vinogradova and Ponte*, 2013). Thus, higher salinities are generally found at mid-latitudes where E is high (Figure 2.1). Significant SSS maxima, associated with each Subtropical high, reside in the latitude band 15°-30° in each Hemisphere, resembling the great Subtropical land deserts at the poleward edges of the atmosphere's Hadley cells (*Gordon and Giulivi*, 2008), and being preserved by E under the trade winds and Ekman convergence (*Lagerloef et al.*, 2010).

In contrast, lower salinities are found near the equator (Figure 2.1) along the Tropical latitudinal band of the highly precipitating InterTropical Convergence Zone (ITCZ), where there is net P (Figure 2.2). In these regions, the temporal variability of P determines much of the net surface freshwater flux temporal variability (*Yoo and Carton*, 1990). In addition, oceanic gain of freshwater and thus low SSS is found in high latitudes polewards of 40° N-S, where in addition to excess P, melted sea ice freshens the surface waters (e.g. *Stewart*, 2007). Finally, terrestrial runoff (R) represents another key hydrological component of freshwater exchanges between the ocean and land. Together with E-P, the resulting ocean surface freshwater flux E-P-R, consist of ∼80% of the Earth's total surface water flux (e.g. *Durack et al.*, 2012). Thus, strong SSS decreases are noted in coastal regions where continental freshwater runoff dilutes the surface ocean (e.g. *Lagerloef et al.*, 2010), particularly close to discharge plumes of major rivers such as the Amazon, Congo, and Ganges/Brahmaputra (Figure 2.1).

The marine hydrological cycle also varies in longitude, revealing significant differences in different oceanic basins, particularly the higher salinities of the Atlantic relative to the Pacific (see, for instance, Figure 2.1), where net input of freshwater results in low salinity (*Schmitt*, 2008). This occurs because the air overlying the

water becomes saturated in humidity, and E, as a function of the latter (*Fairall et al.*, 2003), decreases as the air is driven westward by the trade winds. The arrangement of continents and the narrowness of the Atlantic also play a role, given that a greater fraction of its surface area is under the influence of dry continental air. Thus, moisture is easily transferred to the Pacific across the Central American Isthmus, but there is little transport from the Indian Ocean to the Atlantic and no significant moisture transport from the Sahara Desert (*Schmitt*, 2008). This salinity contrast is the prime reason that the Atlantic supports a Meridional Overturning Circulation (MOC) and the Pacific does not, since the lower salinity of the N. Pacific inhibits deep convection in that basin (e.g. *Emile-Geay*, 2003).

2.1.2 Other controlling mechanisms of near surface salinity

In addition to air-sea freshwater exchange and changes in the balance of E and P at the ocean surface, various other mechanisms are expected to be also vital in controlling the near surface salinity. Therefore, SSS signatures from areas with extreme changes in E-P, affected by variations in river discharge, or subject to sea ice formation/melting variations are also moved by ocean currents, resulting in the advective redistribution of water masses with different salinities (e.g. *Mignot and Frankignoul*, 2003; *Yu*, 2011). Horizontal advection by Ekman currents and mixing play an important role in determining the distribution of SSS, while together with E-P forcing, usually explain reasonably well the magnitude of SSS variability away from the equator (e.g. *Schmitt*, 2008; *Yu*, 2011).

The Subtropical Gyres are characterized by anticyclonic circulation with swift Western Boundary Currents (WBC) and slower, equatorially-bounded return flows in the interior. Thus, the area of maximum E-P, the main process for the formation of the salinity maximum, is displaced equatorwards relative to the SSS maximum region, indicating the role of horizontal transport. Accordingly, the SSS maximum lies towards the eastern-central Subtropical Gyres, controlled by a combination of excess E over P, poleward Ekman (i.e., ageostrophic) advection, subduction and horizontal eddy flux (e.g. *Johnson et al.*, 2002; *Schmitt*, 2008; *SPURS Workshop Report*, 2010). On the other hand, advection by the ocean currents also plays an important role for the transport of freshwater plume over large distances away from the mouth of major rivers, such as the Amazon River (e.g. *Coles et al.*, 2013). Therefore, changes in the advection of water with different salinity characteristics are likely to have a significant impact on the SSS variability, as for instance, at interannual time scales in the Tropics and the Gulf Stream region (*Mignot and Frankignoul*, 2003), where the contribution of advection is large (*Mignot*, 2004). Moreover, changes in both the circulation of currents and the salinity of water carried by them, contribute to freshwater transport anomalies, such as those seen in the N. Subtropics (30°N) and in the high-latitude Atlantic (59°N), (*Pardaens et al.*, 2008).

The upper ocean salinity can be also influenced by vertical mixing entrainment among other processes (*SPURS Workshop Report*, 2010). The stratification of the near surface mixed layer is homogenized by turbulent and convective processes. Within the mixed layer, the salinity budget corresponds to the concentrating impacts of E or the diluting effects of freshwater, balanced by the influence of horizontal freshwater divergence, entrainment flux across the base of the mixed layer, and diffusive processes (*US CLIVAR Group*, 2007). In general, towards the Subtropical salinity maximum, more saline water is subducted, whereas poleward and away from it, more fresh water is subducted (*Durack and Wijffels*, 2010). Polewards of the salinity maximum regions, both salinity and temperature decrease, whereas equatorward, salinity decreases while temperature increases, leading to smaller large-scale meridional density gradients than those expected from temperature alone (e.g. *Johnson*, 2006). These temperature-salinity compensated waters, classified as mode waters due to their relatively vertically uniform temperature, salinity, and especially density (*Hanawa and Talley*, 2001), are subducted in the Eastern Subtropics of most ocean basins poleward of the Subtropical salinity maxima, injecting variable water-mass properties into the Subtropical thermocline.

Finally, neighbouring regions can further influence the salinity content in a region, as for instance the outflow of Mediterranean Sea, which contributes significantly to climatological changes of temperature and salinity at intermediate depths of the mid-latitude N. Atlantic (*Potter and Lozier*, 2004). Hence, changes in mixing processes along the water mass pathways, subduction and circulation by the ocean's mean flow, and the associated advective effects, influence changes both in surface and subsurface salinity (e.g. *Helm et al.*, 2010; *Durack and Wijffels*, 2010). As regards the controlling mechanisms of SSS and near-surface salinity in the Tropical and Subtropical Atlantic basin, more background information are presented in Section 2.3, which focuses further on the region of interest in this thesis.

2.1.3 Global near-surface salinity variability in different scales

Changes in SSS reflect a complex balance between atmospheric and oceanic processes over a large range of time scales from months to years. Over extensive oceanic areas, including Tropical, coastal, and WBC regions, both freshwater fluxes and oceanic dynamics, i.e. mixing, advection, and entrainment, contribute equally to near-surface salinity variability (e.g. *Vinogradova and Ponte*, 2013). In general, if advection and mixing processes occur over long enough time scales (e.g., low-wind, slow-current conditions), salinity fluctuations relate more directly to the freshwater changes. Based on in situ salinity observations, including Argo and World Ocean Database (WOD) data, and National Center for Environmental Prediction (NCEP) E-P estimates, it is shown that, at seasonal time-scales, the cycles of near-surface salinity and freshwater fluxes over the globe compare reasonably well, albeit differences in amplitude and phase-relationship shifts (*Bingham et al.*,

2011). This, in turn, highlights the importance of horizontal salt advection in the seasonal salinity balance as well (e.g. *Foltz et al.*, 2004; *Foltz and McPhaden*, 2008). Thus, observational analysis of the mixed layer salinity (MLS) budget indicates that freshwater fluxes together with oceanic dynamics explain about 40% of the seasonal MLS variability over the global ocean, given uncertainties in the data and unresolved low-order salinity dynamics (*Yu*, 2011).

In general, vast parts of the world ocean are characterized by weak surface salinity variability of typically up to ∼0.1-0.3 pss at all time scales. This is also apparent in Figure 2.3, which shows the annual range of climatological SSS mean field from WOA09 between 0-4 pss (95% quantiles). Smallest variations are found at the SSS maxima and the centers of the Subtropical Gyres, which feature high, but almost constant E rates, while oceanic fluxes display small variability due to light winds and weak currents. Over an annual cycle, most of world ocean is shown to have a relatively small horizontal SSS variability of less than 0.3 pss, particularly in the Subtropics and high latitudes, and secondarily in the WBC regions (e.g. Kuroshio extension, Gulf Stream), (e.g. *Boutin and Martin*, 2006; *Yu*, 2011; *Vinogradova and Ponte*, 2013).

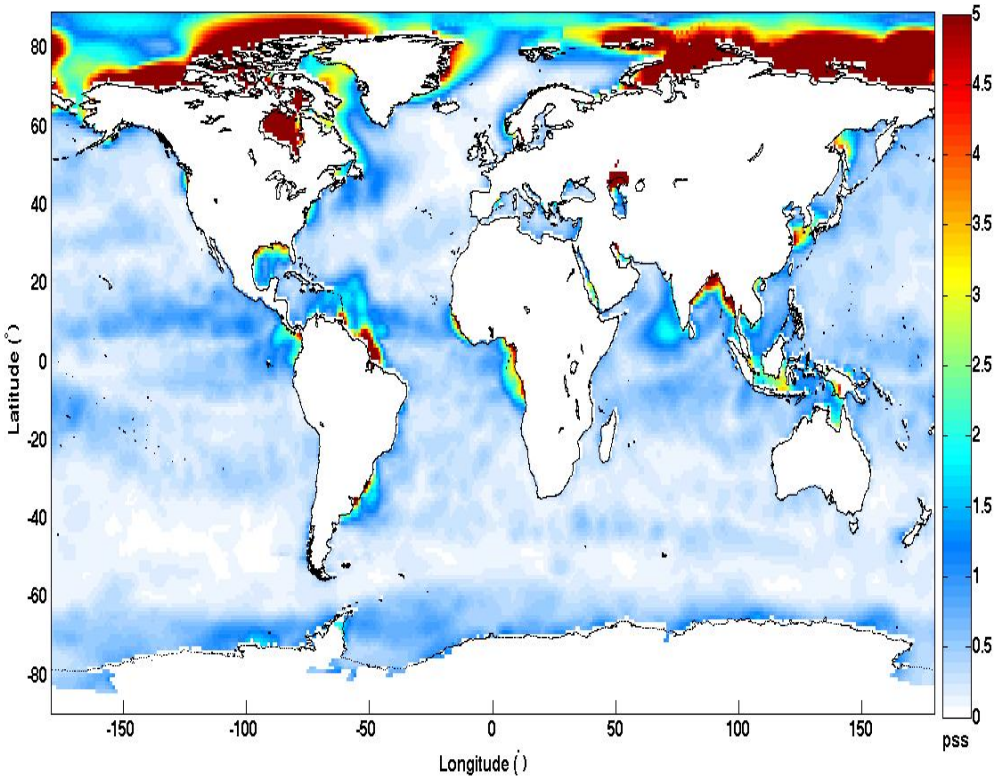

Figure 2.3: Annual range of climatological monthly mean of objectively analyzed SSS from WOA09 (1955-2006).

In contrast, large seasonal variability of the SSS and near-surface salinity is found in the Tropical Oceans, where the amplitude of freshwater variations is comparable with oceanic dynamics, and both mechanisms contribute to sub-annual salinity variations. Thus, both at annual and interannual time-scales, Tropical SSS

variations are induced by changes in P under the migrating ITCZ and South Pacific Convergence Zone (SPCZ), and are further governed by advection processes, partly related to variability in equatorial currents (e.g. *Dessier and Donguy*, 1994; *Donguy and Meyers*, 1996; *Yu*, 2011), or mixing processes, such as in regions of the Tropical Pacific and Atlantic Oceans (*Vinogradova and Ponte*, 2013). Finally, riverine discharge also plays an important role on the annual SSS cycle, particularly the annual range of outflow volume and the month of minimum outflow, while the seasonal variability of the ocean circulation redistributes the riverine freshwater (*Boyer and Levitus*, 2002). Thus, noticeable seasonal variations of SSS also occur in proximity to large river outflow regions, such as close to the Amazon, Congo, Mississippi, La Plata, and Ganges/Brahmaputra River mouths, as also seen in Figure 2.3.

On shorter time-scales, SSS and near-surface salinity also vary at sub-monthly periods. The horizontal SSS variability at 10-days and 200-km scales is generally above 0.1 pss and larger than 0.2 pss in frontal areas characterised by strong mesoscale activity, e.g. the Gulf Stream region, and Tropical regions affected by strong river discharges and intense P events (e.g. *Delcroix et al.*, 2005; *Boutin and Martin*, 2006; *Vinogradova and Ponte*, 2012). Vertical salinity gradients between the 0-5 m and 5-10 m layer depth are, in general, an order of magnitude smaller than the horizontal variability (*Boutin and Martin*, 2006). However, in the Tropics, large vertical gradients can develop in the upper layer of the ocean after heavy P, with this downward freshwater flux at the sea surface establishing a freshwater skin layer, across which salinity differences can exceed sometimes several pss (e.g. *Wijesekera and Gregg*, 1996). Rain-induced freshening has been observed between 15-50 cm depth in the Tropical Oceans (*Reverdin et al.*, 2012), depending among other parameters on wind speed conditions. Under weak wind-induced mixing conditions, the strong vertical salinity gradient can persist for a few hours (e.g. *Reverdin et al.*, 2012; *Boutin et al.*, 2013), and dampen free convection in the upper boundary layer of the ocean (e.g. *Reul et al.*, 2013).

In contrast, under E conditions, latent heat and water vapour are released to the atmosphere, resulting to surface cooling and salt enrichment of the skin layer, respectively (e.g. *Yu*, 2010; *Zhang and Zhang*, 2012), particularly between 25°-35° N-S of the equator, where E forcing is predominant. The skin layer is cooler by 0.2°-0.5°C and saltier by 0.05-0.15 pss (*Yu*, 2010) or 0.1-0.13 pss on average at low latitudes than the warmer and less salty interior, and forms a surface density gradient which is unstable and tends to overturn. Although both cool and haline skin layers, with mean thickness of $\sim$1mm and $<$0.1 mm respectively (*Zhang and Zhang*, 2012), contribute to the surface skin density and density gradient, the surface density flux in the Tropical oceans is controlled primarily by changes of temperature. Hence, cooling rather than salinity increase is more critical in controlling the surface buoyancy and convective instability (*Yu*, 2010; *Zhang and Zhang*, 2012). However, salinity stratification is considered to act as a limiting

factor for strong cooling to develop. After the overturning of the skin layer, the estimated restoration time to re-establish the full increase of skin salinity is of the order of 15 min, i.e. approximately 90 (*Yu*, 2010) or at least 31 times slower than that for skin temperature (*Zhang and Zhang*, 2012).

On an interannual basis, substantial year-to-year variations of the surface freshwater fluxes also reflect the impact of atmospheric modes in modifying the SSS variability, such the El Niño Southern Oscillation (ENSO) in the Tropics (e.g. *US CLIVAR Group*, 2007; *Gouriou and Delcroix*, 2002; *Singh et al.*, 2011). Given that SSS anomalies do not directly introduce air-sea feedbacks like SST, such year-to-year SSS changes last, having an impact on SSS climate (e.g. *Foltz and McPhaden*, 2008). Furthermore, the N. Pacific Oscillation (NPO, or PDO) has a modulating effect on ENSO teleconnections, since during the high phase of the NPO, the typical El Niño patterns are strong and consistent. This has implications on the atmospheric teleconnection of the Pacific climate into the Subtropical N. Atlantic, given that the same shift is found to occur in their El Niño-P relationship (e.g. *Gordon and Giulivi*, 2008). On the other hand, upper ocean salinity in the N.E. Atlantic is also affected by the North Atlantic Oscillation (NAO), having its major impact near 40°-50°N during winter. A positive NAO phase is associated with a northward displacement of the Gulf Stream, and thus, an increase of SSS north of the Gulf Stream, but also with an anomalously negative contribution of Ekman advection due to higher winds (e.g. *Reverdin et al.*, 2007).

Finally, on longer time-scales, regional trends of SSS have been reported in all oceanic basins since 1950s, enhancing its geographical contrasts. Thus, saline SSS waters in the E-dominated mid-latitudes have become more saline, such as the SSS Subtropical maxima, while relatively fresh SSS waters in the P-dominated Tropical and polar regions have become fresher (e.g. *Boyer et al.*, 2007; *Durack and Wijffels*, 2010; *Durack et al.*, 2012). Furthermore, inter-basin salinity differences have enhanced, with the Pacific becoming even fresher, while the relatively salty Atlantic becoming saltier (e.g. *Durack and Wijffels*, 2010). Similarly, the subsurface salinity also exhibits multi-decadal trends, compatible with the observed changes in SSS (e.g. *Boyer et al.*, 2007; *Durack and Wijffels*, 2010; *Helm et al.*, 2010; *Wang et al.*, 2010). These subsurface changes are considered to originate from the surface, mainly due to subduction of SSS anomalies formed by E-P changes (e.g. *Helm et al.*, 2010; *Durack and Wijffels*, 2010; IPCC, 2013).

2.2 Measuring and monitoring salinity

Over the last decade, the importance of surface and subsurface salinity in understanding and predicting the climate variability has been increasingly documented, including the last reports of the Intergovernmental Panel on Climate Change (IPCC, 2007; IPCC, 2013), and the US Climate Variability and Predictability

World Climate Research Program (CLIVAR) Salinity Working Group (*US CLIVAR Group*, 2007). This has provided the motivation to more comprehensively and accurately measure and monitor the ocean salinity. Improved observation systems will give better insight into the processes that control and are controlled by salinity, thus, contributing to better understanding of the oceanic water cycle (*SPURS Workshop Report*, 2010).

Nowadays, SSS measurements are used for a wide range of oceanographic fields of research and applications. These include the ocean's response to meteorological forcing, the description and understanding of climate and multi-decadal variability in the Atlantic (e.g. *Dessier and Donguy*, 1994), Pacific (e.g. *Delcroix and Hénin*, 1991) and Indian Oceans (e.g. *Donguy and Meyers*, 1996). In addition, they inform our understanding of events such as the Great Salinity Anomalies in the N. Atlantic (e.g. *Häkkinen*, 2002), which provide a salinity signature of ocean variability at periods greater than 1 year. Moreover, salinity variations play an important role to the current circulation in regions of the Indian Ocean (e.g. *Menezes et al.*, 2013), or in other oceanic areas such as the California Current System (*Batteen et al.*, 1995), where both salinity and temperature are necessary to adequately characterize the large scale circulations.

Better observations of salinity help understand its role in sea level and geostrophic currents, and can be of use, for instance, in combination with dynamic height measured from altimetry in areas where the halosteric and thermosteric components of sea level are of comparable size and opposite sign (e.g. *Maes*, 1998; *Antonov*, 2002). Salinity observations help identify the formation of barrier layers (BLs), as in the western Tropical Pacific (*Lukas and Lindstrom*, 1991; *Vialard and Delecluse*, 1998), and it is linked to the El Niño generation (*Hénin et al.*, 1998), contributing to ENSO prediction in statistical models (*Ballabrera-Poy et al.*, 2002). Improved model representation of BLs has been shown to result in improved estimates of the P field in ocean coupled models (e.g. *Balaguru et al.*, 2012).

Given the good correspondence between SSS and E-P, salinity data can help to better constrain both the uncertain estimates of E and P (e.g. *Lagerloef et al.*, 2010), as well as freshwater runoff (*Romanova et al.*, 2011). SSS is used as a boundary condition for general circulation models forced by freshwater fluxes at the surface, so that SSS data will contribute to the assessment of numerical model performance (e.g. *Vialard*, 2002) and will enable the improvement of model parameterizations of key processes. These include, among others, ocean mixing and water mass formation that also influence the sequestration of carbon and heat (*Lagerloef and Font*, 2010; *Durack and Wijffels*, 2010), and modelled mixed layer representation via data assimilation (e.g. *Durand and Gourdeau*, 2002). Moreover, salinity observations contribute to hypothesis testing of physical processes (e.g. *Delcroix and McPhaden*, 2002), and reconstruction of CO_2 flux at the ocean-atmosphere interface (*Loukos et al.*, 2000). Last, but not least, routinely collected

and real-time transmitted in situ SSS data are crucial for the validation of the two satellite missions dedicated to SSS observations, the European SMOS (e.g. *Font et al.*, 2010b) and the NASA/Argentina Aquarius/SAC-D (e.g. *Lagerloef et al.*, 2008; *Lagerloef and Font*, 2010). These will be, in turn, a valuable source of SSS information in the aforementioned applications, among others.

2.2.1 In situ observations and observing systems- focus on Atlantic Ocean

Until recently and before the advent of satellite-derived SSS observations, most of the information about the spatio-temporal characteristics and variations of salinity came from series of in situ observing programs such as the Voluntary Observing Ship (VOS) thermo-salinograph (TSG) program (e.g. *Dessier and Donguy*, 1994), climatological fields available in the World Ocean Atlas such as WOA09 (e.g. *Antonov et al.*, 2010), as well as the recently deployed Argo profiling floats (e.g. *Roemmich et al.*, 2009; *Boutin and Martin*, 2006). Consequently, given the distribution, density and availability of the measurements, examination of the salinity budget based on observations has been typically focused on the Tropics (e.g. *Foltz et al.*, 2004; *Foltz and McPhaden*, 2008), and to a lesser degree on high latitudes (e.g. *Bingham et al.*, 2010; *Ren and Riser*, 2009; *Ren et al.*, 2011) and near-globe (e.g. *Yu*, 2011; *Bingham et al.*, 2011).

As regards the Atlantic Ocean, salinity monitoring is an essential part of various research programs, including the Tropical Atlantic Climate Experiment (TACE, 2006-2011), (e.g. *Brandt et al.*, 2013), and the Prediction and Research Moored Array in the Atlantic (PIRATA). The PIRATA array, located at various positions between 21°N-19°S, provides salinity data at four depths between 1-120 m continuously since 1997 (*Bourlès et al.*, 2008). Such measurements have contributed significantly to the examination of various salinity-related processes and the MLS balance in the Tropical Atlantic basin (e.g. *Foltz et al.*, 2004; *Foltz and McPhaden*, 2008). In addition, combined with satellite SSS (e.g. *Grodsky et al.*, 2014b) and/or model outputs (e.g. *Coles et al.*, 2013), they are used for improving the description and understanding of salinity variability close to river plumes, such as the Amazon plume in the Western Atlantic and along its freshwater pathways.

More recently, the Salinity Processes in the Upper Ocean Regional Study (SPURS-1) Field Experiment (*SPURS Workshop Report*, 2010) focuses on the E-dominated Subtropical Atlantic SSS and subsurface salinity maximum region, aiming to determine the physical processes responsible for its location, magnitude and maintenance. For this purpose, the region between ∼15°-30°N, 30°-50°W, is routinely monitored since 2012 by a combined observing system of in situ measurements from profiling floats, moorings, gliders, research cruises and VOS, complemented by satellite SSS observations. Thus, along with ocean models, SPURS-1 hopes to provide a 3-D representation of the salinity field and its variability in the region.

2.2.2 Models

Modelling serves as another source of information on the spatio-temporal characteristics and variability of salinity, and its response to climate change. The main focus of many numerical studies has been the large-scale salinity changes in the Atlantic basin over the last decades (e.g. *Pardaens et al.*, 2008; *Stott et al.*, 2008), in relation to the Thermohaline Circulation (THC) and Atlantic Meridional Overturning Circulation (MOC) variability, potential slowdown and recovery (e.g. *Vellinga et al.*, 2002; *Vellinga and Wu*, 2004; *Wu et al.*, 2004; *Grist et al.*, 2009). On the other hand, outputs from ocean circulation models provide an alternative approach to examine the salinity balance and the relative contribution of each governing process (e.g. *Vinogradova and Ponte*, 2013), given that model-based estimates satisfy the budget closure exactly, both in a specific region (*Qu et al.*, 2011) and globally, on different time scales (e.g. *Vinogradova and Ponte*, 2013). Nevertheless, models contain long term drifts that could degrade any climate change signal, and their relative inability to reproduce the observed SSS changes is largely due to the poor accuracy of air-sea fluxes, particularly of P. Therefore, improved definition of SSS variability would be a valuable constraint on these fluxes (e.g. *Vialard*, 2002).

2.2.3 Remotely-sensed salinity observations from SMOS and Aquarius missions

With different spatio-temporal resolution and sampling, the SSS products from the SMOS (ESA) and Aquarius/SAC-D (NASA) offer complementary information to supplement our knowledge of SSS from in situ measurements and models. Details about remote sensing of SSS and the SMOS mission can be found in Chapter 3. Despite the short record, satellite SSS observations have already proved their value towards a better description of various key processes of the marine hydrological cycle. Nowadays, satellite SSS enables a more detailed analysis of the influence of river plumes (e.g. *Grodsky et al.*, 2014a; *Grodsky et al.*, 2014b), and the seasonal variability of SSS in these dynamic regions of large freshwater input. Furthermore, in synergy with other satellite and in situ data, satellite SSS allows a more comprehensive investigation of the causes and impact of plumes' variability, evolution and advection pathways along surface currents (*Grodsky et al.*, 2014a; *Grodsky et al.*, 2014b; *Reul et al.*, 2013). For example, the spatio-temporal consistency between SSS and optical properties from satellite ocean colour sensors, e.g. CDOM, of the river plume can be now systematically examined (*Salisbury et al.*, 2011).

Moreover, SSS from SMOS is used for the study of E-dominated SSS maximum regions, as shown for the S. Pacific (*Hasson et al.*, 2013). Key oceanic P signatures on SSS variability are investigated in rainy regions such as the Pacific ITCZ, where SSS ($\sim$1 cm) is found systematically freshened with respect to the deeper 5-10 m

depth of Argo salinity likely as a result of vertical salinity stratification, while rain timing also influences these differences (*Boutin et al.*, 2013). Yielding new information on the ocean-atmosphere freshwater fluxes in key Tropical oceanic regions, satellite-derived SSS, combined with other satellite and in situ observations, can be further used as a tracer of the E-P budget in the oceanic mixed layer. Together with ocean models, it offers the potential for quantification of the relative contribution of the different mechanisms to the mixed layer salt budget (e.g. *Reul et al.*, 2013).

SMOS and Aquarius data can further help to qualitatively explore the seasonal dynamics, evolution and interaction of fresh pools with wind-driven atmospheric processes. For example, the erosion of the Eastern Pacific Fresh Pool by the wind-driven Panama upwelling processes is seen by SMOS (*Alory et al.*, 2012). Interestingly, satellite SSS observations are also able to detect other mesoscale features and the amplitude of their seasonal cycle, such as the SSS front at the Western Pacific warm pool (*Qu et al.*, 2014), and Tropical Instability Waves in the Eastern Equatorial Pacific (*Lee et al.*, 2012) from Aquarius data. Combined with Argo profiles, SSS observations from SMOS and Aquarius/SAC-D sensors, offer new insights into the barrier layer variability (*Qu et al.*, 2014), and the response of the upper ocean to the passage of tropical cyclones over the Amazon/Orinoco river plume (*Grodsky et al.*, 2012; *Reul et al.*, 2012a). Thus, the synergy of satellite SSS with other satellite and in situ observations represents a new, powerful tool to examine the role of salinity stratification in mixed layer dynamics, while providing valuable information for hurricane forecasting (*Grodsky et al.*, 2012; *Reul et al.*, 2013).

Finally, the SSS variability on intra-seasonal, due to e.g. the Maden-Julian Oscillation mode (*Grunseich et al.*, 2013), to interannual time scales, due to e.g. La Niña event in the Tropical Pacific (*Reul et al.*, 2013; *Hasson et al.*, 2014), or the Indian Ocean Dipole in the Indian Ocean (*Durand et al.*, 2013), can be clearly detected on satellite SSS signals.

2.3 Sea surface and near ocean salinity in the Tropical/ Subtropical Atlantic basin

2.3.1 Controlling mechanisms on the Tropical/Subtropical Atlantic salinity variability

Figure 2.4 shows a schematic with the main mechanisms that are expected to control the SSS variations in the Atlantic basin 30°N-30°S, where this thesis focuses on. In contrast to the Subtropics, the hydrological cycle in the Tropical Atlantic is characterized by both high E and intense convective monthly P rates exceeding 1.3 cm/day, which lead to strong SSS gradients. Seasonal variations of E-P reflect

the seasonal changes in the position and intensity of the high P band associated with the ITCZ, that migrates latitudinally over the Tropical Atlantic throughout the year (*US CLIVAR Group*, 2007). In boreal winter and spring, the ITCZ lies farthest south (Figure 2.4, a). During these seasons, north-easterly trade winds are strongest and drive a E maximum in the latitude band 10°-20°N, while E-P is negative in the band 0°-5°N. During summer (Figure 2.4, b), the ITCZ moves northward and intensifies, leading to weaker E north of it and strong P shifts eastward towards the African coast (*Foltz and McPhaden*, 2008). Thus, the strongest P regimes occur in the ITCZ near the equator, and together with strong zonal advection, result in stronger short-term salinity variability (*US CLIVAR Group*, 2007).

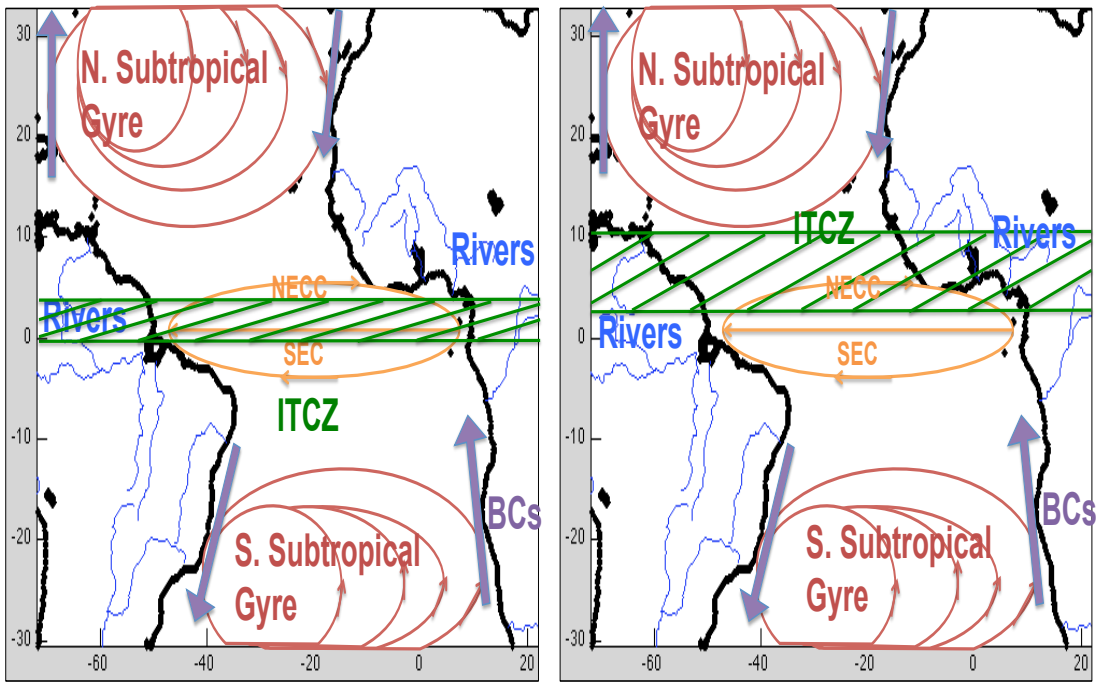

(a) Boreal winter (b) Boreal summer

Figure 2.4: Schematic with the main expected controlling mechanisms on SSS variations in the Tropical/Subtropical Atlantic 30°N-30°S: i) the ITCZ (green) in winter (left) and summer (right), ii) the major river systems of the Amazon/Orinoco and Congo/Niger (blue), iii) the Equatorial currents including the NECC and SEC (yellow), iv) the N. and S. Subtropical Gyres (red), and v) the Boundary Currents (BCs), i.e. the southern part of the Gulf Stream and the Canary Current in the N.H. and the Brazil and Benguela Currents in the S.H. (grey thick arrows).

Many studies over the last few decades have highlighted the role of river outflow in the seasonal salinity balance in the Tropical Atlantic (e.g. *Dessier and Donguy*, 1994; *Foltz and McPhaden*, 2008; *Romanova et al.*, 2011; *Grodsky et al.*, 2014a). Thus, low SSS occurs close to the major river systems located on either side of the Tropical Atlantic basin, which link continental convective zones to the marine hydrological cycle (*US CLIVAR Group*, 2007). The western Tropical Atlantic is mainly influenced by freshwater outflow from the Amazon and Orinoco rivers (e.g.

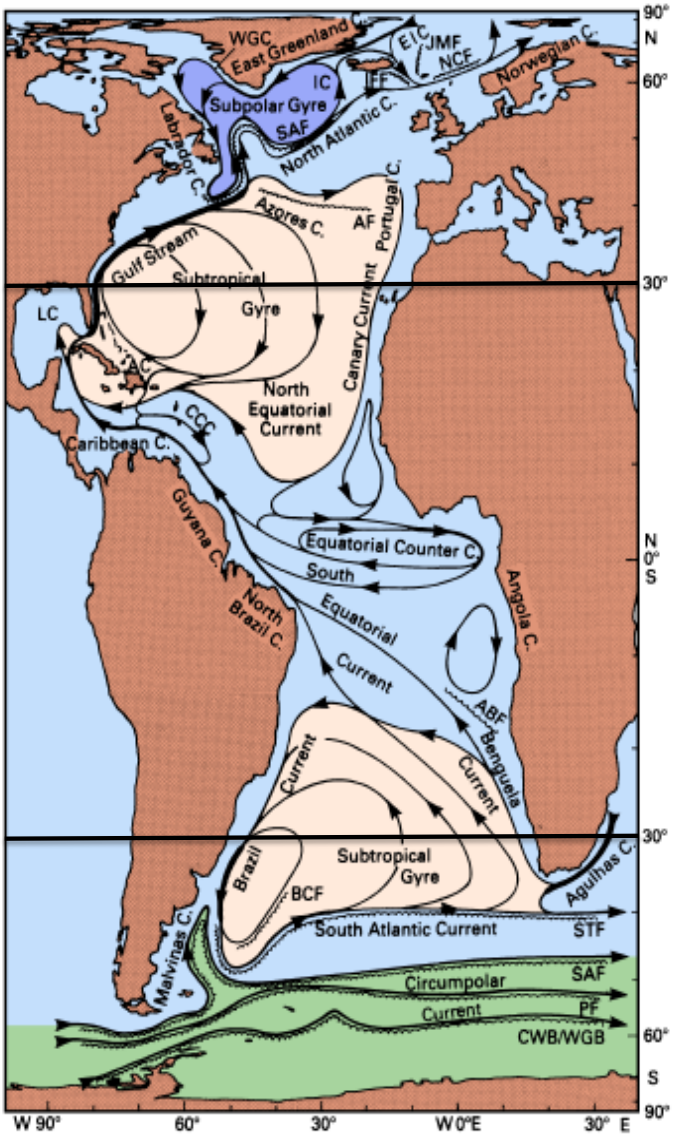

Figure 2.5: Surface currents of the Atlantic Ocean taken from *Tomczak and Godfrey*, 2003. The black lines indicate the region of interest 30°N-30°S.

Dessier and Donguy, 1994). In the eastern basin, SSS in the Gulf of Guinea is mainly controlled by the Congo and Niger discharge (Figure 2.4), in addition to a number of smaller rivers in the region (e.g. *Materia et al.*, 2012). Freshwater discharge close to the rivers mouths results in strong salinity gradients near the coastal regions (e.g. *Foltz and McPhaden*, 2008; *Denamiel et al.*, 2013). The subsequent spreading of freshwater by the upper ocean circulation leads to major low-salinity pools, such as those formed by the Amazon/Orinoco plume, which spread offshore from the S. America north-eastern coasts and influence a large part of the Western Tropical N. Atlantic (e.g. *Lentz*, 1995; *Muller-Karger et al.*, 1988; *Dessier and Donguy*, 1994; *Boyer and Levitus*, 2002). Thus, the MLS balance in the Tropical Atlantic is the result of a complex interplay of surface fluxes, horizontal advection, and vertical entrainment (e.g. *Foltz and McPhaden*, 2008). More information on the SSS and upper ocean salinity distribution and variability

in the two dynamic river-influenced regions in the Western and Eastern Tropical Atlantic are given in Sections 2.3.3 and 2.3.4, respectively.

Figure 2.5 illustrates the surface currents in the Atlantic Ocean, designating the region of interest 30°N-30°S, while Figure 2.6 focuses on the surface circulation along the Equatorial Atlantic basin, depicting particularly the seasonal variability of the North Equatorial Counter Current (NECC). Seasonal Ekman transport constitutes the main component of Tropical advection, while the mean Ekman advection (predominantly north-westward and south-westward in the N. and S. Tropical Atlantic) plays a secondary role. Dominating the zonal velocity, strong geostrophic currents are found especially north of the equator along the basin and towards the Gulf of Guinea i.e. the westward North and South Equatorial Currents (NEC and SEC), and the eastward NECC (Figures 2.5 and 2.6), as well as close to the Boundary Current (BC) regions (Figure 2.4). In contrast, the mean and seasonal variance of meridional velocity is dominated by the Ekman component (*Yu*, 2011), which also results in equatorial and coastal upwelling, such as in the Gulf of Guinea and along the Canary and Benguela Currents, particularly in boreal summer (*Carton and Zhou*, 1997).

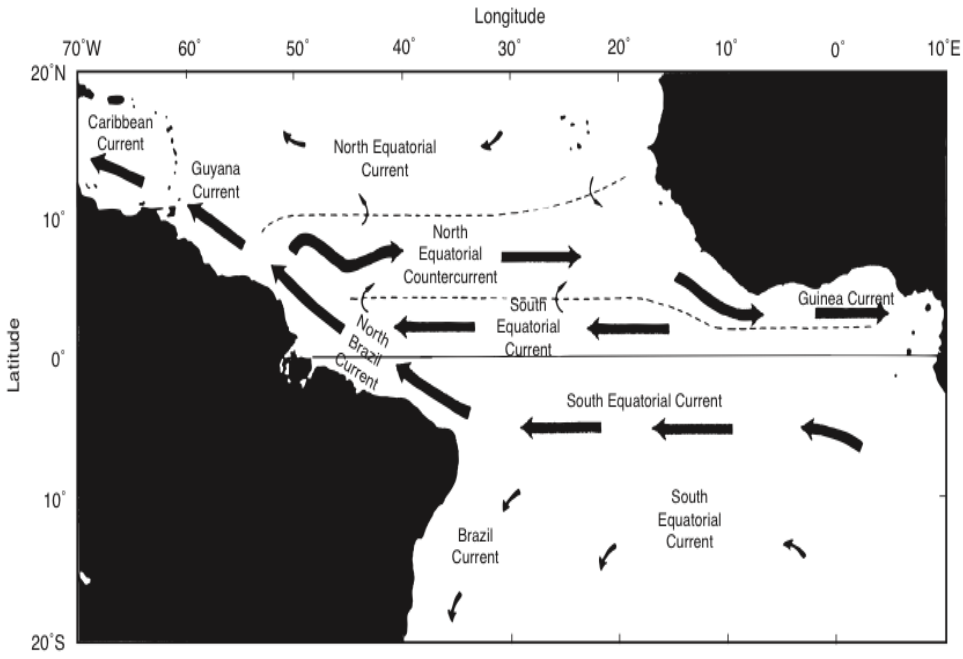

Figure 2.6: The major surface currents of the Tropical Atlantic between July and September when the NECC flows eastward into the Guinea Current in the Gulf of Guinea. From January to May, NECC disappears and the surface flow becomes westward everywhere in the western Tropical basin. Taken from *Philander*, 2001.

Similarly, freshwater fluxes, with E far exceeding P, and horizontal salt advection by the mean ocean circulation play a significant role in determining the mean SSS distribution in the Subtropical Atlantic basin (e.g. *Johnson et al.*, 2002; *Mignot and Frankignoul*, 2003). Small variations of SSS of <0.1 pss at all time scales are found at the centers of the Subtropical Gyres (e.g. *Vinogradova and*

Ponte, 2013) at ∼20°-25°N-S, with the Subtropical salinity maxima lying towards their eastern parts. In general, the main oceanic controlling mechanisms on the Subtropical SSS variability include advection by seasonally varying Ekman and geostrophic components, mixing and entrainment, while large E is also found at the BCs (*Yu*, 2011), where coastal upwelling also takes place (see Figures 2.4 and 2.5, for instance). As regards the N. Subtropics, the maximum E-P, underlying the easterly trade winds at the southern edge of the Subtropical high, is stretched from the Eastern Subtropical basin west of the African continent to the Western Tropical N. Atlantic and then to the Caribbean Sea, the Gulf of Mexico, and the U.S. South-Eastern coast. Consistent with the maximum of E-P and poleward Ekman transport, the SSS maximum region is located northwards relative to the E-P maximum, at ∼15°-30°N in the Eastern N. Subtropical Atlantic (e.g. *US CLIVAR Group*, 2007; *Schmitt*, 2008).

Ekman transport, driven by the trades and westerlies, compensates this E-P and restores the salt balance by injecting lower-salinity surface waters from adjacent latitude belts into the Subtropical hub (*Gordon and Giulivi*, 2008; *SPURS Workshop Report*, 2010). Within the central hub of this Subtropical regime, there is a net convergence and downwelling of surface-layer water due to Ekman transport, which in accordance with the localized influence of E under the trade winds, dominate the upper ocean stratification and circulation (*Gordon and Giulivi*, 2008). The salinity maximum region is characterized by weak geostrophic circulation and eddy fields, and thus, mean advection there is considered of minor importance in the near-surface layer, while together with the relatively small P rates, indicate less SSS variance (*SPURS Workshop Report*, 2010).

Finally, in the Subtropical N. Atlantic, the strong SSS maximum is subducted into the thermocline in the region 15°-30°N, 30°-50°W. This high salinity shallow thermocline water, driven by this Ekman mass transport, invades the Tropical Atlantic as a salinity maximum layer near 150 m, and forms the lower limb of the Subtropical/Tropical shallow Meridional Overturning Circulation (ShallMOC). Thus, the equatorward transport of warm, salty Subtropical water (often exceeding 35 pss) as part of the ShallMOC represents one aspect of the poleward transport of heat and freshwater within the latitudinal band equatorward of $\sim 30°$ in both hemispheres, where the oceans carry the largest portion of the planetary heat transport (*SPURS Workshop Report*, 2010). As a result, it plays a critical role in setting the stratification in the Tropical Atlantic, where vertical salinity differences can reach or exceed 1 pss (e.g. *Henocq et al.*, 2010), influencing the Tropical variability.

2.3.2 Salinity variability in the Tropical/Subtropical Atlantic basin

The SSS variability in the Tropical/Subtropical Atlantic has fairly long, i.e. seasonal, times scales outside the equatorial region, with a wide range of magnitude

and with regional, instead of basin-wide, spatial patterns of typically 500-1000 km (e.g. *Reverdin et al.*, 2007). In the Subtropics, the excess of E over P, with an annual mean of around 0.2 m/yr (*Kalnay et al.*, 1996) and up to 1 m/yr at its maximum, displays evident seasonality. From August to November, E decreases and P increases, resulting in similar rates. In the N. Subtropical Atlantic, the areas at 16°N, 41°W and 16°N, 42°W are considered representative of the seasonal cycle of P and E, respectively, throughout the region between 15°-25°N, 30°-50°W (*SPURS Workshop Report*, 2010). On the other hand, other study suggests a net E of more than 1.4 m/yr at 15° in the Atlantic at 30°W, and over 1 m/yr of net P at 10 degrees equatorward (*Schmitt*, 1995).

SSS fluctuations in the Tropical/Subtropical Atlantic reveal seasonal and interannual variations. On seasonal time-scales, SSS anomalies lag 1-2 months over most of the basin, in response to anomalies in the freshwater flux at the air-sea interface and to horizontal advection (*Reverdin et al.*, 2007). There is persistence over more than one season, and in more localised areas over more than a year, particularly in the central Subtropical Gyre and N.E. Atlantic, with boreal winter/early-spring being more active than the late-boreal spring/summer in forcing the seasonal SSS variability. This is consistent with the seasonality of mixed layer depth and its autumnal deepening which causes SSS anomaly changes as well (e.g. *Reverdin et al.*, 2007). Thus, during winter, E increases salinity near the surface, while small-scale vertical mixing tends to decrease salinity over the lower half of the mixed layer and increase it below it. On the other hand, the small net advection within the upper 150 m, balanced primarily by the aforementioned processes and the salt storage, still represents an important factor, acting to decrease salinity both within and below the mixed layer. Finally, close to the N. Atlantic SSS maximum, mesoscale features further influence the salinity distribution, as well as the mean ocean flow (*SPURS Workshop Report*, 2010).

In the Tropical Atlantic, a pronounced seasonal cycle of SSS is found throughout the basin, primarily governed by seasonal variations of P (and secondarily of changes in E-P) due to the ITCZ migration, and advection (e.g. *Foltz et al.*, 2004; *Foltz and McPhaden*, 2008), which also transfers high salinity waters from the extra-Tropics. Great SSS variations are also noted close to the river outflows, such as in the western basin, where, in addition to the ITCZ impact, the large Amazon/Orinoco freshwater discharge results in strong SSS variability (e.g. *Dessier and Donguy*, 1994; *Boyer and Levitus*, 2002; *Delcroix et al.*, 2005). Sections 2.3.3 and 2.3.4 will focus more on the SSS variability in the Amazon/Orinoco and Congo/Niger regions, respectively. Over the rest of the basin, large seasonal deviations also occur in the region along the NECC, and just south of the Gulf Stream, as well as in the Eastern Gulf of Guinea, where variability has often shorter temporal scales likely due to advection (*Reverdin et al.*, 2007).

Finally, substantial year-to-year SSS variations are predominantly influenced by atmospheric modes, such as the NAO and the ENSO, which through both anomalous freshwater forcing and Ekman advection, modulate the SSS variability in large parts of the Tropical/Subtropical N. Atlantic (*Mignot and Frankignoul*, 2003). Thus, interannual changes in the Tropical Atlantic freshwater flux and SSS are as large as the seasonal cycle, while due to the faster advection time scales, are more likely to penetrate below the mixed layer and alter the subsurface salinity field as well (*Wijffels*, 2001). On these temporal scales, anomalous Ekman advection seems to play a more significant role in generating SSS anomalies than the freshwater fluxes (*Mignot and Frankignoul*, 2003). P has a comparably influential role to anomalous advection towards the N.W. Tropics, where anomalous runoff from the Amazon/Orinoco rivers contributes greatly to interannual SSS anomalies (*Mignot*, 2004). This region experiences large SSS changes primarily in response to ENSO-related P (*Giannini et al.*, 2000), a particularly important mode in the Tropical Atlantic variability (*Mignot*, 2004). ENSO explains ∼20% of the interannual SSS variance in the Western N. Atlantic (*Reverdin et al.*, 2007), with SSS decreasing, in general, during El Niño due to increased P, while La Niña denoting periods of enhanced SSS (*Gordon and Giulivi*, 2008).

2.3.3 Western Tropical Atlantic: the Amazon/Orinoco region and its variability

In the Western Tropical Atlantic, both SSS and salinity within the mixed layer are controlled by several competing processes which vary seasonally (*Foltz et al.*, 2004). Among these, the two major sources of freshwater are the high P rates under the ITCZ, and the discharge of major rivers along the NE coasts of South America (e.g. *de Boyer Montégut et al.*, 2007), namely the Amazon and Orinoco Rivers. The Amazon is the world's largest river in terms of terrestrial freshwater discharge, discharging on average more than 6600 km^3/yr of freshwater into the Equatorial Atlantic. This is about 15-17% of the global annual river discharge, and as much as the combined runoff of the next 8 largest rivers in the world (*Dai and Trenberth*, 2002; *Coles et al.*, 2013), serving as an important connection between the continental and oceanic hydrological cycle. With its main stem stretching 6500 km across S. America, and the contribution of numerous other smaller rivers to its total discharge (*Salisbury et al.*, 2011; *Coles et al.*, 2013), the Amazon River constitutes ∼30% of the total riverine input into the whole Atlantic basin (*Wisser et al.*, 2010), having a large impact on the Tropical Atlantic freshwater budget and its variability (*Coles et al.*, 2013). In addition, NW of the Amazon, at ∼9°N, the Orinoco River, the third largest river globally in terms of volumetric discharge (after the Amazon and the Congo), discharges water from more than 30 major and 2000 minor tributaries into the Western Tropical Atlantic basin. With a mean discharge of ∼1140 km^3/yr (e.g. *Muller-Karger et al.*, 1988), the Orinoco

River represents another important source of the regional freshwater budget (e.g. *Romanova et al.*, 2011).

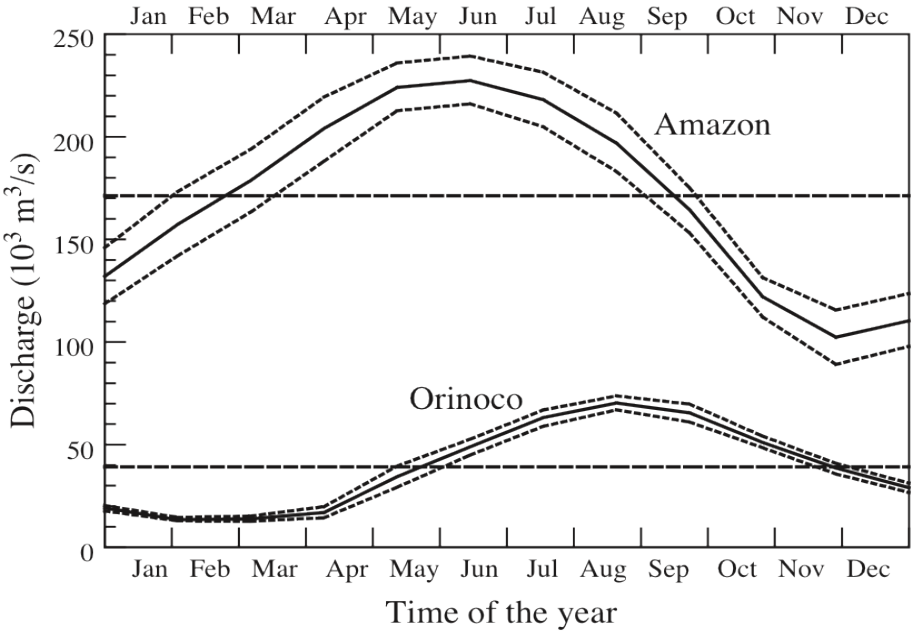

Figure 2.7: The climatological mean seasonal cycle (solid lines) and ±a standard deviation (dashed lines) of the Amazon (1969-1978) and Orinoco (1979-1983) river discharge, respectively. Taken from *Hu et al.*, 2004.

Over the Amazon/Orinoco region, net P follows an annual cycle driven by the migration of the ITCZ, with the northward position of the latter in boreal summer being accompanied by the maximum intensification of P patterns (*Kushnir et al.*, 2006l *Donohoe et al.*, 2014). In accordance, the climatological seasonal cycle of the Amazon River (Figure 2.7) shows, in general, low discharge in November-January, with an ascending period in February-April, high discharge in May-July, and a descending period in August-October (e.g. *Salisbury et al.*, 2011). Nevertheless, the largest extent of its plume (with salinities less than 34 pss) occurs earlier than the maximum discharge, i.e. between March-May (*Boyer and Levitus*, 2002). Similarly, the Orinoco runoff (Figure 2.7) also varies seasonally, with a low discharge during the dry season (January-May) and a minimum in March, and a high discharge during the rainy season (July-October), with a maximum in August (e.g. *Hu et al.*, 2004) or September (*Reul et al.*, 2013).

The dynamics of riverine flow affect significantly the salinity variability. These fresh waters are advected both zonally by the seasonal currents, and meridionally through Ekman transport by the seasonal trade winds (*Muller-Karger et al.*, 1988; *Dessier and Donguy*, 1994; *Foltz et al.*, 2004). Thus, the fresh Amazon/Orinoco plume covers a highly variable area with a mean seasonal extent of 10^6 km^2 (*Grodsky et al.*, 2014a), which together with the plume's structure, are the result of several competing processes. These mainly include changes in the Amazon River discharge; advection by seasonal currents, particularly the North Brazil Current

(NBC) that seems to primarily control the Amazon plume; turbulent mixing by the strong seasonal winds (e.g. *Hu et al.*, 2004; *Zeng et al.*, 2008); and strong currents associated with the tide, which contribute further in mixing the plume on the shallow shelf (e.g. *Nikiema et al.*, 2007).

Ocean currents, including eddies, play an important role in shaping the spatial plume extent and transferring the freshwater in large distances away from the river mouth (*Grodsky et al.*, 2014a), which then, mixes continually with surrounding salty ocean surface water (*Muller-Karger et al.*, 1988). For instance, the NBC rings are important factors in modifying the pathways of the Amazon plume from the river mouth at the equator, northwards up to 20°-22°N (*Reul et al.*, 2013). Thus, along the Brazilian shelf and up to 200 km offshore, the plume is typically 3-10 m thick and between 80-200 km wide (*Lentz and Limeburner*, 1995), while reaches a penetration depth of 40-45 m as far as 2600 km offshore (*Hellweger and Gordon*, 2002; *Hu et al.*, 2004). Consequently, the effects of freshwater from the Amazon/Orinoco plume can be visible in large distances away from the plume, with amplitude of ∼1 pss at 12°N and more than 0.2 pss as far as 24°N (*Pardaens et al.*, 2008).

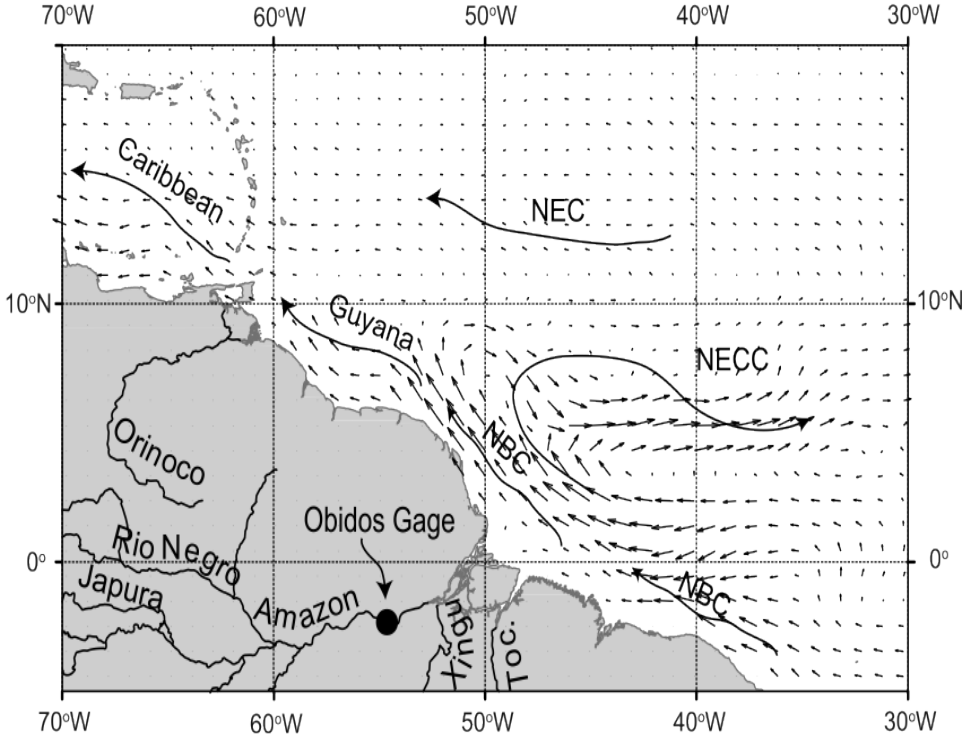

Figure 2.8: The main surface currents in the Amazon/Orinoco region: North Brazilian Current (NBC), Northern Equatorial Current (NEC), North Equatorial Counter Current (NECC), Guyana Current, and Caribbean Current. The small flow vectors show the mean surface current direction and relative velocity during September, based on climatological Argo float trajectory data. Taken from *Salisbury et al.*, 2011.

The most important key features of the seasonal currents are summarized in Figure 2.8, while Figure 2.9 shows the main transport pathways of the Amazon/Orinoco plume. During boreal winter when the ITCZ is at its southernmost position, freshwater is trapped against the coast and stored at the river mouth by onshore winds (*Grodsky et al.*, 2014a). In boreal spring (low flow and ascending periods), relaxing onshore winds and increasing freshwater discharge due to the northward ITCZ migration result in the north-westward transport of the plume along the eastern boundary of S. America (*Muller-Karger et al.*, 1988; *Salisbury et al.*, 2011; *Grodsky et al.*, 2014a) by the NBC and Guyana Current, which primarily controls the Orinoco waters close to the shelf (*Denamiel et al.*, 2013; *Grodsky et al.*, 2014a). In addition, water is transported eastwards into the developing NECC at ∼5°-10°N (e.g. *Romanova et al.*, 2011), which exports water masses to the central Atlantic (Figures 2.8 and 2.9, red and green).

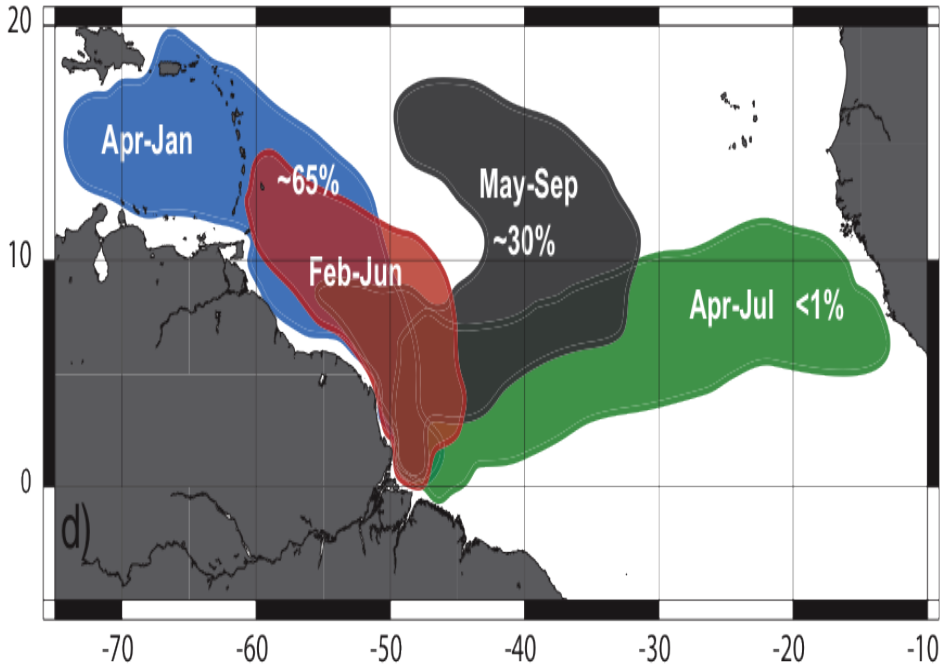

Figure 2.9: Schematic of float transport pathways of the Amazon/Orinoco plume, taken from *Coles et al.*, 2013. The percentage indicates observed and HYCOM-modelled drifters that follow each pathway.

By boreal summer, the ITCZ reaches its northernmost position and the shifting trade winds enable the NBC retroflection, that feeds the intensifying NECC (Figure 2.8). Thus, during this season, the low SSS water is transported mainly by three export pathways, which vary seasonally (*Foltz and McPhaden*, 2008; *Coles et al.*, 2013): i) some continue north-westwards towards the Caribbean current (e.g. *Hellweger and Gordon*, 2002), ii) northwards by Ekman currents and eddies reaching east of the Lesser Antilles (*Mignot et al.*, 2012), and iii) eastwards by the NECC (Figure 2.9). Between August-October, almost 70% of the Amazon plume water is diverted into the NECC, producing a fresh signature in its western part in summer-early fall (high flow and descending periods), (*Romanova et al.*, 2011; *Salisbury et al.*, 2011; *Coles et al.*, 2013).

In contrast, in late autumn-winter, when there is a minimum discharge, but both the NBC retroflection and the eastward NECC are still present (*Coles et al.*, 2013; *Grodsky et al.*, 2014b), salty SSS from the Equatorial and S. Atlantic is transported into the western part of the NECC, causing its salty signature, which weakens during this season (*Grodsky et al.*, 2014b). These saline waters imported from the south through advection by the NBC play an essential role in the change of freshwater content in the region (*Romanova et al.*, 2011), while very sharp salinity gradients can also be found in the northern part of the NECC (*Coles et al.*, 2013). Thus, the MLS balance in the region is primarily controlled by horizontal advection and surface freshwater fluxes (e.g. *Foltz et al.*, 2004; *Foltz and McPhaden*, 2008; *Grodsky et al.*, 2014a), while conversely, the Amazon/Orinoco plume has also a dynamical impact on the circulation and eddy variability (e.g. *Romanova et al.*, 2011; *Coles et al.*, 2013).

Comparison of the relative roles of ITCZ P and river discharge indicates the importance of both controlling mechanisms in maintaining the fresh Tropical Atlantic SSS. The riverine influence is strongest in the Western Tropical Atlantic (West of 40°W), although salinity anomalies propagate eastwards across the basin as far as the westernmost Gulf of Guinea, while P is more broadly distributed over the basin. The river influence lags P associated with the ITCZ migration and the development of NBC by 2 months, while during late summer-autumn, the two mechanisms are of comparable magnitude (*Coles et al.*, 2013). Changes in advection and/or non-local P, contribute to year-to-year variations in the plume and its properties (*Grodsky et al.*, 2014a). Consequently, the plume is a complex mixture of waters with varying age characteristics, salinity, and response to seasonal forcing, where interaction of different current structures and multiple plume pathways occur concurrently, characterized by very different time-scales (*Coles et al.*, 2013).

In general, the broadest range of salinity of 30-34 pss occurs in the main plume in autumn (*Coles et al.*, 2013), while seasonal SSS maxima are observed between January-March and SSS minima in May-July, lagging by 1-2 months the maximum Amazon discharge (e.g. *Salisbury et al.*, 2011; *Romanova et al.*, 2011). Larger lags are also found, as for instance, at the PIRATA location 8°N, 38°W, which, however, may be also attributed to the time required for the river discharge to reach the observation regions (e.g. *Dessier and Donguy*, 1994). This lag between highest discharge and lowest salinity (and vice versa) shows year-to-year variations by ±2 months, indicating the role of other physical processes as well (*Salisbury et al.*, 2011). These include the wind impact on vertical mixing and thus, on SSS and the depth of mixed layer, as well as potentially residual conditions from the previous year (*Grodsky et al.*, 2014a). Thus, during most of the year, the plume consists of two modes, i.e. a fresh young plume and an older saltier plume from the previous year. Finally, Aquarius and in situ observations suggest the seasonal development of a local SSS maximum in the NW Tropical Atlantic (∼8°N) in winter-early spring, bounded by two fresh SSS bands north (10°-15°N) and south

(4°N) of it. This SSS maximum is of up to 0.5 pss saltier than the surrounding water, and given its relative position to the high ITCZ P, results from the different phases in the seasonal variations of continental discharge, mainly of the Amazon, and ocean currents (*Grodsky et al.*, 2014b).

P over the continent, and thus the Amazon discharge, undergo interannual and decadal changes. Year-to-year changes in Amazon discharge play an important role in driving year-to-year changes of the plume, and accordingly of SSS in the Western Tropical Atlantic basin (*Hu et al.*, 2004; *Zeng et al.*, 2008; *Salisbury et al.*, 2011). For instance, during the period 2005-2013, the strongest fresh event occurred in 2009, in response to an anomalous southward shift of the ITCZ (*Foltz et al.*, 2012) and extreme flooding in the Amazon discharge throughout that year (*Chen et al.*, 2010; *Marengo et al.*, 2011), resulting in residual fresh conditions in 2010 (*Coles et al.*, 2013). Contrary to the 2011 fresh event due to increased P, continental discharge was stronger in 2012 (*Grodsky et al.*, 2014a), indicating the impact of water storage on significant phase lags between P and river discharge (*Chen et al.*, 2010). On the other hand, SSS in the plume was saltier by ∼1 pss in late summer-early fall of 2012 relative to 2011, likely due to a reduction in P over the ocean south-east of the plume, and the currents' variability (*Grodsky et al.*, 2014a).

The Amazon plume, and to a lesser degree, neighbouring rivers, including the Orinoco has attracted most of the scientific interest (e.g. *Foltz and McPhaden*, 2008; *Salisbury et al.*, 2011; *Romanova et al.*, 2011; *Grodsky et al.*, 2014a; *Grodsky et al.*, 2014b), primarily due to its importance on the formation of barrier layers (BL), with salinities that are several pss fresher than the water beneath them (e.g. *Lentz*, 1995). The presence of large freshwater lenses on the ocean surface due to strong river discharge and intense local P, and its horizontal divergence/convergence in the ocean primarily driven by seasonal variations in the regional surface circulation, influences the near-surface stratification in the N.W. Equatorial Atlantic, resulting in the BL formation within the mixed layer, with thickness of more than 10 m (e.g. *Romanova et al.*, 2011; *Grodsky et al.*, 2014a). As the freshwater surface layer of the Amazon/Orinoco plume is warmer than the water below, the seasonal BL impacts local sea surface temperature (SST) and inhibits surface cooling (*Ffield*, 2007) by reducing the depth of vertical mixing and entrainment of the cool thermocline water into the mixed layer (e.g., *Vialard and Delecluse*, 1998; *Foltz and McPhaden*, 2008; *Coles et al.*, 2013).

In turn, this warmer SST can affect P rates in the region, including over the N.E. Brazil and the sub-Saharan Africa (e.g. *Giannini et al.*, 2003), thus influencing the frequency and intensity of summertime storm systems over the Atlantic (*Ffield*, 2007; *Vizy and Cook*, 2010), and increasing the hurricanes' maintenance and intensification in the region by up to 50% (e.g. *Vizy and Cook*, 2010; *Grodsky et al.*, 2012). Thus, the warm and low-salinity waters of Amazon/Orinoco plume and

the BLs in the region play an important role in the ocean-atmosphere heat exchange in the N.W. Tropical Atlantic (e.g. *Foltz and McPhaden*, 2008; *Romanova et al.*, 2011; *Coles et al.*, 2013), while modifying also the near-surface circulation (e.g. *Vialard and Delecluse*, 1998). Finally, the rivers, by injecting terrestrial sediments, nutrients, coloured and transparent dissolved organic matter (CDOM, DOM) that are traced thousands of km from the Amazon River mouth (*Hu et al.*, 2004; *Salisbury et al.*, 2011), influence the biological community, while leading to significant uptake of the atmospheric CO_2 in the river plume (e.g. *Cooley et al.*, 2007).

2.3.4 Eastern Tropical Atlantic: the Congo/Niger plume in the Gulf of Guinea region and its variability

The Eastern Tropical Atlantic basin 8°W-12°E, 6°N-20°S, encompassing the Gulf of Guinea, is another key region for the freshwater budget in the Tropical Atlantic, although it has attracted less scientific attention. *Dessier and Donguy*, 1994 emphasized the role of P associated with the ITCZ in the Eastern Tropical Atlantic, however variability of SSS in the Gulf of Guinea is strongly driven by the freshwater discharge from the rivers. Here, the Congo River, the second largest river in the world and the most significant river of the S.H., discharges into the ocean together with the Niger and numerous other smaller rivers. The annual discharge of the Congo (Figure 2.10) reaches ∼1270 km^3/yr (e.g. *Materia et al.*, 2012), and thus is of comparable magnitude to the annual Orinoco outflow, and about 5 times smaller than that of the Amazon River. The Niger River, listed also within the 24 largest rivers globally, has an annual discharge of ∼181 km^3/yr, i.e. about 7 times smaller than that of the Congo River (*Dai et al.*, 2009).

In addition to the large riverine influence, the region is characterized by heavy P (e.g. *Yoo and Carton*, 1990) driven by the periodic ITCZ movement, moving northward and intensifying in boreal summer. The strongest P shifts eastward toward the African coast, and E weakens north of the ITCZ (e.g. *Foltz and McPhaden*, 2008), contributing significantly to the freshening of the upper layer across the basin, between the equator and 20°N (*Coles et al.*, 2013). Consequently, the resulting large freshwater input plays an effective role in modulating the interannual variability in this part of the Atlantic basin, particularly of SST (e.g. *Giannini et al.*, 2005). In turn, along with advection by the regional circulation, and strong seasonal coastal and equatorial upwelling in boreal summer (e.g. *Materia et al.*, 2012; *Reul et al.*, 2013; *Da-Allada et al.*, 2013), P and R also have a significant influence on SSS over the Eastern Tropical Atlantic and the Gulf of Guinea, which exhibits large annual variations of over 0.3 pss amplitude (e.g. *Boyer and Levitus*, 2002).

Driven by intense P by the double passage of the ITCZ within the year (e.g. *Foltz and McPhaden*, 2008), the Congo River shows two peak discharges during the year

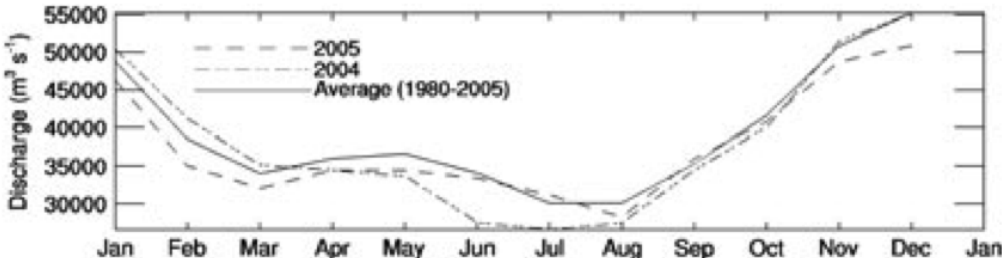

Figure 2.10: The climatological monthly mean discharge (solid line) of the Congo River at Brazzaville station over the dry period (1980-2005) based on the Regional Ocean Modelling System (ROMS). In addition, the simulation (2005) and spin-up (2004) periods of the model are shown (dashed lines). Taken from *Denamiel et al.*, 2013.

in December and April/June (Figure 2.10), with the overall maximum in December lagging the P maximum by two months (e.g. *Denamiel et al.*, 2013). The secondary peak in April-June is associated with increased P over the Congo catchment area during February-April following the northward ITCZ movement. The Congo discharge minima occur in February-March and July-August (Figure 2.10), after the driest period over the central Equatorial Africa in late boreal winter and early summer, respectively. Hence, positive SSS anomalies in the Eastern Equatorial Atlantic occur in late spring and over the entire summer, especially close to the Congo mouth and the Gulf of Guinea, where the riverine discharge is much reduced (e.g. *Materia et al.*, 2012). The SSS maxima in the region occur in August, while the SSS minima occur around April, lagging approximately 4 months behind the maximum Congo discharge at Brazaville station, potentially due to the time required for the freshwater to reach the river mouth and then be advected by the surface currents (*Reul et al.*, 2013).

The Eastern Tropical Atlantic and the Gulf of Guinea are considered a complex region in terms of ocean circulation (Figure 2.11). The surface currents of the Eastern Equatorial Atlantic consist of the NECC flowing eastwards, the westward South Equatorial Current (SEC), and the eastward South Equatorial Counter Current (SECC). South of the equator, the southward Angola Current, representing a branch of the SECC, is a fast, narrow and stable current extending both on the shelf regions and the continental slope (e.g. *Vangriesheim et al.*, 2009). Flowing along the Angola coast, the Angola Current joins the northward Benguela Coastal Current (BCC) at the Angola-Benguela front around 14°S-16°S (Figure 2.11), north of which the BCC flows as a narrow subsurface tongue up to 5°S (*Vangriesheim et al.*, 2009). The extension of the SECC may flow northward or southward (Angola Current) depending on the seasonal and interannual variability (*Denamiel et al.*, 2013). The Angola dome (Figure 2.11), a cyclonic eddy of the thermocline centered near 10°S, 9°E (*Lass et al.*, 2000), is another important feature of the region. Disappearing during the austral winter, the salinity decreases by 0.3-0.5 pss within it due to vertical mixing of low-salinity Congo water from the surface

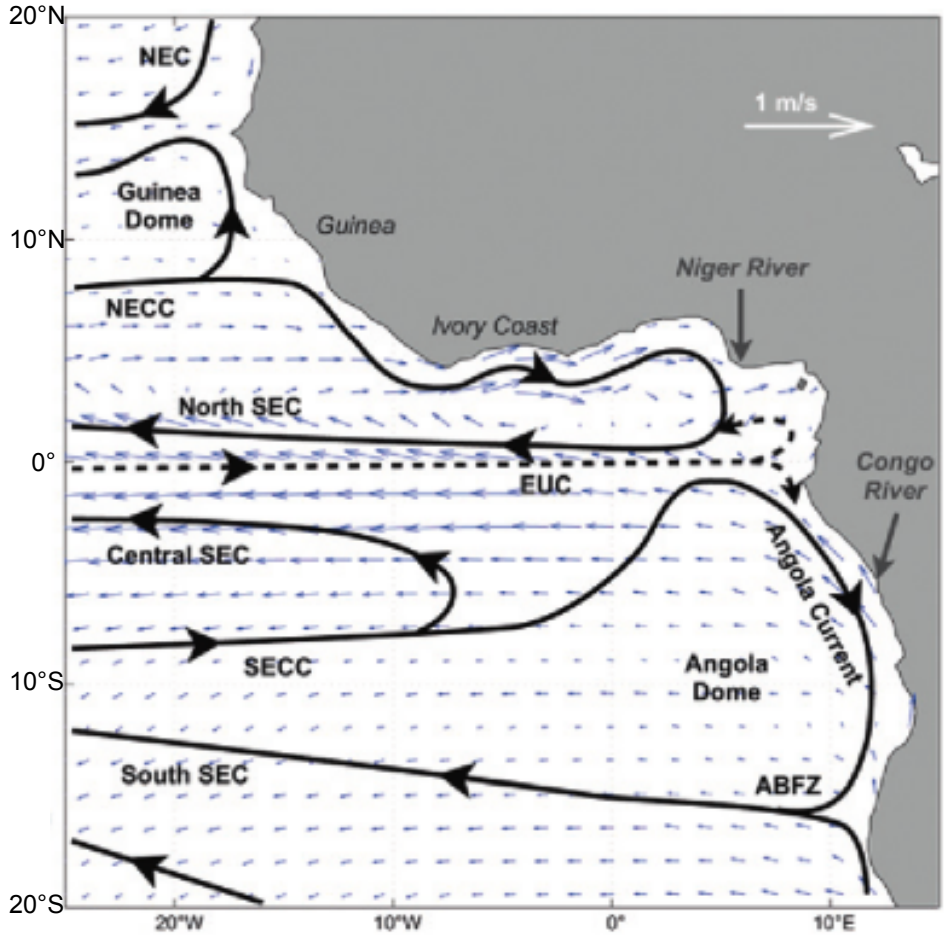

Figure 2.11: The surface (solid lines) and subsurface (dashed lines) current system in the Eastern Tropical Atlantic: the North Equatorial Current (NEC); the North Equatorial Counter Current (NECC); the South Equatorial Current (SEC); the Equatorial Undercurrent (EUC); the Angola-Benguela Frontal Zone (ABFZ). Taken from *Strub et al.*, 2013.

(*Denamiel et al.*, 2013).

The Gulf of Guinea is characterized by intense coastal upwelling (*Foster et al.*, 2009), with significant impact on the climate and fisheries of the area, which however, can be suppressed by the continental freshwater discharge. Thus, although the region is not generally characterized by a barrier layer in boreal summer, anomalously large freshwater river outflow (associated with the second peak discharge of the Congo river) can occasionally develop it (*Breugem et al.*, 2008). Thus, in the event of large riverine freshwater discharge, vertical mixing is inhibited, resulting in strong SSS anomalies (*Materia et al.*, 2012). In contrast, low discharge does not alter noticeably the vertical density stratification, but may still lead to instability of the upwelling region (*Carton*, 1991).

The main characteristics of the Congo plume have been generally described through observational studies since the 1980s (e.g. *Reverdin et al.*, 2007), with data sparsity only improving after 2003 with the inclusion of Argo floats, as well as through

the use of model outputs (*Denamiel et al.*, 2013). Various interdependent environmental factors appear to be responsible for the variability of the main Congo plume and its wider region. Seasonal variations of the river outflow, wind forcing and the complex ocean circulation (e.g. *Signorini et al.*, 1999) result in different dispersions of the plume. The upper-ocean salinity in the main plume area ranges between 1-11 pss, increasing up to around 25 pss over the wider region (*Denamiel et al.*, 2013).

The Congo River plume has a typical northward (*Denamiel et al.*, 2013) or west-north-westward direction near the coast (*Vangriesheim et al.*, 2009), exhibiting strong variations in shape and thickness over the year. Characterized by low-salinity waters of less than 24 pss along the Gabon coast, and thus north of the Congo river mouth, the thickness of the plume varies from 0.3 m in austral winter to 0.7 m in austral summer, when the plume reaches 450 km northward. An exception occurs during February-March, when the plume extends mainly westwards, reaching up to 800-1000 km offshore in austral summer. With $\sim$1 m thickness and SSS values below 33 pss, it covers twice the area ($\sim$6 x 10^9 km^2) compared to the rest of the year, due to the seasonal ocean currents (e.g. *Denamiel et al.*, 2013). Finally, the Congo plume can also extend southwards or south-westwards depending on the prevailing wind stress in the Angola Basin (e.g. *Denamiel et al.*, 2013).

On interannual time scales, the Congo plume, and thus SSS in the region, show great variability. In the Gulf of Guinea, the main mode of interannual variability is associated with an internal Equatorial Atlantic oscillation, the "Atlantic Niño" (e.g. *Zebiak*, 1993). The latter, involving coupled processes similar to ENSO but with different time scales, is influenced by the cold SST tongue in the Eastern Equatorial basin during late spring-early summer (*Latif and Grötzner*, 2000). Finally, on longer, i.e. decadal, time scales, the Congo monthly discharge exhibits a "dry" phase, with a downward trend by 10% in discharge, over the period 1980-2005 (*Laraque et al.*, 2001; *Denamiel et al.*, 2013).

However, significant gaps still remain in our knowledge on the variability of the SSS seasonal cycle in the Gulf of Guinea on different time-scales, and in relation to the relative impact of variations in freshwater fluxes and river runoff, including the combined impact of the Congo and Niger Rivers. The availability of remotely-sensed SSS measurements should contribute to a more comprehensive study of the SSS variations in this part of the Atlantic basin.

Chapter 3

Sources of Data

3.1 Introduction

In this chapter, the datasets used in the rest of this thesis are presented. They include: salinity (Section 3.2), freshwater fluxes (Section 3.3), river discharge (Section 3.4) and mixed layer depth climatological data (Section 3.5). Salinity is presented in Section 3.2 and focuses mainly on sea surface salinity (SSS) from the SMOS mission. Note that SSS from the Aquarius/SAC-D mission is not considered due to the shorter record of available SSS data (launched in June 2011), and its lower sampling frequency and spatial resolution (*Lagerloef et al.*, 2008). Known issues for the SMOS SSS products are discussed. The thesis also considers in situ SSS and upper ocean salinity (UOS) data from the World Ocean Atlas 2009 (WOA09) and Argo profiles. SSS is defined here in the top ∼5 m and corresponds to the SMOS and WOA09 observations, while UOS is between ∼5-10 m depth, typically measured by Argo floats.

Freshwater fluxes are presented in Section 3.3 and consist of Evaporation minus Precipitation, derived from the Objectively Analyzed air-sea Fluxes (OAFlux) and Global Precipitation Climatology Project (GPCP), respectively. Freshwater fluxes are used in Chapters 4, 5 and 7. River outflow datasets are presented in Section 3.4 and correspond to discharge data for the Amazon, Orinoco, Congo and Niger rivers, used in Chapters 4 and 5. Mixed layer depth (MLD) climatology is presented in Section 3.5 and is used in Chapter 7. Given that every dataset has its own weaknesses and uncertainties that should be taken into account when attempting to interpret the findings, a brief description of the individual characteristics of each data source is also presented.

3.2 Salinity

3.2.1 The Soil Moisture and Ocean Salinity (SMOS) satellite mission

Also known as the European Space Agency's (ESA) Water Mission (*Kerr et al.*, 2010; *Mecklenburg et al.*, 2012; *Font et al.*, 2013), the Soil Moisture and Ocean Salinity (SMOS) mission is the first satellite making sea surface salinity (SSS) measurements from space, launched in November 2009. SMOS aims to demonstrate the feasibility of space-borne polarimetric interferometric radiometry (e.g. *Font et al.*, 2010b) at microwave L-band for Earth Observation and to provide global and continuous coverage of soil moisture and SSS with adequate resolution and accuracy. The globe is fully imaged twice (ascending/descending orbits) every 3 days (*Kerr et al.*, 2010). SMOS has a polar, sun-synchronous (mean altitude of 758 km) orbit at 6 a.m./6 p.m. local solar time (equator crossing time), but a very long exact repeat, i.e. the surface is imaged with exactly the same view angle only every 149 days (*Kerr et al.*, 2010; *Mecklenburg et al.*, 2012). The spatial resolution of SMOS over land is 30 to 50 km depending on the view angle.

3.2.1.1 SMOS salinity measurement principles

The remote sensing of ocean salinity is based on the measurement of ocean brightness temperature at the lower L-band microwave frequency. At L-band, the signals over the ocean correspond typically to a surface skin layer of ∼1 cm thickness (*Kerr et al.*, 2010). Brightness temperature (Tb) is a function of effective emitting temperature of the surface multiplied by the emissivity. Sea surface emissivity is linked to the dielectric constant of sea water, which in turn is a function of ocean salinity and temperature (*Klein and Swift*, 1977). Tb also depends on surface roughness, incidence angle and polarization (*Font et al.*, 2010b). In practice, many other non-oceanic factors (e.g. extra-terrestrial sources, ionospheric effects, RFI) affect the Tb observed by the satellite and need to be accounted (*Kerr et al.*, 2010; *Reul et al.*, 2013).

The SMOS instrument (Figure 3.1), the Microwave Imaging Radiometer using Aperture Synthesis (MIRAS) operates at L-band frequency (*Font et al.*, 2010b), which is reserved for astronomical and geophysical observations. L-band is centred at 1.413 GHz (wavelength of 21 cm) and represents the part of the electromagnetic spectrum where the sensitivity of Tb to salinity changes is high enough to make SSS remote sensing possible (*Boutin and Martin*, 2006; *Font et al.*, 2010b; *Lagerloef and Font*, 2010). MIRAS can make observations in dual-polarization (i.e. horizontal and vertical polarization) and full polarization (*Martín-Neira et al.*, 2002), which is the mode it presently operates in (*Mecklenburg et al.*, 2012). In the SMOS synthetic aperture imaging technique, a Tb image is reconstructed through Fourier synthesis from cross correlations between simultaneous signals derived from pairs

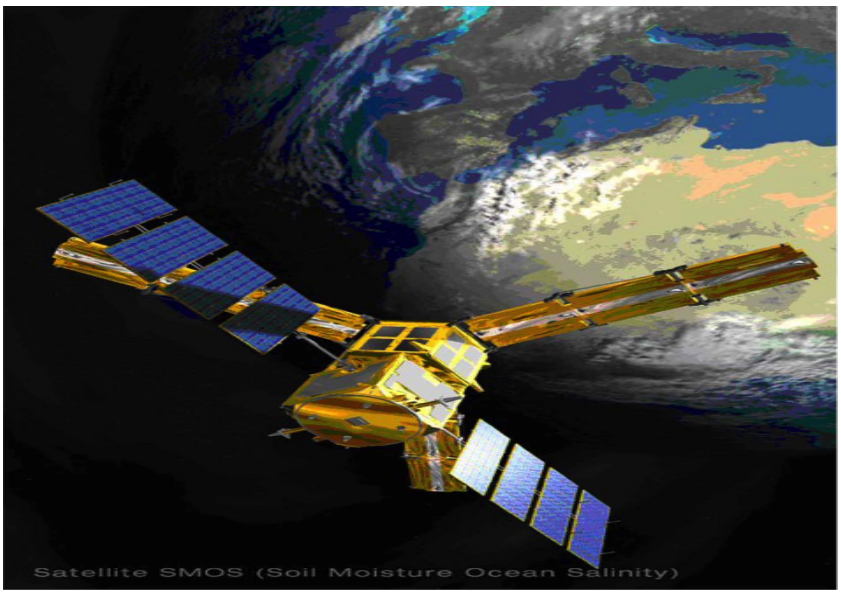

Figure 3.1: Artist's view of SMOS with the three MIRAS arms deployed and the 69 antenna elements. Taken from *Kerr et al.*, 2010.

of the 69 radiometer elements situated along the Y-shaped antenna (Figure 3.1). This results in an hexagonal Field of View (FOV), (e.g. *Kerr et al.*, 2010), as shown in Figure 3.2. This method introduces additional complexities for the SSS retrieval, as for instance in strong Tb contrast transitions between land-ice/ocean/sky. In addition, a further challenge is to ensure high temporal stability and calibration accuracy of the 69 radiometer elements with varying individual behaviour (*Reul et al.*, 2012b).

The mission's goal is to derive SSS with an accuracy of 0.1-0.2 pss over the GODAE defined scales of 100 km, 1 month or 200 km and 10 days (*Lagerloef and Font*, 2010; *Font et al.*, 2010b). This is a challenging objective for several reasons. First, the absolute sensitivity of Tb to SSS variations is low, i.e. of the order of 0.8 K/pss at 30°C. Given a typical instrument noise of 2-5 K, it is clear that only the largest SSS contrasts will register above the noise in unaveraged signals. This sensitivity reduces significantly in cold waters, i.e. to 0.2 K/pss at 0°C (e.g. *Mecklenburg et al.*, 2012), setting the SSS retrieval to be at its most demanding at higher latitudes (North Atlantic, Polar and Subpolar regions), (*Kerr et al.*, 2010).

Moreover, there are many geophysical sources that influence Tb, and accordingly, the SSS retrieval at L-band. These include numerous effects that change the Tb from the idealized surface emission to what is actually measured by the satellite, such as Faraday rotation in the ionosphere, galactic contributions, sun glint and moon glint, that may impact up to the monthly-averaged SSS products (*Kerr et al.*, 2010; *Reul et al.*, 2012a and references therein). Nevertheless, the major error source is the effect from surface roughness due to wind (speed and direction) (*Boutin et al.*, 2004), sea state, wave breaking and foam (*Lagerloef and Font*, 2010; *Font et al.*, 2010b). Finally, Radio Frequency Interference (RFI) from man-made emissions contaminates data collected over many oceanic regions (*Reul et al.*,

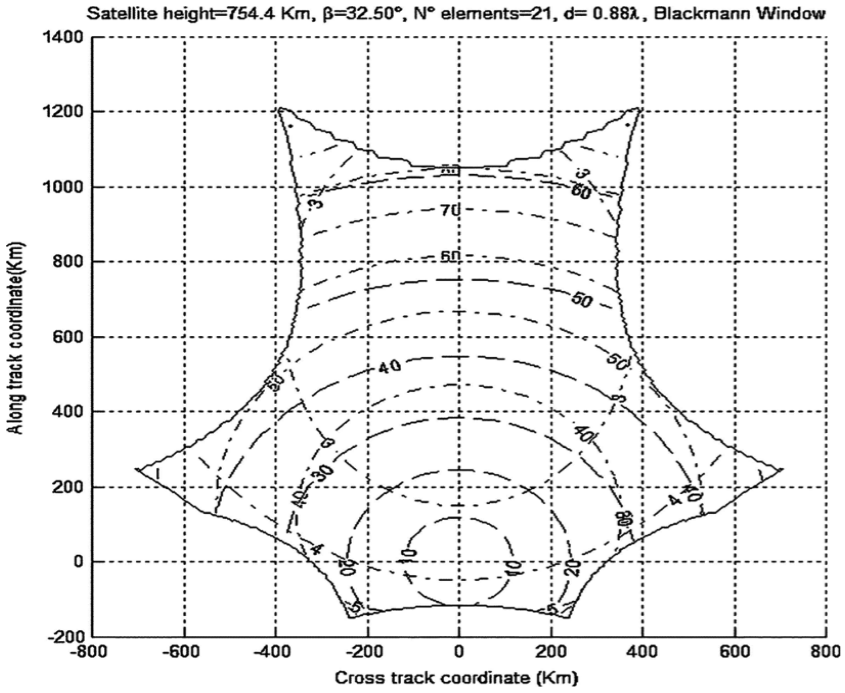

Figure 3.2: SMOS instantaneous alias-free field-of-view (irregular curved hexagon), illustrating the multi-angular and spatially variable resolution of the measurements. Incidence angle (dashed lines) ranges from 0 to 65, spatial resolution (dashed-dotted lines) from 32-100 km, and radiometric sensitivity (dashed-dotted) from 2.60 K at boresight to 5 K. As the satellite advances, a single spot is seen in successive snapshots under different angles and spatial and radiometric resolutions depending on its position within the instrument field of view. Taken from *Font et al.*, 2013.

2013). Section 3.2.1.3 provides more information on the various error sources and uncertainties in SMOS products.

The SMOS L2 SSS retrieval algorithm is based upon a classical inversion method by minimization of the differences between the antenna multi-angular, multi-polarization Tb measurements and the simulated Tb by a forward transfer model (*Kerr et al.*, 2010; *Reul et al.*, 2012b), corresponding to instantaneous SSS retrievals under the satellite swath (*Reul et al.*, 2013). The forward model takes into account among other factors, atmospheric, ionospheric and geophysical effects as well as surface roughness effects by one of three scattering models (*Mecklenburg et al.*, 2012; *Reul et al.*, 2012b). Therefore, in the SMOS L2 products, 3 different SSS values are provided, corresponding to 3 retrieval algorithms with different assumptions for the surface roughness and with individual uncertainty estimates (*Johnson and Zhang*, 1999; *Dinnat et al.*, 2003; *Gabarró et al.*, 2004). Simultaneous auxiliary information on the sea surface conditions (sea surface temperature, roughness) is needed from external sources, as they are not directly measured by SMOS. This can add to the inaccuracy of the retrieved salinity (*Lagerloef and Font*, 2010; *Font et al.*, 2010b), due to e.g. errors in the ECMWF wind speed or the OSTIA L4 SST products used as external sources for SMOS (*Reul and*

Ifremer CATDS-CECOS Team, 2012; *Yin et al.*, 2013). Potentially erroneous retrieval results are identified through a series of flags, including values where the retrieved SSS exceeds the mean climatological value from the World Ocean Atlas 2009 (WOA09) used as input for the SSS inversion (e.g. *Yin et al.*, 2013) plus/minus five times the climatology standard deviation (*Reul et al.*, 2012b). Further details on the SMOS SSS retrieval approach can be found in e.g. *Kerr et al.*, 2010; *Font et al.*, 2010b; *Font et al.*, 2013.

Given the complex relationship between SSS and Tb and the technical limitations in achieving highly stable and calibrated measurements (*Boutin and Martin*, 2006; *Font et al.*, 2010b), the mean theoretical error of SMOS is 0.6 pss in Tropical and Subtropical waters, making spatio-temporal averaging necessary (*Boutin and Martin*, 2014). Thus, in order to achieve improved accuracy of SSS adequate for oceanographic studies, the L2 single-pass measurements are averaged over multiple orbits to produce gridded L3 products with reduced random error and improved accuracy of the retrieved SSS (*Boutin et al.*, 2004; *Kerr et al.*, 2010). Typically, L3 products are available over 10-30 days and 0.5° to 1° resolution.

3.2.1.2 Validation of SMOS against in situ measurements

In addition to the challenging SSS retrieval from interferometric radiometer measurements of upwelling L-band radiation, validation of SMOS SSS observations represents another challenging task. A factor making validation difficult is the effect of SSS variability in short horizontal scales, i.e. shorter than the SMOS footprint (∼40 km), that can contribute to differences when comparing the horizontally averaged satellite and the localized in situ measurements. The sampling error resulting from small-scale noise can be considerable in regions with strong currents and river outflows (*Vinogradova and Ponte*, 2013). In addition, the vertical salinity stratification in the upper sea surface layer recently revealed by SMOS in rainy regions when compared to the 5-10 m depth Argo (*Boutin et al.*, 2013) requires salinity measurements to be performed at several depths and as closest as possible to the surface. For instance, the recent attempts with high resolution Argo-STS profilers (*Anderson and Riser*, 2012) and autonomous drifters (*Reverdin et al.*, 2012) are of high priority for the validation of satellite SSS (*Boutin and Martin*, 2006).

Nevertheless, overall, SMOS measures the global distribution of SSS reasonably well (*Font et al.*, 2013). The first validation studies of SMOS SSS L3 data indicate a generally good agreement with in situ observations and ocean model outputs (*Banks et al.*, 2012; *Boutin et al.*, 2012; *Reul et al.*, 2013), having an accuracy (based on reprocessed data for 2010 on monthly or 10-days averages over 1° x 1° boxes) on the order of 0.5-0.6 pss globally and in cold waters, which degrades in proximity to land (*Reul et al.*, 2012b; *Boutin et al.*, 2013). Biases are larger at high latitudes, mainly due to uncertainties associated with the lower sensitivity

in cold waters and the roughness correction models (strong wind), as well as RFI contamination particularly at the Northern high latitudes and over the Arctic. The Tropical/Subtropical region (warm waters, less RFI impact), chosen as a focus in this thesis, is characterized by smaller errors and an improved SMOS accuracy of the order of 0.3-0.4 pss for monthly (*Reul et al.*, 2012b) and 10-day L3 products (*Boutin et al.*, 2012; *Boutin et al.*, 2013), primarily thanks to the region's warmer waters.

3.2.1.3 Sources of uncertainties in SMOS data

As demonstrated above, lack of previous experience on the SMOS interferometric concept and complex image reconstruction data processing introduce various imperfections and errors that impact the accuracy of the retrieved SSS (e.g. *Reul et al.*, 2013). This section summarizes the main error sources on SMOS L2 and L3 SSS products, including solar contamination, RFI, land contamination and geophysical corrections, i.e. sky noise, roughness-induced biases and spatio-temporal drifts, e.g. due to instrumental drifts. For further information on the mission performance and operations as well as first results of the SMOS mission, see for instance, the IEEE Geoscience Remote Sensing Society (GRSS) special issue on SMOS (May, 2012).

Sea surface roughness and wind speed A major source of uncertainty for the remotely sensed SSS is the impact of sea surface roughness on the L-band emissivity, which is the dominant factor affecting the signals, and therefore, needs to be carefully corrected for. Errors can be also induced by the use of operational three-hourly ECMWF wind fields as input to the SSS retrieval, which can differ from the surface conditions observed by SMOS (*Yin et al.*, 2013).

High latitudes The L-band sensitivity of emissivity to SSS reduces significantly in cold waters, particularly below 6-7°C where sea ice may be present. SMOS L2 SSS mean error is found to increase with decreasing SST by about 0.05 pss/°C, varying significantly from ascending to descending passes. This likely indicates that other error sources (apart from low SST) may also contribute to a reduced accuracy, including the transition between open ocean and land/ice in Antarctica, ice contamination, high winds model biases, and RFI in Northern latitudes (*Reul et al.*, 2012b).

Radio Frequency Interference (RFI) Although L-band is an internationally protected radio frequency band, RFI from man-made emissions, such as military radars and telecommunication networks, significantly affect the SMOS multi-angular Tb measurements. RFI effect is noticeably large in Europe and Asia, as

well as in regions of Africa, America, Greenland and numerous islands globally. While the RFI signal originates mainly from land sources, the effect can extend over long distances and have dramatic consequences on the accuracy of SMOS SSS retrieval over the ocean (e.g. *Mecklenburg et al.*, 2012). Key oceanic regions like the Northern latitudes of the Atlantic, Pacific and Indian oceans are particularly badly affected. Highly variable in space and time, the RFI impact strongly depends on SMOS polarization and observation angles, and can contaminate large parts of the extended Alias-free Field of View domain (AF-FOV) of the SMOS reconstructed Tb images, showing as large spatial ripples in the images far from the sources. For instance, until summer 2011, no accurate salinity measurements were possible with SMOS above 45° latitude (*Reul and Ifremer CATDS-CECOS Team*, 2012; *Reul et al.*, 2012b). Instead of applying detection and mitigation techniques prior to image reconstruction, a simple detection algorithm can be applied to the reconstructed Tb images by identifying anomalous values compared to the neighbouring ones (in space, time and probing angles), exploiting the strong amplitude of RFI signals in relation to the oceanic geophysical signal (*Reul and Ifremer CATDS-CECOS Team*, 2011; 2012).

Land-induced contamination Land contamination strongly biases SMOS SSS (in general too salty) within a ∼1500 km wide belt along the world coasts and sea ice edges (*Reul et al.*, 2012b), due to strong brightness temperature gradients associated with sea/land/ice transitions (*Mecklenburg et al.*, 2012). This bias is systematically present in the first ESA data versions due to a bug in the initial L1B processor, when brighter land or ice masses are located in the extended FOV domain of the antenna (*Reul and Ifremer CATDS-CECOS Team*, 2011; 2012). Its spread and intensity strongly depend on pass direction, increasing in magnitude towards the coasts, i.e. the median ΔSSS as a function of distance to the coast reaches an amplitude of ∼0.7 pss at about 150 km away from it (*Reul et al.*, 2012b).

Galactic noise Modelling of the galactic signal and its reflection on the sea surface is considered another important geophysical source of error for SMOS L2 SSS data (*Reul et al.*, 2012b). Sky noise originates from downwelling celestial radiations at L-band that are scattered back by the sea surface toward the upper atmosphere. For sun-synchronous polar-orbiting SMOS measurements of upwelling L-band radiation over the ocean, this source of Tb contamination impacts on the quality of SSS retrieval. The effect highly depends on pass direction, time of the year and surface roughness (wind speed) (*Reul and Ifremer CATDS-CECOS Team*, 2011; 2012). Strongest impact is expected for descending passes in mid-August to mid-October and for ascending passes in March-April, when the reflected galactic equator where L-band galactic emission is maximum crosses the SMOS FOV (*Reul et al.*, 2012b). To minimize the impact of that spurious signal, the sky-noise correction needs to account for surface roughness induced scattering. Therefore,

modelling of the celestial noise scattering has been under continuous development within the ESA L2 processor framework (*Reul and Ifremer CATDS-CECOS Team*, 2011; 2012).

Spatio-temporal drifts Finally, spatio-temporal drifts due to instrumental drifts, erroneous accounting of the seasonal cycle in the forward Tb model contributions and varying solar radiation effects, are evident in both L2 and L3 SSS. Among them, the latitudinal biases in descending orbits are considered most crucial for the generation of L3 products. Being maximum at the end of the year, they translate into significantly too fresh and too salty SSS in the Northern and Southern oceans, respectively, restricting the opportunity for L3 SSS error reduction by the combination of ascending and descending passes (*Reul et al.*, 2012b). In addition, the so-called "1-slope" calibration in SMOS L1 to account for thermal drifts still produces a residual seasonal cycle in Tb toward the end of each year, which appears as a seasonal cycle in the mean bias of retrieved SSS of ∼2 pss peak-to-peak amplitude (without periodic Ocean Target transformation correction). Finally, an erroneous correction of the direct sun aliases on the Extended FOV in the ESA L1A to L1B processor is likely responsible to a great extent for the large spatio-temporal drifts in the ESA reprocessed L1B data (*Reul and Ifremer CATDS-CECOS Team*, 2011; 2012).

Despite considerable improvements in the SMOS instrument calibration and image reconstruction, systematic bias patterns of several Kelvins in the FOV are still observed between averaged measured and simulated Tb. These biases are currently estimated and mitigated using the Ocean Target Transformation (OTT) technique, i.e. a practical approach which aims to reduce the impact of any residual bias, regardless of its origin, in the reconstructed Tb images over the ocean (*Yin et al.*, 2013; *Font et al.*, 2013). The OTT includes the computation of 2-D median differences between the forward model simulations estimated using the WOA 2005 monthly climatology and the measured L1 Tb over a relatively homogeneous ocean area in the Eastern Pacific Ocean, which needs to be removed before the L2 SSS retrieval (*Reul et al.*, 2012b; *Yin et al.*, 2012).

3.2.1.4 Available L3 SMOS SSS products

Global SMOS L3 SSS products are produced from the ESA SMOS Expert Support Laboratory Centers, i.e. the SMOS Barcelona Expert Centre (SMOS-BEC), the LOCEAN/IPSL Laboratory and the CNES/IFREMER Centre Aval de Traitement des Données SMOS (CATDS) Ocean Salinity Expertise Center (CECOS) (*Font et al.*, 2013; *Reul et al.*, 2012b; *Boutin et al.*, 2012). Information on the SMOS mission and data availability can be found in the ESA monitoring facility: https://earth.esa.int/web/esa-operational-eo-missions/smos. The work in this

thesis is based on the Ifremer CATDS-CECOS L3 products, which are described in the following section.

3.2.1.5 CATDS-CECOS SMOS SSS products used in this thesis

Research SMOS SSS L3 monthly mean products for the period January 2010 - December 2012 are acquired from the Ifremer CATDS-CECOS website (http://www.catds.fr) at 1.0° x 1.0° spatial resolution. Data for the years 2011 and 2012 come from the latest version at this time (V02), (*Reul and Ifremer CATDS-CECOS Team*, 2012). For 2010, data are taken from version V01 (*Reul and Ifremer CATDS-CECOS Team*, 2011) in order to obtain three complete years (2010-2012) of SMOS SSS, as V02 covers only the period May-December for the year 2010. In version V02, data for the period January-April 2010 of the SMOS commissioning phase were not reprocessed, due to reduced quality of the SMOS data in the initial post-launch phase, and users are advised to use version V01 products to cover this period of time (*Reul and Ifremer CATDS-CECOS Team*, 2012).

The input data used to generate version V01 of the CATDS-CECOS research L3 products are the ESA reprocessed L1A data for the year 2010, from both the dual and full polarization modes, as during the commissioning phase (January to end of June 2010), the instrument was operating alternatively in both polarization modes (*Reul and Ifremer CATDS-CECOS Team*, 2011). In contrast, version V02 is built from the ESA's first reprocessing of L1B data from May 2010 to December 2011, while the operational L1B data are used for the period January-December 2012. Further information on the main characteristics of the CATDS-CEC SSS L3 products from version V02 is provided in Table 3.1. The V01 L3 product has a SSS standard deviation of ∼0.25-0.35 pss for the Tropical Atlantic in 1.0° x 1.0° grid cell from January-December 2010, increasing in November-December 2010 to ∼0.25-0.45 pss for unknown reason (*Reul and Tenerelli*, 2011). Validation document for V02 from the CATDS-CECOS is not yet available while this thesis is written up.

Recently, the Ifremer CATDS-CECOS V02 product has been compared with other SMOS L3 SSS products from LOCEAN, Aquarius as well as with In Situ Analysis System (ISAS) SSS over the North Subtropical Atlantic. The CATDS-CECOS V02 product, although may modify artificially the spatial SSS distribution given its adjustment to the climatology (See paragraph "Spatio-temporal drifts" at the end of this section), still reproduces the SSS seasonal variability indicated by the ISAS products (*Hernandez et al.*, 2014). However, its correlation coefficient with TSG SSS data, i.e. r=0.85 at 0.25° x 0.25° or r=0.88 at 1° x 1° spatial resolution, remains lower than that for the other products, as its relaxation to the climatology likely modifies artificially the spatial distribution of the SSS field (*Hernandez et al.*, 2014). This may smooth some of the interannual SSS variability, and this will be further discussed in Chapter 5. Nevertheless, the CATDS-CECOS products are

Table 3.1: Summary of the main characteristics of Ifremer CATDS-CEC SSS L3 products from version V02, used in this thesis. The table is adapted from *Reul et al.*, 2013.

	Version V02
Brightness temperature (Tb)	L1b reconstructed on Equal-Area Scalable Earth (EASE) grid
SSS retrieval	SSS retrieved from first Stokes parameter $Tb_x + Tb_y$ (*Reul and Tenerelli*, 2011) +: not affected by Faraday rotation -: no check of dwell line consistency
Wind model	Model 2 (Empirical adjustment of Tb dependencies to wind speed by using bin average)
Calibration	Single ocean target transformation (OTT) and daily 5°x 5° adjustment wrt WOA01 SSS climatology +: single OTT calibration -: need additional bias correction (in time and space) that mask part of interannual variability
Flagging	Tb filtering method: interorbit consistency in incidence angles classes and thresholding RFI % +: more refined than L2OS flags
Region of the instrument field of view (FOV) considered for SSS retrieval	Alias free field of view (AFFOV) only +: avoid suspicious Tb in EAFFOV -: reduced number of Tbs
Galactic model	Geometrical optics model (wind speed dependence)
Average	Simple average after thorough filtering of inconsistent SSS + interorbit consistency check
Format	Netcdf – rectangular grid
Access	support@catds.fr
Period	June 2010-December 2012
Resolution	Daily, 10-days, Monthly, 0.25°, 0.5°, 1°

chosen in this thesis given their main advantage of a better RFI filtering approach, and thus, of a potentially better detection of SSS close to the coast and the river plumes, as it will be seen in the rest of this Section and in Section 3.2.1.6.

The main corrections applied in the CATDS-CECOS products (V01 and V02) for some of the known uncertainties in SMOS are briefly described below. For further information on the product algorithms used in each version, the reader is referred to the Algorithm Theoretical Baseline Document for V01 and V02, available from the CATDS-CECOS ftp server (eftp.ifremer.fr). Finally, the rest of this section presents a comparison of SSS in 2010 from the two versions (paragraph I in 3.2.1.6),

and an examination of RFI in the region of interest for the years 2011 and 2012 (V02), (paragraph II in 3.2.1.6).

- **Solar contaminations:** To account for solar radiation impact, SSS retrieval in CATDS-CECOS products is limited to the AF-FOV instead of applying a "direct sun" correction (*Reul and Ifremer CATDS-CECOS Team*, 2011). Moreover, in version V02, in order to best mitigate this effect, a mask is applied to eliminate the reconstructed Tb in the proximity of the aliased sun-disk, which is sometimes located at the border of the AF-FOV, particularly at the end of all years (November-December) in descending passes (*Reul and Ifremer CATDS-CECOS Team*, 2012). However, spurious stripe-like fresh anomalies in the composite L3 SSS data are still observed, which progressively amplify at the end of the years (October to December) and may be related to residual solar contamination in the ESA L1 data (*Reul and Ifremer CATDS-CECOS Team*, 2011; 2012).

- **Land-induced contamination:** Correction for land contamination is applied in the CATDS-CECOS products so that its impact is much more limited in spread and intensity than in other L3 products. However, too salty a signal is still found along some coasts (*Reul and Ifremer CATDS-CECOS Team*, 2011; 2012).

- **RFI:** Robust threshold detection criteria for RFI contamination have been established at CATDS-CECOS based on a global analysis of the spatio-temporal characteristics of RFI signals as a function of instrument probing configuration (incidence angle, orbit direction) over the whole period of the SMOS mission. Thus, using a multiple criteria mitigation approach, SSS is retrieved after most of the contaminated Tb in the FOV is filtered out. Nevertheless, residual RFI-induced signals still persist, resulting in lower quality SSS retrieval, but now only limited regions such as the Northern latitudes, the Mediterranean sea, and along the Asian coastlines (*Reul and Ifremer CATDS-CECOS Team*, 2011; 2012).

  Moreover, in version V02, a new approach is applied by identifying RFI signals over the whole fundamental hexagon using simple, empirically determined Tb thresholds. However, this method filters out a large amount of both bad and good quality SMOS data along the coastlines. Therefore, a new variable (RFI_{stat}) is provided in V02, corresponding to the probability of remote RFI detection in the ensemble of multi-angular measurements used for the SSS retrieval, enabling the user to perform his own filtering. This RFI probability criterion is used to weight the SSS swath data used for the CATDS-CECOS L3 composite products, while pixels with RFI probability exceeding 80% in the input data over the considered space-time window have been removed. In general, over the oceans, the mean RFI probability is stable in time and reaches 3%, decreasing considerably in the N. Atlantic

from ∼10-12% in early 2010 to 4-5% end of 2012 (*Reul and Ifremer CATDS-CECOS Team*, 2012). See paragraph II of this section (3.2.1.6) for the mean RFI probability over the Tropical/Subtropical Atlantic 30°N-30°S.

- **Sky noise:** Corrections for scattered sky noise in CATDS-CECOS V01 products are generated based on the Kirchhoff scattering model, which lacks wind speed dependence, and thus can result in fresher SSS in L2 products (*Reul and Ifremer CATDS-CECOS Team*, 2011; *Reul et al.*, 2012b). Erroneous correction can lead to non-geophysical variability in the L3 V01 products from August to October (*Reul and Ifremer CATDS-CECOS Team*, 2011). Scattered sky noise in version V02 is corrected with a new semi-empirical correction algorithm based on the Geometric Optics (GO) scattering solution, which retains wind speed dependence and results in improved predictions compared to the Kirchhoff model. Nevertheless, residual erroneous correction might still cause some non-geophysical variability in V02 data, particularly under low wind speed conditions (*Reul and Ifremer CATDS-CECOS Team*, 2012).

- **Spatio-temporal drifts:** The above mentioned (See Section 3.2.1.3) instrumental drifts, mainly related to unsolved calibration (thermal) and image reconstruction issues, e.g. solar effects in L-band imaging and antenna patterns uncertainties, introduce significant latitudinal and seasonal drifts in the retrieved SSS, with amplitude depending on pass direction. In CATDS-CECOS, a large scale bias correction method is applied in V02 products, which, in contrast to ESA L2, uses only one Ocean Target transformation (OTT) determined in the Pacific in 2012. In addition, L3 SSS is bias-adjusted using a large-scale correction based on 5° x 5° spatial filter derived from the World Ocean Atlas 2001 monthly SSS climatology, temporally interpolated at the SMOS acquisition date (*Reul and Ifremer CATDS-CECOS Team*, 2012).

3.2.1.6 Assessment of CATDS-CECOS products

Comparison of CATDS-CECOS version V01 and version V02 in the region of interest Preliminary assessment of the L3 V02 products performed from the CATDS-CECOS indicates, overall, a comparable quality to those from V01 (*Reul and Ifremer CATDS-CECOS Team*, 2012), despite the relaxation of SSS data from V02 to the climatology. In turn, comparison of the Ifremer CATDS-CECOS V02 product with In Situ Analysis System (ISAS) SSS over the North Subtropical Atlantic indicates that, although adjustment to the climatology may modify artificially the spatial SSS distribution, the V02 product still reproduces the SSS seasonal variability indicated by the ISAS products (*Hernandez et al.*, 2014). Here, monthly differences of SMOS SSS from V01 minus V02 versions are examined for their common period May-December 2010 (Figure 3.3). Version V02 often gives more data in grid cells close to the coast compared to V01. Therefore, in the present thesis, SMOS SSS fields for 2011 and 2012 (V02) are masked out to cover

the same grid cells as 2010 (V01), in order to ensure spatial consistency of the SSS fields between the two versions and throughout the period 2010-2012.

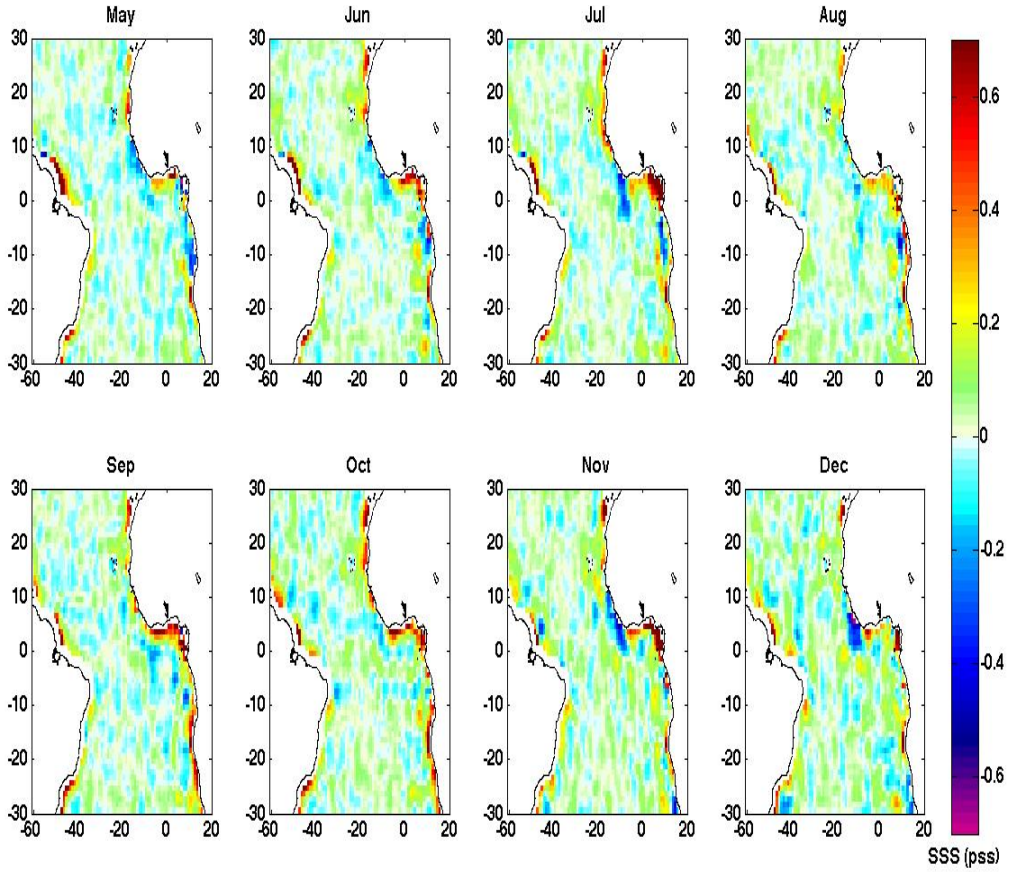

Figure 3.3: Monthly mean differences of SMOS SSS from version V01 minus V02 in the Atlantic basin 30°N-30°S for their common period May-December 2010.

The SSS differences between V01 and V02 for May-December 2010 are seen in Figure 3.3 in a range ±0.7 pss. Varying, in general, between -0.23 and 0.63 pss (99% quantile) in the Tropical Atlantic 30°N-30°S, there is good consistency between them, given all the uncertainties associated with data processing and the different corrections applied in each version. The largest discrepancies are observed close to the major river systems, where V01 displays almost always higher values than V02 throughout their common period. For instance, there are few (1-2) grids in the Amazon/Orinoco plume where the differences exceed 5 pss. Some large discrepancies occur also near the coasts north and south of the Gulf of Guinea, where V02 displays higher values, as for instance, in the meridional band 5°-10°W (between 5°N-5°S) in July, November and December (Figure 3.3). One of the possible causes of these differences is RFI flagging.

II. Examination of RFI probability in the region of interest V02 products provide an estimate of RFI probability (RFI_{stat}) in the ensemble of multi-angular measurements used for the SSS retrieval (*Reul and Ifremer CATDS-CECOS Team*, 2012), which enables the examination of RFI impact in the region of interest.

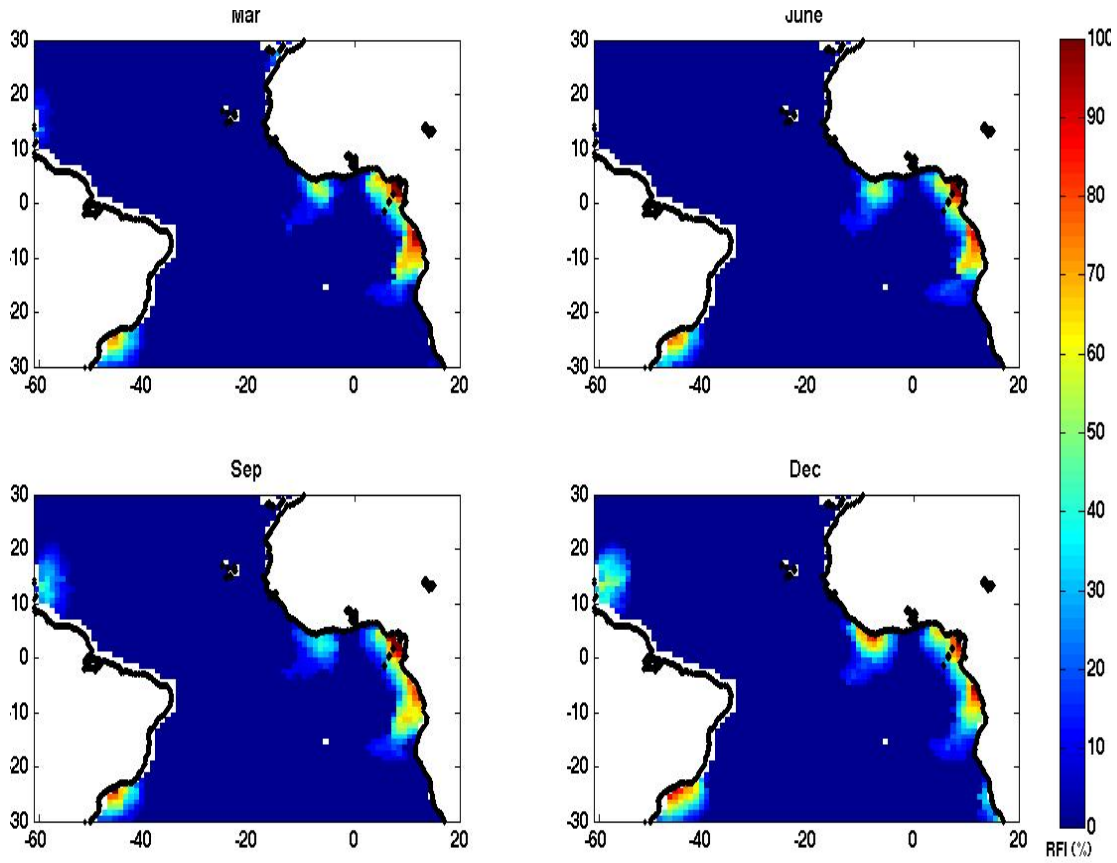

Figure 3.4: RFI probability percentage per pixel of CATDS version V02 data in 2011 for March, June (top left and right), September and December (bottom left and right).

Figure 3.4 shows the mean RFI probability percentage in the Tropical/Subtropical Atlantic 30°N-30°S for selected months in 2011, as typical examples for the whole period 2011-2012. The Gulf of Guinea and its wider region display a very high likelihood of RFI contamination throughout the years 2011 (Figure 3.4) and 2012 (plot not shown), that can often exceed 80%. In the western basin and close to the Amazon/Orinoco plume, the mean RFI probability increases noticeably towards the end of 2011 (Figure 3.4, bottom plots for September and December, respectively) and most of 2012, reaching up to 60% in some cases, but still remains lower compared to the eastern Tropical basin.

Wishing to perform an analysis based only on a priori free from RFI SSS fields, i.e. by filtering the data for 2011 and 2012 from grid cells that suffer from RFI and keeping only clear grid cells with 0% or even 10% percent probability, would mask out all or large part of the eastern and western subregions of interest (plots not shown). Thus, it would set the examination of the SSS seasonal cycle close to the river outflows impossible. Given that within the improved RFI mitigation approach applied in the CATDS-CECOS V02 data, pixels with RFI probability contamination larger than 80% have been excluded (*Reul and Ifremer CATDS-CECOS Team*, 2012), no further RFI filtering is performed in the present thesis.

However, it confirms that RFI is the likely cause of the observed differences between V01 and V02 in May-December 2010 seen in Figure 3.3.

3.2.2 Sea Surface (SSS) and Upper Ocean Salinity (UOS) from WOA09

Objectively analyzed monthly climatological means of in situ SSS and salinity at the top 10 m (S10) in 1.0° x 1.0° grid cell are obtained from the World Ocean Atlas 2009 (WOA09) which covers the period 1955-2006 (*Antonov et al.*, 2010). WOA09, providing climatological salinity fields in various depths, is an expansion of earlier atlas series, such as the WOA05, WOA01, WOA98, WOA94 and Climatological Atlas of the World Ocean (*Levitus*, 1982), based on objective analyses of historical oceanographic profile data.

WOA09 S10 bins together all observations in the top 10 m of the water column, while the depth of the SSS measurements ranges between 1-5 m (*Antonov et al.*, 2010). Differences between WOA09 SSS and S10 indicate a fresher SSS by ∼1 pss relative to S10 in the proximity of these rivers (plots not shown). Noticeably larger deviations reaching or even exceeding ∼10 pss are found in few grid cells close to the Amazon/Orinoco region (∼1-7°N) for some months during the year, such as in January, March, May and July. Despite the ∼50 years of climatology and the inclusion of Argo floats in more recent versions, WOA09 data still remain very sparse in time and space. For instance, Figure 3.5 shows the number of observations (N_{obs}) per 1° x 1° grid cell in the Atlantic 30°N-30°S for March, chosen as a typical month in terms of N_{obs} density in this region. the N_{obs} of samples per 1° grid cell varies around ∼10-15 observations on average over ∼50 years of data, with a few exceptions along the African coast or in the middle of the basin. However, there is also a large number of grid cells with no observations at all, further limiting the objective analysis technique used and making the WOA09 SSS and S10 subject to significant bias and uncertainty. The standard error of the statistical SSS from which the objectively analysed fields are produced generally varies up to 0.4 pss, but can even exceed 4.5 pss close to the major river outflows and along the Equatorial Atlantic (plots not shown).

Preliminary comparison of WOA09 SSS and SMOS Figure 3.6 shows monthly SSS fields from SMOS in 2010 (V01) and the WOA09 climatology for January, April, July and October, respectively, chosen as typical examples of the rest of the year. The SSS fields from the two datasets show broadly the same large scale features and magnitudes, but indicate also some differences. Among the main differences is the impact on SSS of the seasonal cycle of freshwater river outflow depicted by SMOS. Close to the Amazon/Orinoco region, SMOS displays a strong fresh SSS signature from mid-spring reaching its maximum around June-July (Figure 3.6 a), when the Amazon discharge is also at its peak (e.g. *Romanova et al.*, 2011), which spreads eastwards along the basin in autumn (October). The fresh

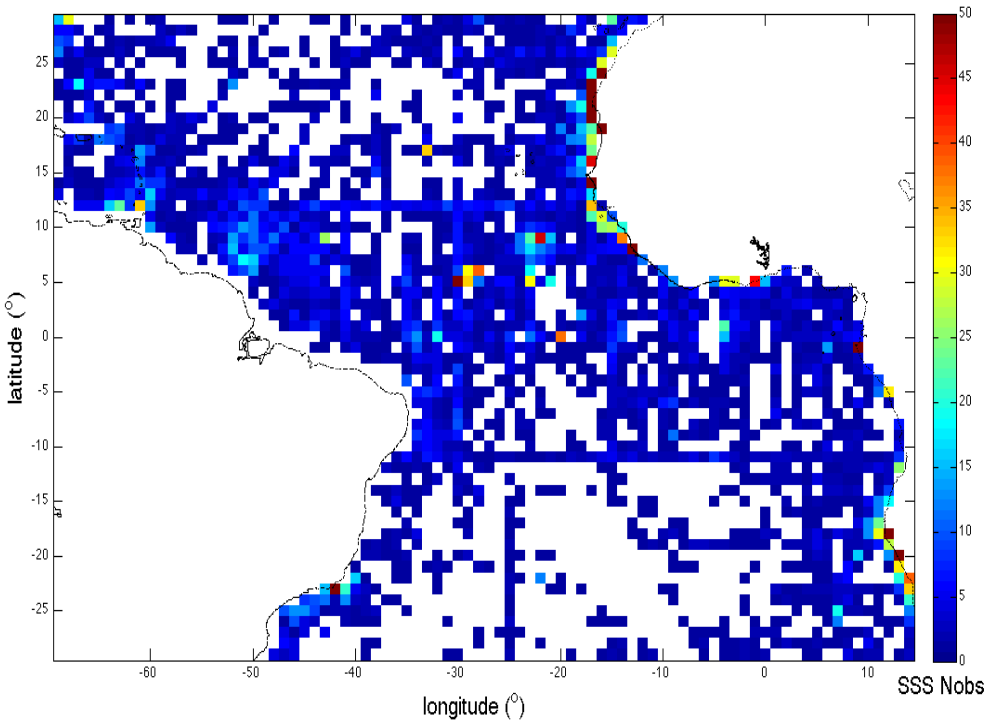

Figure 3.5: Number of WOA09 SSS observations per 1° x 1° grid cell in the Atlantic region 30°N-30°S for March over the period 1955-2006. White gaps indicate grid cells with no measurements at all.

SSS signal fades gradually locally towards the end of the year, in accordance with the river's minimum discharge (plots not shown). On the other side of the basin, the fresh signals of SMOS SSS from the Congo and Niger rivers are particularly strong in winter and spring (Figure 3.6 a, January and April). In contrast, the long-term climatological monthly averages from WOA09 smooth out the seasonal SSS variability, which appears just as very fresh SSS values close to both river systems during most of the year (Figure 3.6 b). This is also evident along the Tropical band ∼15°N-5°S that embraces the zone of maximum precipitation over the year, with SMOS providing a more detailed depiction of the SSS seasonal features during the year (Figure 3.6, top panel). Such discrepancies highlight the added value of SMOS to examine the seasonal to interannual variability in SSS in these regions.

The above differences between SMOS and the climatology are further illustrated in Figure 3.7, which shows the long-term monthly mean anomalies of SSS, i.e. the differences of SMOS SSS in 2010 minus WOA09 SSS. Assuming that the 50-year WOA09 climatology is representative of the long-term mean SSS, Figure 3.7 provides an insight into how typical the year 2010 is for SSS. The deviations between the two datasets, displayed here in a range of ±1 pss, vary in general between ∼-1 (i.e. WOA09≫SMOS) and 0.7 pss, but can reach up to ∼-3.8 and 5.6 pss, particularly in grid cells close to the major river plumes. As regards the patchiness of the differences between the climatology and SMOS throughout the year and along most of the basin, their magnitude varies around 0-0.2 pss, thus

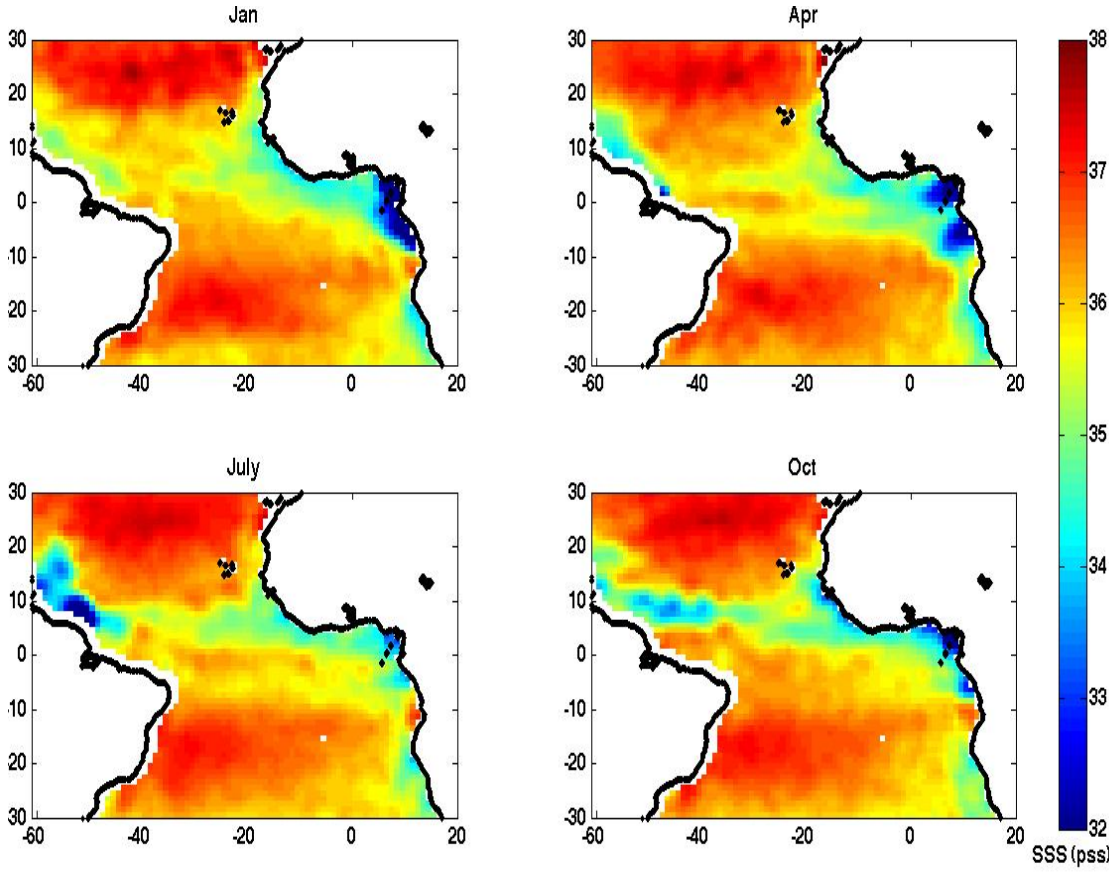

(a) SMOS SSS in 2010

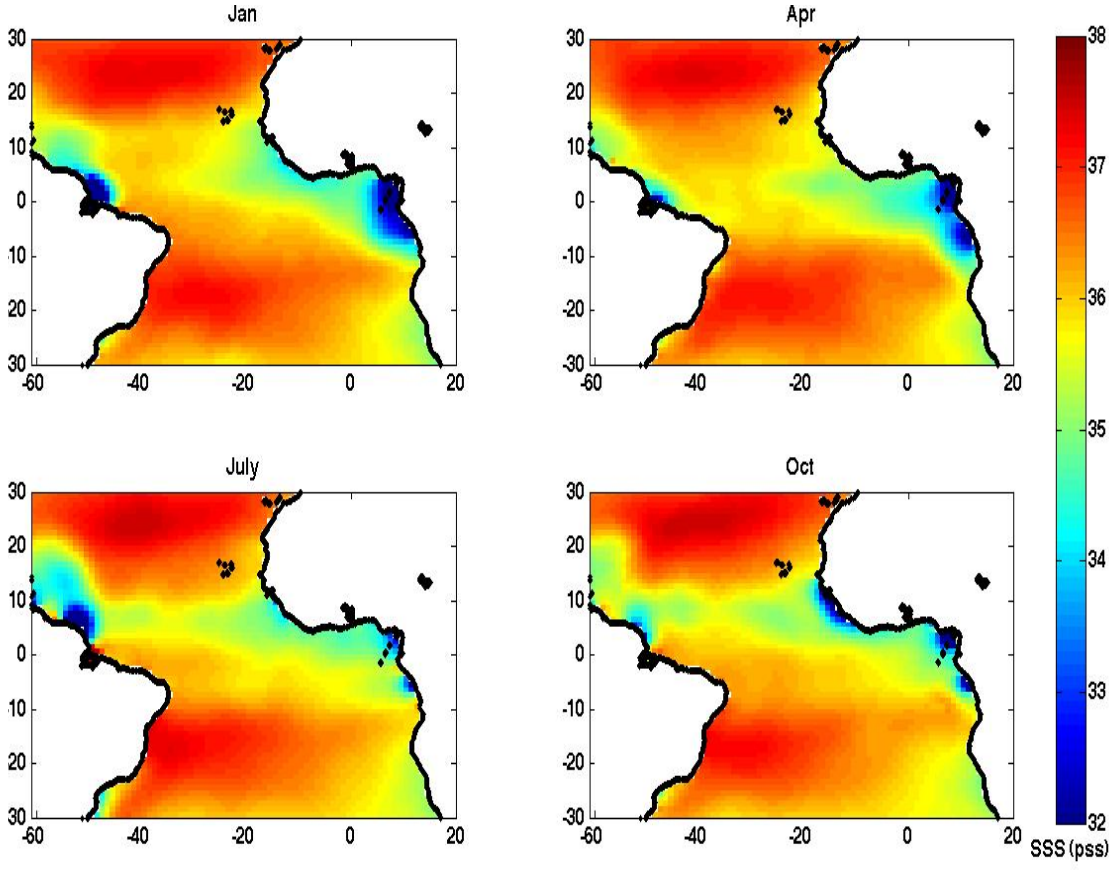

(b) WOA09 climatological obectively analysed SSS

Figure 3.6: a) SMOS SSS in 2010 and b) WOA09 objectively analyzed SSS monthly fields for January, April (top left and right), July and October (bottom left and right).

lying within the SMOS measurement uncertainty. Whether they are actually noise or real features displayed by SMOS will require further investigation.

3.2.3 Argo Upper Ocean Salinity (UOS)

The Argo (Array for Real-Time Geostrophic Oceanography) project has been fully operational since 2005 and provides continuous observations of temperature and salinity in near real time (*Gould et al.*, 2004). Argo floats collect temperature and conductivity vertical profiles from 2000 meters depth to a few meters below the sea surface, every 10 days. The project's target is to maintain about 3000 floats over the global ocean, with one measurement every 3°, providing about 10^5 SSS measurements each year. Over the last few years, in addition to the number of floats, the quality of recent SSS measurements has also improved, while the depth of the surface measurement is decreasing; 95% of upper Argo measurements are taken shallower than 10 m depth, and 77% shallower than 5 m (*Boutin and Martin*, 2006).

In this work, Argo salinity observations for 2010 are obtained from the Coriolis Argo Global Data Assembly Centre (GDAC; ftp.ifremer.fr/ifremer/argo) for the

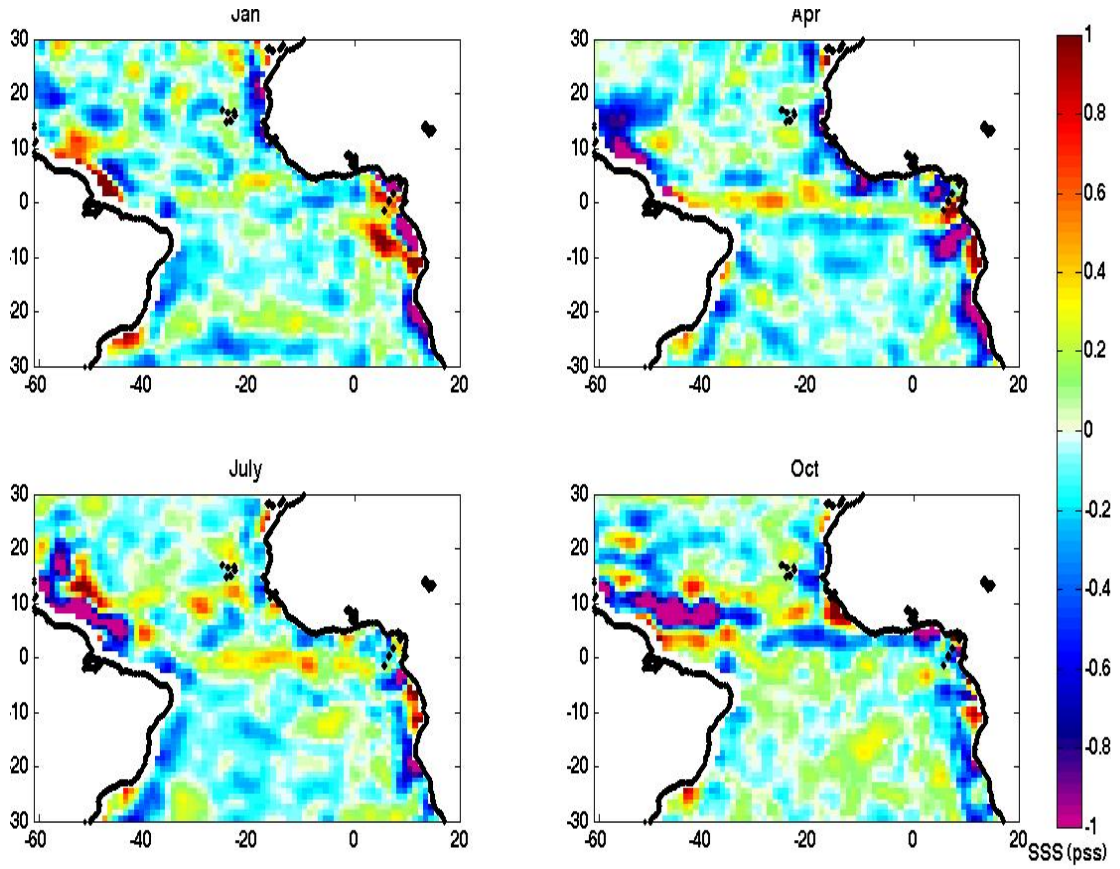

Figure 3.7: Monthly anomaly fields of SMOS SSS in 2010 minus WOA09 objectively analysed SSS for January, April (top left and right), July and October (bottom left and right) in a range of ±1 pss.

region of interest. These data, downloaded on December 1, 2011, correspond to profiles with at least one measurement shallower than a threshold of 10 m, while satisfying all Argo real-time quality control tests (*Carval et al.*, 2006). The upper ocean salinity (UOS) for each profile is obtained by averaging all measurements in the top 10 m and the monthly UOS mean is computed based on all profiles in each 1.0° x 1.0° grid cell within the range 30-40 pss. Examples of monthly mean UOS fields from Argo for selected months in 2010 are shown in Figure 3.8. Figure 3.8 also provides an illustration of the spatial coverage of Argo measurements over the region of interest, which, although significantly greater in the Atlantic basin 30°N-30°S compared to other regions, is still not very good and there are large areas with no measurements at all. Equally important, the number of Argo observations per 1.0° x 1.0° grid cell varies in general around 1-3 per month, with only a few exceptions reaching up to ∼8 observations in isolated grid cells and only during 1 or 2 months (plots not shown).

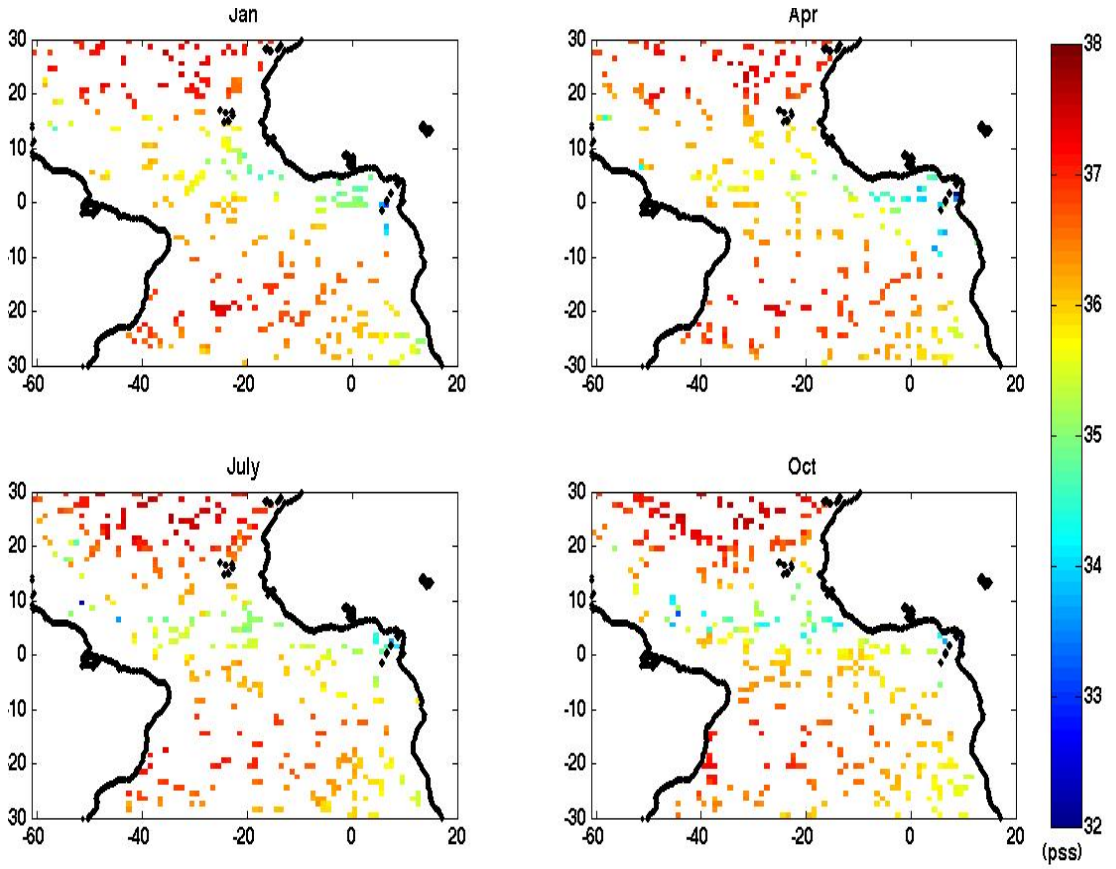

Figure 3.8: Monthly UOS fields from Argo for January, April (top left and right), July and October (bottom left and right) 2010 in 1° x 1° spatial resolution.

Preliminary comparison of Argo UOS and SMOS Figure 3.9 shows the difference of monthly means of SMOS SSS (Figure 3.6 a) and Argo UOS (Figure 3.8) for 2010, indicating discrepancies that vary around ±1 pss. However, salinity deviations between the two datasets can reach up to -4 pss (i.e. Argo≫SMOS), such as in few grid cells close to the Amazon/Orinoco region in October (Figure 3.9, July

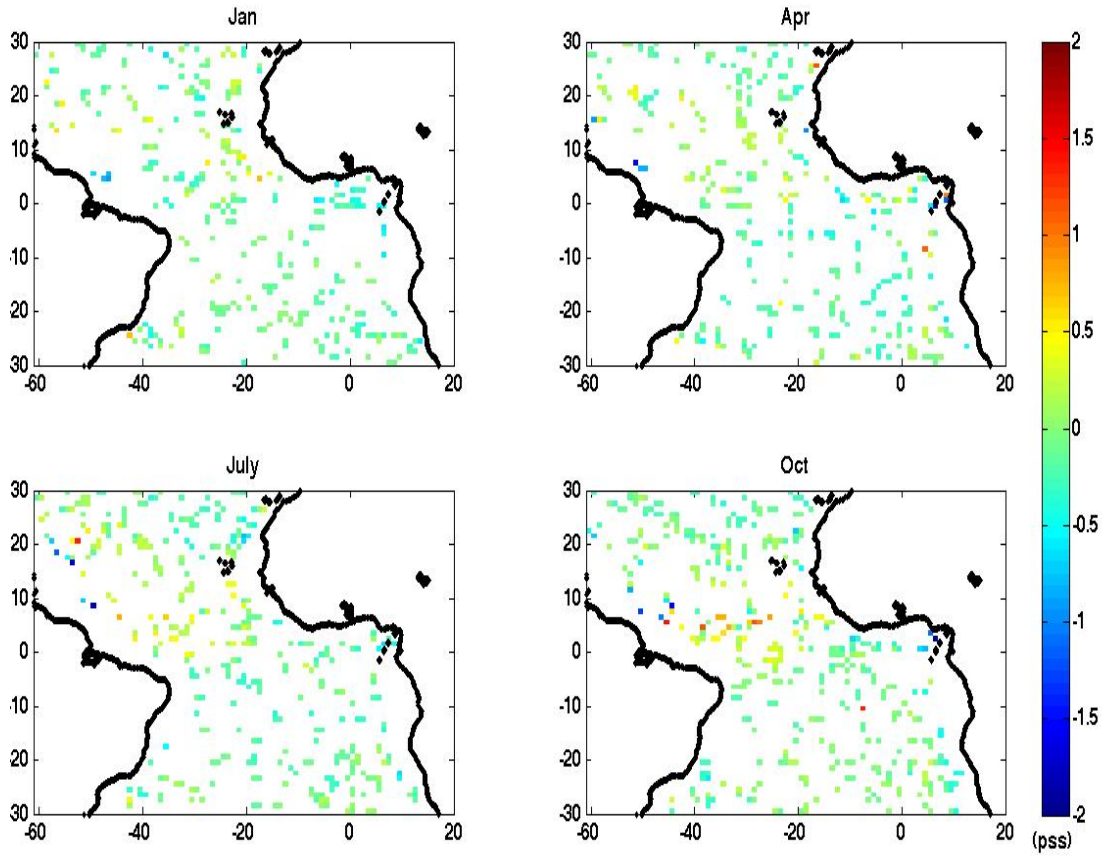

Figure 3.9: SMOS SSS minus Argo UOS monthly differences in 2010 in 1° x 1° spatial resolution.

and October plots). In general, the largest (positive and negative), differences are observed in the N. Subtropical and Tropical Atlantic basin, although the scarcity of data makes it difficult to discern spatial patterns. Looking at the scatterplot for the whole year 2010 (Figure 3.10), where the region of interest is divided into the open ocean and the western and eastern riverine-regions (See Chapters 4 and 5 for their definition), there is quite good agreement for the bulk of the data. However, there are cases, particularly for the lower salinity values which correspond to the river plumes, where SMOS SSS is ∼2 pss fresher than Argo UOS.

Another important parameter for such differences though is the different depth of the salinity measurements, i.e. SMOS observations correspond approximately to the first 1 cm of the sea surface while Argo refers to ∼5-10 m depth. The standard deviation of Argo UOS measurements for 2010 mainly varies around 0-0.6 pss, but can reach ∼1 pss and even exceed 2 pss in a few grid cells close to the Amazon/Orinoco region in some months (plots not shown), explaining to a great extent the significant aforementioned differences with SMOS SSS. Table 3.2 includes the mean, standard deviation and root mean square error (RMSE) of the SMOS SSS minus Argo UOS differences based on their monthly means for 2010 for each region, accounting for both all values and when potential outliers are excluded. For the whole Tropical/Subtropical Atlantic basin 30°N-30°S, the uncertainty of SMOS relative to Argo (without excluding any potential outliers) is about 0.31

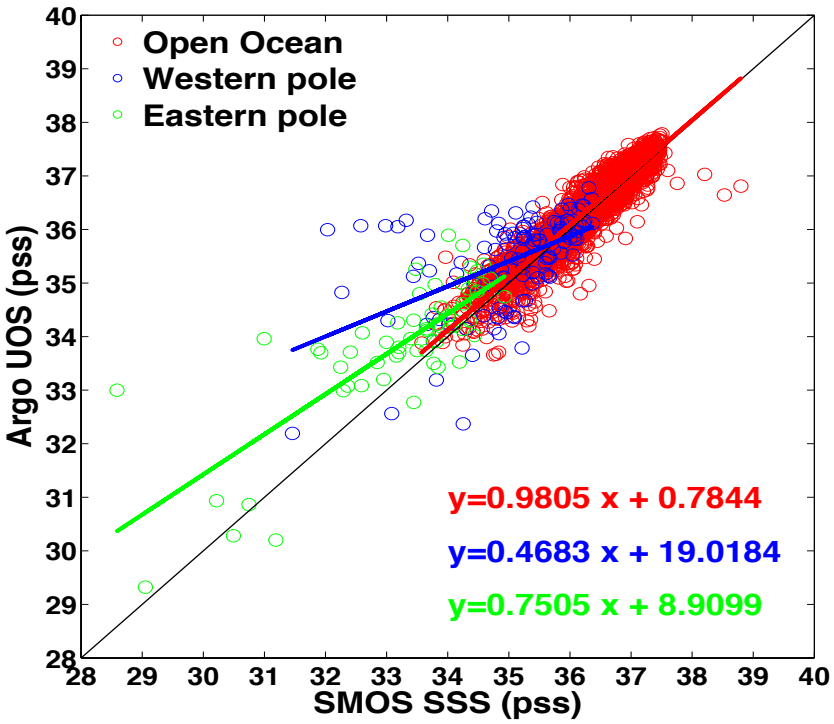

Figure 3.10: Scatterplot of monthly SMOS versus Argo SSS monthly means for 2010 over the open ocean (red), the western (blue) and eastern (green) poles (See Chapters 4 and 5 for their definition).

pss and their RMSE difference equals ∼0.33 pss, decreasing to ∼0.24 pss and ∼0.25 pss, respectively, over the open ocean, i.e. when the two riverine-influenced are excluded. The SMOS uncertainty increases noticeably to about 0.91 pss over the Amazon/Orinoco plume and to ∼0.85 pss in the Congo/Niger plume region. As expected, removing any potential outliers improves their statistics (Table 3.2). However given the different measurement depth between SMOS and Argo, for the rest of thesis, no values are excluded and any reference to the SMOS uncertainty in the text refers to the statistics being produced with any potential outliers.

Table 3.2: Statistics of the SMOS minus Argo differences in each region based on their monthly means for 2010. Values inside brackets are calculated after removal of the outliers.

	Mean (SMOS-Argo)	**St. dev. (SMOS-Argo)**	**RMSE (SMOS-Argo)**
Whole region	-0.0930 (-0.0844)	0.3115 (0.2594)	0.3251 (0.2728)
Open Ocean	-0.0761 (-0.0772)	0.2410 (0.2367)	0.2527 (0.2489)
Western pole	-0.3754 (-0.1902)	0.9131 (0.5650)	0.9838 (0.5936)
Eastern pole	-0.6129 (-0.3929)	0.8483 (0.5124)	1.0409 (0.6419)

To conclude, the SMOS uncertainty in the Tropical/Subtropical Atlantic 30°N-30°S of 0.3 pss does not still meet the mission goals. Nevertheless, it comes in agreement with other validation studies in the region of interest (*Reul and Tenerelli*, 2011; *Hernandez et al.*, 2014).

3.3 Freshwater fluxes

The ocean surface freshwater fluxes consist of Evaporation minus Precipitation minus River discharge (E-P-R), and constitute ∼80% of the Earth's total surface water fluxes (e.g. *Durack et al.*, 2012). Nevertheless, their direct measurement still involves many difficulties and thus, they are often estimated from other oceanic or atmospheric variables. These include the use of direct bulk-formulas for the E estimation (e.g. *Sohn et al.*, 2004), atmospheric reanalysis products (e.g. *Kalnay et al.*, 1996; *Schanze et al.*, 2010), and via inverse methods based on the divergence of ocean freshwater transports (e.g. *Wijffels et al.*, 1992; *Talley*, 2008).

In the last decades, satellite remote sensing and its global coverage has contributed significantly to the improvement of atmospheric (e.g. moisture content and surface humidity) and key air-sea flux related variables (e.g. SST, wind speed) (see for instance, *Robinson*, 2004; *Robinson*, 2010). Such satellite observations are used together with in situ measurements in empirical formulas and data assimilation models to derive E and P fields with near-global coverage (*Schanze et al.*, 2010). However, despite continuous progress, there are still large uncertainties, and these indirect techniques and the irregular sampling in space and time can also result in varying spatio-temporal error characteristics (e.g. *Schlax et al.*, 2001) and significant deficiencies in the air-sea flux estimates (e.g. *Grist and Josey*, 2003; *Yu and Weller*, 2007; *Schanze et al.*, 2010).

In addition to the actual difficulty of making these measurements, validation of freshwater fluxes over the ocean is a challenging task, particularly due to lack of high quality precipitation (P) data as a reference (*Wijffels*, 2001; *Yu et al.*, 2008). The nature of P, i.e. occurring on small and rapidly varying scales, makes in situ measurements inaccurate, biased and generally unreliable (*Quartly et al.*, 2002). As a consequence, P is the least well-determined surface exchange field, characterized by major uncertainties. Among the various available flux products, with their individual in general advantages and disadvantages, those based on satellite data are considered to display, in general, more accurately the geographical P features (*Quartly et al.*, 2007). Nowadays, only surface-based radars and/or satellites, offer good spatial coverage at short revisit internals of approximately 1 day (e.g. *Schanze et al.*, 2010). P can be determined from satellites with various techniques, including passive microwave and infrared (IR) measurements, which capture different aspects of the rain systems (*Quartly et al.*, 2002). Combination of different sensors with varying spatio-temporal span and additions of new instruments can lead to significant differences between the various P datasets and climatologies from satellites. An overview of them can be found, for instance, in *Quartly et al.*, 2007 and *Sapiano and Arkin*, 2009.

In this thesis, P and E fields are obtained from the Global Precipitation Climatology Project (GPCP) and the Objectively Analyzed air-sea Fluxes (OAFlux), which

are presented in Sections 3.3.1 and 3.3.2, respectively. The choice of these sources is made based on the expectation from the literature, and given their observational-based nature, that they are the most reliable. It is noted that reanalysis data for P and E from the National Center for Environmental Prediction/National Center for Atmospheric Research (NCEP/NCAR) Global Reanalysis Project 1 (NCEP-1, *Kistler et al.*, 2001) were considered in the initial stage of the PhD and were compared with GPCP P and OAFlux E (plots not shown), with the latter being a combination of NCEP, ECMWF and satellite products. However, reanalysis data lack accuracy (*Taylor*, 2000), given the wide range of error and uncertainty sources. These include, among others, model geometries and physics, parameterizations, data sources for constraint and changing data density, which result in large biases, particularly in the P field, and often in unrealistic trends and incorrect seasonal cycles (e.g. *Quartly et al.*, 2007). Moreover, the NCEP-1 record is not self-consistent and the full reanalysis period could be divided into three major epochs based on the nature of the observations being incorporated (*Kistler et al.*, 2001), further hindering the quantification of NCEP uncertainties. For these reasons, the work in this thesis focused on the observation-based GPCP.

3.3.1 GPCP P fields

Monthly P fields for the period 2010-2012 are taken from the latest satellite-gauge product (PSG) of the Global Precipitation Climatology Project (GPCP), version 2.2 (*Huffman and Bolvin*, 2013), released in August 2012, at 2.5° x 2.5° spatial resolution. GPCP P over the ocean is primarily a satellite product, adjusted to gauge measurements only close to the coasts. In version 2, among the major changes from previous GPCP datasets is the availability of geostationary satellites, providing more frequent coverage at 40° N-S, and the addition of microwave data since 1987 (*Adler et al.*, 2003; *Quartly et al.*, 2007), which results in higher estimates (*Schanze et al.*, 2010). The version 2.2 used here, replacing all previous versions, includes upgrades in many of the dataset components and the Global Precipitation Climatology Centre (GPCC) precipitation-gauge analysis, as well as the inclusion of the Special Sensor Microwave Image/Sounder (SSMI/S) data (*Huffman and Bolvin*, 2013).

To give a view of the GPCP P mean fields over the region of interest, Figure 3.11 shows examples of monthly P for 2010 in a range of 0-4.5 m/yr. GPCP indicates the maximum P patterns along the Tropical Atlantic between ∼0°-10°N, reflecting the position of the ITCZ, which moves northwards from April onwards (see for instance, Figure 3.11, July and October). P along this band has a magnitude of up to 4.5 m/yr during the year, but can reach up to 8 m/yr in a few grid cells in the middle of the Equatorial basin during August (plot not shown). In contrast, over most of the Subtropical Atlantic, P does not generally exceed 1 m/yr. Exceptions occur over the western S. Subtropical basin and along the Brazilian coasts, where

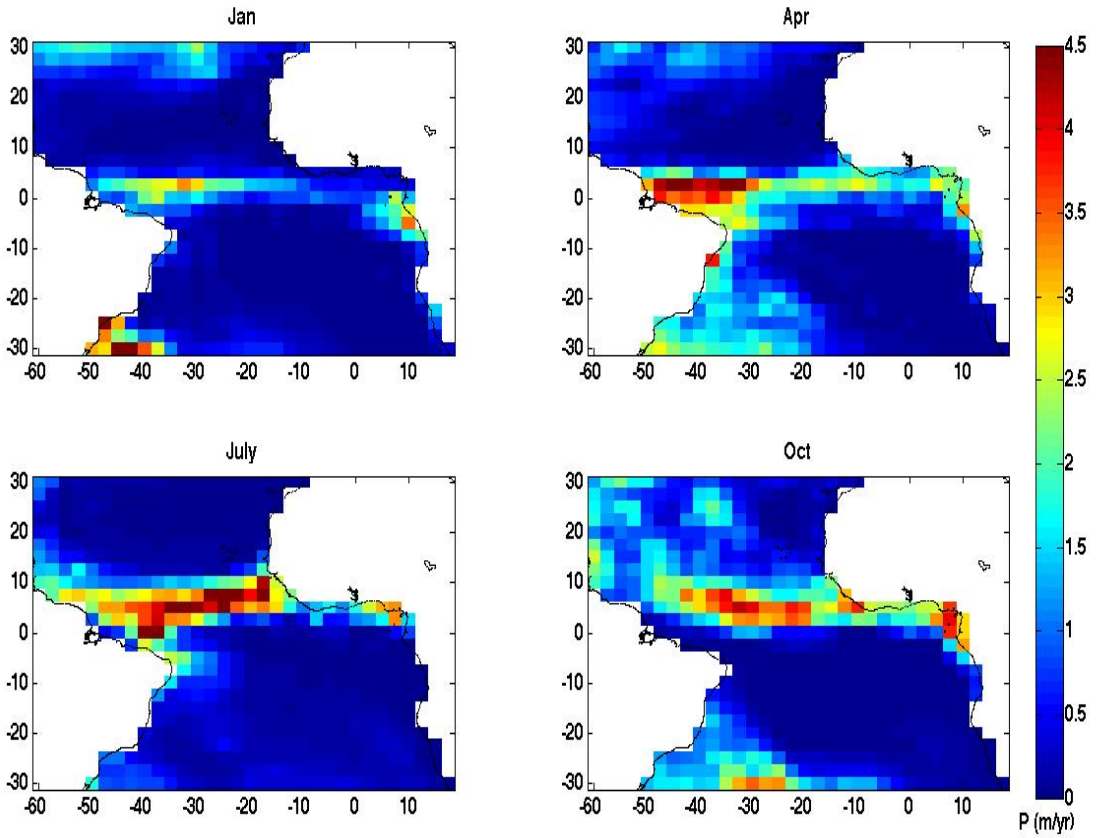

Figure 3.11: GPCP P monthly averages for January, April, July and October 2010 in 2.5° x 2.5° resolution.

P reaches up to ∼3 m/yr in spring and autumn, while exceeding 4 m/yr in winter (Figure 3.11, April, October and January, respectively). Less intense P patterns are also observed in the western and central N. Subtropical latitudes, particularly during autumn and winter (Figure 3.11, October and January), where P can reach up to 2 m/yr.

3.3.2 OAFlux E fields

Monthly E fields for the years 2010-2012 are acquired from the Objectively Analyzed air-sea Fluxes (OAFlux) hybrid dataset (*Yu and Weller*, 2007; *Yu et al.*, 2008) which has a 1.0° x 1.0° spatial resolution. The Woods Hole Oceanographic Institution (WHOI) OAFlux products are constructed from optimal blending of multi-platform satellite observations (e.g. wind speed, SST, near-surface humidity) and reanalysis outputs from NCEP-1, NCEP-2 and ECMWF ERA-40 numerical weather prediction models (e.g. air temperature, humidity, 10-m wind speed). Based on advanced objective analysis of the surface meteorological variables, flux fields including E over the ocean are computed from the Coupled Ocean-Atmosphere Response Experiment (COARE) Bulk flux algorithm version 3.0 (*Yu et al.*, 2008). OAFlux, by blending satellite data and reanalyses, reduces the often large differences between data sources. However, like all reanalysis products, it

may still suffer from changes in the observing network and the assimilation system (*Fairall et al.*, 2010).

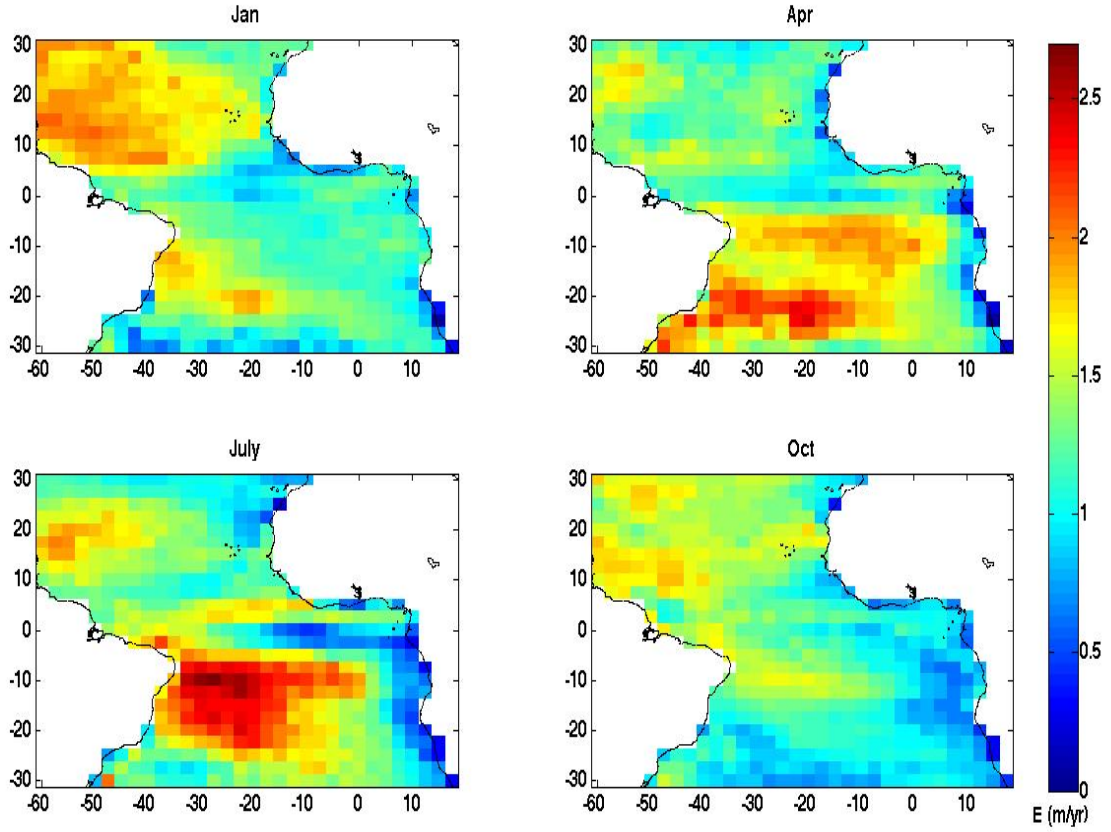

Figure 3.12: OAFlux E monthly averages for January, April, July and October 2010, regridded in 2.5° x 2.5° resolution.

Figure 3.12 displays examples of monthly mean E fields from OAFlux in 2010. As expected, the largest E values occur in the Subtropical latitudes. E is strongest in the northern basin during boreal winter (January) towards its western part, where it exceeds 2 m/yr (Figure 3.12). Over the southern basin, E displays the largest magnitudes in austral winter (July), reaching over ∼2.5 m/yr (Figure 3.12, July). The smallest E values of 0.5 m/yr or less are generally observed towards the southern edges of the region of interest in boreal autumn and winter (Figure 3.12 January and October), and along the African coasts throughout the year. During summer, a band of minimum E also extends from the Gulf of Guinea towards the middle of the Equatorial basin (Figure 3.12, July).

3.3.3 The resulting OAFlux-GPCP E-P field

To obtain an insight into the resulting OAFlux-GPCP monthly E-P mean field over the Tropical/Atlantic basin 30°N-30°S, Figure 3.13 shows the examples of E-P for 2010 obtained from the combination of the data in Figures 3.11 and 3.12. OAFlux-GPCP E-P fields in Figure 3.13 indicate the dominance of E in the Subtropics and the strong P patterns over the Tropics. E-P is strongest in the N. Subtropical Atlantic during boreal winter (January), and over the S. Subtropical basin during

austral winter (July), reaching up to 2.4 m/yr (Figure 3.13, January and July, respectively). As seen previously for the GPCP P fields (Figure 3.11), P dominates along the Tropical band ∼0°-10°N throughout the year, indicating the influence of the ITCZ, with E-P magnitude up to -3.5 m/yr or even greater than ∼-6.5 m/yr in some cases (overall E-P range in 2010 between -6.8 m/yr and 2.4 m/yr). These strong P patterns move northwards in summer onwards, and from west to east as the year proceeds (Figure 3.13). Finally, strong negative E-P values are also seen over the river-influenced regions, as for instance in the Gulf of Guinea where P dominates over E throughout the year (Figure 3.13). In contrast, over the Amazon/Orinoco region, no such persistent P signature is observed.

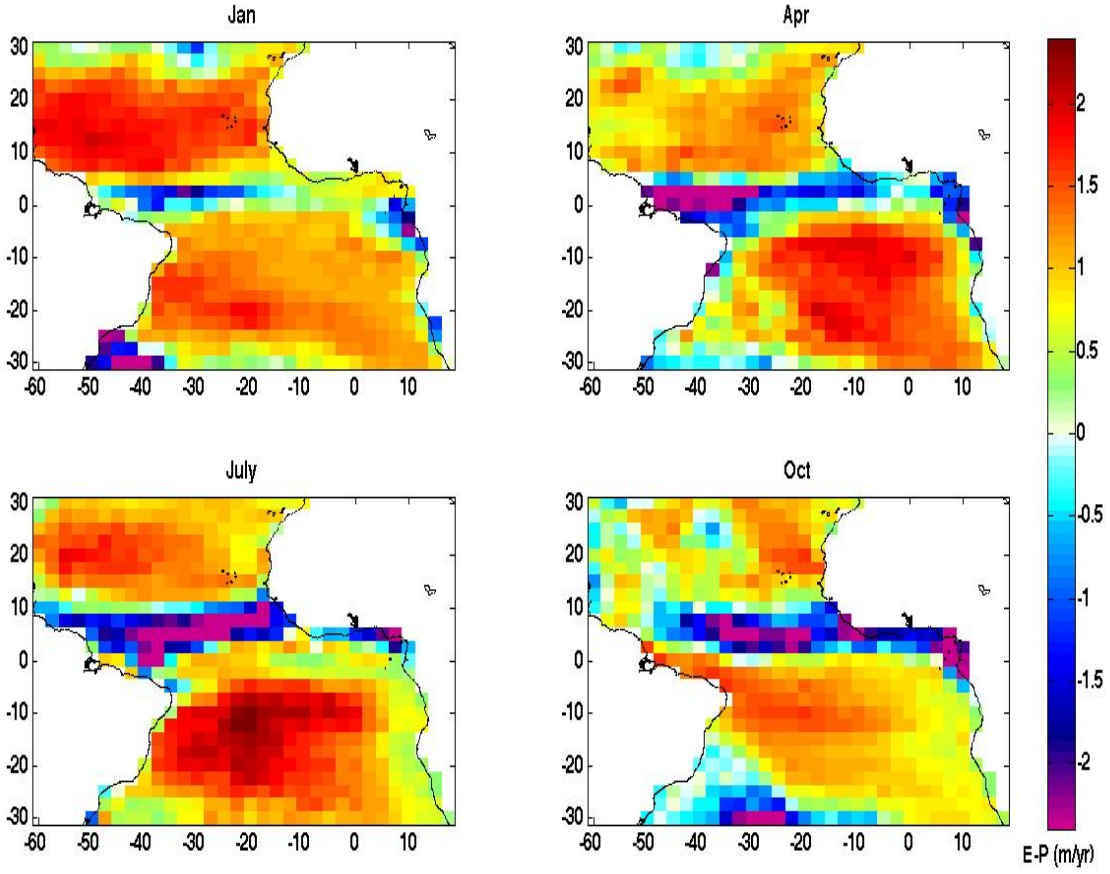

Figure 3.13: OAFlux-GPCP E-P monthly averages for January, April, July and October 2010 in 2.5° x 2.5° resolution.

3.4 River flow data

Monthly river discharge data for the Amazon, Orinoco and Congo rivers for 2010, 2011 and 2012 are obtained from the Environmental Research Observatory-Hydrogeodynamics of the Amazon Basin Observatory (ORE-HYBAM) network (www.ore-hybam.org). The data correspond to the Obidos, Ciudad Bolivar and Congo á Beach Brazzaville stations, respectively. Annual data for the Niger river are not available from this source, and thus are not included in this thesis. The

ORE-HYBAM network, operating since 2003, aims to provide high quality scientific data of biochemical, hydrological and geodynamical properties needed to understand and model the systems behaviour and their long-term dynamics.

In addition, time series of monthly river flow rates at the farthest downstream station for the Amazon (Obidos station), Orinoco (Pte Angostu station), Congo (Kinshasa station) and Niger (Lokoja station) rivers are derived from the Dai and Trenberth Global River Flow Dataset (*Dai and Trenberth*, 2002; *Dai et al.*, 2009) to form climatological means for the common period of January 1941-December 1992 when data are available for all four rivers.

Despite the increasing demand of accurate and continuous global river discharge estimates, data availability, even for major river systems such as those in our region of interest, still remains sparse and discontinuous. One of the major obstacles in estimating continental freshwater discharge is the insufficient gauge records, which results from limited station network coverage and large unmonitored areas, including a great number of smaller rivers that need to be accounted for. In addition, further uncertainties in the discharge estimates are related to the adjustment for river mouth flow rates, the diverse period and length of discharge records, errors in accounting for groundwater runoff, and the various human influences on the natural streamflow, e.g. water extraction. The available flow rates correspond to measurements in the furthest down river station, which is often some distance from the river mouth. Thus, they may potentially differ from the true seasonal river runoff into the ocean, due for instance, to irrigation and other human water uses (*Dai and Trenberth*, 2002; *Dai et al.*, 2009).

3.5 Mixed Layer Depth (MLD)

The mixed layer depth (MLD) is the layer between the ocean surface and a depth within which, salinity, temperature, and density are almost vertically uniform due to strong turbulent mixing processes active in the upper ocean. MLD can be determined with various methods. Some definitions use a threshold criterion in density, e.g. corresponding to 0.03 kg/m^3 (MLD_{DR003} hereafter) or 0.2°C variation in local temperature conditions (MLD_{DT02}) (*de Boyer Montégut et al.*, 2004), or a hybrid density algorithm (MLD_{DA}, *Holte and Talley*, 2009). In the present thesis, Argo MLD_{DT02} and MLD_{DA} (and similarly for the available mixed layer salinity data) from profiles between 2000-2011 were compared with climatological, interpolated Ifremer MLD_{DT02} and MLD_{DR003} fields from data over the period 1961-2008 (See Section 3.5.1 for description of the latter), and did not reveal significant differences between them (plots not shown). Therefore, the interpolated Ifremer MLD climatology is used in this thesis, given also that it covers a greater period of time and is based on a larger number of observations per grid cell, as

compared to that from Argo. Note that mixed layer salinity is not available from this source.

3.5.1 Ifremer MLD monthly climatology

Monthly climatological data of mixed layer depth (MLD) are obtained from Ifremer (www.ifremer.fr/cerweb/deboyer/mld/Surface_Mixed_Layer_Depth.php) at 2° x 2° spatial resolution. MLD is defined according to a fixed threshold criterion in density of 0.03 kg/m^3 difference from the sea surface (MLD_{DR003}), as described in *de Boyer Montégut et al.*, 2004. Estimated directly from individual profiles at observed levels, the MLD is then linearly interpolated between the levels to determine the exact depth at which the difference criterion from a near-surface reference depth, i.e. at 10-m depth in order to exclude some impact of the strong diurnal cycle in the top few meters. Further information on the methodology used for the construction of these data can be also found in the Ifremer website.

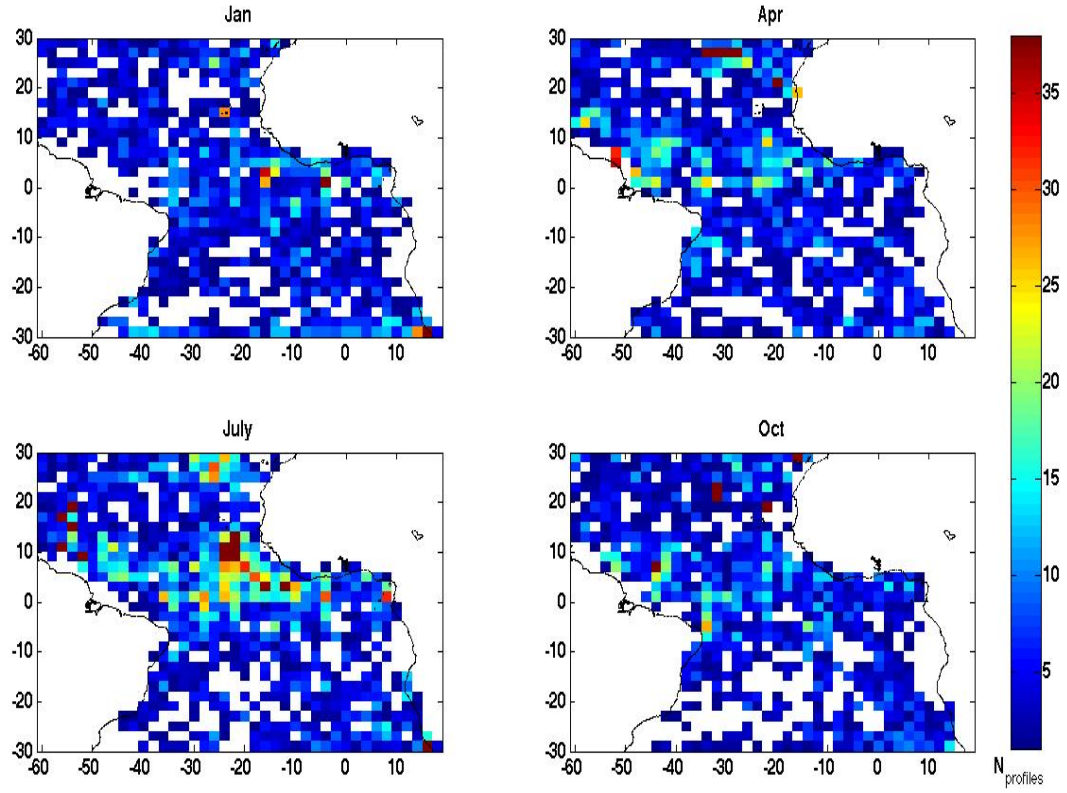

Figure 3.14: The number of profiles per 2° x 2° grid cell over the period 1961-2008 used to construct the interpolated, climatological MLD_{DR003} fields from Ifremer. White gaps indicate the grid cells with no measurements.

The T/S profiles used for the climatological MLD_{DR003} dataset cover the period 1961-2008, corresponding to National Oceanographic Data Center (NODC) WOA09 conductivity - temperature - depth (CTD) data (1961 to 2008), World Ocean Circulation Experiment (WOCE) 3.0 CTD and profiles (all from 1990 to 2002) and Argo profiles (1995 to September 2008), that result in ∼880000 density profiles. Figure 3.14 shows the number of profiles per 2° x 2° grid cell used

to form the Ifremer MLD_{DR003} climatology for four selected months, as typical examples for the rest of the year. In general, the number of profiles over most of the Tropical/Subtropical Atlantic 30°N-30°S is below 10 per 2° x 2° grid cell over 1961-2008, reaching up to 38 profiles in some cases, such as towards the western Tropical and N. Subtropical basin. Along the Tropical Atlantic band, the number of profiles increases in some months, such in April and July (Figure 3.14). On the other hand, over the S. Subtropical basin and towards the African coast there are large areas with no observations at all throughout the climatology.

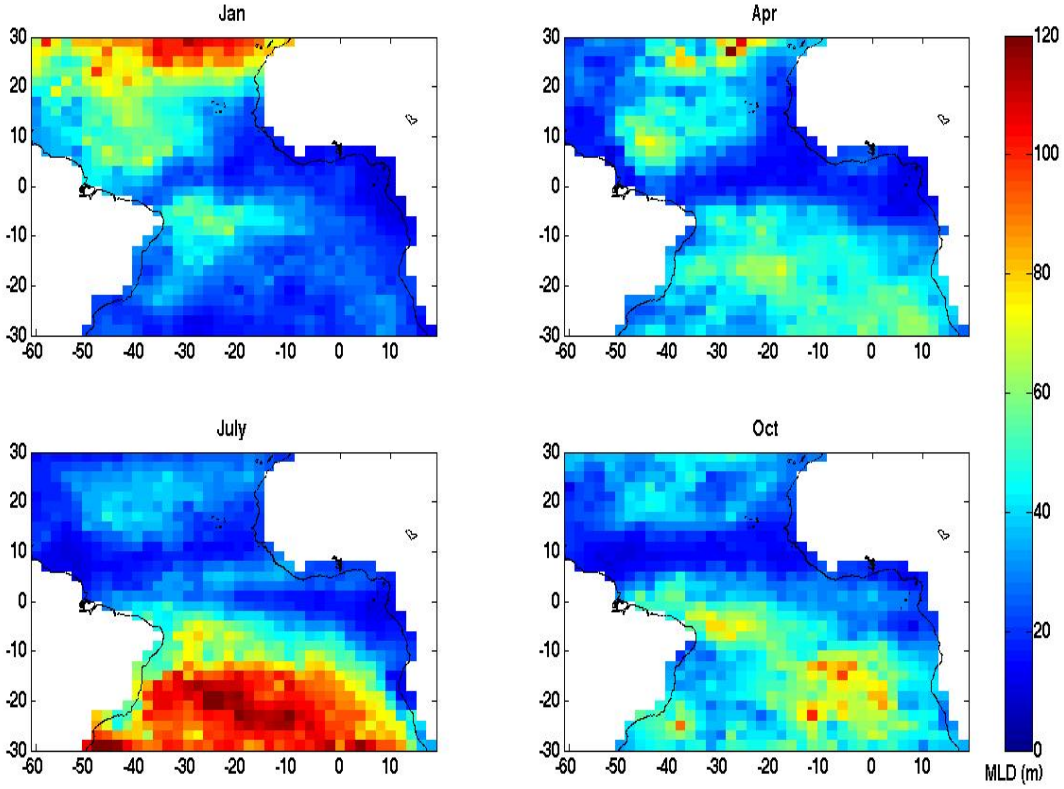

Figure 3.15: The Ifremer climatological MLD based on the fixed density threshold criterion, i.e. MLD_{DR003}, for January, April (top plots), July and October (bottom plots), in 2° x 2° spatial resolution.

Finally, to obtain an insight into the seasonal variability of MLD_{DR003} in the region of interest, Figure 3.15 displays 4 examples of the monthly mean MLD_{DR003} fields for Jan, April July and October, respectively. Plotted here in a range of up to 120 m (99% quantile), it can reach up to 160 m locally in the N. Subtropical Atlantic during January. Overall, the MLD_{DR003} is deepest in the N.E. Subtropical Atlantic in boreal winter and over most of the S. Subtropical basin in austral winter (see for instance, January and July in Figure 3.15). Over the rest of the year, MLD_{DR003} varies by as much as 60-80 m in the Subtropical latitudes, while it remains relatively constant and does not exceed ∼30-40 m in the Tropical Atlantic (±10°) over most of the year (Figure 3.15).

To summarize, the datasets used in this thesis are:

- SMOS SSS from CATDS-CECOS (versions V01 and V02) for 2010-2012

- SSS and UOS (S10) from WOA09 and Argo, which show good consistency with SMOS on monthly scales
- P from GPCP at 2.5° x 2.5° spatial resolution due to the observation-based nature of the data for 2010-2012
- E from OAFlux for 2010-2012
- Annual ORE-HYBAM (2010-2012) and climatological Dai and Trenberth (1941-1992) river discharge data for the Amazon, Orinoco, Congo and Niger rivers.
- Interpolated climatological MLD from Ifremer based on a fixed threshold criterion in density of 0.03 kg/m^3.

Chapter 4

Seasonal variability of SSS in the Tropical Atlantic from SMOS

4.1 Introduction

This Chapter presents the first analysis of SSS variability at seasonal time scales in the Tropical Atlantic using data from SMOS. The salinity balance in this region is expected to be influenced by variations in precipitation (P) and evaporation (E) associated with the north-south movement of the InterTropical Convergence Zone (ITCZ) and outflow from two of the largest global river systems, the Amazon/Orinoco and Niger/Congo. Therefore, SMOS SSS observations are used in combination with P, E and river flow (R) datasets to determine SSS changes throughout the annual cycle over the Tropical Atlantic basin 20°N-20°S and investigate the key processes that control this variability. The content of this Chapter was published as *Tzortzi et al.*, 2013 in the Geophysical Research Letters (GRL). A copy of the original paper is provided in the Appendix B at the end of the thesis.

4.2 Datasets and Methodology

For this study, research SMOS SSS Level 3 monthly mean products (V01) for the first complete year (2010) were employed (See Chapter 3, Section 3.2.1.5). Monthly P fields for the same period have been taken from the Global Precipitation Climatology Project (GPCP) (See Section 3.3.1), while monthly E fields are acquired from the Objectively Analyzed air-sea Fluxes (OAFlux) hybrid dataset (See Section 3.3.2). In order to ensure consistency throughout the analysis and between the different data sources and versions, a uniform domain is determined by initially masking all datasets (SSS, E and P) to display the same grid cells along the coasts.

Climatological monthly means of river flow rates for the Amazon, Orinoco, Congo and Niger Rivers are derived from the Dai and Trenberth Global River Flow Dataset for their common period 1941-1992. Finally, annual river discharge data for 2010 from the ORE-HYBAM network stations for the Amazon, Orinoco and Congo Rivers are used (See Section 3.4). Note that data from this source are not available for the Niger River, thus only the annual Congo discharge is included in the eastern subregion analysis of Section 4.4.

4.3 SSS Variability in the Tropical Atlantic from SMOS

Monthly mean fields of SSS from SMOS in the Tropical Atlantic are shown in Figure 4.1 for January and July 2010. SSS displays its highest values at the northern and southern extremes of this region throughout the year, reaching up to ∼37.4 pss (practical salinity scale). In contrast, in the equatorial band, SSS is reduced, varying around 34.5-35.0 pss and the location of this band is displaced northward in July relative to January. This is consistent with the northward displacement of the ITCZ and hence the zone of maximum P in boreal summer, as shown by the contours in Figure 4.1.

By combining SMOS data with the latest version of the GPCP satellite precipitation dataset and evaporation from OAFlux, an observation based comparison of these terms can be carried out for individual months in 2010. Zonal means for January and July are shown in Figure 4.2, where the average at a given latitude is taken across the width of the basin. There is a clear alignment between the SSS minimum and the maximum (minimum) in P (E-P), indicating that at basin wide scales the position of the salinity minimum is generally tied to the P maximum during most of the year (the variation in E is relatively small across the Tropics). This is also seen in Figure 4.3 which displays the latitude of zonal means of SSS minimum and P (E-P) maximum (minimum) for each month in 2010 (Note that here SSS is re-gridded to the coarser spatial resolution 2.5°x 2.5° of GPCP P in order to enable plotting). The magnitude of zonal P maximum doubles in July (Figure 4.2), in accordance with the maximum P intensity in ITCZ during the boreal summer (e.g. *Kushnir et al.*, 2006) when it reaches its farthest north position. This increase of zonal P maximum results in a small decrease (0.14 pss) of zonal SSS minimum in July relative to January (Figure 4.2).

In addition, the SMOS data reveal the presence of seasonally dependent SSS minima (referred to hereafter as 'poles') on opposite sides of the basin located north/-south of the equator in the western/eastern basin (Figure 4.1). These poles are close to the outflows of the major river systems, which play a significant role in their generation, as has been previously observed from climatological ship datasets (*Dessier and Donguy*, 1994). In the western Tropical Atlantic pole, the fresh signal is stronger in July (SSS as low as 29.7 pss) than January (SSS minimum ∼35.0

pss). In contrast, the eastern Tropical Atlantic pole in the Gulf of Guinea has its lowest salinity in January (SSS ∼28.8 pss) and is more saline in July (SSS minimum 33.5 pss). The two salinity poles are clearly evident in Figure 4.4, which shows the seasonal range of SSS in 2010 (i.e. the difference between the maximum and minimum monthly mean values in each grid cell). The magnitude of the range in each pole is similar, up to 6.5 (6) pss in the eastern (western) Tropical Atlantic. In contrast, the SSS seasonal range over the rest of the region typically lies between 0.1-1.5 pss .

The area-weighted mean SSS is quantified for subregions that encompass the two poles defined according to the criterion that the seasonal range in SSS exceeds 1.5 psu. These subregions are indicated by the areas outlined in black in Figure 4.4. The seasonal cycle of SSS for these two subregions, and the region from 20°N - 20°S as a whole, is shown in Figure 4.5. SSS is typically fresher in the eastern subregion and has a slightly larger seasonal variability (here by ∼0.35 pss) compared to the western subregion. The subregions are characterized by out of phase seasonal

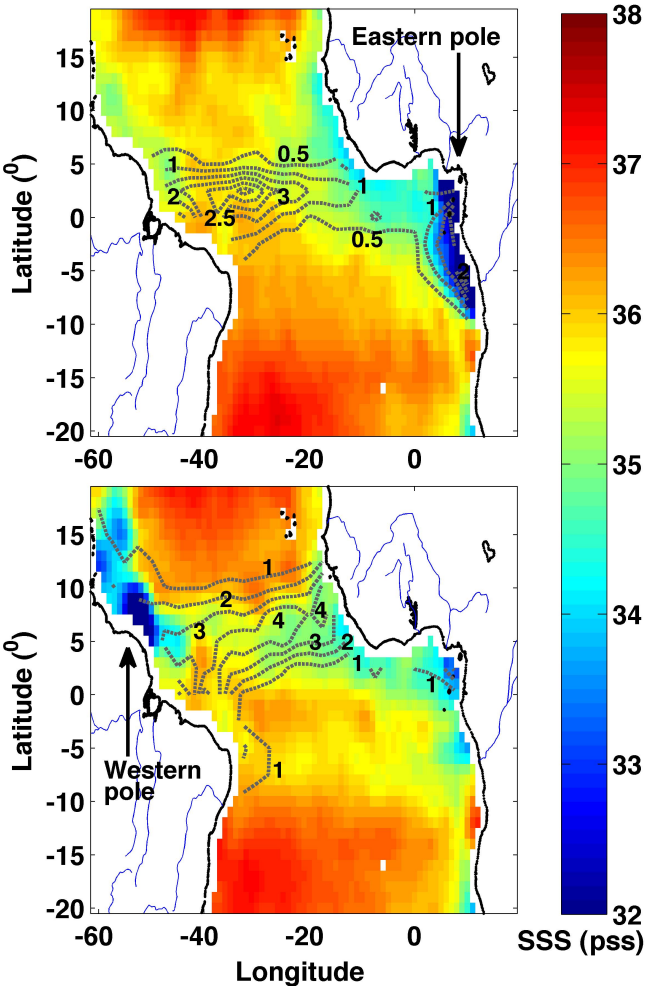

Figure 4.1: SMOS SSS mean (pss) in the Tropical Atlantic for January (top) and July (bottom) 2010, with GPCP P mean contours (m/yr) overlaid. Note, P contours for January are shown every 0.5 m/yr, while those for July are every 1 m/yr (to avoid overcrowding of contour lines).

cycles and tend to compensate as the mean SSS for the whole region shows little seasonal variation. The seasonal range for the eastern subregion is 1.92 pss, for the western subregion 1.57 pss and for the region as a whole 0.08 pss (Figure 4.5). Note

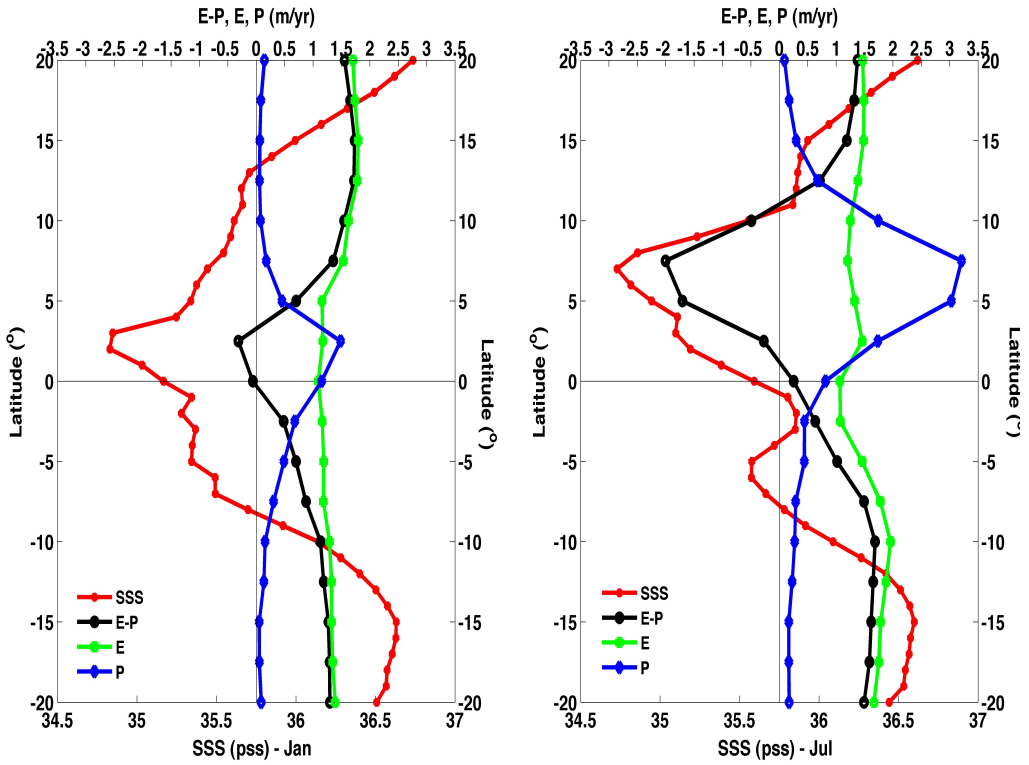

Figure 4.2: Tropical Atlantic zonal mean values for SSS (red), E (green), P (blue) and E-P (black) for Jan 2010 (left panel) and July 2010 (right panel). The zonal mean at a given latitude is taken across the width of the basin.

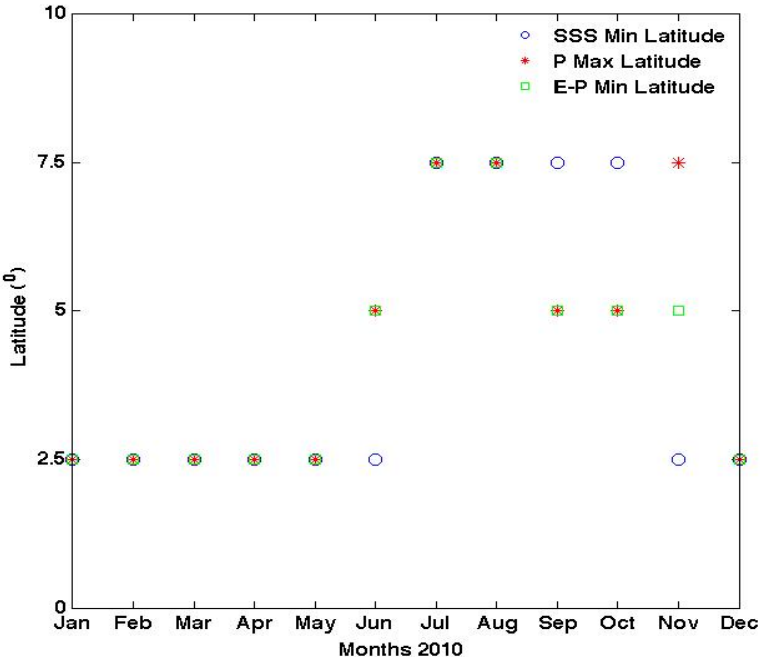

Figure 4.3: Scatterplot of the occurrence of monthly zonal means of the SSS minimum (blue circle), the E-P minimum (green square), and the P maximum (red star) in 2010.

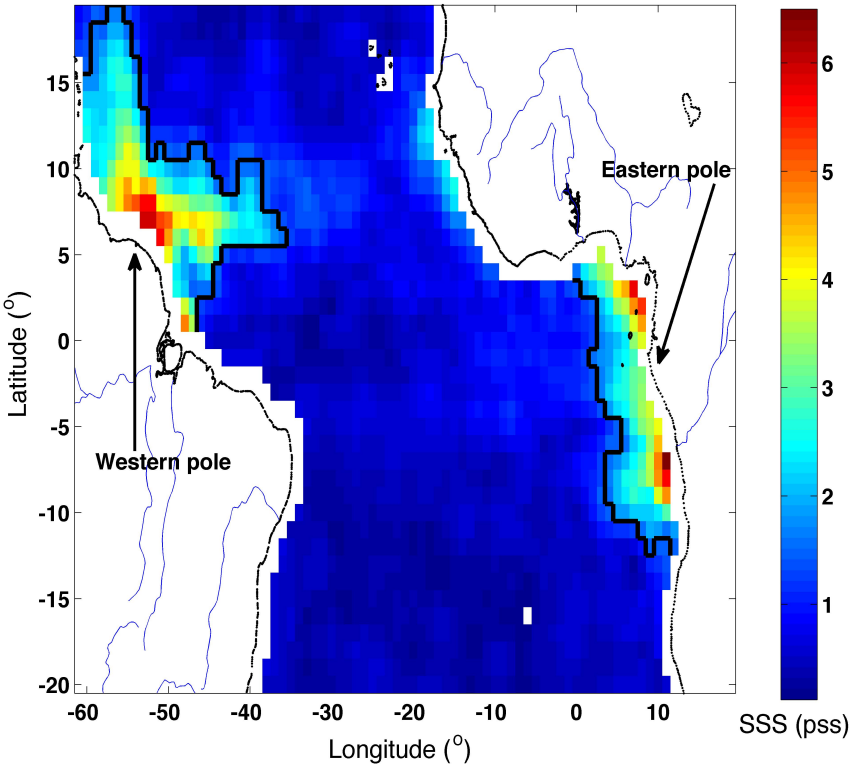

Figure 4.4: SMOS SSS range (maximum minus minimum during the year) in the Tropical Atlantic 20°N-20°S for 2010. The solid black lines indicate the boundaries of the western and eastern subregions defined according to the condition that the seasonal range in SSS is greater than 1.5 pss.

that different choices of threshold have been considered and do not significantly modify the results, as also shown in Figure 4.6, where thresholds of 1.3 pss and 1.7 pss have been applied instead.

4.4 Relationship of SSS Variability to E, P and R

Next, the extent to which the strong seasonal variability in SSS revealed by SMOS in the eastern and western subregions may be linked to variations in surface freshwater forcing due to evaporation, precipitation and runoff is examined. For this analysis the focus is on the phase relationships between the seasonal cycles of the different terms. This is supported by estimates of the relative magnitudes (in km^3/year) of the E, P and R seasonal ranges (obtained by integrating over the relevant subregions in the case of E and P). The seasonal cycles of SSS, E-P, E, P and R in each subregion are shown in Figure 4.7. Note that for a direct comparison between all terms, SSS and E are re-gridded here on the coarser, 2.5° x 2.5° spatial resolution of GPCP P. In addition to climatological R, Figure 4.7 includes annual river discharge for 2010 obtained from the ORE-HYBAM network stations for the Amazon and Orinoco Rivers in the western subregion, and for the Congo in the eastern subregion.

In the western subregion, strong seasonal cycles are evident in SSS, P, E-P and R (Figure 4.7, left panel). SSS varies in (opposite) phase with E-P (P), and lags R by about 1 month. To show the phase relationships more clearly, vertical lines on the figure indicate the months of maximum (February) and minimum (August) SSS. These coincide, respectively, with the minimum and maximum months of the P cycle and lag the minimum (maximum) in R by 2 (1) months. Their close phase relationship is further supported by the high correlation coefficient, r, of SSS with P (E-P), i.e. r equals 0.83 (0.85), and 0.59 with R (all values are significant at 95% significance level using the t statistic (*von Storch and Zwiers*, 2001)). In contrast to the other terms, E is relatively constant throughout the year and is thus unlikely to play a significant role in the strong SSS variability observed by SMOS. Consequently, the E-P seasonal cycle closely follows the variation found for P alone. The amplitudes of the E-P and R seasonal cycles are similar in magnitude implying a roughly equal contribution of variability in the air-sea freshwater flux (dominated by P) and the river outflow, R, to the seasonal variability in SSS.

Caveats that need to be borne in mind here are that the R data are climatological in nature and that mixing and advective processes have been ignored. Nevertheless, the ORE-HYBAM data for R in 2010 show the same maximum and minimum months as the climatological data indicating that the phase relationship conclusions drawn above are not affected by the use of climatological R data (Figure 4.7,

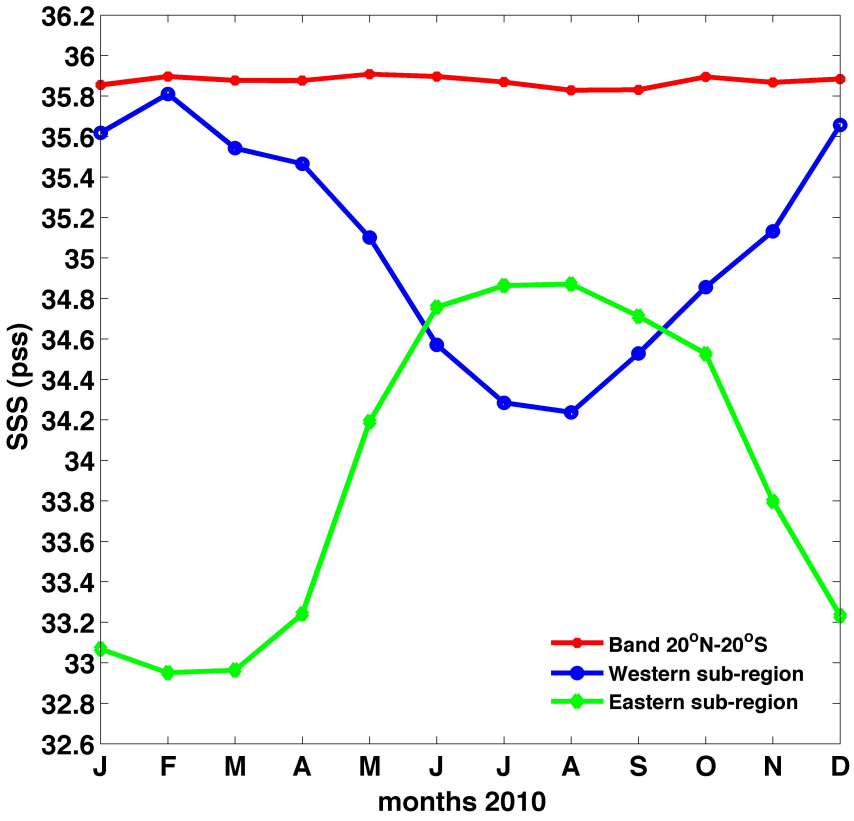

Figure 4.5: Area-weighted mean of SMOS SSS (pss) over the whole region 20°N-20°S (red), the western subregion (blue), and the eastern subregion (green), in 2010.

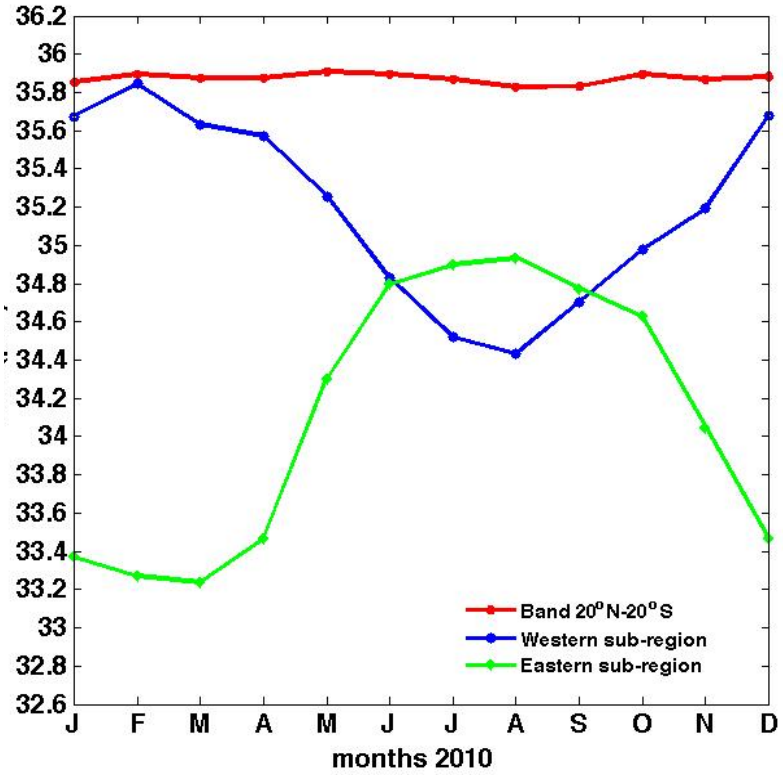

(a) threshold of 1.3 pss

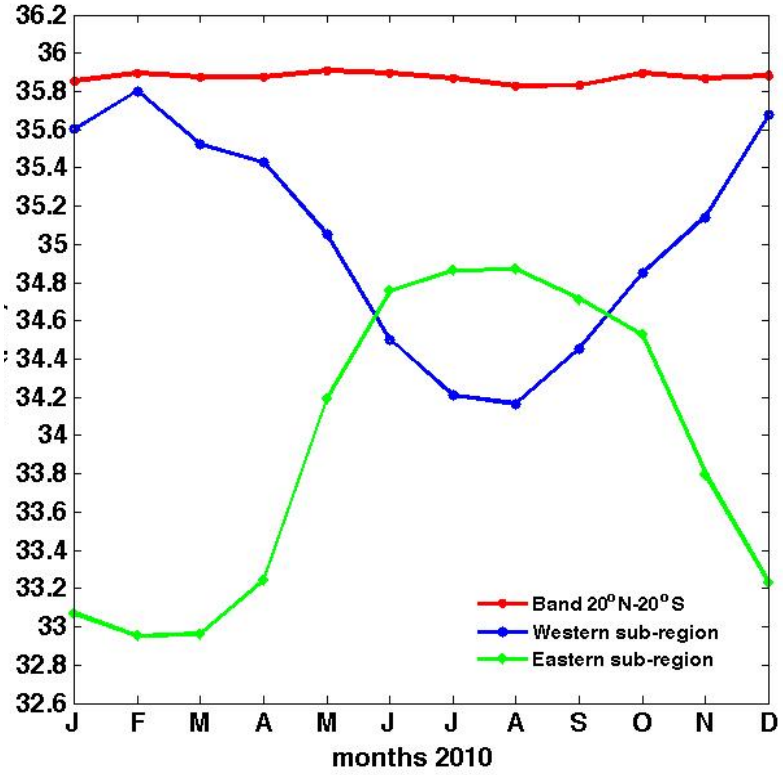

(b) threshold of 1.7 pss

Figure 4.6: Area-weighted mean of SMOS SSS (pss) over the whole region 20°N-20°S (red), the western subregion (blue), and the eastern subregion (green), in 2010, based on a threshold of a) 1.3 pss and b) 1.7 pss for the determination of the two poles.

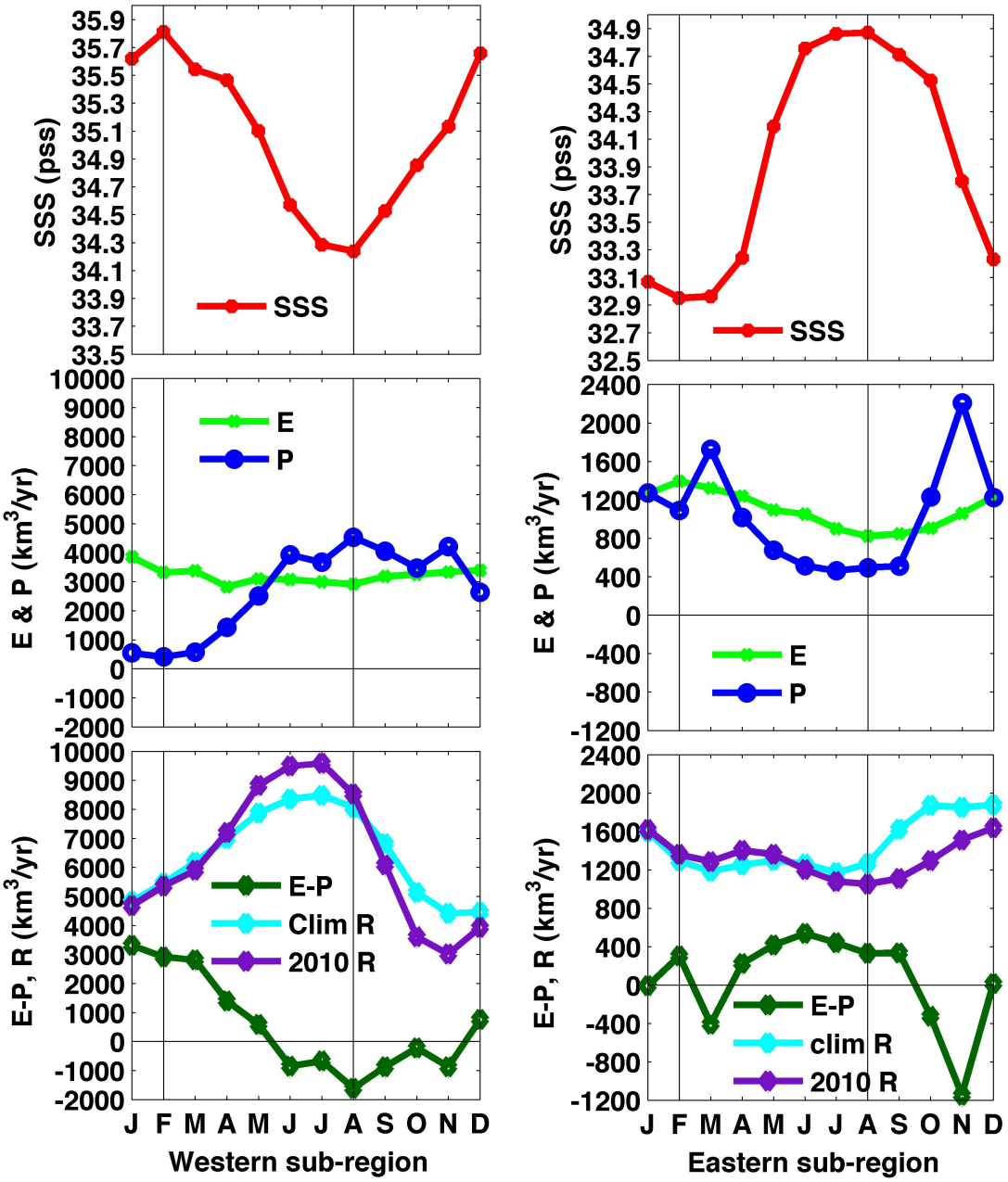

(a) Western subregion (b) Eastern subregion

Figure 4.7: Seasonal cycles for 2010 of area-weighted mean SMOS SSS (red) and integrated OAFlux E (light green), GPCP P (blue) and OAFLUX-GPCP E-P (dark green) for a) the western subregion (left panel) and b) the eastern subregion (right panel). Also shown are the sum of the long-term climatological means of riverine flow rates (R, cyan lines) for the period 1941-1992 for the Amazon and Orinoco in the western subregion (bottom left panel), and for the Congo and Niger in the eastern subregion (bottom right panel). ORE-HYBAM monthly river discharge data for 2010 for the Amazon and Orinoco in the western subregion, and for Congo in the eastern subregion are shown in purple. The units of E, P, E-P and R are in km^3/year and of SSS in pss.

left panel, cyan and purple lines). The amplitude of the R seasonal cycle is larger in 2010 than the climatological range indicating a potentially more significant role for R in this particular year relative to the long-term mean.

Seasonal cycles in all terms are observed in the eastern subregion as E now has a clearer seasonal variation than in the western subregion, although its amplitude remains smaller than P (Figure 4.7, right panel). The clear in-phase relationship between SSS and P observed in the western subregion is no longer evident, while the correlation of SSS with P (E-P) also decreases to 0.62 (0.41) compared to the western pole. The maximum in SSS falls within a prolonged 4-month period, July-September, in which P is at a minimum. However, the SSS minimum in February occurs at a time when P is close to the average for the year as a whole and at this time P exhibits strong inter-month variability. The inter-month variability may reflect limitations in the satellite dataset, as the eastern subregion is more coastally confined than the western subregion and the accuracy of the GPCPv2.2 precipitation retrievals are potentially influenced by the proximity to land.

The relationship between SSS and R in the eastern subregion is also unclear, since both the SSS maximum and minimum months have similar values for the climatological R (although there is some consistency as the SSS maximum falls at the end of a prolonged period, March-July, of low climatological river outflow), (Figure 4.7, right panel, purple line). The difference in strength of the SSS-R phase relationship between the two subregions may arise from the considerably lower climatological outflow rates in the Congo/Niger river system (about 1500 km^3/year) compared to the Amazon/Orinoco (about 7000 km^3/year) that are likely to result in a weaker impact on SSS. Nevertheless, the annual Congo discharge from ORE-HYBAM indicates that the SSS maximum occurs in phase with the R minimum for 2010, while the SSS minimum lies within a period of increased, in general, R runoff (Figure 4.7, cyan line). The correlation coefficient between SSS and R for 2010 is 0.78.

In summary, the western subregion shows a clear relationship between SSS, P and R, with in-phase agreement between SSS and P and a 1-2 month lag of SSS with respect to R. The relationships in the eastern subregion are not well defined and this may reflect a weaker impact of the R seasonal cycle in 2010, although SSS displays a stronger correlation with annual R in this side of the basin, at least for 2010. Thus, other processes including horizontal advection by the surface currents (e.g. *Yu*, 2011), may contribute significantly to determining the SSS variability in this side of the basin. In both cases, a more detailed treatment of the budgets, that takes into account advection and mixing, is required to make further progress.

4.5 Summary and Conclusions

Analyses of ocean surface salinity variability to-date have been severely limited by lack of data as they have primarily relied on irregular, spatially inhomogeneous measurements from ships (e.g. *Dessier and Donguy*, 1994). With the advent of spatially dense salinity measurements from space through the SMOS and

Aquarius/SAC-D satellites, it is now possible to characterize the SSS variability in more detail to investigate the processes that drive it. Here the first satellite-based analysis of SSS variability at seasonal time scales is presented for the Tropical Atlantic using the first full year, 2010, of SMOS measurements. The results presented here show that, in the Tropical Atlantic at least, the SMOS SSS data from CATDS-CECOS are of sufficient quality to provide valuable scientific insight into processes governing the SSS variability.

The Tropical Atlantic has a relatively constant salinity throughout the year during 2010, varying by just 0.08 pss when averaged over the region as a whole. However, strong local variations are evident at two poles on opposite sides of the basin that are close to the outflows from the Amazon/Orinoco and Congo/Niger river systems. The SMOS measurements reveal large amplitude seasonal cycles up to 6.5 pss at these two sites, that are out of phase by 6 months and compensate each other in their influence on the whole region's mean salinity. The relationships between these seasonal cycles and the surface forcing terms of E, P and R, were investigated. For the western pole, SSS varies in-phase with P and lags R by 1-2 months, while E has little seasonal variability. In contrast, it is difficult to establish a clear relationship between SSS and the surface forcing terms for the eastern pole, and this may indicate a significant role for advection and mixing (*Yu*, 2011).

The SMOS SSS uncertainty relative to Argo upper ocean salinity (UOS) for the region of interest is ∼0.31 pss, increasing to ∼0.91 pss and ∼0.85 pss in the western and eastern pole, respectively (See Chapter 3, Section 3.2.3). This may have some impact on the quantitative results on the SSS variability in each region, although calculation of area-weighted means should potentially decrease these uncertainties. Moreover, the large magnitude of annual SSS range and the pronounced seasonal cycles of area-weighted means in the eastern and western river-influenced poles, with amplitudes of 1.92 pss and 1.57 pss, respectively, are considerably larger than the SMOS uncertainty there. This gives confidence that the conclusions drawn here and the observed compensation between the strong seasonal SSS cycles in the two poles remain unaffected. As regards the rest of the datasets used in this work, no uncertainty estimates are currently available (to the author's knowledge) while this thesis is written up, given also the numerous challenges to calculate an error estimate for the OAFlux E which is itself derived from other variables, as well as the even more challenging task to estimate uncertainties for river discharges (See Chapter 3 for further discussion on each dataset and their individual uncertainties). An exception occurs for the GPCP v2.2 P, whose uncertainty is estimated to be about 0.25 m/year in the Tropical/Subtropical Atlantic basin, increasing up to ∼0.45-0.6 m/year in the Tropical ITCZ band, slightly north of the equator (plot not shown), which is in general much smaller than the magnitude of P values over the region of interest (See for instance, Figure 4.1).

The amplitude of the seasonal cycle in SSS for the full region doubles to about 0.16 pss if either pole is excluded from the full regional mean, indicating the sensitivity of the Tropical Atlantic salinity budget to their influence. Thus, variations in the amplitude or phasing of the salinity variability in either pole have the potential to significantly modify the Tropical Atlantic SSS with consequences for the higher latitude Atlantic circulation, through modified surface layer density (*Vellinga and Wu*, 2004). Such variations may be expected as result of natural variability (e.g. through the influence of El Niño) and anthropogenic climate change. Further analysis of the developing data record from SMOS, supplemented by Aquarius/SAC-D and Argo float data (which provide useful complementary information on surface salinity but do not achieve the spatial and temporal sampling possible using satellites), will reveal whether the seasonal compensation between the two poles continues to hold at multi-annual time-scales. A first insight into the interannual variability of SSS seasonal cycle in the examined regions is obtained in Chapter 5, where this study is extended to include the next two years of SMOS data. To conclude, the novel results presented here clearly demonstrate a) the potential of harnessing satellite based SSS and P observations to develop our understanding of controls on SSS and b) their value in monitoring salinity variability over Tropical regions that have the potential to influence the larger scale ocean circulation.

Chapter 5

Interannual variability of SSS in the Tropical Atlantic

5.1 Introduction

In this chapter, the analysis presented in the previous Chapter (Chapter 4 and published in *Tzortzi et al.*, 2013) on the seasonal variability of sea surface salinity (SSS) from SMOS in the Tropical Atlantic 20°N-20°S during 2010, is extended to the following two years of complete SMOS data (2011-2012). A first insight is obtained into the interannual variability of the seasonal cycle of Tropical Atlantic SSS from space. A particular focus is on whether the seasonal compensation of SSS between the western and eastern subregions seen in 2010 continues to hold on multi-annual time scales.

Given the dominance of seasonal variations of SSS over the Tropical Atlantic basin, this analysis also considers deviations during the years 2010-2012 from the 3-year climatological SSS mean cycle from SMOS in each subregion. Comparisons are also made against the longer-term climatological SSS means from the World Ocean Atlas 2009 (WOA09). Finally, the chapter considers the role of freshwater fluxes, i.e. Evaporation (E), Precipitation (P) and river outflow (R) from the Amazon/Orinoco and Congo/Niger river systems on the observed SSS variability in each pole. Therefore, the corresponding seasonal and interannual variations of E-P, P, E and R are examined over the same period and their interannual phase relationships with SSS are explored.

5.2 Datasets

For this analysis, monthly mean SSS products are derived from SMOS for the complete years 2010 (CATDS-CECOS Version V01), 2011 and 2012 (CATDS-CECOS Version V02). Details of the SMOS CATDS-CECOS data and an analysis of

the consistency between the two versions, including a discussion on RFI contamination in the region of interest for 2011 and 2012, are included in Chapter 3, Section 3.2.1.5. In addition, a comparison of the SSS annual range in 2010 from the two versions over their common period and the indicated grid cells in each subregion, is presented in Appendix A. The SMOS data are used to form climatological monthly means by averaging over the 3 years for each month. They are subsequently removed from each month in the 3-years SMOS time-series in each grid cell to obtain the SSS anomaly field without the seasonal cycle. Longer-term climatological means of objectively analyzed in-situ SSS measurements are taken from the World Ocean Atlas 2009 (WOA09), (See Section 3.2.2).

The freshwater fluxes are obtained from monthly P fields from the Global Precipitation Climatology Project (GPCP) and monthly E from the Objectively Analyzed air-sea Fluxes (OAFlux) for the period 2010-2012 (See Sections 3.3.1 and 3.3.2, respectively). In order to ensure consistency throughout the analysis and between the different data sources and versions, a uniform domain is initially determined by masking all datasets (SSS, E and P) to display the same grid cells along the coasts.

Climatological monthly means of river flow rates for the Amazon, Orinoco, Congo and Niger Rivers are derived from the Dai and Trenberth Global River Flow Dataset, while annual discharges for the Amazon, Orinoco and Congo Rivers for 2010, 2011 and 2012 are obtained from ORE-HYBAM (See Section 3.4). This source does not provide annual data for Niger outflow, and thus are not included in the eastern subregion analysis presented in Section 5.6.

5.3 SSS variability in the Tropical Atlantic in 2010-2012

Monthly mean fields of SSS from SMOS in the Tropical Atlantic 20°N-20°S are shown in Figure 5.1 for January and July 2010 (as in Chapter 4, Figure 4.1), 2011 and 2012. In general, throughout the three years, SSS from SMOS displays similar distribution patterns across the Tropical basin, being lowest slightly north of the equator and increasing further away from it. At the northern and southern extremes of the region of interest where SSS is expected to display its highest values, SMOS indicates a very constant magnitude of SSS maximum both annually and interannually. In good agreement with 2010 (Figure 5.1, top plots), the SSS maximum reaches ∼37.4 pss in January and ∼37.3 pss in July of 2011 (Figure 5.1, middle) and 2012 (Figure 5.1, bottom).

In contrast, at the equatorial band where SSS is lowest, winter (Jan) and summer (Jul) SSS minima show a strong interannual variability in terms of magnitude over the three years, particularly from 2010 to 2011-2012. There is a decline of 0.5 pss in January SSS minimum from ∼33.9 pss in 2010 (at 2°N, 7°E) to ∼33.4

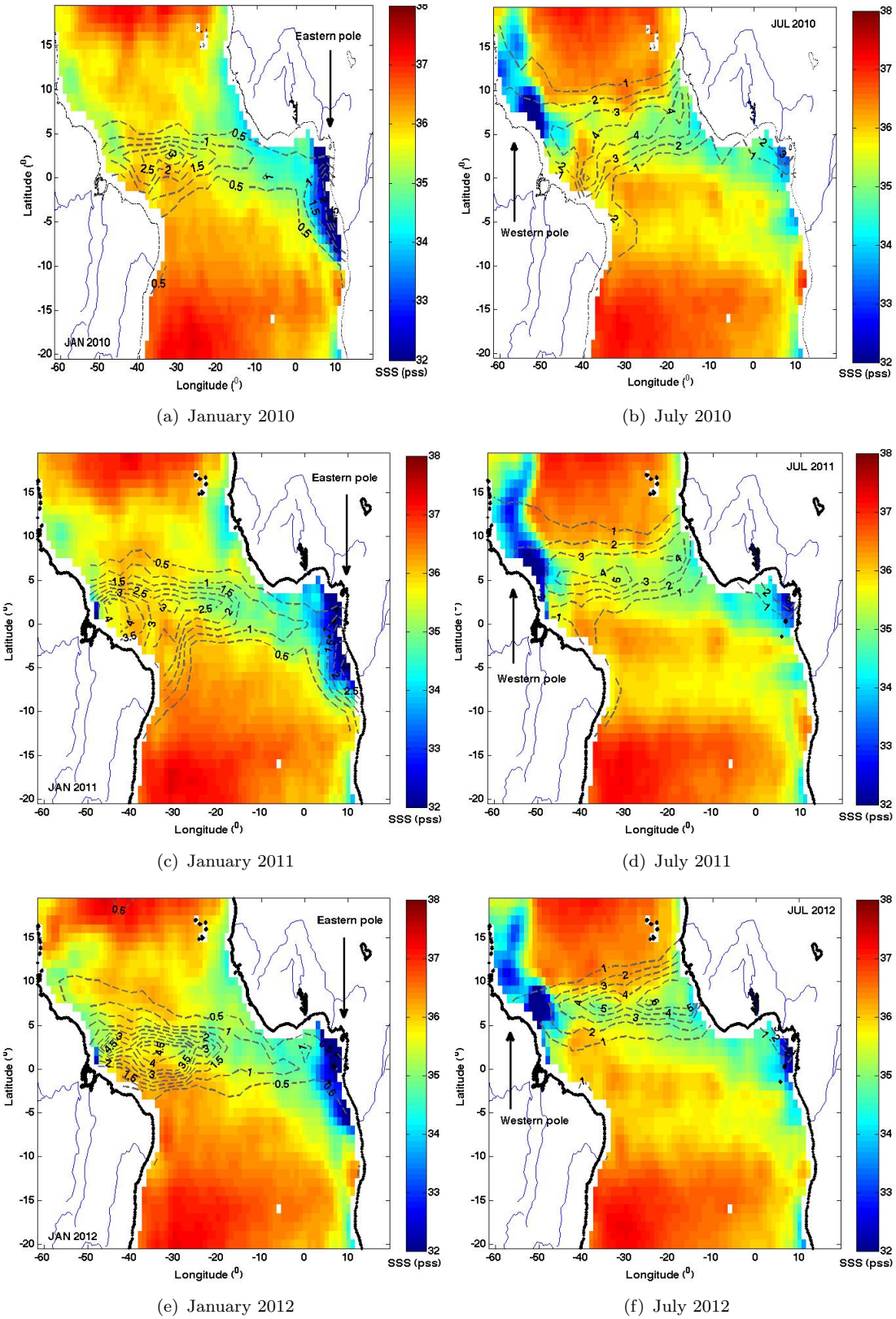

(a) January 2010

(b) July 2010

(c) January 2011

(d) July 2011

(e) January 2012

(f) July 2012

Figure 5.1: SMOS SSS mean (pss) in the Tropical Atlantic for January (left) and July (right) 2010 (as in Chapter 4, Figure 4.1), 2011 and 2012 (from top to bottom), with GPCP P contours (m/year) overlaid. Note that P contours for January are shown every 0.5 m/year, while those for July are every 1 m/year (to avoid overcrowding of contour lines).

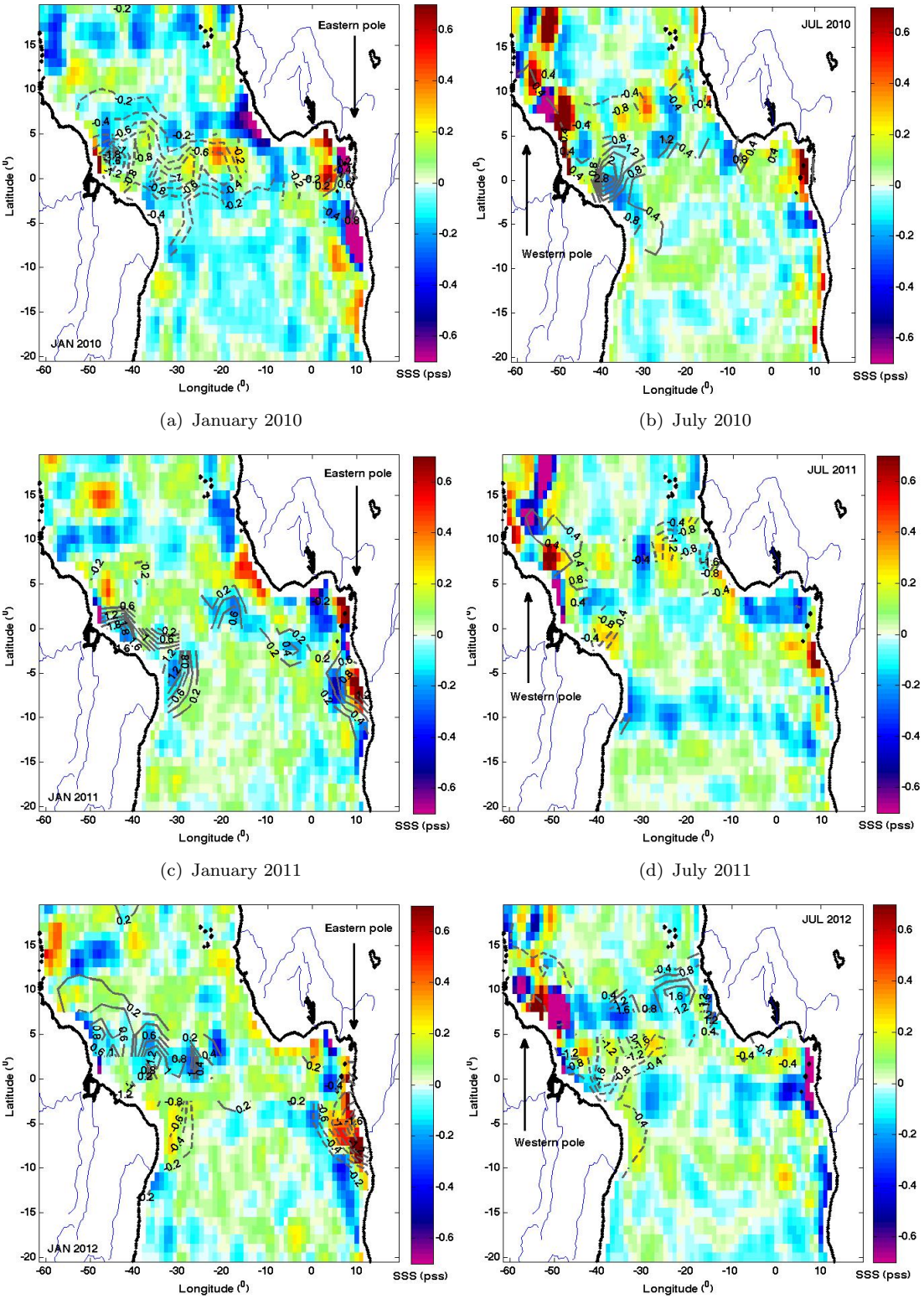

Figure 5.2: SMOS SSS anomaly fields without the 3-year climatological mean (pss) in the Tropical Atlantic for January (left) and July (right) 2010, 2011 and 2012 (from top to bottom), with GPCP P anomaly contours (m/year) overlaid. Solid contour lines indicate positive P anomalies, while dashed lines negative P anomalies. Note that P contours for January are shown every 0.2 m/year, while those for July are every 0.4 m/year (to avoid overcrowding of contour lines).

pss in both 2011 (at 3°N, 4°E) and 2012 (at 2°N, 4°E), (Figure 5.1, left plots). The summer SSS minimum increases by up to 0.6 pss, from ∼33 pss in July 2010 (at 9°N, 51°W) to ∼33.6 pss in July 2011 (at 8°N, 49°W) and ∼33.3 pss in 2012 (at 7°N, 47°W), (Figure 5.1, right plots). Thus, over an annual cycle, the large variation of 0.9 pss of freshest SSS along the equatorial band observed in 2010 (Chapter 4), is not present the next two years. The equatorial SSS minima vary by only 0.1-0.2 pss from winter to summer in 2011 and 2012.

In addition, large deviations of SSS are observed between the western and eastern basin from winter to summer, as seen in Figure 5.2 which displays the corresponding monthly mean anomaly fields of SSS without the 3-year climatological mean from SMOS for the period 2010-2012. In winter, strong SSS deviations of up to 0.6-0.7 pss occur particularly along the African coasts and the Gulf of Guinea, with negative SSS anomalies in 2010 and positive in 2011-2012 (Figure 5.2, left plots). In summer, strong (positive and negative) SSS anomalies are mainly seen along the north-western basin and to a lesser extent in the Gulf of Guinea in all three years (Figure 5.2, right plots).

The equatorial fresh band of SSS is displaced northwards in summer, in accordance with the northward location of the ITCZ and thus of maximum P, as shown by the P contour lines in Figure 5.1. This is also seen in Figure 5.3, which displays the zonal means of SSS, P, E and E-P across the width of the basin for January and July (left and right) in 2010, 2011 and 2012, respectively (top to bottom). The position of the SSS minimum is closely aligned with the P maximum (and the E-P minimum) in all three years. This is also supported by lagged correlations in space between the equatorial zonal monthly means of SSS and P in all three years, which indicate the strongest correlation (correlation coefficient, r, up to 0.8-0.9) between them in lag 0 both in winter (Jan) and summer (Jul), (plots not shown).

Similarly to SSS, P over the Tropical Atlantic basin is seen to have large variability on annual and interannual time-scales in terms of magnitude and location of its highest rates (Figures 5.1 and 5.3). Over an annual cycle, P increases considerably in summer (Jul) in the middle of the equatorial band (Figure 5.1, right plots), with the fresh SSS band spreading across the whole basin width from summer until October-November in all three years (not shown here). As observed in 2010 (Chapter 4), the northward ITCZ position in boreal summer is accompanied by the maximum P intensity (e.g. *Kushnir et al.*, 2006; *Donohoe et al.*, 2014), due to intensification of the Hadley cell and deep convection north of the equator (*Donohoe et al.*, 2014). Thus, the zonal P maxima double in magnitude in summer relative to winter in all three years (Figure 5.3). This summer increase of P in the middle of the basin and north-eastwards exceeds 5.5 m/yr in 2012, compared to ∼4 m/yr the previous two years (Figure 5.1, b, d and f). In accordance, during this season, P displays strong positive anomalies of up to 1.6 m/yr relative to the 3-year climatological mean in the middle and eastern basin north of the equator

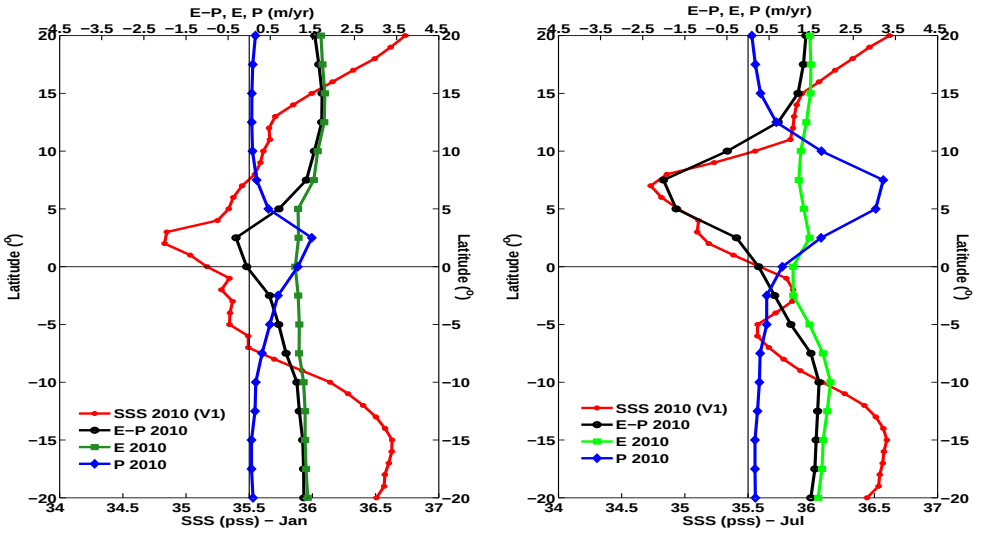

(a) January and July 2010

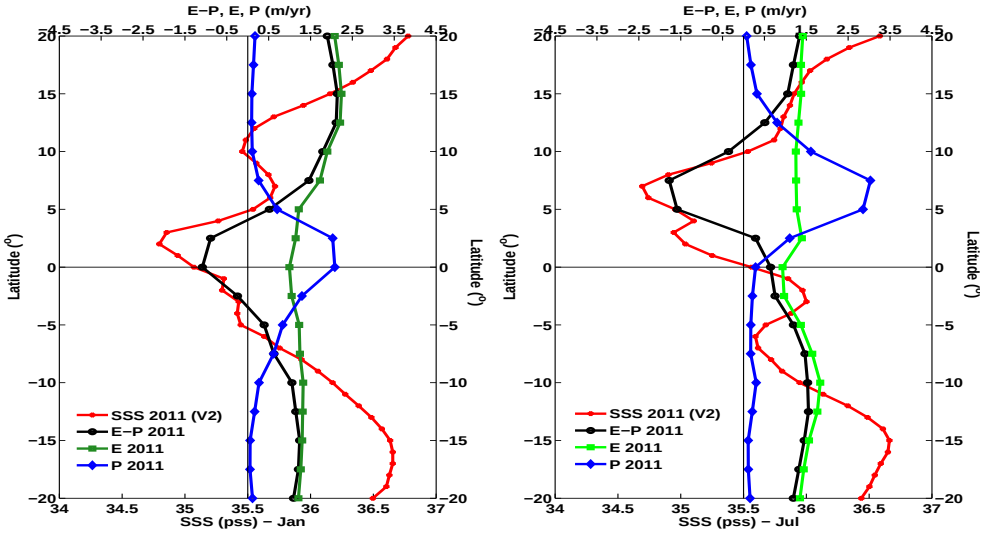

(b) January and July 2011

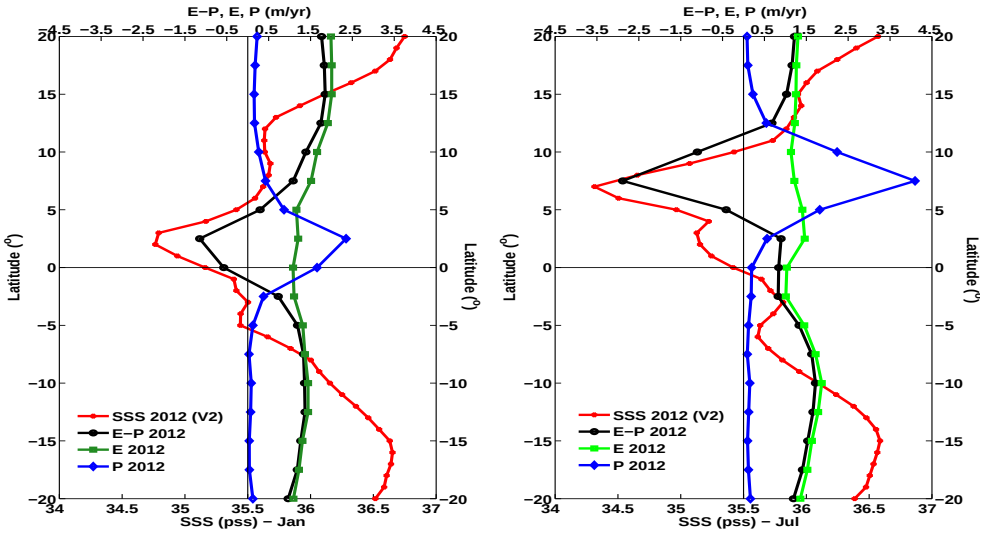

(c) January and July 2012

Figure 5.3: Tropical Atlantic zonal means for SSS (red), E (green), P (blue), and E-P (black) for January (left panels) and July (right panels) in a) 2010 (as in Chapter 4, Figure 4.2), b) 2011 and c) 2012. The zonal mean at a given latitude is taken across the width of the basin.

in 2012, as indicated by the anomaly P contours in Figure 5.2 (right plots). At basin wide scales, the ∼1 m/yr increase of the P maximum in summer (from ∼3 m/yr to ∼4 m/yr) between 2010-2011 and 2012 coincides with a decrease in the SSS zonal minimum of 0.4 pss during the same period (Figure 5.3, right panels).

In winter (Jan), strong P patterns dominate towards the western basin, where a significant interannual variability is also observed. The January P rates increase from up to ∼2 m/yr in 2010 to ∼4.5 m/yr in 2011 and ∼4 m/yr in 2012 (Figure 5.1, left plots). This large increase of P in winter at this side of the basin corresponds to strong positive P anomalies, that reach up to 1.6 m/yr in 2011 and 1.2 m/yr in 2012 relative to the 3-year climatological mean close to the Amazon/Orinoco region (Figure 5.2, c and e). In contrast, the winter P rates over the eastern basin remain relatively constant, particularly in 2010-2011 (Figure 5.1, left plots), while strong negative P anomalies of up to 1.6 m/yr are observed in 2012 (Figure 5.2, e). The zonal P maximum, located slightly above the equator during winter, is enhanced from ∼1.5 m/yr in 2010 to 2.4 m/yr in 2011-2012, while the SSS minimum appears relatively constant (Figure 5.3, left panels). Finally, contrary to P, E shows very little variability across the Tropics on annual and interannual time scales, with the exception of a small variation between 7°-20°N in winter (Figure 5.3, green lines).

5.4 SSS variability in the Western and Eastern Tropical Atlantic subregions in 2010-2012

The seasonally dependent SSS minima close to the outflows of the major river systems, revealed by SMOS in 2010 as "poles" on opposite sides of the basin (Chapter 4), continue to be present the following years 2011 and 2012 (Figure 5.1). These two subregions of strong SSS variability, located north/south of the equator, are also evident when looking at the SSS annual range (i.e. the difference between the maximum and minimum monthly mean values during the year in each grid cell) in 2011 and 2012 (Figure 5.4, top and bottom respectively, displayed on a same scale of up to 6.5 pss as for 2010 in Chapter 4, Figure 4.4). In 2011, the SMOS SSS annual range, varying in general between ∼0.3-4.6 pss (99% quantiles), reaches up to 7.6 pss in the Amazon plume region (Figure 5.4, top). In 2012, the range reaches 7.1 pss, with values generally between ∼0.3-5.0 pss (99% quantile), (Figure 5.4, bottom).

Figure 5.4 (bottom plot) shows solid lines indicating the boundaries of the western and eastern subregions for each year, defined according to the criterion that the seasonal range in SSS exceeds 1.5 pss in that year. The spatial extent of these poles of high SSS variability displays some year-to-year differences, potentially as a result of the combined effect of differences in P, river runoff (R) and/or advection processes by the ocean currents. For instance, in 2012, a small area characterized by large SSS annual range is observed in the middle of the basin (Figure 5.4, orange

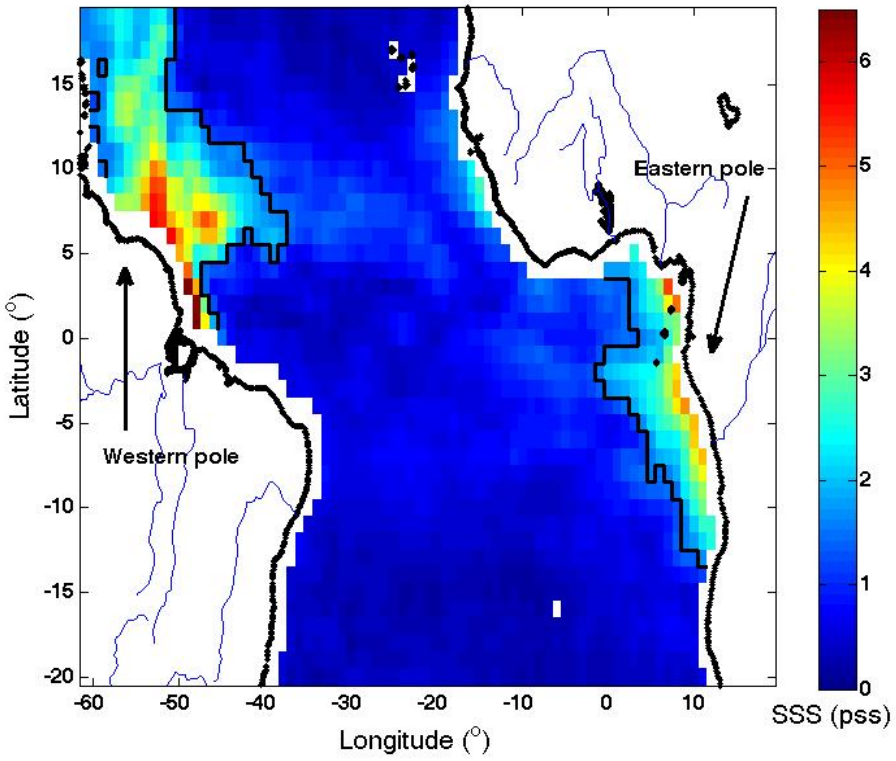

(a) SSS annual range 2011

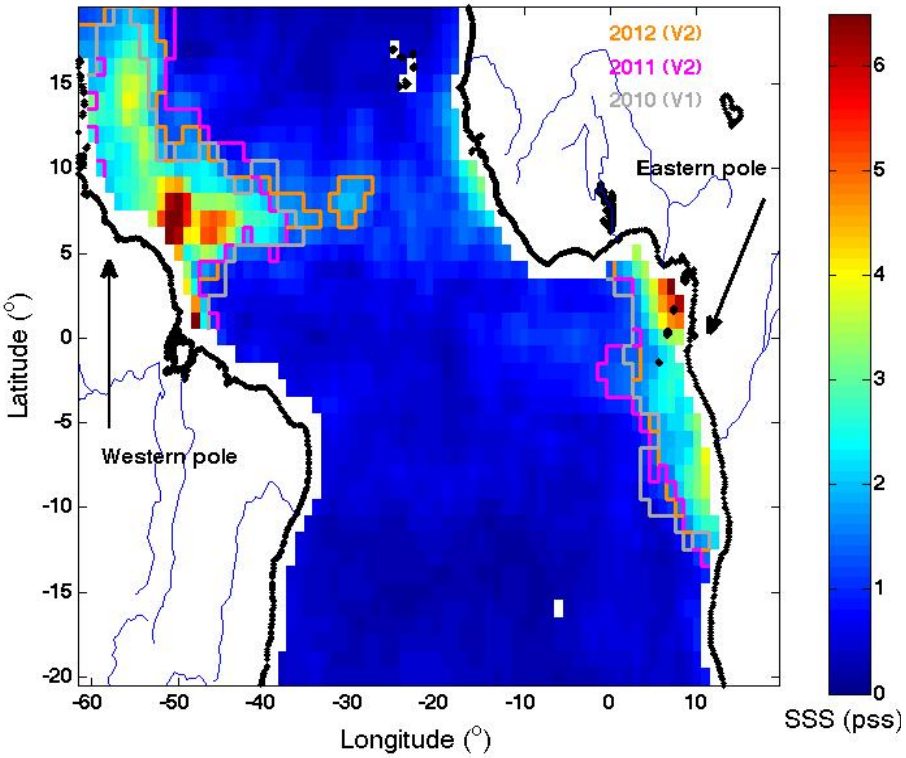

(b) SSS annual range 2012

Figure 5.4: SMOS SSS annual range (maximum minus minimum during the year) in a) 2011 and b) 2012. The solid coloured lines indicate the boundaries of the western and eastern subregions defined according to the condition that the seasonal range in SSS is greater than 1.5 pss. Panel b displays the boundary lines for all three years: i) 2010 (grey), ii) 2011 (magenta) and iii) 2012 (orange).

line), that could be due to the local enhancement of P in the middle of the basin during that year, particularly in summer (See Figures 5.1 and 5.3). On the other hand, this pool of strong annual variability of SSS, apparently disconnected from the western pole, could also originate from an increase in the Amazon/Orinoco River discharge in 2012, and enhanced north-eastwards advection of the freshwater plume or eddies towards the middle of the basin. The controlling processes of P and R at the western and eastern subregions are examined in more detail in Section 5.6.

Nevertheless, it can be suggested that, overall, the same grid cells are influenced by the river plumes throughout the 3 years. Thus, for the rest of the analysis, the pole subregions are defined as the common grid cells that exhibit an annual SSS range above 1.5 pss in all 3 years of SMOS data. The resulting mask is shown in Figure 5.5. Note that different choices for determining the poles have been considered and do not modify significantly the results and the conclusions drawn. The different boundaries of the two subregions lead to small numerical differences for 2010 compared to those shown in Chapter 4 and *Tzortzi et al.*, 2013. However, the use of a common mask ensures a better consistency and a more direct comparison of the seasonal variability of SSS in each pole over all 3 years.

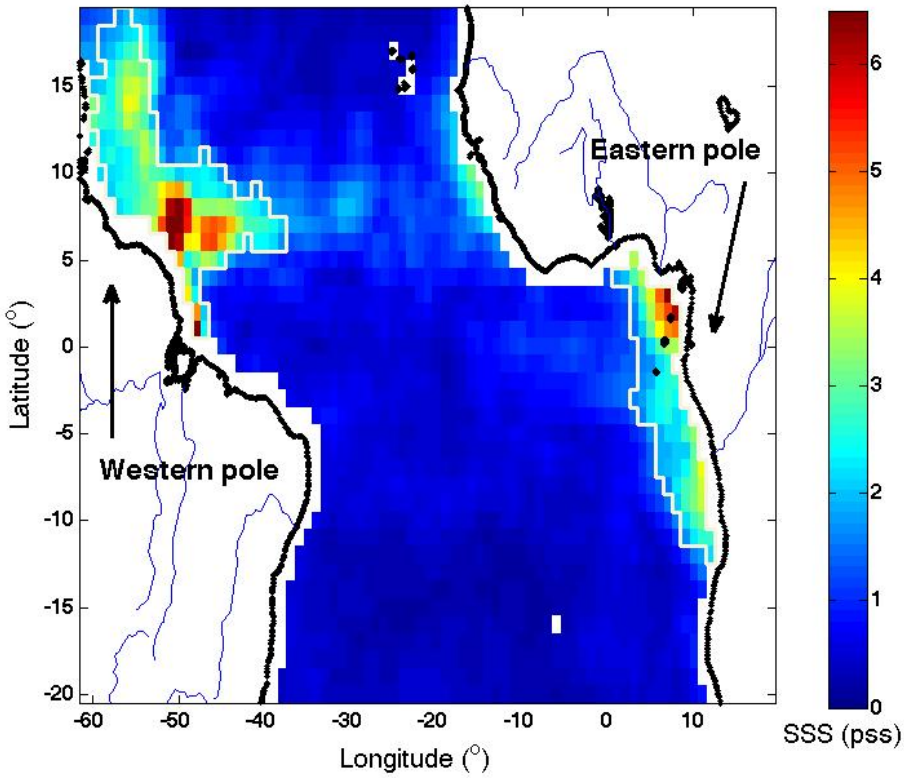

Figure 5.5: SMOS SSS annual range in 2012 showing the common boundaries of the western and eastern subregions defined according to the condition that SSS seasonal range is greater than 1.5 pss in any of the years 2010-2012.

5.4.1 SSS minima and maxima

Focusing now on the two poles (Figure 5.5), the variability in the SSS extrema is considered, particularly the SSS minima, over the 3 years. In the eastern subregion (Table 5.1), the minimum SSS values vary significantly on an interannual basis, both in winter (Jan) and in summer (Jul). In January, the SSS minimum increases from 27.6 pss in 2010 to 29.7 pss in 2011 and 28.9 pss in 2012 (Figure 5.1, left plots). In July, the lowest SSS is more saline, but decreases steadily from 33.2 pss in 2010 to 32.3 pss in 2011 and 31.0 pss in 2012 (Table 5.1 and Figure 5.1, right plots). On the other hand, the SSS minimum in the western pole shows its freshest signal in summer, decreasing from 29.6-29.8 pss in July 2010-2011 to 28.7 pss in July 2012 (Table 5.2). A very larger interannual variability is observed in the January SSS minimum there, which drops significantly from ∼35.0 in 2010 to 31.3 pss in 2011 and increases again to 32.5 pss in 2012. In contrast, the SSS maxima in both subregions show almost no interannual variability throughout the three years, being equal to 36.8-37.0 pss and 36.6-37.0 pss in the western and eastern pole, respectively (Figure 5.1 and Tables 5.2 and 5.1). An exception occurs in summer (Jul) maximum over the eastern pole which decreases by 1 pss from 2010 to 2012 (Table 5.1).

Table 5.1: January, July and annual minima and maxima, and the annual range of SSS (pss) in the eastern subregion.

Eastern Subregion							
	January		July		Overall		Annual
	Min	Max	Min	Max	Min	Max	Range
2010	27.6	36.3	33.2	37.0	27.6	37.0	6.5
2011	29.7	35.9	32.3	36.5	27.1	36.6	5.2
2012	28.9	36.4	31.0	36.0	25.0	36.6	7.0

Table 5.2: January, July and annual minima and maxima, and the annual range of SSS (pss) in the western subregion.

Western Subregion							
	January		July		Overall		Annual
	Min	Max	Min	Max	Min	Max	Range
2010	35.0	36.4	29.6	36.4	29.6	37.0	6.0
2011	31.3	36.4	29.8	36.3	28.3	36.9	7.6
2012	32.5	36.7	28.7	36.5	28.6	36.8	7.1

5.4.2 SSS annual range

Over an annual cycle, the SSS range in the western pole increases noticeably from ∼6 pss in 2010 (Chapter 4, Figure 4.4) to 7.6 pss in 2011 and 7.1 pss in

2012 (Figure 5.4 and Table 5.2). Interestingly, in contrast to this strong increase (∼1-1.6 pss) over the western subregion, the annual SSS range in the eastern pole shows more interannual variability, decreasing significantly from 6.5 pss in 2010 (Chapter 4, Figure 4.4) to 5.2 pss in 2011, and increasing again sharply to about 7.1 pss in 2012 (Figure 5.4 and Table 5.1). Thus, the balance of SSS annual range between the two subregions of 6 pss (W)/ 6.5 pss (E) in 2010, and 7.1 pss in both poles during 2012, is "stretched" in 2011 with values of 7.6 pss (W) / 5.2 pss (E), respectively. Nevertheless, given the sensitivity of the annual range to SSS extremes in each cell, it is difficult to draw conclusions and a more thorough examination of this observed balance/imbalance between the two poles is conducted in the following Section (Section 5.5), by examining area-weighted SSS means.

5.5 Does the East-West SSS seasonal compensation hold on multi-annual time-scales?

Next, the study focuses on the interannual variability of the SSS seasonal cycle in each subregion, with a particular interest as to whether the observed seasonal compensation of SSS between the two poles seen in 2010 (Chapter 4) continues to hold in 2011 and 2012. Figure 5.6 shows the area-weighted mean of SSS in 2010, 2011 and 2012 for the Tropical Atlantic basin 20°N-20°S as a whole and the two subregions that encompass the western and eastern pole, respectively (Note that here SSS is re-gridded on 2.5° x 2.5° spatial resolution as GPCP, to enable consistency and direct comparison with the plots in Section 5.6 including the freshwater forcing terms). It is immediately evident that the SSS exhibits the same seasonal behaviour in each region throughout the 3 years. The pronounced, out-of-phase seasonal cycles of SSS in the two poles and the small seasonal variation over the whole region 20°N-20°S observed in 2010 are clearly visible in 2011 and 2012 as well.

Given that results for the (complete) year 2010 are obtained from SMOS CATDS-CECOS products V01, while results for 2011 and 2012 are from V02, Figure 5.6 also includes the corresponding V02 2010 results for the available period May-December. Despite some small differences in magnitude during some months, the V01 and V02 datasets for 2010 display the same seasonal behaviour of SSS in the three regions over their common period. This gives confidence that combining the two versions does not affect the consistency of the results.

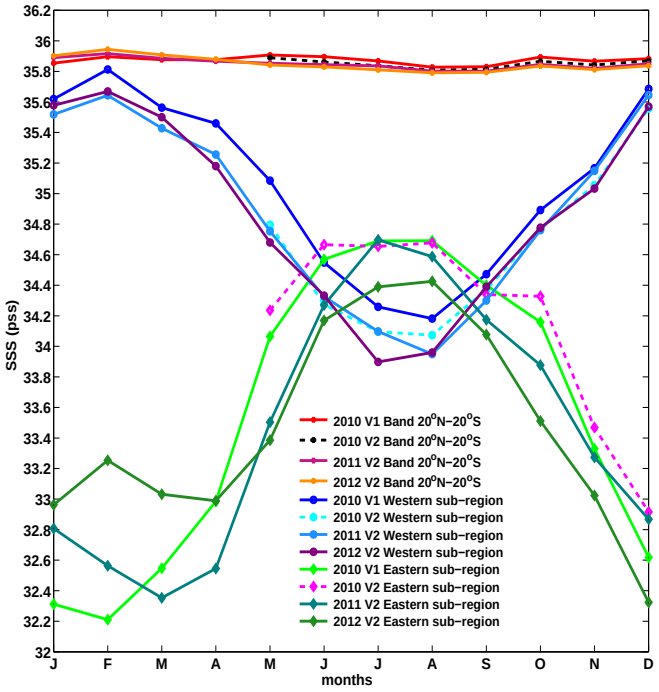

Figure 5.6: Area-weighted mean of SMOS SSS (pss) over the whole region 20°N-20°S, the western subregion, and the eastern subregion in 2010 (V01), 2011 (V02) and 2012 (V02). In addition, dashed lines for 2010 V2 (May-December) are also displayed in each case for comparison.

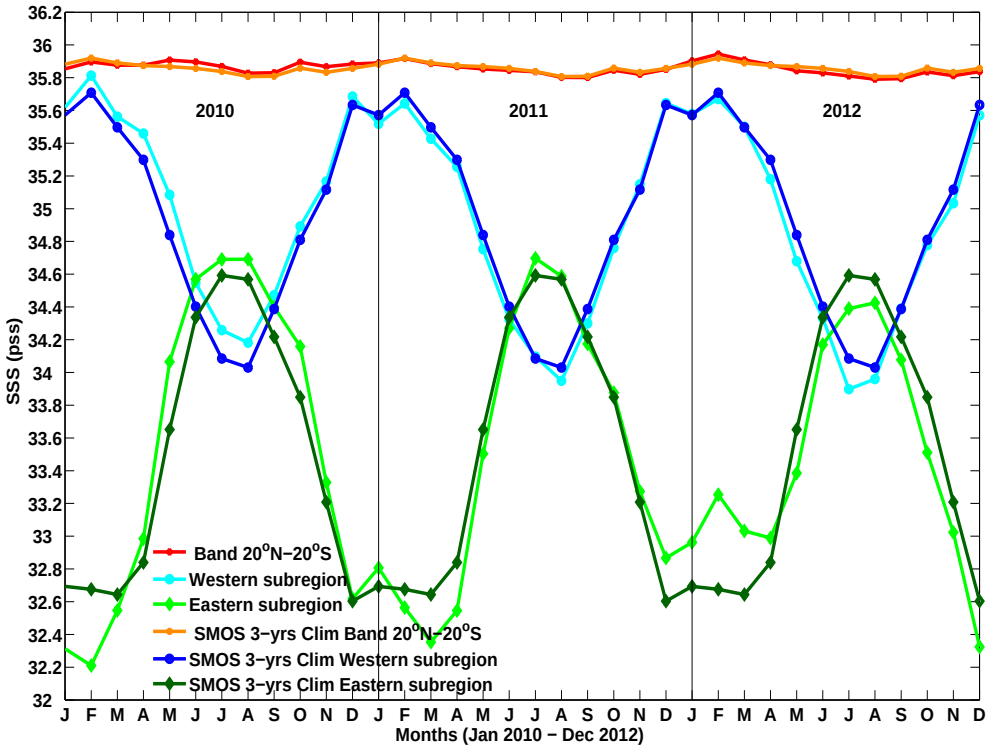

Figure 5.7: Interannual variability of the area-weighted mean of SMOS SSS (pss) over the whole region 20°N-20°S (red), the western (light blue) and the eastern (light green) subregions for the period January 2010 - December 2012. Also shown is the 12-month climatological mean time-series of the 3-year SMOS data for each region (orange, dark blue and dark green lines, respectively).

5.5.1 Amplitude of seasonal cycle

Figure 5.7 shows the time-evolution of the area-weighted SSS mean for the period January 2010-December 2012, providing a clearer insight into the interannual variability of SSS in each region. As noted above, the pole regions are defined as the common grid cells that exhibit a large annual SSS variability in all three years, and thus, the numerical results for 2010 are slightly different from those shown in Chapter 4. Nevertheless, the overall conclusions are unchanged. Over the eastern subregion, the area-weighted SSS is typically fresher and displays a larger seasonal cycle by 0.33-0.85 pss over the 3 years compared to the western pole (Figures 5.6 and 5.7, and Table 5.3). However, the amplitude of the SSS seasonal cycle of ∼2.5 pss in 2010 (as compared to 1.92 pss in Chapter 4) decreases by 0.2 pss (∼8%) in each of the following years in the eastern pole, reaching 2.1 pss in 2012 (Figure 5.7, light green line, and Table 5.3). Over the same period, the SSS seasonal range in the western pole increases gradually by ∼4%, reaching from 1.63 pss in 2010 (compared to 1.57 pss in Chapter 4) to 1.77 pss in 2012 (Figure 5.7, light blue line, and Table 5.3).

Table 5.3: Amplitude of seasonal cycle of area-weighted SSS (in pss) in the different regions of study for 2010, 2011 and 2012.

	Western pole	Eastern pole	Whole basin	Pure ocean	No Western pole	No Eastern pole
2010	1.63	2.48	0.08	0.06	0.14	0.16
2011	1.70	2.34	0.12	0.09	0.12	0.20
2012	1.77	2.10	0.15	0.09	0.12	0.20

In contrast, the amplitude of the SSS seasonal cycle over the whole Atlantic basin 20°N-20°S, although increases from 0.08 pss in 2010 to 0.15 pss in 2012, still remains small compared to the two poles over the 3 years (Figure 5.7, red line, and Table 5.3). Considering only the oceanic basin 20°N-20°S without the two subregions influenced by the river outflows ("open ocean"), SSS shows a smaller seasonal variability of ∼0.06-0.09 pss throughout the period 2010-2012 (Table 5.3, plots not shown). However, the SSS seasonal cycle is noticeably amplified if either pole is excluded from the full regional mean, particularly the eastern pole (Table 5.3). Excluding the latter, the seasonal range of SSS over the rest of the study region doubles to ∼0.16 in 2010, and reaches ∼0.20 in 2011 and 2012. Alternatively, without the western pole, the SSS range is enhanced to 0.14 pss in 2010 and to 0.12 pss the next two years (Table 5.3).

5.5.2 Anomalies from the climatology

Figure 5.7 also shows the 3-year climatological mean time-series from SMOS for each region in order to examine the deviation of the SSS seasonal cycle in each

year from the mean seasonal behaviour during 2010-2012. The weighted SSS mean over the whole Atlantic region 20°N-20°S displays the smallest deviation from the SMOS climatological mean. In contrast, over the poles, SSS shows some deviation from the mean seasonal cycle in all three years, particularly in the eastern subregion. This is also seen in Figure 5.8 which displays the area-weighted mean SSS anomalies (without the seasonal cycle).

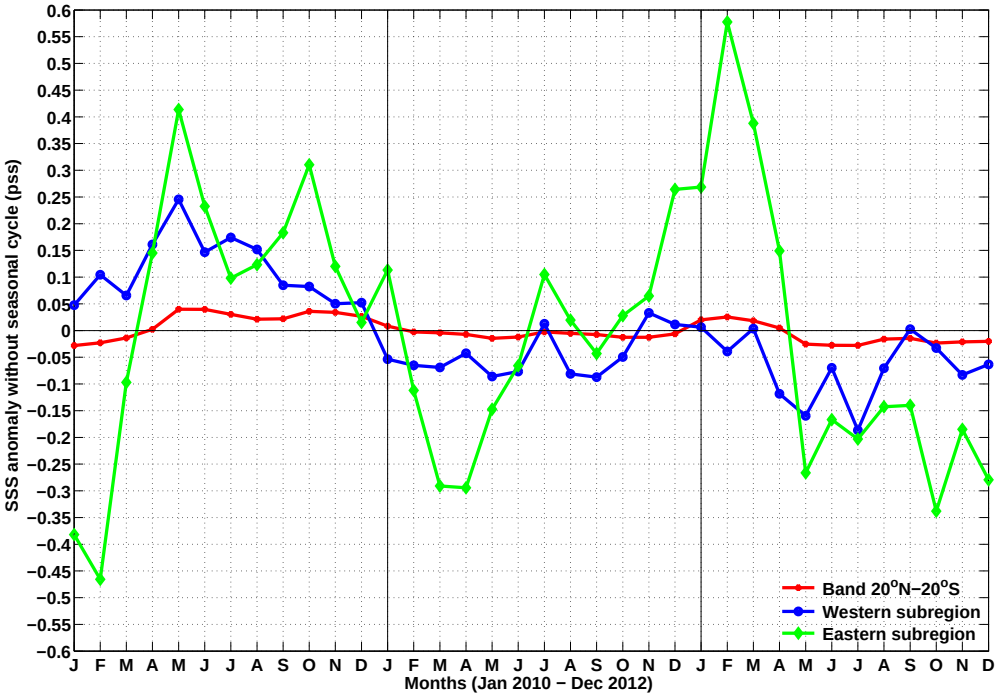

Figure 5.8: Area-weighted mean anomalies without the seasonal cycle of SMOS SSS (pss) over the whole region 20°N-20°S (red), the western (blue) and the eastern (green) subregions for the period January 2010 - December 2012.

The area-weighted SSS mean over the whole region (Figure 5.8, red line) displays the smallest deviation from the SMOS 3-year climatology in 2011 (-0.015 to 0.008 pss), with larger deviations in 2010 and 2012, especially from May onwards. Over the western subregion, the SSS anomalies are larger and more variable, with positive anomalies between 0.05-0.25 pss in 2010, as compared to smaller negative anomalies in 2011 (-0.09 to 0.03 pss) and 2012 (-0.19 to 0.01 pss), (Figure 5.8, blue line). In the eastern subregion, the anomalies are larger in all 3 years, particularly in 2010 and 2012, reaching from -0.47 pss to 0.41 pss in 2010, -0.29 pss to 0.26 pss in 2011 and -0.34 pss to 0.58 pss in 2012 (Figure 5.8, green line).

Finally, the 3-year climatological SMOS SSS mean for the period 2010-2012 is shown against the longer-term area-weighted SSS climatology from WOA09 in Figure 5.9. Both climatologies agree relatively well for the region as a whole (Figure 5.9, magenta and purple lines), with SMOS being smaller than WOA09 by 0.01-0.13 pss throughout the calendar year. In contrast, the SMOS climatological mean shows considerably larger differences in the two subregions, with deviations between -0.82 pss to 0.22 pss over the western pole (Figure 5.9, blue and cyan

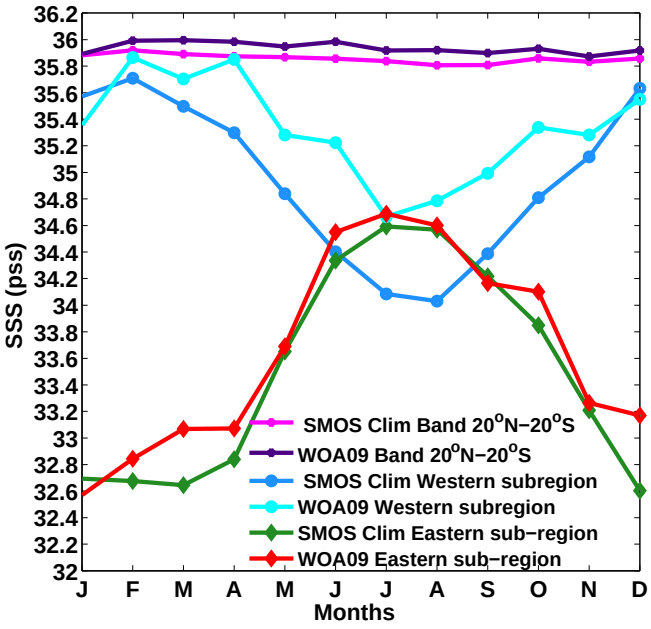

Figure 5.9: Area-weighted SSS mean (pss) over the whole region 20°N-20°S, the western and the eastern subregions based on i) the 3-year (2010-2012) SMOS (magenta, blue and green lines, respectively) and ii) WOA09 (purple, cyan and red lines, respectively) monthly mean SSS climatologies.

lines), and -0.57 pss to 0.12 pss over the eastern pole (Figure 5.9, green and red lines).

5.6 Relationship of SSS interannual variability to E, P and R

The analysis in Section 5.4 suggested some compensation between the SSS range in the western and eastern pole in 2010 (6 pss and 6.5 pss) and 2012 (7.1 pss and 7 pss), which was interrupted in 2011 (7.6 pss and 5.2 pss). The seasonal cycle of the area-weighted SSS in the two subregions seen in Section 5.5, showed that the eastern pole displays the largest interannual variability. In order to better understand this interannual variability of the SSS seasonal cycle over the Tropical Atlantic 20°N-20°S and each subregion, the analysis next examines the contribution of surface freshwater forcing due to evaporation (E), precipitation (P) and river runoff (R). Particularly, the focus is on the potential link variations in these terms with the strong SSS seasonal variability revealed by SMOS in the two poles over the 3 years.

Figure 5.10 shows the seasonal cycle of the area-weighted SSS mean for 2010, 2011 and 2012 together with the corresponding integrated monthly E-P, E and P mean values (in km^3/year) for each subregion. Note that for a direct comparison, all variables are re-gridded on the GPCP 2.5° x 2.5° spatial resolution. In addition to the long-term climatological mean of R (1941-1992), Figure 5.10 also includes the

annual discharges for 2010, 2011 and 2012 from the ORE-HYBAM network stations

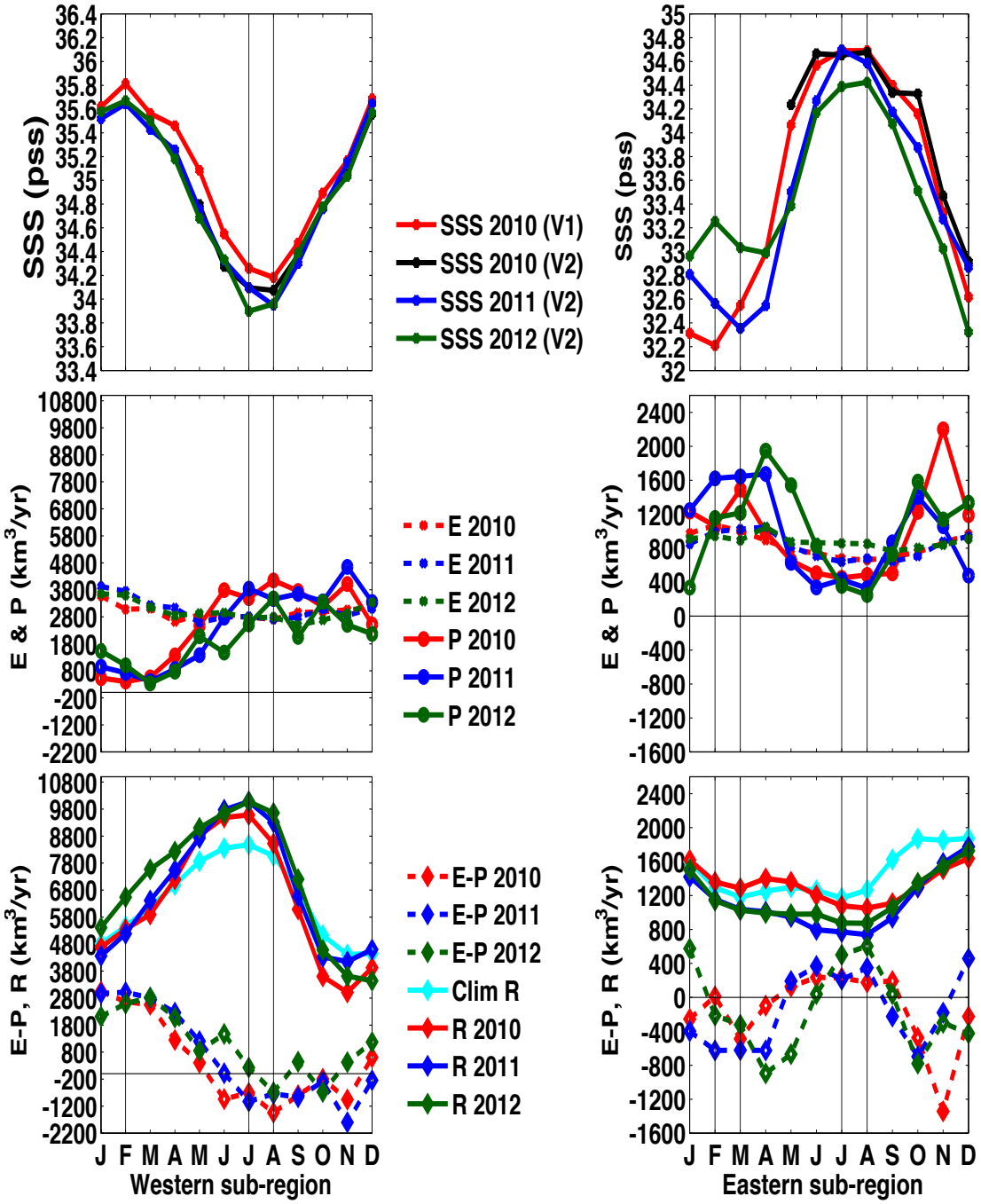

(a) Western subregion (b) Eastern subregion

Figure 5.10: Seasonal cycles for 2010, 2011 and 2012 of area-weighted mean SMOS SSS and integrated OAFlux E, GPCP P, and OAFlux-GPCP E-P (in km^3/year) for the western subregion (left panel) and the eastern subregion (right panel). Also shown are the sum of the long-term climatological means of riverine flow rates (R) for the period 1941-1992 for the Amazon and Orinoco in the western subregion (bottom left panel) and Congo and Niger in the eastern subregion (bottom right panel). Annual ORE-HYBAM river discharge data for 2010, 2011 and 2012 for the Amazon and Orinoco in the western subregion and for the Congo in the eastern subregion are also included in the bottom panels, respectively. The units of E, P, E-P and R are in km^3/year and of SSS in pss.

of the Amazon and Orinoco Rivers in the western subregion, and the Congo River only in the eastern subregion (in km^3/year). Figure 5.11 shows the time-series of each variable over the three years at each pole, enabling a more comprehensive examination of the interannual phase relationships between the seasonal cycles of the different terms. Overall, in good agreement with the processes seen in 2010 (Chapter 4), P and R continue to control the SSS variability in each pole for the whole period 2010-2012. SSS, P and R display strong seasonal cycles in both subregions, although the subtle interannual variations in their phase relationships complicate the interpretation and identification of which is the main, dominant freshwater term in each subregion.

Western pole In the western subregion, SSS, P, E-P and R display strong seasonal cycles over the whole 3-year period (Figure 5.10, left panel, and Figure 5.11, top panel). In contrast, E shows small seasonal variability, which is consistent over the 3 years. There is a small increase of the amplitude of E seasonal cycle from only ∼950 km^3/yr in 2010 to 1340 km^3/yr in 2011 and back down to ∼1160 km^3/yr in 2012. This may have a small impact on the SSS variability, at least in 2011 (Figure 5.11, top, yellow line), but its magnitude is still significantly smaller than that of the other terms of freshwater forcing (P and R) at the western pole.

P has an annual range typically between ∼3150-4230 km^3/yr in all 3 years, displaying a similar behaviour as E-P (Figure 5.10, left panel, and Figure 5.11, top panel). Since E shows little seasonal and interannual variability, E-P is dominated by the variability in P. The seasonal variability in P is largest in 2011, but with relatively similar annual P rates between 2010-2011. In contrast, in 2012, P displays both the lowest annual rate and the smallest annual variation. For R, the climatological Amazon/Orinoco outflow shows a relatively similar amplitude of the seasonal cycle (∼4070 km^3/yr) with E-P in all 3 years, implying a roughly equal contribution of E-P (dominated by P) and R to the interannual variability of SSS at this side of the basin (Figure 5.10, left panel). The ORE-HYBAM annual R estimates indicate a considerably larger amplitude of the R seasonal cycle, i.e. from ∼5920 km^3/yr in 2011 to ∼6600 km^3/yr in 2010 and 2012, likely indicating a more significant influence of R on the SSS variability during these years (Figure 5.11, top, purple line).

The area-weighted SSS minima (∼33.9-34.2 pss) occur in boreal summer (July or August) in all 3 years (Figure 5.11, top panel, red line), in close occurrence with the P maxima. They are strictly in phase with the P maximum (E-P minimum) only in 2010, while lies within a prolonged period of increased P rates in 2011 and 2012 (Figure 5.11, top, blue and green lines). The SSS minimum precedes the E-P minimum by 3 (1) months in 2011 (2012), given also the strong interannual variation in the occurrence of E minima (i.e. April 2010, May 2011, September 2012), (Figure 5.11, top, yellow line). Finally, the SSS mimimum generally lags R by 1-2 months, i.e. by 2 (1) months the ORE-HYBAM (climatological) R

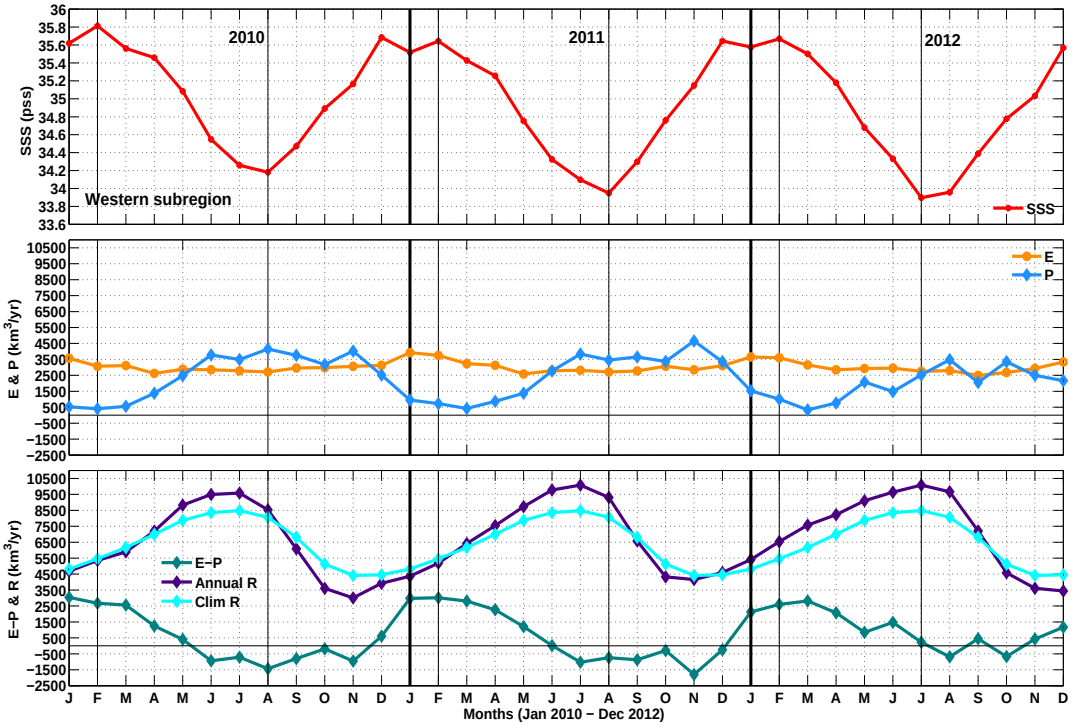

(a) Western subregion

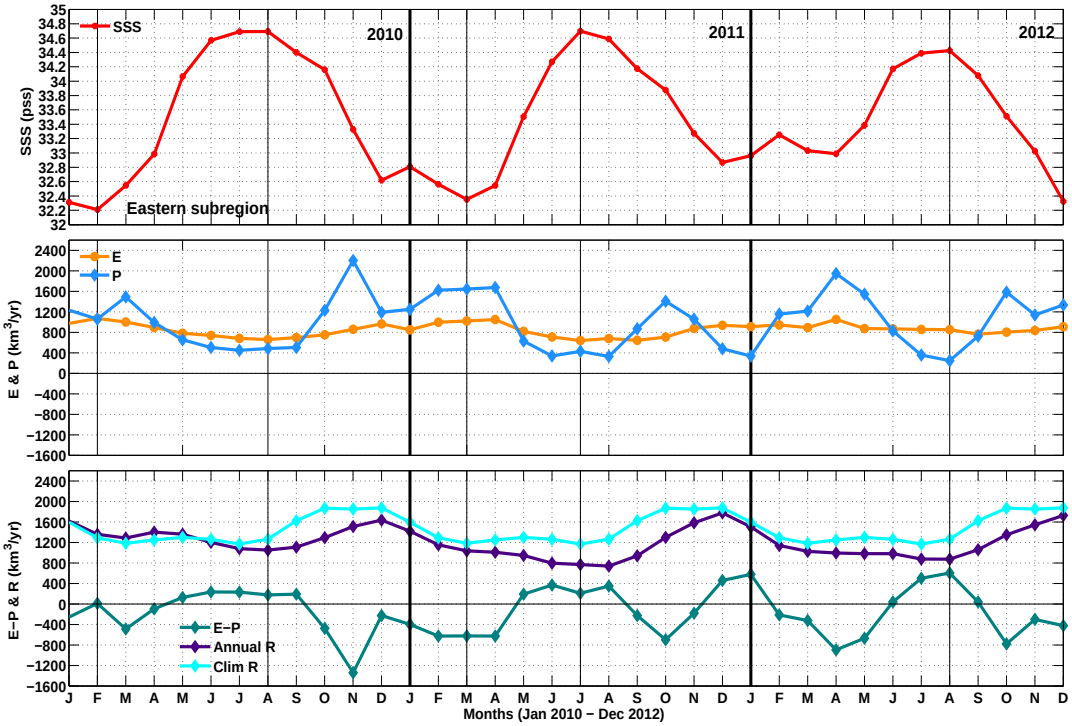

(b) Eastern subregion

Figure 5.11: Interannual variability of the seasonal cycle of area-weighted mean SMOS SSS (red) and integrated OAFlux E (yellow), GPCP P (blue), and OAFlux-GPCP E-P (green) for a) the western subregion and b) the eastern subregion, in 2010, 2011 and 2012. Also shown are the 12-month climatological (cyan) and the annual ORE-HYBAM R discharge data (purple) for the period 2010-2012 for i) the Amazon and Orinoco in the western subregion and for ii) the Congo in the eastern subregion. The units of E, P, E-P and R are in km^3/year and of SSS in pss.

maximum in 2010, by 1 month in 2011 (both the annual ORE-HYBAM and the climatological R) and is in phase with it in 2012 (Figure 5.11, dark purple line).

The area-weighted SSS maxima over the western pole show almost no interannual variability in terms of magnitude (35.6-35.8 pss) and occur in boreal winter throughout the period 2010-2012 (Figure 5.10, left panel, and Figure 5.11, top panel). Generally observed in February, they are in close occurrence with P minima (E-P maxima) and within a prolonged period of low R runoff, while lag the E maxima by 1 month in all 3 years. Furthermore, high SSS values, with magnitude comparable to the annual maxima, are also observed in December, despite the prolonged periods of high P rates. Interestingly, they seem to be primarily linked to the R minima during the whole period of interest (Figure 5.11, red and purple lines).

Eastern pole Focusing on the eastern subregion, SSS displays, in general, its lowest values between December-April, and thus, over a longer period within an annual cycle compared to the western subregion (Figure 5.10, right panel and Figure 5.11, bottom panel). Overall, the area-weighted SSS minimum, with a roughly constant magnitude of 32.2-32.4 pss over the 3 years, shows a noticeable interannual variation in terms of occurrence, i.e. from February-March in 2010 and 2011, it is postponed to December in 2012, with a secondary minimum around April 2012. The annual SSS maxima, with a stable magnitude of 34.4-34.7 pss, occur in boreal summer (July-August) throughout the 3-year period.

P and E-P show a smaller magnitude and seasonal variability in the eastern than the western subregion in all 3 years, but a much stronger SSS interannual variability (Figures 5.10 and 5.11, and Table 5.3 for SSS in each pole). P (E-P) has a similar seasonal amplitude in 2010 and 2012 ($\sim$1700-1750 km^3/yr), which is noticeably reduced in 2011 ($\sim$1350 km^3/yr), (Figure 5.11, bottom, blue line), displaying the largest annual P rates in 2012. A much smaller variability characterizes E throughout the 3 years, with a constant annual range of $\sim$410 km^3/yr in 2010-2011 and an even smaller amplitude ($\sim$290 km^3/yr) in 2012 (Figure 5.11, yellow line). Thus, E seems to play no significant role on the E-P and SSS seasonal variability in the eastern subregion throughout the 3 years, as was also the case for the western pole.

In contrast, R is characterized by strong interannual variability. Considering only the annual discharge of Congo River from ORE-HYBAM, the amplitude of the R seasonal cycle doubles from 2010 ($\sim$590 km^3/yr) to 2011 ($\sim$1040 km^3/yr), when it is comparable in magnitude to the (reduced) seasonal range of P in that year. In 2012, the R seasonal range, reducing again to $\sim$850 km^3/yr (Figure 5.11, bottom panel, purple line), still remains larger than the range of only $\sim$705 km^3/yr for

both the Congo and Niger outflows indicated by the long-term climatology (Figure 5.10, right, cyan line). The annual Congo outflow is considerably larger in 2010 compared to 2011-2012, when it displays a roughly similar magnitude.

As seen in 2010 (Chapter 4), the relationship between SSS and surface freshwater forcing continues to be complex in the eastern pole for the whole 3 years. Nevertheless, as for the western pole, the SSS minima in the eastern subregion also occur within prolonged periods of high annual P and R rates, and are in general agreement with the decreased E-P magnitude (Figure 5.11, red, blue, purple and green lines, respectively). A more clear relationship is found for the SSS maxima, which are generally in phase or lag by 1 month the P and R minima in all 3 years. The good agreement between the long-term climatological R for Congo/Niger and the ORE-HYBAM annual discharge only for Congo for the occurrence of R maximum in December throughout the period 2010-2012, confirms that the phase relationships presented here are not sensitive to the use of climatological R or to the lack of annual Niger discharge data (Figure 5.10, right, bottom).

5.7 Summary, discussion and conclusions

Based on 3 years of data, the SSS seasonal cycle over the whole Tropical Atlantic basin is relatively constant on interannual time scales, showing a small increase in magnitude from 0.08 pss in 2010 to 0.15 pss in 2012. In contrast, close to the major Amazon/Orinoco and Congo/Niger river outflows, strong local variations of SSS, first revealed by SMOS for 2010 (*Tzortzi et al.*, 2013), continue to be apparent the following years. On an annual basis, the SSS range of 6 pss/6.5 pss in the western/eastern pole in 2010, reaches ∼7 pss at both subregions in 2012, while there is a noticeable imbalance in 2011, of ∼7.6 pss/5.2 pss, respectively.

Given that the SMOS uncertainty over the whole Tropical Atlantic basin is calculated to be ∼0.3 pss, increasing to up to ∼0.9 pss close to the river plumes (See Chapter 3, Section 3.2.3), this may have some impact on the above qualitative results. However, it is unlikely to influence noticeably the quantitative results and the conclusions drawn, since analysis of area-weighted means (which is expected to decrease data uncertainty) reveals the same pronounced, out-of-phase seasonal cycles of SSS in the two poles throughout the period 2010-2012 and that the seasonal compensation between them holds on interannual time scales. The results for 2010 are obtained from V01 of the SMOS CATDS-CECOS product, while for 2011-2012 from V02, which is relaxed to climatology and thus may artificially modify the spatial distribution of SSS field (*Hernandez et al.*, 2014) and smooth some of the interannual SSS variability. Consequently, this may affect, for instance, the annual SSS range values, given their sensitivity to the SSS minima/maxima of each year. Nevertheless, as above, the strong SSS behaviour being repeated in each of the 3-year period, ensures that the main conclusions remain unaffected. Moreover,

comparison of the seasonal cycle of area-weighted SSS mean in 2010 from the two versions over their common period (Figure 5.6) indicates the same seasonal behaviour of SSS in the three regions, with differences that do not exceed in general ∼0.03 pss. This reinforces further the confidence that adjustment of V02 to the climatology does not alter noticeably the interannual variability of area-weighted SSS means, and that combining the two versions does not affect the consistency of the results.

Year-to-year variations of the SSS seasonal cycle in both subregions are primarily due to strong interannual variations of their SSS minima, as opposed to the generally constant SSS maxima over the 3 years, particularly in the western pole. In this subregion, the boreal winter (summer) SSS minimum decreases remarkably by 2.5 pss (∼1 pss) from 2010 to 2012 (See Table 5.2). In the eastern subregion, SSS displays a much stronger seasonal and interannual variability throughout 2010-2012. This is also apparent when compared to the climatological SMOS (and WOA09) SSS mean, with deviations that reach up to ∼0.9 pss in 2010 and 2012. The SSS minimum in winter increases by ∼1-2 pss from 2010 to 2012, but decreases by ∼1 pss in summer (See Table 5.1).

As regards the western subregion, a recent study by *Grodsky et al.*, 2014a indicates 1 pss salinification of the SSS minimum in early autumn 2012 as compared to autumn 2011. This feature is not directly evident in the present analysis, which focuses on the January and July monthly SSS averages over these years. The 12-monthly variations of SSS for each year are examined over area-weighted means (and in the coarser, 2.5° x 2.5° spatial resolution of GPCP) that smooths out this localized (in September, around 8°N, see *Grodsky et al.*, 2014a; *Grodsky et al.*, 2014b) signal and thus, it is not visible in Figure 5.10. Nevertheless, examination of the difference between the SSS fields in September 2011 and 2012 (plots not shown) does reveal a similar SSS increase of up to ∼ 1.4 pss in the plume from one year to the next, as seen in their study (Figure 4, *Grodsky et al.*, 2014a), despite some differences in the SSS spatial patterns. On the other hand, the different choice of datasets for SSS (Aquarius/SAC-D and SMOS from LOCEAN/IPSL) and R, which corresponds to the combined Amazon/Tocantins River discharge (from ORE-HYBAM and the Brazilian water agency), as compared to the Amazon/Orinoco outflow examined here, may further explain any differences between the two studies.

Freshwater forcing by P and R are the primary drivers of the SSS variability in both poles throughout the period 2010-2012, displaying, like SSS, strong seasonal cycles. In contrast, E displays small variability (both seasonally and interannually), and therefore, does not play an important role on the Tropical Atlantic SSS variability. SSS minima (maxima) occur in line with increased (decreased) P and R at both poles. However, the interannual variability in the magnitude and phase

relationships between SSS, P and R hinders any firm conclusions on which is generally the dominant term of freshwater forcing on the SSS variations at each pole. For instance, over the western pole, the increase of SSS seasonal variability from 2010 to 2011 is mainly driven by corresponding enhanced variations in P. In 2012, R (Amazon/Orinoco) displays overall the largest variability and annual discharge that may explain the further increase of the SSS seasonal variations. This competition between P and R influence on SSS is further evident in the eastern pole, while in 2011, the comparable amplitude of P and R seasonal cycles potentially indicates their equal contribution on the SSS variability for that year.

The observed interannual variations in freshwater forcing (P and R) over both subregions seem to be mainly influenced by the ENSO phases, i.e. the mature phase of El Niño in DJF 2009/2010 (e.g. *Wang et al.*, 2011), the prolonged La Niña event in 2010-2011, and the following weak El Niño in early 2012. Therefore, the maximum Amazon/Orinoco discharge, for instance, is found in 2012 in agreement with other studies for the Amazon runoff only, being attributed to the 2011 La Niña conditions (*Satyamurty et al.*, 2013). In both subregions, R appears to lag P by few months, potentially due to water storage that leads to noticeable lagging in the P-R phase relationship (e.g. *Chen et al.*, 2010). This delay of freshwater outflow to reach the river mouth and then be advected by the surface currents further away from it, is also evident in the lag between R maxima and SSS minima.

In addition to P (and R), changes in zonal advection by the surface currents represents another main mechanism responsible for the ENSO signatures on SSS, as has seen documented for the Equatorial Pacific (e.g. *Singh et al.*, 2011). Variations in advection and mixing processes may also contribute to the SSS interannual variability over the two subregions. In the western pole, changes in export of low-salinity waters through the different advection pathways of the Amazon/Orinoco plume (e.g. *Foltz and McPhaden*, 2008; *Grodsky et al.*, 2014a), in saline water import into the region from south through the Brazil Current pathway (*Romanova et al.*, 2011), or from east through the North Equatorial Counter Current (e.g. *Grodsky et al.*, 2014b), or even maintenance of rivers' outflow for longer close to the plume as occurs generally in boreal winter (e.g. *Foltz and McPhaden*, 2008) are likely to modify SSS at the western pole to some extent.

Similarly, different P patterns over the eastern pole due to ENSO, variations in continental river discharge from a number of other rivers, including the Niger, as well as seasonal variations of advection by the ocean currents, such as the large westward extension of Congo plume in February-March (*Materia et al.*, 2012; *Denamiel et al.*, 2013), may have an impact on the observed strong SSS variability in the Gulf of Guinea. Furthermore, equatorial and coastal upwelling might be another factor influencing SSS changes in the Eastern Tropical Atlantic (e.g. *Reul et al.*, 2013), which in turn, may also impact on the ocean stratification and lead to suppression of vertical mixing and coastal upwelling (e.g. *Materia et al.*, 2012),

affecting, subsequently, SSS in the region. Nevertheless, the strong link of SSS to P and R (and thus P over land) in both subregions over the 3 years likely indicates the secondary role of these processes in the SSS variations, while demonstrating clearly that salinity can serve as a natural indicator of the water cycle.

SSS variations in the two subregions seem to play a key role on the Tropical Atlantic variability. The SSS seasonal cycle of the oceanic basin 20°N-20°S without the river-influenced poles ("open ocean") weakens, while is noticeably amplified if either pole is excluded from the full regional mean in all 3 years, particularly the eastern pole. This highlights the sensitivity of the Tropical Atlantic salinity budget to such regional variations in SSS, and the need to better understand their potential link to the larger-scale Atlantic ocean circulation and variability. The different spatio-temporal coverage of satellite SSS observations from SMOS and Aquarius/SAC-D, clearly offers the potential for a more detailed depiction of SSS variations such as in the two subregions, contributing to studies on regional salinity and freshwater budgets. For this, an essential step towards a more comprehensive understanding and description of SSS variations is the determination of their time and space scales over the Tropical/Subtropical Atlantic. This task is addressed in the following Chapter (Chapter 6).

Chapter 6

Space and time scales of SSS variability from SMOS

6.1 Introduction

This chapter takes advantage of the availability and different spatio-temporal coverage of satellite sea surface salinity (SSS) observations from SMOS in order to examine for the first time the characteristic scales of SSS variations in space and time. In contrast, previous observational-based attempts (e.g. *Delcroix et al.*, 2005; *Reverdin et al.*, 2007) have been necessarily constrained to the limited coverage of in situ measurements. The focus is over the whole Tropical/Subtropical Atlantic 30°N-30°S, in order to include both the precipitation (P)- and evaporation (E)-dominated regimes. For the spatial scales of SSS (Section 6.3.1), the aim is to identify potential regions over the basin, where SSS varies concurrently in space on relatively short, i.e. subannual to interannual, time scales and are characterized by a homogeneous SSS behaviour. Similarly, a first insight is obtained into the persistence of consistent SSS changes in time (Section 6.3.2), i.e. how quickly temporal SSS variations evolve over the different regions, by assessing decorrelation lengths of SSS on subannual to interannual time scales over the first three complete years (2010-2012) of SMOS data.

The motivation of this work is that improved knowledge of SSS variations will provide valuable information for optimally interpolated products and data assimilation procedures. Nowadays, advances within the framework of data assimilation allow for synthesis of complex ocean general circulation models and different types of observations (satellite-derived, hydrographic, etc), which result in estimates of ocean state that generally represent more accurately the system than could be obtained from the model or observations alone. Therefore, it serves as a powerful tool for oceanographic research and recent attempts have been already accessing the impact of satellite SSS data to improve predictions and ocean state estimates,

with promising outcomes (*Vernieres et al.*, 2014; *Hackert et al.*, 2014; *Vinogradova et al.*, 2014; *Köhl et al.*, 2014).

Moreover, a better description and understanding of the spatio-temporal characteristic length scales of SSS variations will also help with the interpretation of the influence of the different controlling mechanisms acting on SSS in the region of interest. These are described in detail in Chapter 2. Briefly, in the Tropical/-Subtropical Atlantic (see Chapter 2, Figure 2.4 for a schematic), SSS changes are expected to be primarily controlled by the surface forcing of freshwater fluxes and advection by the ocean surface circulation. The former comprises, in general, of the excess of precipitation (P) along the Tropics associated with the position of the InterTropical Convergence Zone (ITCZ), the dominance of evaporation (E) in the Subtropics associated with the winds of the Subtropical high-pressure systems, as well as freshwater discharge from the Amazon/Orinoco and Congo/Niger river systems in the western and eastern Equatorial Atlantic, respectively. Advection is due to the surface current circulation along the equator and the branches of the Northern and Southern Subtropical Gyres (See Chapter 2, Figure 2.5). Finally, other factors that are expected to influence the SSS variations in the basin are mixing processes and entrainment, including the equatorial and coastal upwelling.

6.2 Data, statistical methods and approach

Monthly mean SSS products are derived from SMOS for the complete years 2010 (CATDS-CECOS Version V01), 2011 and 2012 (CATDS-CECOS V02). Details on the SMOS CATDS data are provided in Section 3.2.1.5. For the examination of the spatial scales of SSS, maps of SSS correlations are obtained by calculating the correlation coefficient, r, between the 3-year time-series of monthly SSS mean in each target grid cell and the rest of the grid cells in the Tropical/Subtropical Atlantic basin 30°N-30°S. The statistical significance is tested by calculating the p-value, i.e. the probability of obtaining a correlation value as strong as that observed by random chance, using the t statistic (*von Storch and Zwiers*, 2001). Using 3 complete years of SMOS SSS data on 1°x1° spatial resolution, the analysis is first performed on the monthly mean SSS, and then on the SSS anomaly fields without the seasonal cycle. The seasonal signal is estimated by calculating the climatological mean SSS map from SMOS over 3 years for each month, which is subsequently removed from each month in the 3-years time-series in each grid cell.

For the computation of the spatial length scales of SSS in km, the interest is in the homogeneous SSS changes, i.e. in-phase variations relative to a target grid point. Here, homogeneous SSS changes are defined as those corresponding to positively correlated SSS patterns ($0 \geq r \geq 1$) around the target grid point, and exceeding a chosen threshold. Assuming that the spatial distribution of r decays exponentially from the target grid cell, the threshold of 1/e ($\approx$0.37) is chosen to determine the

length of the SSS characteristic spatial scales, i.e. the limit of the spatial feature with $r \geq 0.37$ extending from the target grid to the West, East, North and South direction, respectively. The time scales of SSS are determined by calculating lagged autocorrelations of SSS in each target grid cell with itself for the 3-year time-series of the monthly mean and the SSS anomaly field, respectively. As above, a threshold of 1/e is applied, i.e. $r \geq 0.37$, in order to define the temporal decorrelation lengths of SSS in each grid cell over the Tropical/Subtropical Atlantic basin 30°N-30°S.

6.3 Scales of mean SSS from SMOS

6.3.1 Spatial scales of SSS mean (with the seasonal cycle included)

The calculation of r over the Tropical/Subtropical Atlantic basin 30°N-30°S (with a size of 61 x 82 grid cells in latitude x longitude) results in over 5000 correlation matrices for the monthly mean, and similarly for the SSS anomaly fields (Section 6.4.1). Here, in order to obtain an initial idea of the spatial correlation patterns of SSS, Figure 6.1 shows an example of the SSS correlation coefficient (r) map corresponding to a target grid cell, Point A, in the S. Subtropical Atlantic (23°S 13°W). Grid cells where regressions are not significant at 95% significance level (p-value>0.05) are shaded with a cross. An alternation of strong positive and negative SSS correlation bands extending across the whole basin width is evident, particularly between ∼17°N-10°S. The southern basin is dominated by a large strongly correlated circular feature, which also encompasses the target Point A. The observed features dominating the basin are characterized by r values that are statistically significant (p-value≤0.05), (Figure 6.1).

The spatial homogeneity of changes in SSS within regions characterized by high (positive or negative) r values is further examined by looking at the time evolution of SSS at Point A relative to another selected grid cell B in a different region which also displays high -positive or negative- r values. Figure 6.2 shows the time-series and scatterplot of the monthly mean SSS at Point A (23°S 13°W) against Point B (6°N 25°W), located north of the equator (as shown in Figure 6.1). SSS at the two locations has a similar, in-phase seasonal behaviour during most of the 3-year period, although displaying different values in terms of SSS magnitude and a smaller seasonal range at Point A compared to the equatorial Point B, both on an annual and interannual basis (Figure 6.2).

Figure 6.2 (top plot) also includes the climatological SSS mean at each grid cell over the 3 years of SMOS data, to show their deviation from the mean seasonal cycle from year to year. On an annual cycle, SSS at Point A deviates from its climatological mean by only small amounts, i.e. -0.07 to 0.16 pss in 2010, -0.10 to 0.09 pss in 2011 and -0.14 to 0.05 pss in 2012. In contrast, north of the equator,

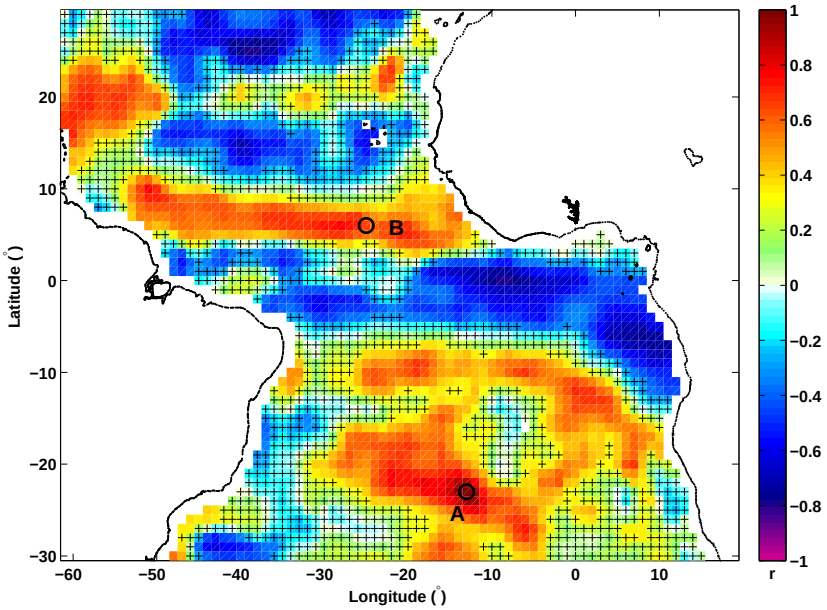

Figure 6.1: The correlation coefficient, r, of the 3-year time-series (2010-2012) of SMOS SSS monthly means between the target Point A in the S. Subtropical Atlantic at 23°S 13°W (indicated by the black circle) and the rest of the Atlantic basin 30°N-30°S. Also shown is Point B at 6°N 25°W. Grid cells that are not significant at 95% significance level, are shaded with a cross (+).

SSS at Point B shows larger deviations from its climatology, ranging between -0.29 to 0.33 pss in 2010, -0.15 to 0.18 pss in 2011 and -0.25 to 0.15 pss in 2012, respectively.

Figure 6.3 shows another example of the spatial r map for SSS at a grid cell in the Tropical Atlantic basin, south of the equator at 7°S 12°W (Point C). When the seasonal cycle is included, strong correlated and anti-correlated features extend across the width of the basin and dominate the regions close to the major rivers (a pattern also seen in Figure 6.1). The strong anti-correlation of SSS at Point C and the region of high negative r values in the North Tropics is evident when looking at the time-series of SSS at Point C and another selected grid cell, Point D (Figure 6.4, top plot), along the central N. Tropical Atlantic, at 13°N 23°W (also shown in Figure 6.3). SSS is characterized by similar magnitudes but opposite seasonal cycles at the two locations for most of the 3 years (Figure 6.4, top plot), while their strong anti-correlated relationship is further highlighted by the scatterplot (Figure 6.4, bottom plot). Again, the climatological annual cycle is shown at both points in Figure 6.4 (top plot). Deviations from the climatology at Point C and Point D can be large, reaching over 0.3 pss at times.

6.3.1.1 Spatial distributions of correlation coefficient, r

Unlike the examples seen in Section 6.3.1 (Figures 6.1 and 6.3), the analysis of r also revealed many cases where SSS is strongly correlated only locally around the target grid cell, with strongly anti-correlated or no correlated signals over large

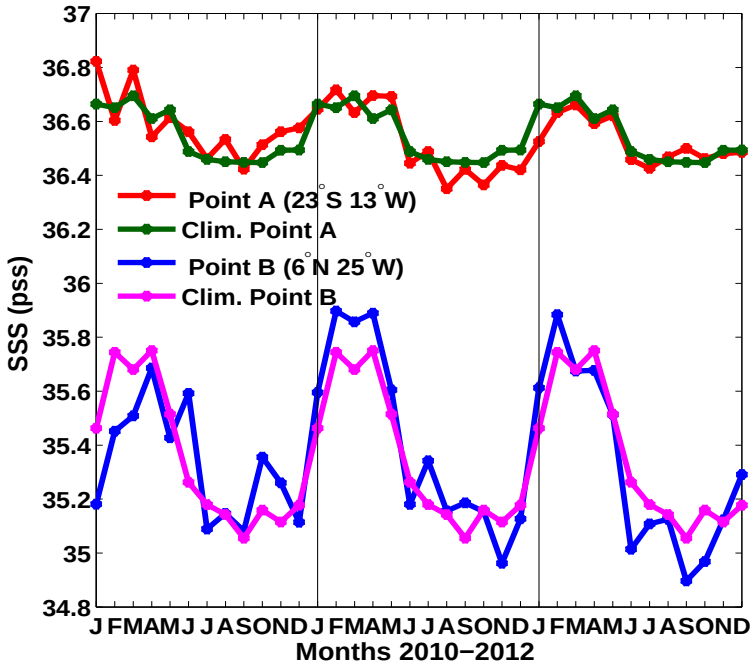

(a) Time-series of mean SSS at Points A and B

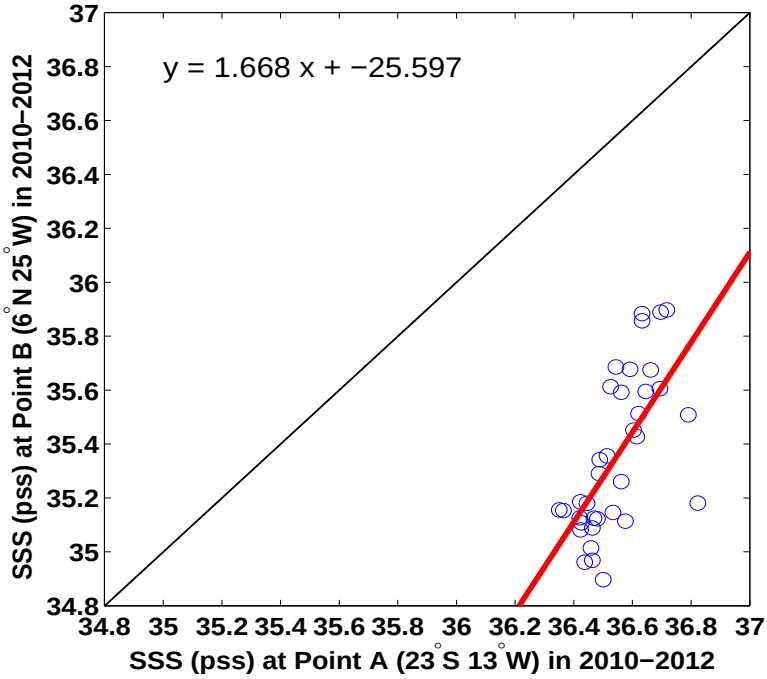

(b) Scatterplot of mean SSS at Points A and B

Figure 6.2: a) The monthly 3-year time-series and b) scatterplot of SMOS SSS mean at the target Point A (23°S 13°W) in the S. Subtropical Atlantic versus a strongly correlated Point B (6°N 25°W) north of the equator (indicated in Figure 6.1). Also shown in a) is the 12-month climatological mean of SSS for each grid cell.

distances away from it (plots not shown). This behaviour has been observed for various target grid points regardless of their location over the Tropical/Subtropical Atlantic basin. Given the large number of r matrices, a more appropriate method is adopted here to examine the spatial variations of SSS, by looking at

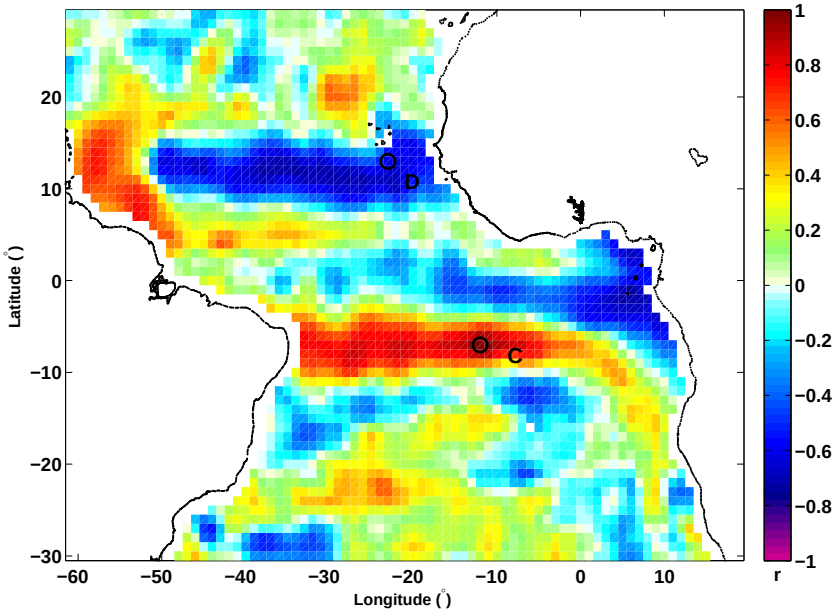

Figure 6.3: The correlation coefficient, r, of the 3-year time series (2010-2012) of SMOS SSS monthly means between the target Point C (7°S 12°W) in the central S. Tropical Atlantic (indicated by the black circle) away from river influence, and the rest of the Atlantic basin 30°N-30°S. Also shown is Point D (13°N 23°W).

how the distribution of r varies zonally and meridionally. The aim is to identify regions in the Tropical/Subtropical Atlantic where the SSS variability may reveal a homogeneous behaviour.

Figure 6.5 shows in each subplot the distribution of r in the West-East (W-E) direction for various grid cells in specific latitudes every 10° between 30°N-30°S. Each curve corresponds to r obtained for one grid cell at a given longitude every 12°, indicated by the colourbar. Figure 6.6 shows the r distributions in a North-South direction (N-S) for selected longitudes with a zonal step of 12°, focusing particularly on the centre of the basin, where there is a larger range of latitudes between 30°N-30°S (due to the curved shape of the basin). Centred at the target grid cell where r=1, the x-axis represents the distance in km (∼111 km x cos(Latitude) for the W-E and ∼111 km for the N-S direction), i.e. the number of grid cells at each side of the target point, after which r falls below the chosen threshold (1/e), indicated by the thin black lines. (Note that both Figures 6.5 and 6.6 display a threshold of ±1/e to provide an insight into the whole spatial distribution of r, however the main interest here is on the positively correlated patterns, i.e. the homogeneous SSS changes relative to the considered target grid cell in each case.) Thus, these plots give an illustration of the spatial decorrelation length of SSS from SMOS in the W-E (Figure 6.5) and N-S direction (Figure 6.6), respectively, over the Tropical/Subtropical Atlantic basin.

In general, SSS displays a homogeneous behaviour over larger distances in the W-E than in the N-S direction, where r shows a noticeably faster decrease to the threshold of 0.37 (Figure 6.5 compared to Figure 6.6). Thus, the spatial correlation

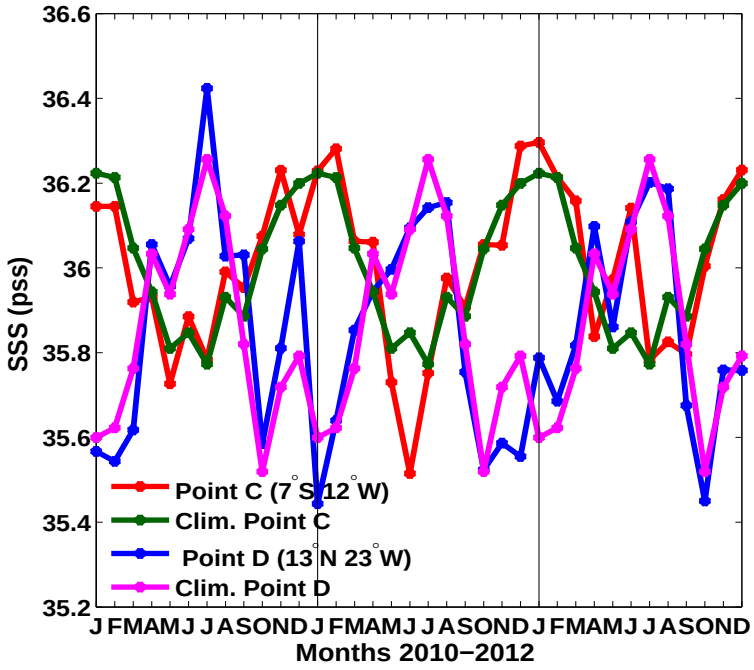

(a) Time-series of mean SSS at Points C and D

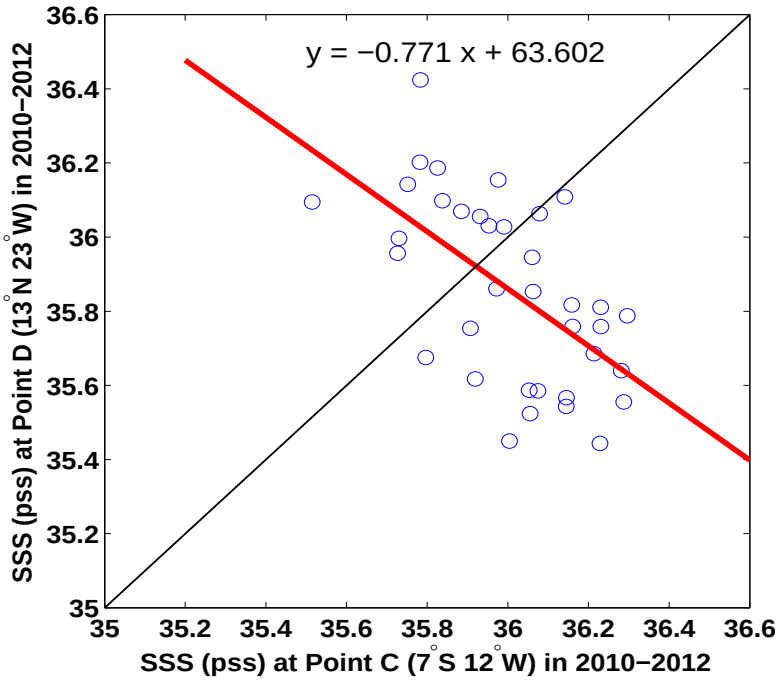

(b) Scatterplot of mean SSS at Points C and D

Figure 6.4: a) The monthly 3-year time-series and b) scatterplot of the SSS monthly mean at the target Point C (7°S 12°W) versus a strongly anti-correlated Point D (13°N 23°W), (indicated in Figure 6.3). Also shown in a) is the 12-month climatological mean of SSS at each grid cell.

scales of SSS from SMOS are anisotropic over the Tropical/Subtropical Atlantic, with typical lengths of more than ∼1700 km in the zonal and ∼1000 km in the meridional direction. In the W-E direction, SSS variations appear homogeneous over larger distances towards the equator compared to the higher latitudes, with a noticeably different shape of the r distributions (Figure 6.5). Overall, the largest

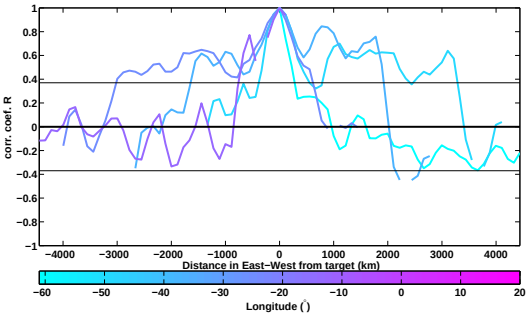

(a) 30°N

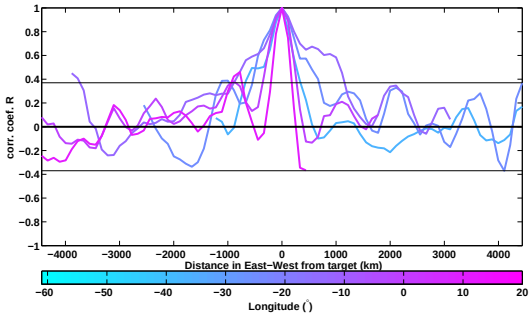

(b) 30°S

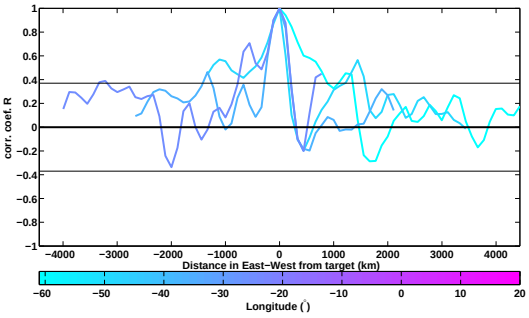

(c) 20°N

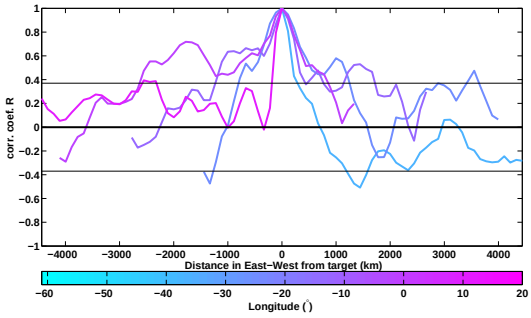

(d) 20°S

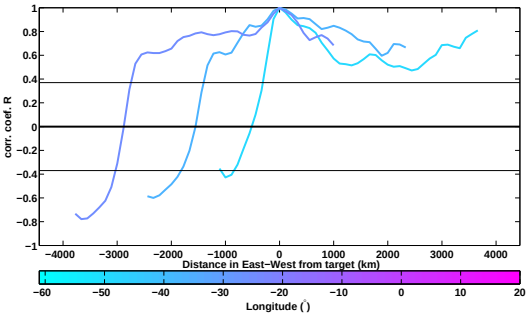

(e) 10°N

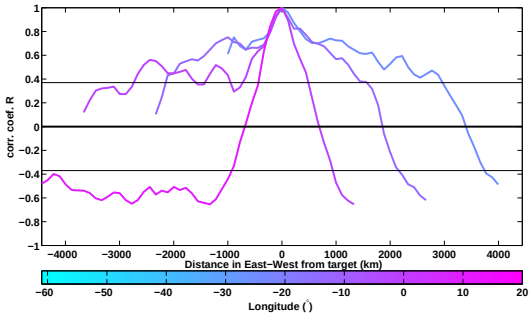

(f) 10°S

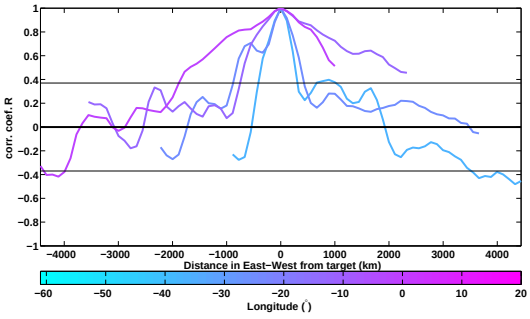

(g) Equator

Figure 6.5: Distributions of the correlation coefficient (r) in the W-E direction of the 3-year time-series of SMOS SSS means between each grid cell (target) and the rest of the basin. The distributions, centred at the target grid cell where r=1, are shown for specific latitudes between 30°N-30°S with a zonal step of 10°, along the basin width 61°W-20°E, with a meridional step of 12°. The colourbar shows the longitudes. Thin black lines indicate a threshold of $\pm 1/e$ ($\approx$0.37). Distributions are displayed for a) 30°N, b) 30°S, c) 20°N, d) 20°S, e) 10°N, f) 10°S, and g) the equator.

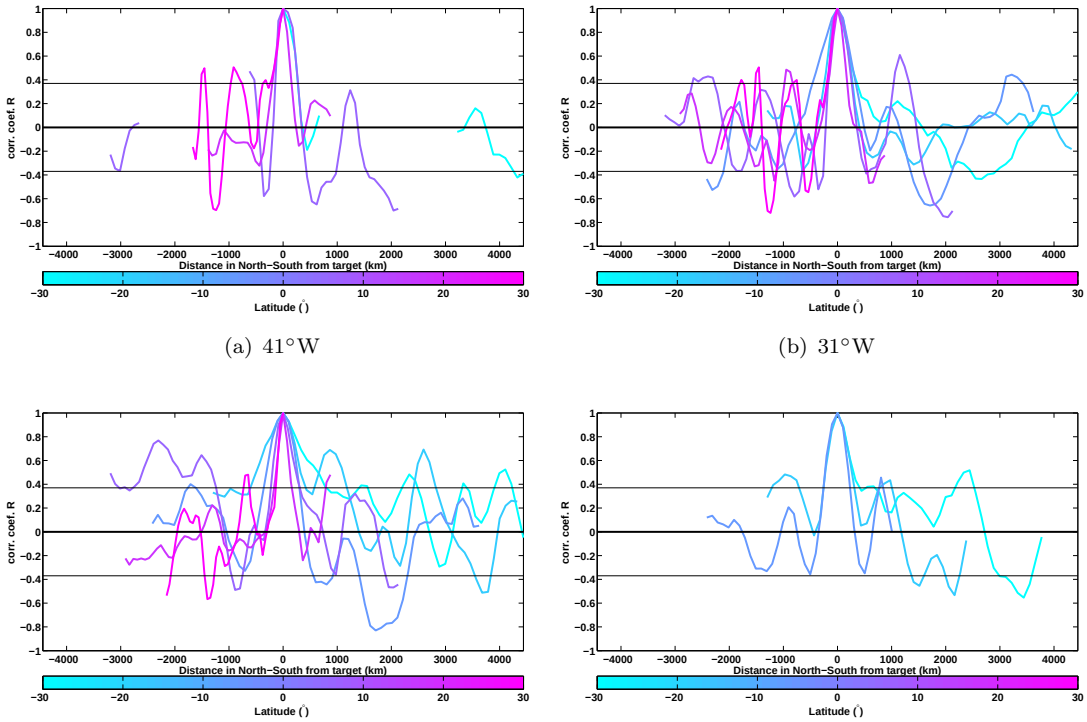

(a) 41°W (b) 31°W

(c) 21°W (d) 11°W

Figure 6.6: Distributions of the correlation coefficient (r) in the N-S direction of the monthly mean time-series of SSS at the longitudes a) 41°W, b) 31°W, c) 21°W, and d) 11°W along the length of the Atlantic basin 30°N-30°S with a latitude step of 12°. Latitudes are shown by the colourbar. Thin black lines indicate a threshold of ±1/e.

zonal spatial scales are found in the northern and southern Tropics at 10°N and 10°S (Figure 6.5, e and f), reaching more than 3000 km, or indicating r values that never meet the threshold close to the coast, north of the equator. In contrast, at the equator, homogeneous SSS changes occur over shorter distances that do not exceed 1000 km, with the exception of the most eastern equatorial basin where they reach up to ∼2000 km (Figure 6.5, g).

At the highest latitudes, SSS correlations show the largest length scales in the N. Subtropical Atlantic 30°N, particularly at the central basin (∼20°-40°W) of up to ∼3000 km (Figure 6.5, a). Interestingly, further south at 20°N, the zonal lengths are much shorter and do not exceed ∼1000 km, suggesting a reversed relationship between the central and western basin length scales (about ∼500 km and ∼1000 km, respectively), (Figure 6.5, a and c). In the S. Subtropics, the zonal scales of SSS at 30°S are much shorter than 30°N, reaching up to ∼1000 km at ∼10°-30°W. Further north, at 20°S, SSS displays similar lengths, except towards the eastern basin (∼0°E), where they exceed ∼2500 km (Figure 6.5, b and d).

Looking at particular longitudes, Figure 6.6 shows much shorter spatial scales relative to Figure 6.5 over most of the basin length, that do not generally exceed ∼500 km. Largest deviations are seen particularly in the central and eastern

basin, i.e. 21-31°W and 11°W (Figure 6.6, b-d), of the Tropical band between ∼10°N and ∼10°S. There, the spatial lengths of SSS are reduced from ∼2000-3000 km (Figure 6.5, e-g) to ∼500 km (Figure 6.6, b-d), highlighting the strong responsiveness of SSS characteristic scales to the zonal or meridional direction. Overall, the central S. Subtropical basin at 30°S 21°W shows the largest length scales of SSS of up to 1000 km (Figure 6.6, c, cyan line).

6.3.1.2 Spatial length scales (in km) of SSS with the seasonal cycle included

Next, the findings of the previous section are summarized by focusing on the spatial patterns of the computed length scales in km. For this, the number of highly correlated grid cells relative to the target grid point, i.e. r≥0.37, is determined in each direction, and the distance is calculated in km. Figure 6.5 and Figure 6.6 showed that r distributions are generally symmetric around the target grid cells. The four-directional computation of the scales in km confirms this symmetry in distance around the target point (plots not shown). The calculation of the averaged zonal (W-E) and average meridional (N-S) length scales at each point helps to comprehensively describe the spatial lengths of SSS variability over the Tropical/Subtropical Atlantic basin, and summarize the regions characterized by the longest characteristic scales in each case. Figure 6.7 shows the mean W-E and N-S length scales of monthly SSS mean in a range up to 2000 km. The zonal length scales along the basin are significantly longer compared to the meridional ones, demonstrating the anisotropic spatial scales of SSS in the region of interest. Figure 6.8 shows the same as Figure 6.7 bottom subplot, but with a shorter colourbar scale.

Overall, the longest mean W-E length scales lie on either side of the equator, at ∼5°-15°N and ∼3°-12°S (Figure 6.7, top). With lengths that reach up to ∼2660 km, homogeneous SSS changes along these bands span over more than half of the basin width (∼4300-4800 km and ∼4900-5700 km in the N. and S. Tropics, respectively). Figure 6.9 (left, red line) shows the zonal averages over the basin width, highlighting two pairs of maxima of similar magnitude and mirrored shapes on either side of the equator. The first pair of peaks, reaching over 2000 km, are centred at 6°N and 3°S, while the second pair reach ∼1700 km at 9°N and 6°S. Moreover, SSS displays large mean W-E length scales of ∼1500-1700 km in the eastern equatorial basin (∼3°N-4°S), including most of the Gulf of Guinea except for its northern part (Figure 6.7, top). In Figure 6.9 (right, red line), the meridionally averaged W-E length scales show a maximum at the central-eastern basin, around 15°W. In contrast, the western Equatorial Atlantic (∼5°N-2°S) shows much shorter zonal length scales that reach only up to ∼900 km, and even less than ∼600 km along the northern Brazilian coast (Figure 6.7).

In the N-S direction (Figure 6.7, bottom and Figure 6.8), the Tropical Atlantic and most of the rest basin 30°N-30°S is dominated by very short scales that do

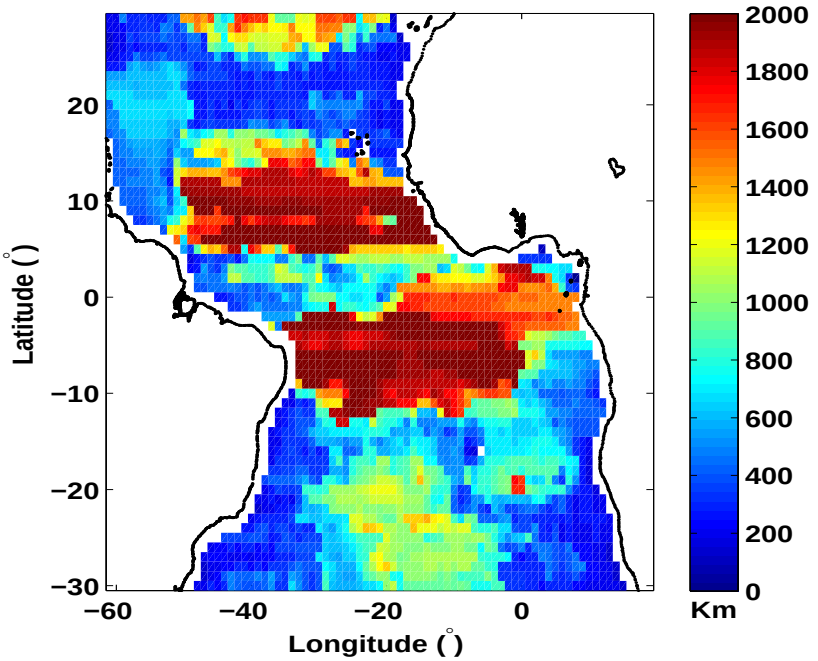

(a) Mean W-E length scales of SSS

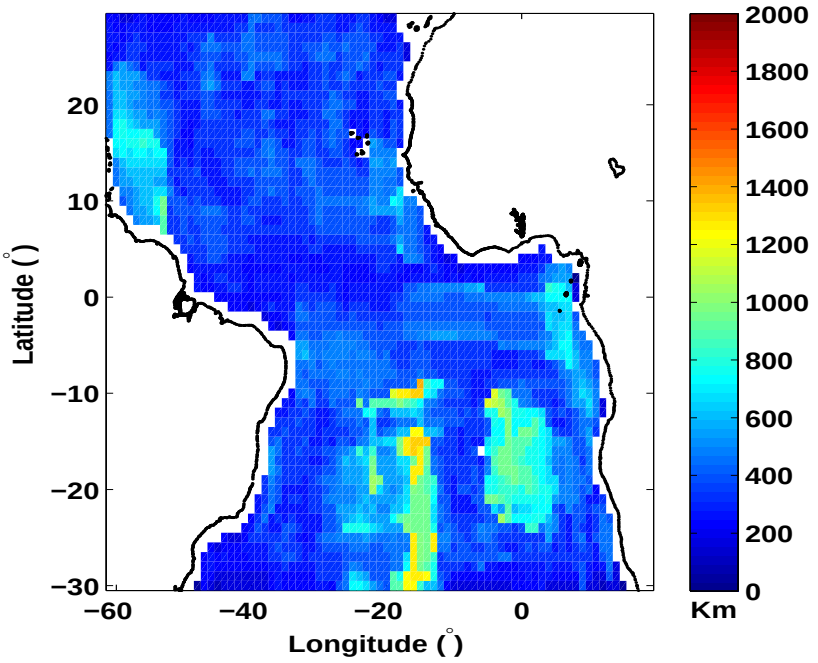

(b) Mean N-S length scales of SSS

Figure 6.7: Computed mean length scales (km) of SSS from SMOS in the a) W-E and b) N-S direction for a correlation coefficient $r \geq 0.37$, derived from the monthly mean SSS field.

not generally exceed ∼400 km. A band of noticeably shorter lengths under 300 km spans over the whole width of the equatorial basin between ∼0°-5°N, extending slightly southwards over the western basin. The zonal averages of the mean N-S length scales calculated over the basin width (Figure 6.9, left, blue line) display the overall minimum close to the equator at 3°N. An exception is seen in the eastern Equatorial Atlantic along the African coast between ∼3°-12°S, where the mean

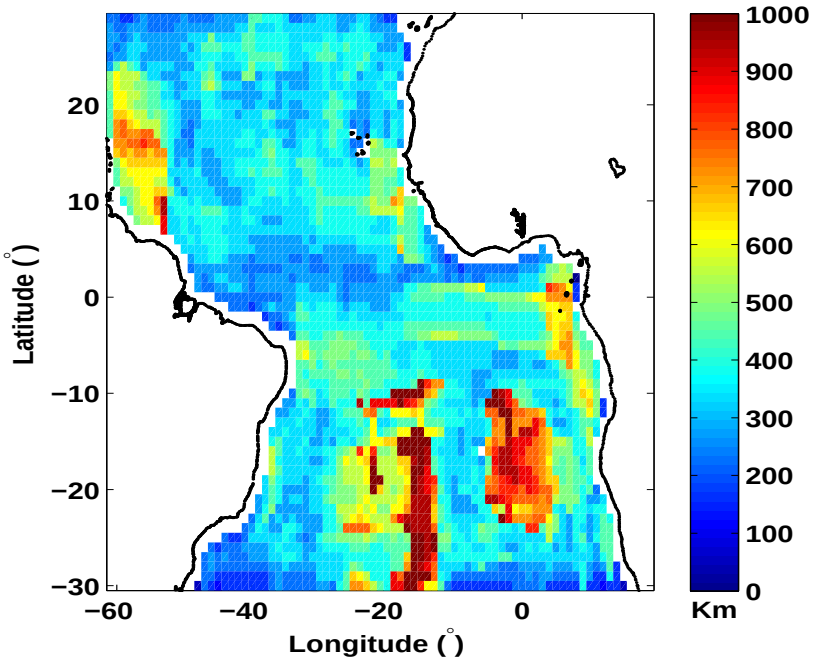

Figure 6.8: Computed mean length scales (km) of SSS in the N-S direction (same as in Figure 6.7, bottom) displayed in a shorter colourbar scale.

N-S length scales increase up to ∼600-700 km (Figure 6.8).

At the Subtropical latitudes, large mean W-E length scales are observed towards the centres of the Subtropical Gyres, reaching over ∼1200-1500 km and ∼1200-1400 km in the N. (25°-30°N) and S. (20°-30°S) Subtropical Atlantic, respectively

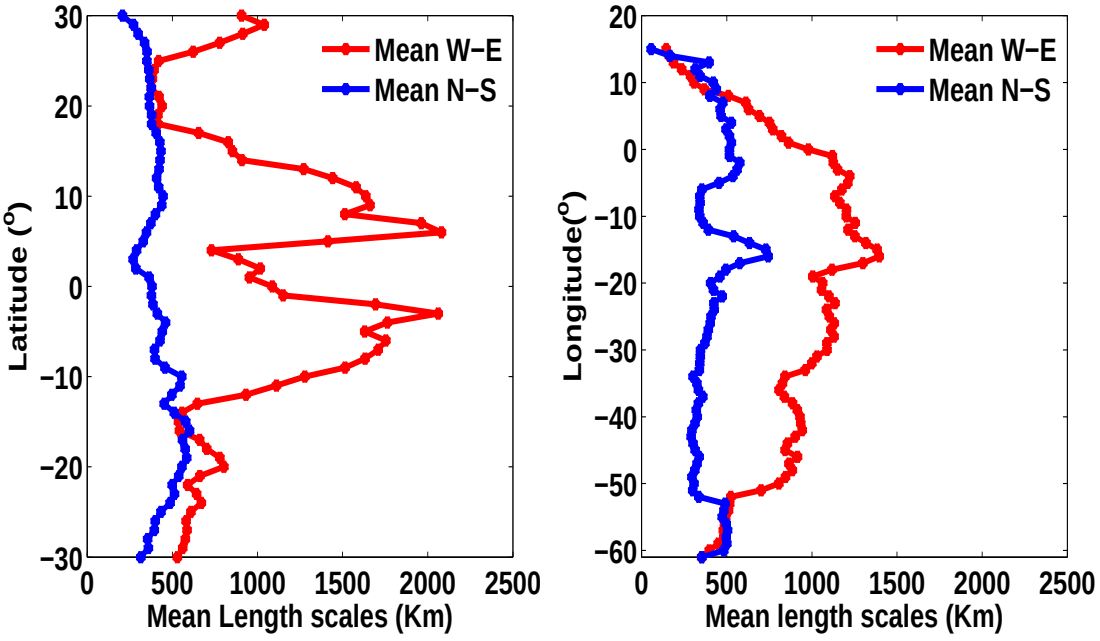

(a) Zonal averages

(b) Meridional averages

Figure 6.9: a) Zonal and b) meridional averages of the mean W-E (red) and N-S (blue) length scales (km) of monthly mean SSS. The zonal (meridional) mean at a given latitude (longitude) is taken across the width (length) of the basin.

(Figure 6.7, top). In addition, most of the S. Subtropical basin displays the largest, overall, mean N-S lengths of up to ∼1200-1300 km, particularly along two meridional bands at ∼15°W and ∼0°E (Figures 6.7, bottom, and 6.8). Relatively large characteristic scales, both in the W-E and N-S direction, are also seen in the northwestern basin between ∼8°-25°N, reaching up to ∼700-800 km. In accordance, the zonal averages of mean N-S length scales indicate slightly larger distances in the southern compared to the northern basin (Figure 6.9, left, blue line), while the meridional averages, both in the W-E and N-S direction, show maximum lengths at 15°W (Figure 6.9, right). Finally, over the rest of the basin and near the coasts, SSS has length scales of less than ∼500-600 km in both directions (Figure 6.7 and Figure 6.8).

6.3.2 Temporal scales of mean SSS from SMOS

Next, the analysis focuses on the time scales of SSS from SMOS with the aim to determine how quickly SSS varies over the Tropical/Subtropical Atlantic basin 30°N-30°S and identify regions where consistent SSS variations display the same level of persistence over time. For this, the interest is on the decorrelation time scales of SSS, i.e. the temporal length scales, which correspond to r greater or equal to the threshold ($r \geq 0.37$). Similarly to the assessment of the spatial SSS scales and given the dominance of the seasonal cycle on the SSS variability, the analysis is initially performed on the monthly SSS means(Section 6.3.2.1), and then on the SSS anomaly fields without the climatological seasonal cycle (Section 6.4.2).

6.3.2.1 Decorrelation time scales of SSS with the seasonal cycle included

Figure 6.10 shows the temporal decorrelation scale of the 3-year monthly mean time-series of SSS in each grid cell in the Atlantic basin 30°N-30°S. In general, SSS persists in time for up to ∼3-4 months over most of the basin. Shorter time scales of 2-3 months are observed in the western Equatorial basin and in parts of the Subtropics, particularly at the branches of the Subtropical Gyres. Elsewhere, SSS occasionally persists for up to 4 months, with the exception of a few "hotspots" along the African (∼25°N, ∼18°S and ∼25°S), and S. American (∼10°S and ∼25°S) coasts, where SSS persists for up to 5-6 months.

Figure 6.11 (left plot) displays the zonally averaged temporal scales of mean SSS. It confirms that SSS variations have the longest persistence in time (more than 3 months) in two bands in the northern and southern Tropical basin, around 9°N and 10°S. In contrast, close to the equator, SSS decorrelates faster in time by around 1 month, i.e. up to ∼2-3 months, while similar or shorter time scales also characterize most of the Subtropics. The meridionally averaged temporal scales (Figure 6.11, right) suggest the longest time scales at the African coast and the central longitudes, linked primarily to the "hotspots" mentioned previously.

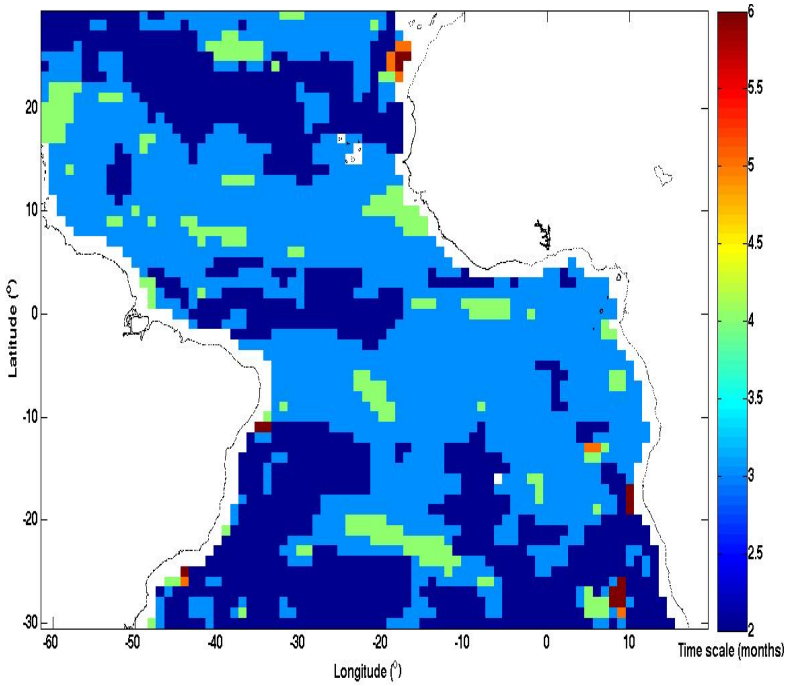

Figure 6.10: The temporal decorrelation scale of each grid cell for a correlation coefficient, r, greater or equal to the threshold 0.37 ($r \geq 0.37$), for the monthly SSS mean field.

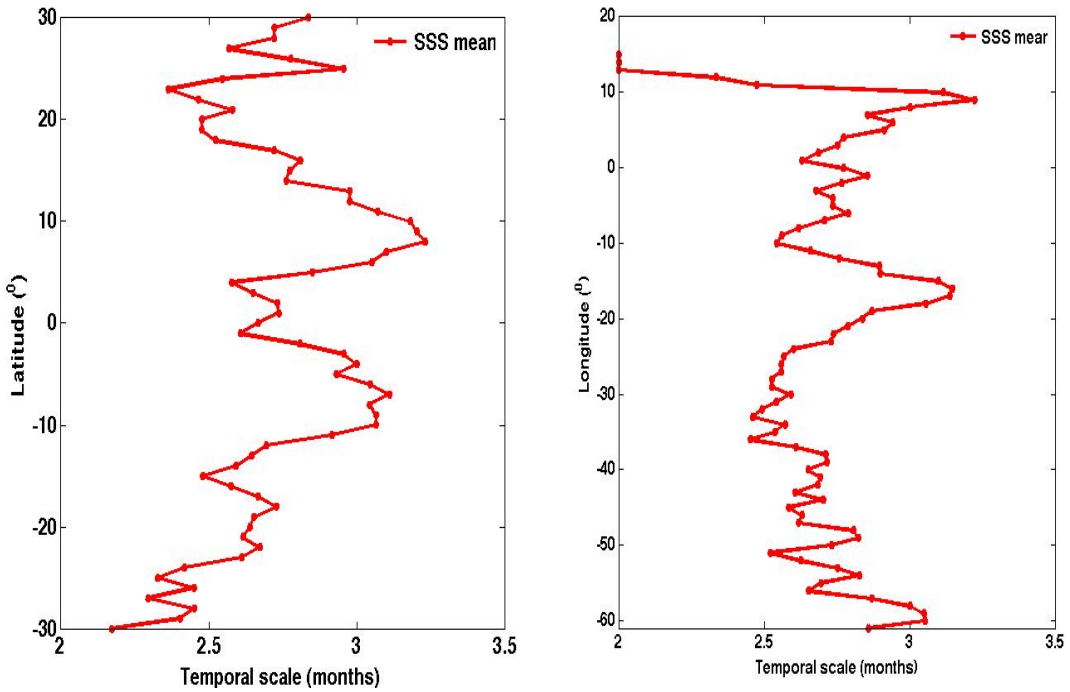

(a) Zonal Averages

(b) Meridional Averages

Figure 6.11: a) Zonal and b) meridional averages of the temporal decorrelation scales of mean SSS. The zonal (meridional) mean at a given latitude (longitude) is taken across the width (length) of the basin.

6.3.3 Summary and discussion of the spatio-temporal length scales of mean SSS

SSS from SMOS displays, in general, decorrelation time scales of up to 3-4 months and anisotropic spatial scales over the Tropical/Subtropical Atlantic basin 30°N-30°S, with typical lengths that exceed ∼2000 km in the W-E, and up to ∼1000

km in the N-S direction. SSS shows homogeneous zonal spatial variations over considerably larger distances particularly along two bands north and south of the equator (centred at 6°N and 3°S, respectively), which extend over the whole oceanic basin. In accordance, averaged zonally, SSS has the longest persistence exceeding 3 months along these bands, particularly north of the equator, which primarily encompasses the seasonal influence of the ITCZ across the equator, and thus of maximum P patterns. Moreover, horizontal advection, mainly driven by the North (NEC) and South Equatorial Currents (SEC) whose flow paths generally lie along these bands, may also contribute to the consistent SSS changes there.

In contrast, along the equator, the characteristic scales of SSS are noticeably shorter both in space (up to ∼600 km and 400 km in the W-E and N-S direction, respectively) and time (up to ∼2-3 months), likely due to the combined effect of convectional Equatorial P patterns, advection along the North Equatorial Counter Current (NECC) and equatorial upwelling. This is particularly evident in the central and western equatorial basin between ∼5°N-2°S, as well as close to the Amazon/Orinoco river system, where SSS displays short spatial scales that do not generally exceed ∼600 km in the zonal and ∼300 km in the meridional direction. The dynamic conditions in the latter region resulting from the integrated effect of variations in freshwater fluxes and the strong interaction of the Amazon/Orinoco plume with the surface circulation, such as the North Brazilian Current and the NECC, probably prohibit homogeneous SSS variations over large distances. Similarly, SSS changes have a short persistence in time of ∼2-3 months along the central and western equatorial basin. However, close to the Amazon river mouth, SSS variations persist for up to 4 months, likely indicating the amplitude of the riverine seasonal cycle and the relatively constant influence of freshwater discharge over such long periods.

Likewise, SSS changes close to the Congo river mouth show a similar time persistence of up to 4 months, and up to ∼3 months over the rest of the Gulf of Guinea. Spatial SSS changes at the eastern equatorial basin and the Gulf of Guinea (with the exception of its northern part) display long zonal lengths of ∼1500 km or more, driven potentially by horizontal advection from the regional circulation, including the eastward-flowing NECC. In this region, meridional SSS variations also occur homogeneously over large distances that can exceed 700 km. The two river-influenced regions opposite of the basin display strong spatial anti-correlated signals (see for instance, Figures 6.1 and 6.3), clearly demonstrating the opposite SSS seasonal cycle in these two regions of strong variability, as shown previously in Chapters 4 and 5, and *Tzortzi et al.*, 2013.

In the Subtropics, the largest zonal spatial scales of up to ∼1500 km are found towards the centres of both Subtropical Gyres and the SSS maximum regions. There, SSS changes also display a longer stability over time of up to 4 months, due to the slower advection and mixing processes. In contrast, the decorrelation

time lengths of SSS do not generally exceed ∼2-3 months along the branches of the Subtropical Gyres. Over the rest Subtropical basin, SSS variations also display noticeably shorter spatial length scales, reaching only 300 km towards its boundaries. In the N. Subtropical Atlantic, an exception occurs at the western basin around ∼20°N, where SSS changes persist for up to ∼3-4 months locally. At this side of the basin between ∼10°-20°N, and thus close to the Antilles Current and Caribbean Counter-current, SSS also shows homogeneous spatial variations over relatively large distances both in the zonal and meridional direction. In the S. Subtropics, in addition to long zonal lengths at the central basin, SSS displays the largest, overall, meridional spatial scales, particularly along the bands centred at ∼15°W and ∼0°E, which extend up to ∼10°S. Furthermore, relatively large meridional length scales are observed along the S. African and parts of the S. American coasts, likely attributed to the South Hemisphere (S.H.) Boundary Currents (BCs) and the associated coastal upwelling.

6.4 Scales of SMOS SSS anomalies without the seasonal cycle

6.4.1 Spatial scales of SSS anomalies

Given the dominance of the seasonal cycle on the spatial characteristic scales of SSS variability in the Tropical/Subtropical Atlantic, next, the analysis focuses on the spatial length scales of SSS anomalies in the region, after the 3-year climatological seasonal cycle from SMOS has been removed. Figure 6.12 shows the r map of SSS anomalies corresponding to the target Point A in the S. Subtropical basin, shown in Figure 6.1 for the SSS mean field. The removal of the seasonal cycle results in significantly different spatial maps of correlation patterns with less coherent signals. SSS can be only locally strongly -positively/negatively- correlated around the target grid cell, as seen in Figure 6.12 for Point A, compared to the pronounced features dominating the whole basin width for the mean SSS (Figure 6.1). The time-series and scatterplot of SSS anomalies at Point A and Point B lying north of the equator, also suggest that the observed coherent SSS behaviour at the two locations is no longer evident and SSS changes at the two locations appear uncorrelated (Figure 6.13 as compared to Figure 6.2).

Nevertheless, in many cases, the spatial correlations of SSS anomalies still indicate long characteristic scales that extend across the basin width, e.g. in the S. Tropics, as seen in Figure 6.14, which displays r for the target Point C with the rest of the basin (relative to Figure 6.3). The corresponding SSS anomaly time-series in Figure 6.15 confirm these large departures, while indicating an out-of-phase SSS behaviour between the Point C and Point D over most of the 3 years and

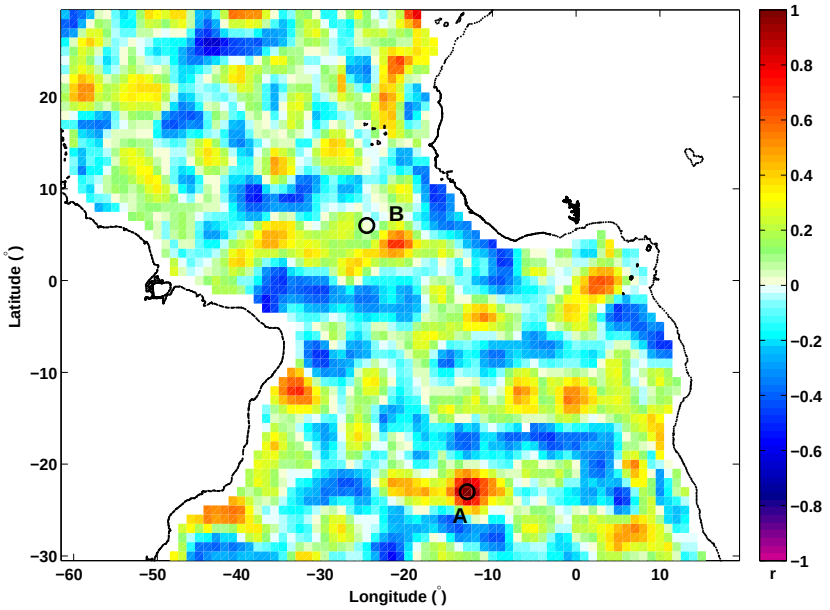

Figure 6.12: The correlation coefficient, r, of the 3-year time-series (2010-2012) of SMOS SSS anomalies between the target Point A in the Southern Subtropical Atlantic at 23°S 13°W (indicated by the black circle) and the rest of the Atlantic basin 30°N-30°S. Also shown is Point B at 6°N 25°W.

no correlation between the SSS anomalies at the two points (even when the two outliers are removed).

6.4.1.1 Spatial distributions of correlation coefficient, r, of SSS anomalies

Figures 6.16 and 6.17 show the distribution of the correlation coefficient, r, for various target grid cells at specific latitudes and longitudes, obtained for the SSS anomaly fields. The removal of the seasonal cycle results in a substantial decrease of the spatial scales of SSS across most of the basin. This is particularly evident in the zonal changes of r (Figure 6.16 versus Figure 6.5 for mean SSS) as compared to the meridional (Figure 6.17 versus Figure 6.6 for mean SSS). The most pronounced differences occur in the Tropical bands between 10°N and 10°S, where lengths are typically decreased by ∼2/3 on either side of the equator, and up to half over most of the Subtropics, reaching up to ∼500 km in both cases. For instance, at 10°N and at the equator (Figure 6.16, e and g), r falls quickly below the threshold 0.37 within a short distance from the target grid cell, even in cases where the correlations of mean SSS indicated long zonal length scales that extended up to the coast (see Figure 6.5). On the other hand, contrary to SSS, the zonal scales of SSS anomalies are slightly longer at the equator than north and south of it, i.e. ∼700 km as compared to less than ∼500 km (Figure 6.16, e and f). Finally, the removal of the seasonal cycle does not generally modify the meridional r distribution of SSS anomalies (Figure 6.17 as compared to Figure 6.6 for mean SSS), except for a decrease in the S. Subtropical central basin (Figure 6.17, c, cyans lines, as compared to Figure 6.6, c).

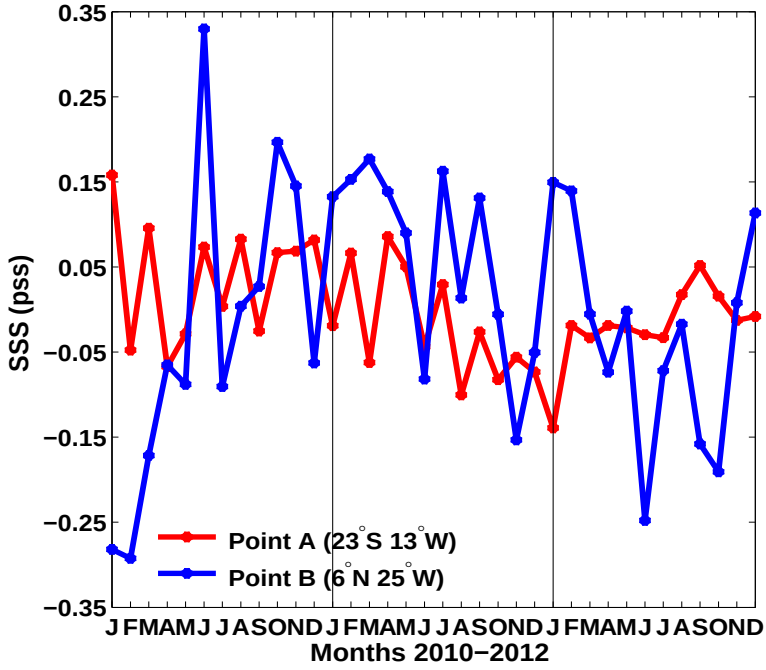

(a) Time-series of SSS anomalies at Points A and B

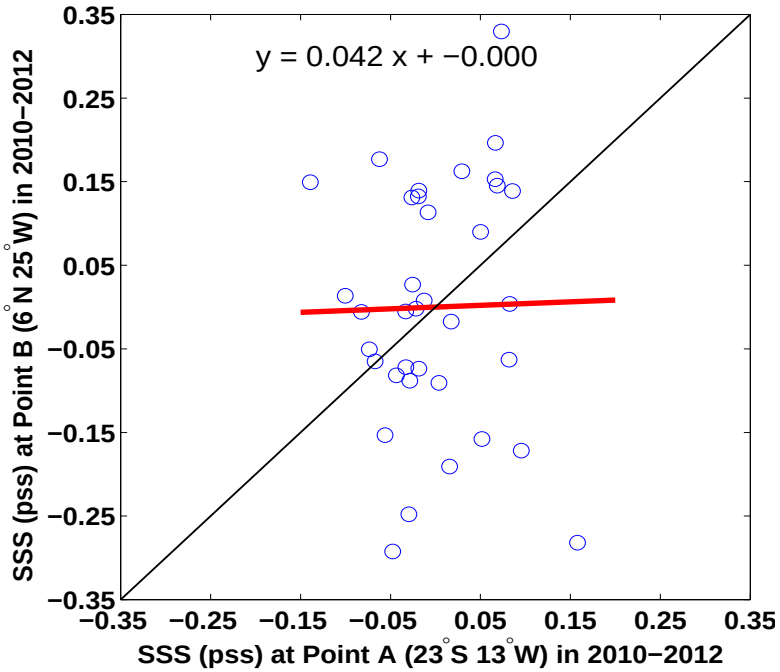

(b) Scatterplot of SSS anomalies at Points A and B

Figure 6.13: As for Figure 6.2, but based on the monthly SSS anomaly field without the climatological seasonal cycle: a) the time-series and b) scatterplot of SSS anomalies at the target Point A (23°S 13°W) versus the strongly correlated Point B (6°N 25°W), seen in Figures 6.1 and 6.2.

6.4.1.2 Spatial length scales (in km) of SSS anomalies

To summarize the regions with the longest spatial characteristic scales of SSS anomalies and enable a direct comparison with the zonal and meridional length scales of mean SSS (Figures 6.7 and 6.8), Figure 6.18 shows the averaged W-E and

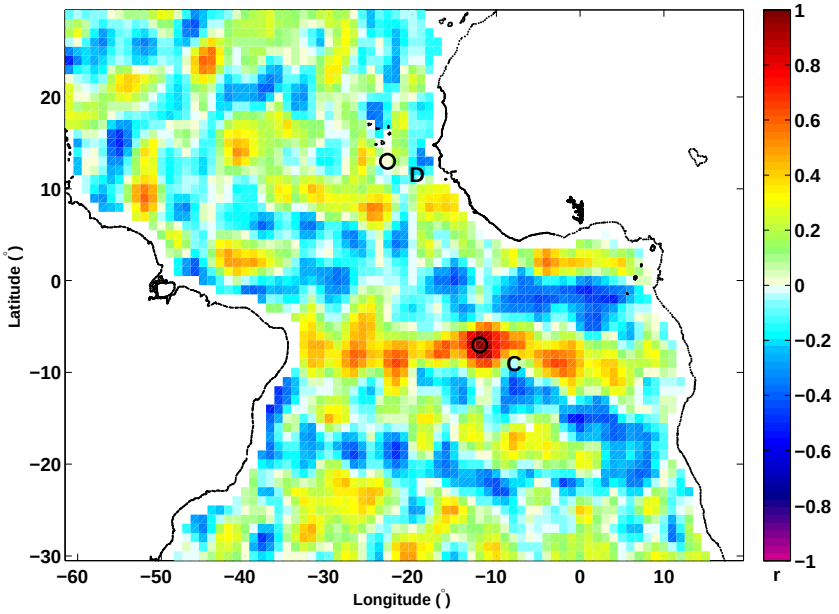

Figure 6.14: The correlation coefficient, r, of the 3-year time series (2010-2012) of SMOS SSS anomalies between the target Point C (7°S 12°W) in the central S. Tropical Atlantic (indicated by the black circle) away from river influence, and the rest of the Atlantic basin 30°N-30°S. Also shown is Point D (13°N 23°W).

N-S length scales for the SSS anomaly field. In addition, Figure 6.19 shows the same as Figure 6.18, bottom subplot, in a shorter colourbar scale. A decrease by ∼1000 km, i.e. about 38% of their maximum magnitude, is evident in the mean zonal length scales of SSS anomalies (Figure 6.18, top) compared to those for SSS (Figure 6.7, top), although there is still some coherence spanning the width of the basin (Figure 6.18, top). Generally shorter than the zonal lengths, the mean N-S length scales of SSS anomalies show a reduction of more than ∼60% relative to SSS (Figure 6.18, bottom as compared to Figures 6.7, bottom and 6.8).

The longest zonal length scales reach up to ∼1660 km and are located on either side of the equator at 4°-5°N and 3°-8°S, respectively (Figure 6.18, top). Averaged zonally across the basin (Figure 6.20, left, red line), there is a clear maximum in the zonal scales of more than 700 km at 8°S. This is in contrast to the symmetric double peaks seen for SSS (Figure 6.9, left, red line). The rest of the basin displays some smaller features with relatively long zonal scales, particularly in the eastern basin slightly south of the equator, and at the central N. and S. Subtropical regions (∼12°-17°N and ∼20°-28°S), (Figure 6.18). The meridionally averaged W-E scales indicate similar lengths of around 350 km over the whole basin (Figure 6.20, right, red line).

The meridional (N-S) spatial scales of SSS anomalies (Figures 6.18, bottom, and 6.19 shown in a smaller colourbar scale), indicate much shorter lengths than the zonal scales, and do not generally exceed ∼350 km. This is also apparent in their zonal averages, which show a very small variation across the whole basin (Figure 6.20, left, blue line). Some larger N-S length scales (up to ∼600 km) are

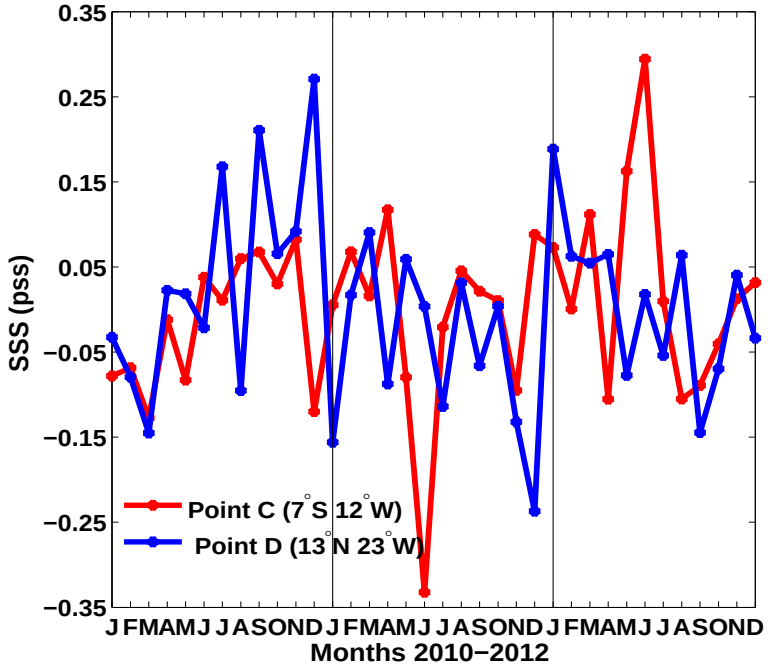

(a) Time-series of SSS anomalies at Points C and D

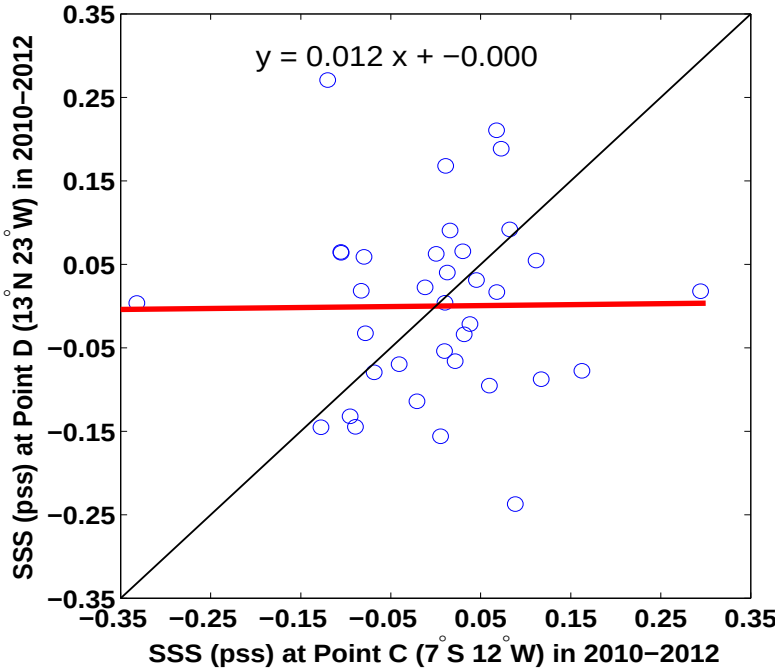

(b) Scatterplot of SSS anomalies at Points C and D

Figure 6.15: As for Figure 6.4, but based on the monthly SSS anomalies without the climatological seasonal cycle: a) the time-series and b) scatterplot of SSS anomalies at the target Point C (7°S 12°W) versus the strongly anti-correlated Point D (13°N 23°W).

found along the S. Brazilian and S. African coasts (Figure 6.19), which are also depicted in the meridional averages (Figure 6.20, right, blue line), as a peak at 14°E.

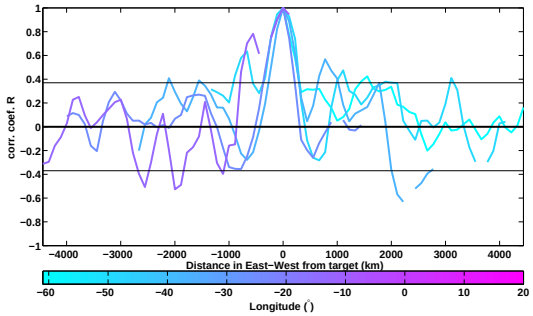

(a) 30°N

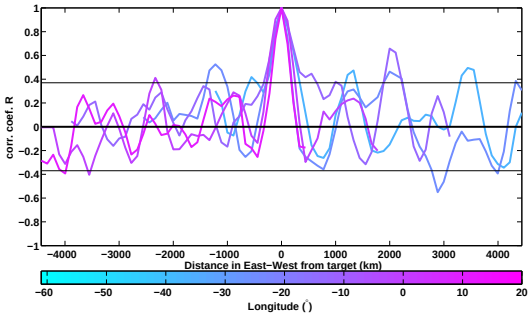

(b) 30°S

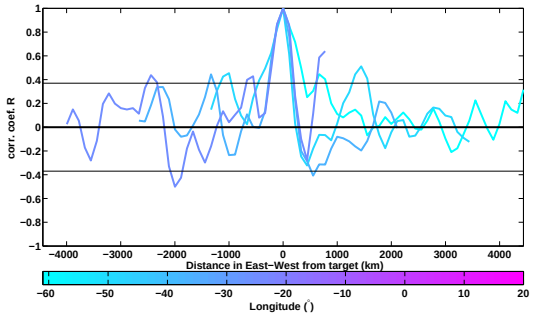

(c) 20°N

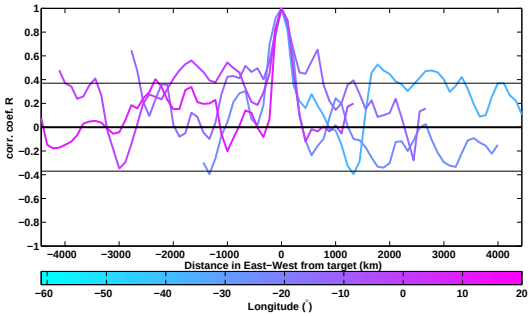

(d) 20°S

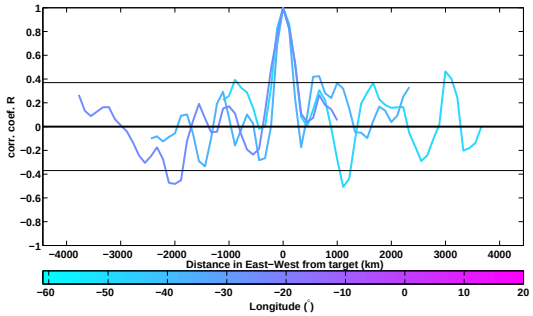

(e) 10°N

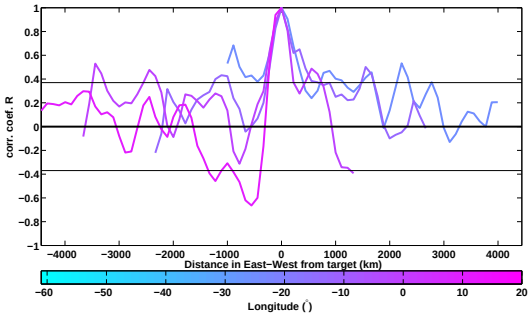

(f) 10°S

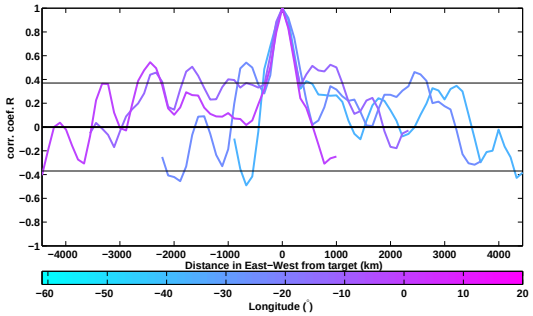

(g) Equator

Figure 6.16: Distributions of the correlation coefficient (r) in W-E direction of the 3-year SMOS SSS anomaly time-series between each grid cell (target) and the rest of basin. The distributions, centred at the target grid cell where r=1, are shown for specific latitudes between 30°N-30°S with a zonal step of 10° along the basin width 61°W-20°E with a meridional step of 12°. Longitudes are shown by the colourbar, while thin black lines indicate a threshold of ±0.37. Distributions are displayed for a) 30°N, b) 30°S, c) 20°N, d) 20°S, e) 10°N, f) 10°S and g) the equator.

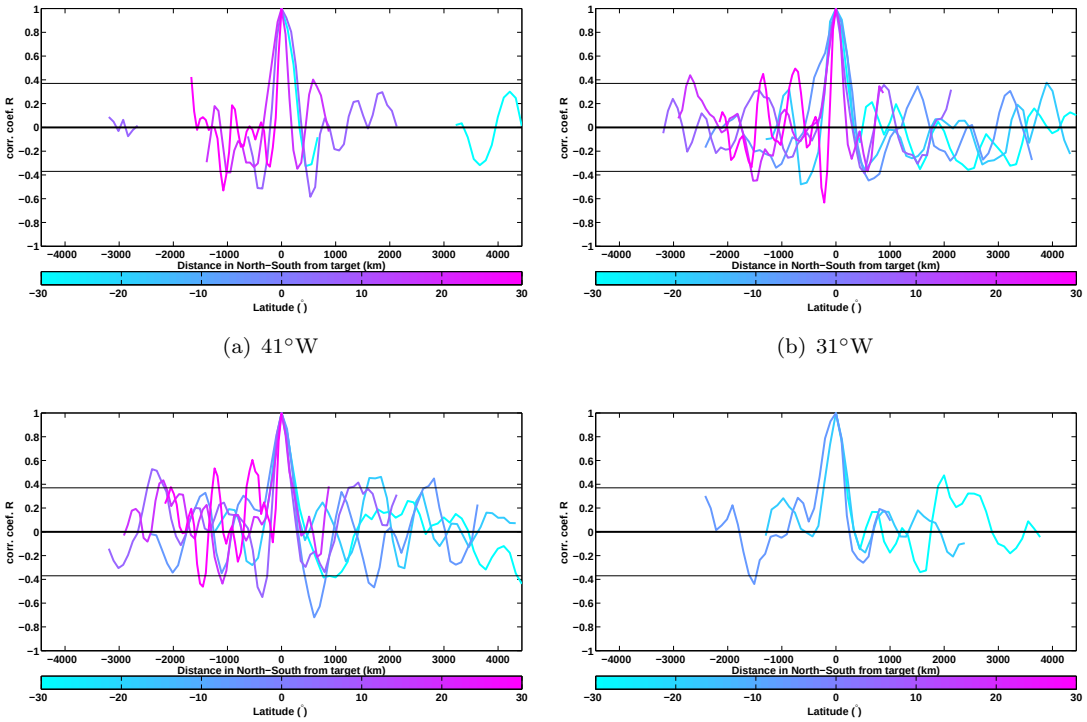

(a) 41°W (b) 31°W

(c) 21°W (d) 11°W

Figure 6.17: Distributions of the correlation coefficient (r) in the N-S direction of the 3-year SMOS SSS anomaly time-series at the longitudes a) 41°W, b) 31°W, c) 21°W, and d) 11°W along the length of the Atlantic basin 30°N-30°S with a latitude step of 12°. Latitudes are shown by the colourbar. Thin black lines indicate a threshold of ±0.37.

6.4.2 Decorrelation time scales of SSS anomalies

Figure 6.21 shows the spatial distribution of the temporal decorrelation scales for the SSS anomaly field, while Figure 6.22 displays it in a shorter colourbar scale for clarity and to enable also a direct comparison with Figure 6.10 for the mean SSS. Figure 6.23 shows the difference between Figure 6.10 for the mean SSS and Figure 6.21. The removal of the 3-year climatological seasonal cycle results in a reduction of the decorrelation time scales, with SSS anomalies persisting only up to ∼2.5 months over most of the basin (Figures 6.21 and 6.22). The largest decreases are seen along the two bands in the N. and S. Tropics, and towards the centres of the Subtropical Gyres (Figure 6.23). Longer time scales of ∼3-4 months are occasionally observed, but without showing spatially coherent patterns, with the exception of the branches of the N. Subtropical Gyre and a band centred at ∼10°S extending along the basin width (Figures 6.21 and 6.22). The localized "hotspots" along the African and S. American coasts last noticeably longer and can persist up to 9 months.

Averaged zonally (Figure 6.24, left, blue line), the time scales of the SSS anomalies clearly show a sharp decrease from those seen for the SSS mean (red line) in some latitude bands. More specifically, the northern and southern Tropics display now

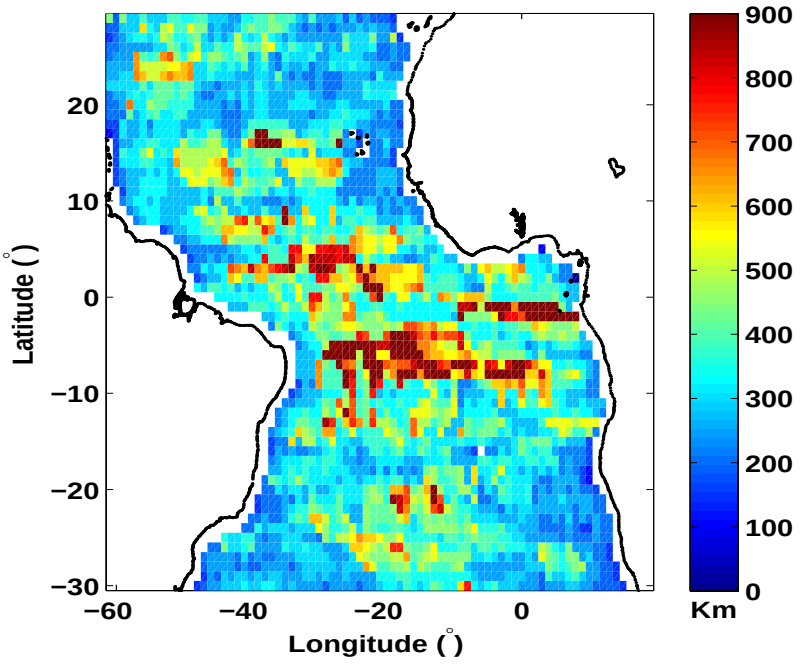

(a) Mean W-E length scales of SSS anomalies

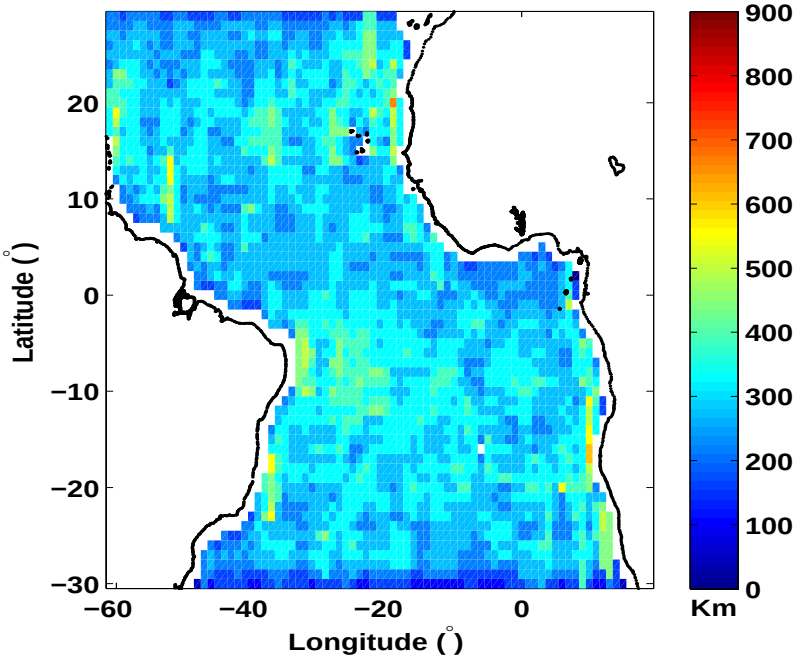

(b) Mean N-S length scales of SSS anomalies

Figure 6.18: Mean length scales (km) of SSS in the W-E (top) and N-S (bottom) direction for a correlation coefficient $r \geq 0.37$ derived from the anomaly SSS field without the climatological seasonal cycle.

the fastest SSS anomalies, that generally persist over only 2 months, in accordance with most of the rest basin. SSS shows the longest persistence in time slightly north of the equator and between ∼13-15°S. More interestingly, there are latitudes where the exclusion of the seasonal cycle does not alter the time scales of SSS, as for instance, at the equator, between 18°-24°N and 23°-30°S (Figure 6.24, left, blue and red lines), as also seen in Figure 6.23. In contrast, the meridionally averaged

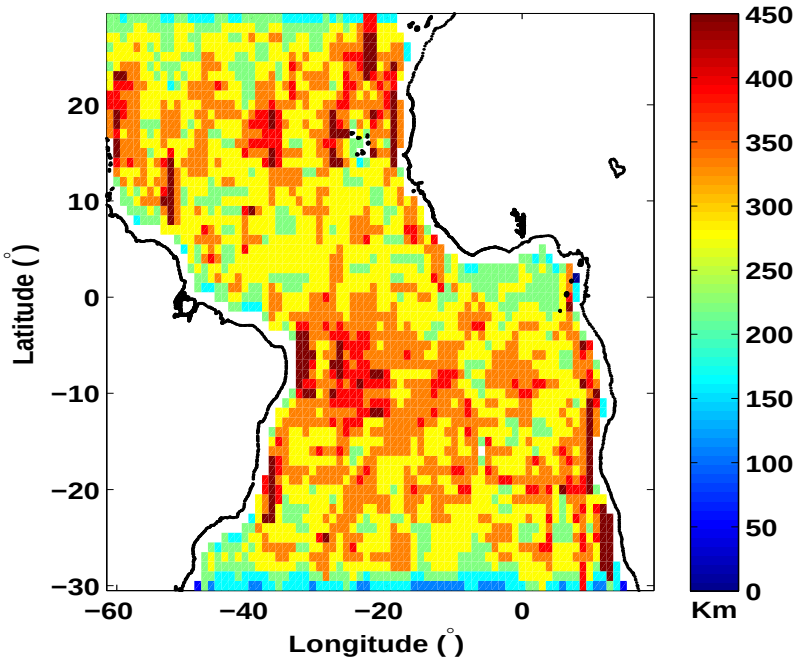

Figure 6.19: Mean length scales (km) of SSS anomalies in the N-S direction (same as in Figure 6.18), shown in a shorter colourbar scale.

temporal scales of SSS anomalies (Figure 6.24, right, blue line compared to red line for mean SSS) indicate no significant impact of the removal of the seasonal cycle, other than a decrease of about half month at all longitudes.

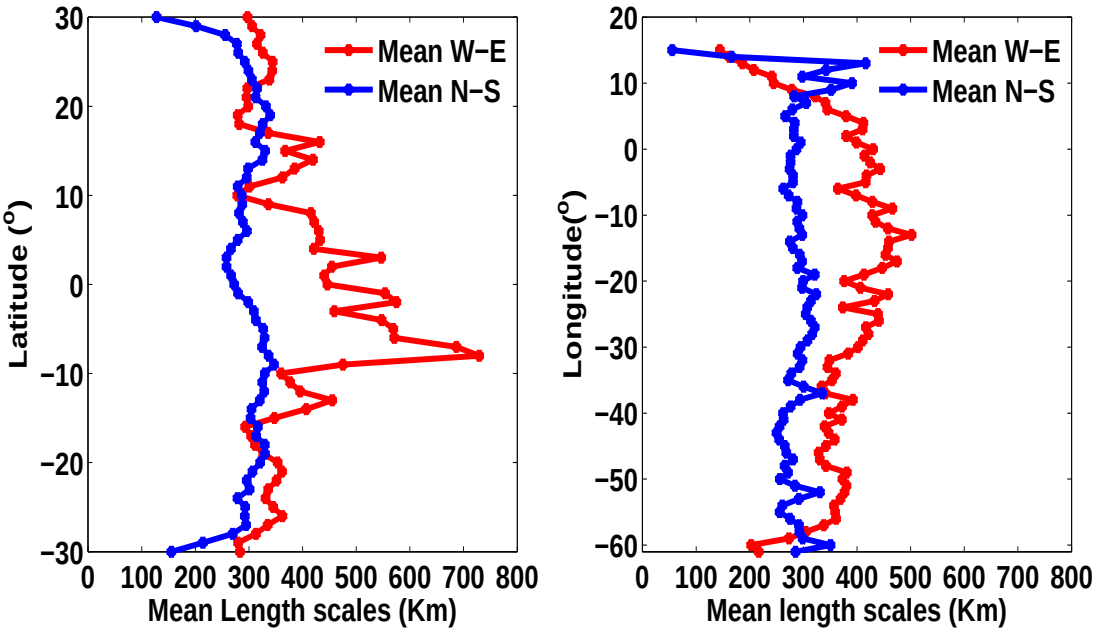

(a) Zonal averages

(b) Meridional averages

Figure 6.20: a) Zonal and b) meridional averages of the mean W-E (red) and N-S (blue) length scales (km) for the SSS anomalies. The zonal (meridional) mean at a given latitude (longitude) is taken across the width (length) of the basin.

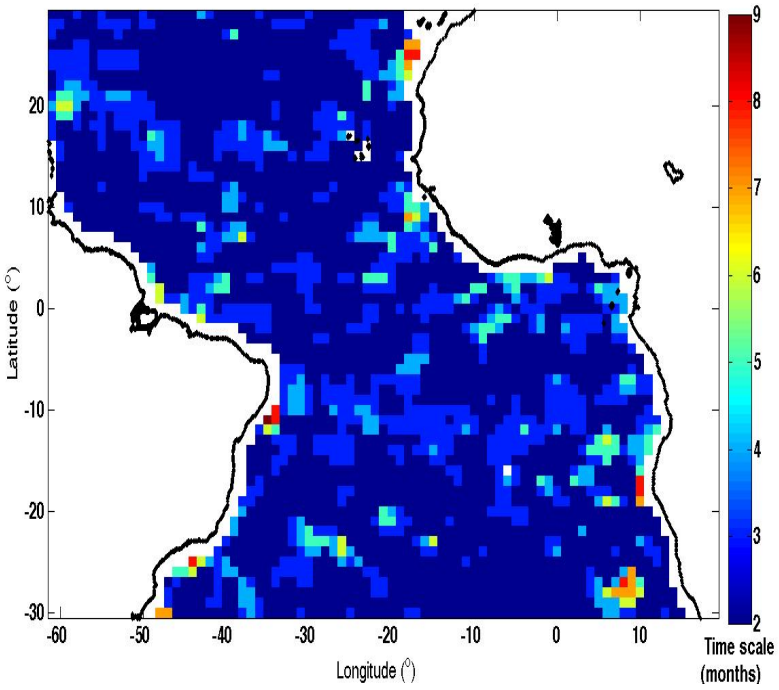

Figure 6.21: The temporal decorrelation scale of each grid cell when the correlation coefficient, r, greater or equal to the threshold 0.37 ($r \geq 0.37$), for the SSS anomaly field.

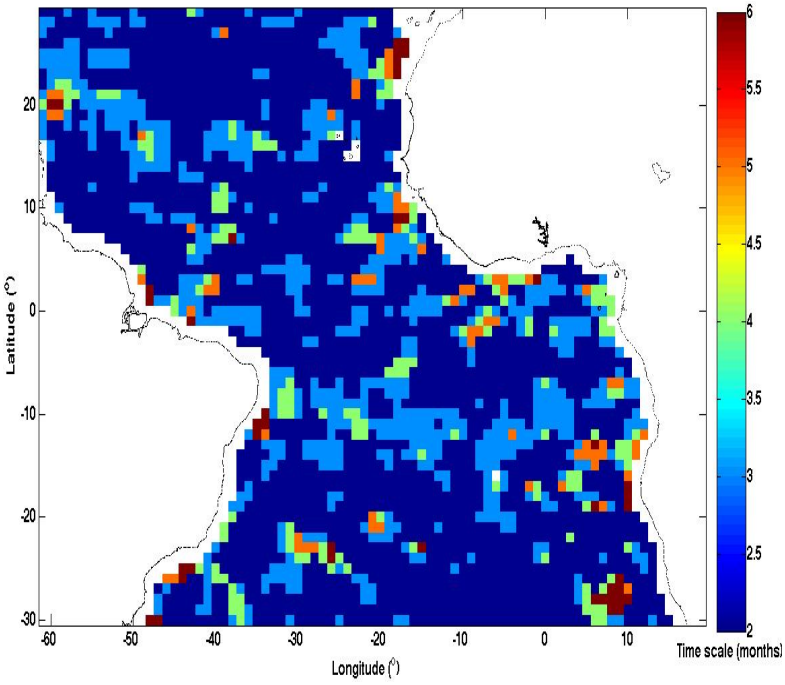

Figure 6.22: Same as in Figure 6.21, but in a shorter colourbar scale for clarity and to enable a direct comparison with Figure 6.10 for the mean SSS field.

6.4.3 Summary and discussion of the spatio-temporal length scales of SSS anomalies

Decorrelation spatial lengths of SSS anomalies over the Atlantic basin 30°N-30°S are characterized by anisotropic scales in the W-E and N-S direction, in agreement with mean SSS. The characteristic scales of SSS anomalies are substantially

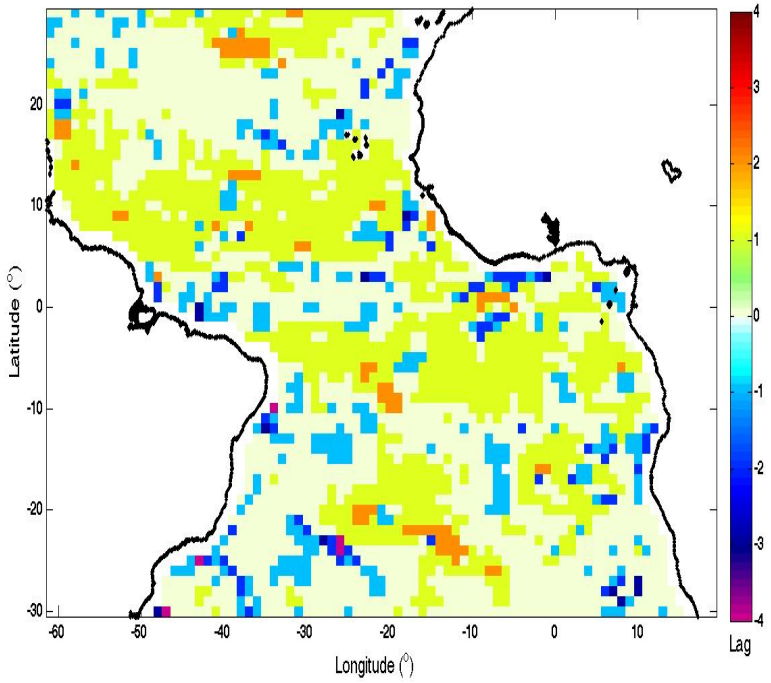

Figure 6.23: The difference of temporal decorrelation scale in each grid cell for the monthly mean (Figure 6.10) minus the SSS anomaly field (Figure 6.21).

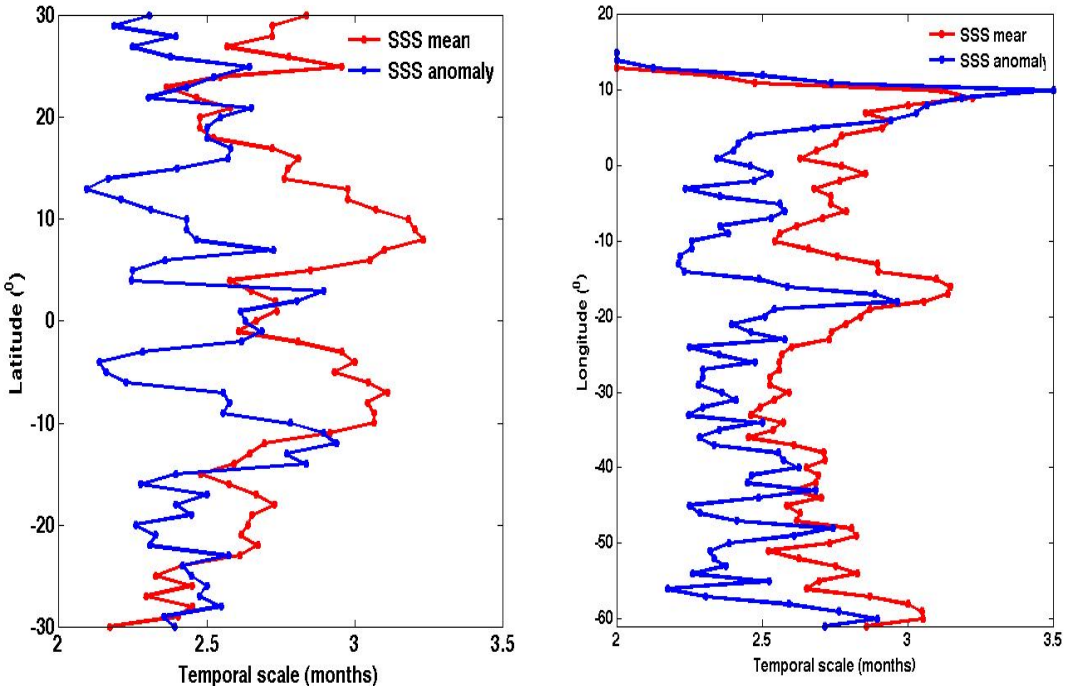

(a) Zonal Averages

(b) Meridional Averages

Figure 6.24: a) Zonal and b) meridional averages of the temporal decorrelation scales of SSS anomalies (blue lines). In addition, the corresponding lines for the SSS mean (red lines) are included for comparison (as shown in Figure 6.11). The zonal (meridional) mean at a given latitude (longitude) is taken across the width (length) of the basin.

shorter across most of the basin compared to SSS, by 38% in the zonal and 62%

in the meridional direction, reaching up to ∼1660 km (W-E) and ∼500 km (N-S),respectively. Similarly, the time persistence of SSS anomalies is generally reduced by about half month, persisting up to ∼2-3 months over most of the region of interest. The most noticeable reduction in the W-E scales is observed in the Tropical Atlantic bands north and south of the equator, which embody the seasonal variation of the ITCZ movement during the year, as well as the seasonal variability of the ocean currents. Nevertheless, after the removal of the seasonal cycle, zonal length scales of SSS anomalies of up to ∼900 km still continue to dominate in these northern and southern equatorial bands, spanning most of the basin width. These spatial patterns of SSS anomalies likely reflect large scale processes that remain stable over interannual scales and are probably linked to horizontal advection from the mean surface circulation. In the N-S direction, the spatial lengths of SSS anomalies along the two bands reach up to ∼350 km, particularly towards the western basin.

Along the equator, the temporal scales of SSS changes continue to be preserved for more than ∼2-3 months, regardless of the exclusion of SSS seasonal cycle or not. The combined effect of the different controlling mechanisms acting in this region, primarily the seasonal ITCZ influence, advection (seasonal and anomalous) by the current circulation, especially the NECC, and equatorial upwelling, likely results to these constant decorrelation time lengths of SSS on subannual to interannual time periods. On the other hand, excluding the effect of the seasonality of P patterns (both over the ocean and on land), and thus of river discharge, as well as of the seasonal advection, SSS anomaly changes occur homogeneously over shorter distances close to the major river systems of Amazon/Orinoco, and particularly Congo/Niger in the eastern basin. The zonal length scales of SSS anomalies generally span up to ∼400 km in both river regions, but can reach up to 900 km in the Gulf of Guinea along the band 1°-2°S. Their meridional lengths do not generally exceed ∼300 km, with the exception of slightly longer distances along ∼5°E in the eastern basin. In contrast, the removal of the seasonal cycle increases the time scales of SSS anomalies by about 1 month close to the Amazon and Congo river mouths.

In the Subtropics, the spatial decorrelation scales of SSS anomalies indicate less pronounced features, which however, persist over long time lengths of up to 3-4 months, especially along the southern and northern branches of the N. and S. Subtropical Gyres, respectively. The enhanced persistence in time of SSS anomalies relative to SSS by ∼1 month, likely indicates the impact of seasonal variability of the surface current circulation which forces quicker changes of the mean SSS. Zonally averaged, the decorrelation time scales of SSS anomalies display an opposite latitudinal pattern compared to SSS over most of the basin. On the other hand, the removal of the seasonal cycle does not alter the times scales of SSS close to the centres of the Subtropical Gyres between 18°-24°N and 23°-30°S, that encompass the SSS maxima. Thus, the expected small variations of SSS there have, in

general, a constant persistence in time of ∼2-3 months, both throughout the year and from one year to the next. In accordance, SSS anomalies at the S. Subtropical Atlantic display long zonal spatial scales of up to ∼700 km over the central basin and towards the centre of the S. Subtropical Gyre. Similar lengths are also seen in the western N. Subtropical basin at 25°N and along its southern central part at ∼15°N, potentially pointing to the role of mean circulation by the southern branches of the N. Subtropical Gyre, including the NEC.

Advection seems to also play an important role in the N-S direction, as homogeneous SSS anomaly changes with large meridional lengths of up to ∼450 km occur along the coasts of mainly the S.H, primarily controlled by the BCs and coastal upwelling. Similarly, the long meridional scales of SSS anomalies at the central northern basin likely indicate the role of mean advection by the different branches of the N. Subtropical Gyre, while shorter lengths of up to ∼300-350 km dominate most of the rest Subtropical latitudes. Finally, long temporal lengths of more than 5 and up to 9 months characterize localized SSS anomaly changes over most of the basin, particularly towards the coasts of the BCs. These decorrelation time scales may suggest the presence of very slow processes, such as stationary eddies (H. Bryden, 2014, *personal communication*), on SSS variations there, and thus their long maintenance over time, but do not exclude the possibility of an artefact in the data, given that SMOS uncertainty increases closer to the coasts (*Reul et al.*, 2012b).

6.5 Final discussion and conclusions

Taking advantage of the better coverage of satellite SSS observations, this novel work explores the spatio-temporal scales of SSS variations from SMOS in the Tropical/Subtropical Atlantic 30°N-30°S. SMOS reveals different SSS characteristic scales at different latitudes and longitudes, pointing to the influence of various controlling mechanisms on the SSS changes over the different regions of the basin (given that the dependence of a variable can arise both from itself and the factors that influence it, e.g. *Dale and Fortin*, 2009). On subannual to interannual time scales, the spatial characteristic lengths of SSS are anisotropic, i.e. the zonal (W-E) lengths are significantly longer compared to the meridional (N-S) ones, reaching up to ∼2660 km and ∼1300 km for SSS and ∼1660 km and ∼500 km for the SSS anomalies, respectively. Consistent SSS changes generally persist up to 2-4 months over most of the Tropical/Subtropical Atlantic, while only up to ∼2-3 months for the SSS anomalies.

Subannual to interannual SSS variations display the longest spatial zonal scales along two Tropical Atlantic bands on either side of the equator, which are also characterized by the longest temporal decorrelation lengths (exceeding 3 months), particularly in the north. SSS changes in these two bands are primarily governed

by seasonal variations in P (and secondarily of changes in E-P) driven by the ITCZ migration, which actually remained mainly north or at the equator during the examined years 2010-2012 (See, for instance, Chapter 5, Figure 5.3 displaying zonal averages of P and E-P across the basin width for January and July 2010-2012). Moreover, advection (seasonal and anomalous), associated with variability in the equatorial currents (e.g. *Foltz et al.*, 2004; *Vinogradova and Ponte*, 2013), including the NEC and SEC flowing on opposite sides of the equator, represents the other major controlling mechanism contributing to the long characteristic scales of SSS there.

The main component of Tropical advection is the seasonal Ekman transport, although strong geostrophic components dominating the zonal velocity are also found in proximity to the zonal currents along the basin, particularly north of the equator (*Yu*, 2011). Nevertheless, the removal of the seasonal cycle still reveals long spatial lengths of SSS anomalies along these bands, which, however, occur faster by more than half month, i.e. up to ∼2-3 months, compared to mean SSS. This highlights the predominant role of advection from the mean circulation on longer time scales compared to freshwater fluxes, while indicating that the zonal ITCZ influence mainly acts to increase both the zonal spatial and temporal length scales of SSS. In accordance, previous studies suggest the more important impact of anomalous Ekman advection in generating interannual SSS changes (*Mignot and Frankignoul*, 2003), in addition to the geostrophic components (*Mignot*, 2004).

In contrast, along the equator, subannual to interannual SSS changes display shorter spatial lengths and have less persistence in time, i.e. of ∼2-3 months, particularly towards the western and central basin. In addition to receiving large freshwater amounts due to the seasonal ITCZ presence and convectional equatorial P events, this region is also dominated by advection, particularly from the NECC, which is associated with the largest seasonal variability in the Tropics (*Yu*, 2011) and relatively strong W-E salinity gradients (*Donguy and Meyers*, 1996). Likewise, equatorial upwelling, displaced generally westwards at the Equatorial Atlantic (*Zebiak*, 1993) and being strongest during late boreal spring and early summer (*Keenlyside and Latif*, 2007), may force SSS to vary faster in time and over shorter distances. Interestingly, the longer meridional length scales of SSS anomalies occur at the equator than north/south of it compared to SSS, likely pointing to salt exchange between the boundaries of NECC and/or with the surrounding equatorial currents (i.e. NEC and SEC) on either side of it, as well as a potential interaction of the currents with the equatorial upwelling.

Close to the Amazon and Congo river mouths, SSS variations occur over long time scales of up to 4 months, likely reflecting the amplitude of rivers' seasonal cycle. Interestingly, the removal of the seasonal cycle, although decreases the spatial scales of SSS, increases the temporal decorrelation lengths of SSS anomalies by up to ∼1 month. The relatively constant influence of large freshwater river discharge,

together with advection by the mean regional circulation seem to generally preserve SSS changes over such long periods. On the other hand, the northern part of the Gulf of Guinea displays a different behaviour compared to the rest equatorial eastern basin, with notably shorter spatial scales, primarily due to potential strong freshwater forcing variations. This region receives the discharge from several rivers located at the northern and eastern coast, with a typical northward orientation of the Congo plume (*Materia et al.*, 2012; *Denamiel et al.*, 2013), as well as heavy P by the double passage of the ITCZ within a year. The latter may have also been enhanced during the examined years by a potentially anomalous, longer stay of the ITCZ over the N. African continent (*Foltz and McPhaden*, 2008) during the ENSO phases in 2010-2012. Thus, the combined effect of freshwater fluxes and regional advection likely prevent homogeneous SSS changes to span over long distances in this part of the Gulf of Guinea.

As regards the Subtropical Atlantic, homogeneous SSS changes occur over large zonal spatial scales towards the centre of the Subtropical Gyres and in proximity to the SSS maximum regions, in line with the expected small SSS variations there on subannual to interannual time scales. Not surprisingly, the longest meridional spatial scales are also found in the Subtropics, away from the equator and the zonal impact of the ITCZ and Equatorial currents. The central S. Subtropical Atlantic primarily displays long characteristic lengths of SSS, both in the W-E and N-S direction, while long meridional scales of SSS anomalies are also found in the central N. Subtropical basin. Similarly, SSS variations in the centres of the Subtropical Gyres show a longer stability in time of up to ∼4 months due to slower advection processes in these E-dominated regions. In contrast, the surface current dynamics along the branches of both Subtropical Gyres result in a shorter persistence of SSS variations of ∼2-3 months. Interestingly, the removal of SSS seasonal cycle reveals longer temporal scales of up to 3-4 months, particularly along equatorward branches of the N. and S. Subtropical Gyres, respectively. This increase by ∼1 month of the SSS persistence likely indicates the impact of the seasonal variability of surface current circulation and the associated mesoscale features, which force quicker SSS changes. Finally, long meridional length scales of SSS along the Subtropical Atlantic coasts may point to controlling role of advection from the BCs and associated coastal upwelling.

The above characteristic length scales of SSS from SMOS are generally in agreement with the decorrelation scales of other ocean and atmospheric parameters in the Tropical/Subtropical Atlantic basin, although some noticeable differences are also observed. Based on TOPEX/POSEIDON altimeter data, the decorrelation spatial scales of sea surface height anomalies (SSHA) are anisotropic, with longer length scales in the Tropics compared to the Subtropical latitudes, where they are characterized by mesoscale eddies (*Kuragano and Kamachi*, 2000). However, in contrast to SMOS SSS, SSHA displays large spatial lengths in the Equatorial compared to the N. and S. Tropical Atlantic basin, while the opposite is suggested

for the SSHA time scales. Similarly, *Doney et al.*, 2003 using a semivariogram approach on ocean colour images, find a directional anisotropy in the spatial scales of mesoscale ocean biological variability. However, although their zonal spatial scales also exhibit a strong banded latitudinal pattern similar to that seen in SMOS SSS variations, the largest lengths occur along the equator and decrease poleward, with the equatorial meridional lengths being somewhat shorter than the zonal ones. Moreover, the mesoscale biological variability displays in general shorter spatial (and temporal) length scales in upwelling regions, due to associated offshore gradients and episodic upwelling jets and filaments, as opposed to the observed long meridional SSS length scales there. Anisotropic spatial length scales also characterize the eddies in the N. Atlantic basin south of 30°N (*Eden*, 2007) as well as the SST variations based on the Comprehensive Ocean-Atmosphere Data Set (COADS), with representative lengths of 7-10 degrees in the zonal and 3-6 degrees in the meridional direction (*Molinari and Festa*, 2000).

In turn, as regards the turbulent fluxes, the spatial variability in both latent and sensible heat fluxes is anisotropic and more consistent in the zonal than meridional direction, with the trade wind belt exhibiting the largest coherence, which reduces at higher latitudes (*Romanou et al.*, 2006). Smaller spatial patterns are found in the storm track regions of the Atlantic basin. Being dominated by the SST patterns, sensible heat fluxes have larger spatial scales than the latent heat. In addition, both latent and sensible heat fluxes have the longest temporal decorrelation scales in the Equatorial Atlantic, where the dominant cause of the slower E variations in the ITCZ 0°-10°N is the persistent and unidirectional trade winds system, which, in turn, displays similar, long time scales. In addition to zonal winds, their long temporal scales in the Equatorial Atlantic are also associated with SST, and coastal upwelling along the African coast, while near the Congo mouth, with extensive and persistent cloud cover. In contrast, shorter time scales characterize the Subtropical Gyres. Overall, the S.H. is dominated by shorter spatial and temporal scales of turbulent fluxes compared to the N.H., as a result of the unequal land-ocean distribution in the two hemispheres (*Romanou et al.*, 2006), which comes in contrast to what is observed here for SMOS SSS. Such dissimilarities (both in terms of patterns and magnitude) between the spatio-temporal characteristic scales of SSS from SMOS and the other oceanic and atmospheric parameters, may be, at least, partly attributed to the different methods applied for their estimation and the different space-time data resolution, in addition to the actual comparison of different variables in nature.

To conclude, the analysis presented here reveals that advection plays a critical role on the spatio-temporal characteristic scales of SSS over the whole Tropical/-Subtropical Atlantic basin, both in the P- and E-dominated regions. Combined with the seasonal ITCZ migration, advection by the zonal surface currents results in long zonal spatial scales of SSS changes along two equatorial bands centred at ∼10°N and ∼5°S, which persist in time, especially in shorter, i.e. subannual,

than interannual time scales. In contrast, at the equator, these controlling mechanisms together with the additional impact of equatorial upwelling lead to noticeably shorter spatio-temporal SSS decorrelation lengths. Towards the centres of the E-dominated Subtropics, weak advection and mixing processes allow for SSS variations with long characteristic scales both in time and space. However, along the branches of the Subtropical Gyres, advection and associated mesoscale features prohibit SSS changes to occur over long temporal and zonal spatial lengths, except for long meridional spatial scales, especially along the branches of the S. Subtropical Gyre. On interannual time scales, advection together with coastal upwelling and mixing processes close to the E-dominated BCs, seem to primarily drive SSS anomaly changes over long meridional spatial scales along the coasts, but with a shorter persistence in time by$\sim$1 month relative SSS.

Improved description of the characteristic scales of SSS in time and space provides a better understanding of both the SSS itself and the processes that control and are influenced by it. These serve, among others, to refine studies of SSS variability and freshwater budgets, where knowledge on the persistence of homogeneous SSS changes in space and time, and the importance of each controlling mechanism on it, becomes essential. Equally important, comprehensive description of the decorrelation length scales of SSS serves as a better constraint when assimilating observations into ocean models. Having described the spatio-temporal scales of SSS variations from SMOS over the P- and E-dominated regions, the final results' chapter in this thesis presents a first attempt towards a regional SSS budget from SMOS over the Tropical and Subtropical Atlantic (Chapter 7).

Chapter 7

Estimating E-P from SMOS SSS variability

7.1 Introduction and motivation

Direct measurements of the ocean surface freshwater fluxes, i.e. Evaporation minus Precipitation (E-P), or their accurate estimation from other atmospheric variables, involves many difficulties. An increasing number of studies suggest the estimation of E-P from salinity variations may be possible, as the latter are caused by freshwater transport in and out of the ocean (e.g. *Lagerloef et al.*, 2010; *Helm et al.*, 2010; *Yu*, 2011; *Vinogradova and Ponte*, 2013). However, the evolution of salinity within the mixed layer also includes the tendencies of oceanic fluxes of salt, seen in Equation 7.1, which shows the salinity budget equation (*US CLIVAR Group*, 2007). More specifically, integrated vertically through a mixed layer depth *h(x,y,t)*, the time rate of salinity change (*dS/dt*) is defined by a combination of surface freshwater fluxes, horizontal advection, subsurface processes (e.g. entrainment/detrainment through the base of the mixed layer) and mixing (Equation 7.1). The effects of oceanic fluxes in the salinity budget are considered non-negligible, and thus, a one-to-one correspondence between salinity changes and E-P does not generally hold (e.g. *Yu*, 2011; *Vinogradova and Ponte*, 2013). Nevertheless, an adequate resolution of sea surface salinity (SSS), surface current velocities and mixed layer depth (MLD) would offer the potential of inferring E-P only from ocean data (*Schmitt*, 1995).

$$\frac{dS}{dt} = \frac{(E-P)S}{h} - \overrightarrow{v} \cdot \nabla_h S + subsurface + [MLmixing] \tag{7.1}$$

This chapter presents a first attempt to estimate the E-P field from SMOS SSS observations, and assess whether and how SSS variations may be used as a proxy to determine E-P, even in the presence of other oceanic fluxes. This would provide a first insight into the SSS budget from satellite observations from SMOS.

Considering the simple case that SSS changes as sensed by SMOS are equivalent to the freshwater that enters/leaves the ocean surface over the same period, the work focuses on the first term on the right-hand side of the Equation 7.1:

$$\frac{dS}{dt} = \frac{(E-P)S}{h} \tag{7.2}$$

where S is the mixed layer salinity (MLS) and h is the MLD.

The relation between E-P and SSS has been examined previously. Among other studies, *Yu* (2011), based on climatological WOA05 salinity and MLD observations, combined with GPCP P, E and wind stress from OAFlux (over their common period 1993-2008), and altimeter and in situ sea level data to obtain mean geostrophic currents (1992-2002), looked at the global salinity budget on long (i.e. climatological) time scales. *Vinogradova and Ponte* (2013) assessed the global link between SSS and E-P on seasonal to interannual (1992-2004) time scales based on outputs from the ECCO ocean general circulation model. On shorter time scales, *Boutin et al.* (2013), examined the global and regional, i.e. over the Tropical Pacific, impact of P events on SSS changes every 10 days from SMOS and Argo data. Finally, *Reul et al.* (2013) studied the freshwater forcing and horizontal advection terms of the salt budget using 10-days SMOS data and OSCAR surface currents (both Ekman and geostrophic currents), and suggested a good agreement between negative SSS and strong positive P anomalies at a fixed point (16°N 35°W) or in averaged monthly bins over the northern Tropical Atlantic for 2010.

This work aims to examine whether and where the link between SSS variations from SMOS with E-P still holds on monthly to seasonal time scales and whether and to what extent the E-P field can be reconstructed from SMOS observations. Although Chapter 6 revealed different regions where SSS variations occur on different spatial and temporal scales, this chapter initially examines SMOS E-P over the whole Tropical/Subtropical Atlantic 30°N-30°S basin for the period 2010-2012, and then proceeds in the different regimes.

In this part of the Atlantic basin, different terms from the salt budget equation (Equation 7.1) are expected to dominate over the different regimes. In the Subtropics, the high SSS values are expected to display small seasonal variations, particularly towards the centres of the Subtropical Gyres, where E rates are also high but almost constant throughout the year. In addition, variability of the oceanic processes there is small, given the weaker winds and ocean currents. Over the rest of the Subtropical Gyres, earlier studies (e.g. *Yu*, 2011; *Vinogradova and Ponte*, 2013) indicate that variability in freshwater and oceanic fluxes appears to be of comparable amplitude, but the influence of oceanic fluxes on annual and shorter time scales may allow the examination of a linear relation between salinity changes and freshwater fluxes.

In contrast, large seasonal variability of SSS is observed in the Tropics (as shown in Chapters 4 and 5), primarily driven by the InterTropical Convergence Zone (ITCZ) migration and heavy P associated with deep atmospheric convection (e.g. *Boyer and Levitus*, 2002; *Bingham et al.*, 2010), as well as freshwater outflows from the major river systems of the Amazon/Orinoco and Congo/Niger (Chapter 4, Chapter 5). In addition, strong ocean currents, including the North and South Equatorial Currents (NEC and SEC), and the North Equatorial Counter Current (NECC), have a significant influence on SSS in the region. The E-P effect on SSS variations is mostly prominent in regions where E-P displays large seasonal variability, mainly induced by changes in P under the migrating ITCZ (e.g. *Dessier and Donguy*, 1994). At annual and interannual time scales, Tropical E-P variations generally have a comparable amplitude with those of oceanic fluxes, while subannual variations of the latter can even dominate those of E-P (e.g. *Vinogradova and Ponte*, 2013). However, in some Tropical ITCZ regions, such as towards the north-eastern Equatorial Atlantic, E-P variability is seen to be larger than that in oceanic processes (See for instance, Figure 9 in *Yu*, 2011). Finally, advection and mixing processes play an important role in regions of strong salinity gradients, such as along the Western Boundary Currents (WBCs).

Given the above, the E-P fields reconstructed from SMOS in the period 2010-2012 are examined over the Atlantic basin 30°N-30°S, in order to include both the Subtropics and Tropics. The objective is to identify whether and where SMOS can generally depict the expected patterns of the E-P distribution over the region of interest, i.e. the highly positive E-P values in the Subtropical latitudes and the dominance of P in the Tropics and under the influence of the ITCZ. Next, the SMOS E-P distribution and variability are assessed separately in each regime, by tracking the zonal E-P maxima in two E-dominated subregions in the N. and S. Subtropical Atlantic, and the zonal E-P minima in a P-dominated Tropical band across the basin, on monthly and seasonal time-scales. For this, the significant influence of freshwater discharge from the major Amazon/Orinoco and Congo/Niger rivers on the SSS fields is excluded from the analysis by masking the western and eastern river-influenced regions (See Chapter 5 and Figure 5.5 for the definition of their boundaries) and focusing over the "open" oceanic basin. Finally, the characteristics of SMOS E-P are compared to those from OAFlux-GPCP over the same time period.

7.2 Methodology and data

Assuming that the other terms are negligible to first approximation, Equation 7.2 is re-written as follows for the estimation of E-P from SMOS:

$$E - P = \frac{dS}{dt}\frac{h}{S} \tag{7.3}$$

where *dS/dt* is produced by differentiating initially monthly SSS fields over the Tropical/Subtropical Atlantic 30°N-30°S for the period 2010-2012. This results in 35 monthly E-P fields, where each field can be considered as representative of SSS changes occurring from the middle of the first month to the middle of the following. Therefore, for the terms h and S, monthly MLD and MLS fields are averaged every two months in order to correspond to the mean field over the same period, leading respectively to 35 monthly MLD and MLS fields.

The monthly mean SSS products derived from SMOS for the complete years 2010 (CATDS Version V01), 2011 and 2012 (CATDS Version V02) are described in detail in Chapter 3, Section 3.2.1.5. SSS observations from SMOS are used to replace the MLS (S in Equation 7.3), with the assumption that SSS from SMOS is representative of the salinity over the whole mixed layer on monthly time scales. Note that MLS data from the Argo climatology (2000-2011) defined according to two different criteria (i.e. hybrid density algorithm and variable density threshold criterion corresponding to 0.2°C variation) were also considered in this work (plots not shown), however did not reveal any differences in the reconstructed SMOS E-P fields presented here. Moreover, the scarcity of Argo MLS data still leaves large areas of the Tropical/Subtropical Atlantic basin without any observations (plot not shown), and thus, SMOS spatio-temporal coverage was preferred instead. The estimation of MLS from monthly SSS data has been also made previously by *Foltz and McPhaden* (2008), who although based on limited in situ data from the PIRATA moorings along 38°W, found small differences between the MLS and SSS seasonal variations in the Tropical N. Atlantic. Finally, climatological MLD monthly fields, defined according to a fixed density threshold criterion of 0.03 kg/m^3 difference from the sea surface, are obtained from Ifremer and are described in Section 3.5.1 of Chapter 3.

For comparison with the reconstructed E-P fields from SMOS, freshwater fluxes are obtained from monthly P fields from the Global Precipitation Climatology Project (GPCP) and monthly E from the Objectively Analyzed air-sea Fluxes (OAFlux) for the period 2010-2012 (See Sections 3.3.1 and 3.3.2, respectively, in Chapter 3). The OAFlux-GPCP E-P fields are averaged every two months, in order to be directly comparable with the month-to-month SSS differentiations for the estimated SMOS E-P values. Finally, to ensure consistency throughout the analysis and between the different data sources and versions, a uniform domain is determined by masking all datasets (SSS, E and P) to display the same grid cells along the coasts.

7.3 Does SMOS depict the main characteristics of E-P field in the Atlantic basin 30°N-30°S?

7.3.1 Description of the reconstructed monthly E-P fields from SMOS

Figure 7.1 shows the reconstructed monthly E-P fields from SMOS for 2010 (including January 2011 minus December 2010 as the last field), as typical examples for the years 2011-2012 as well. SMOS E-P fields are presented in 2.5° x 2.5° spatial resolution in order to enable a direct comparison with the corresponding OAFlux-GPCP E-P fields. Analysis on slightly finer, 2° x 2° grid cells (same as the MLD field) does not reveal any significant differences in the observed E-P patterns or their magnitude (plots not shown). Overall, SMOS captures only locally some of the expected E-P patterns, i.e. the dominance of E in the Subtropical latitudes and the excess of P along the Tropical Atlantic basin. However, the monthly SMOS E-P fields for the 3 years are generally noisy, hindering the clear identification of the expected E-P distribution. SMOS E-P magnitude varies between ±0.7 m/month (99% quantiles) but can exceed this range, reaching up to -6 and ∼2 m/month in isolated grid cells, particularly towards the northern and southern boundaries of the region of interest.

Nevertheless, strong negative E-P values along the equatorial basin may indicate the ITCZ position in some months (Figure 7.1). For instance, the P-dominated band in the beginning of the year, i.e. Feb-Jan and Mar-Feb, centred at ∼5°S may represent the ITCZ, which is expected to lie south of the equator at this time of the year, as well as during summer (Jun-May up to Sep-Aug) when it moves northwards at ∼5°-10°N. Over the Subtropics, the expected strong positive E-P values are only weakly displayed by SMOS throughout the year (Figure 7.1).

Comparison of SMOS with OAFlux-GPCP monthly E-P fields Next, the monthly E-P distribution from SMOS is compared with that from OAFlux-GPCP. Figure 7.2 shows two typical examples of the OAFlux-GPCP E-P fields averaged over 2 months, in order to be comparable to the reconstructed SMOS E-P. The fields correspond to January+February (left) and July+August (right) for 2010, but are representative for the rest of 2010 as well as for 2011 and 2012. For comparison, OAFlux-GPCP E-P is displayed on the same scale of ±0.7 m/month as SMOS E-P in Figure 7.1, although its magnitude generally ranges between -0.25 m/month and 0.16 m/month (99% quantiles), but reaching up to -0.45 m/month and 0.19 m/month in few cases. SMOS E-P fields differ significantly from those from OAFlux-GPCP, as also seen in Figure 7.3, which shows their corresponding differences for 2010. Contrary to the generally noisy SMOS fields, OAFlux-GPCP E-P clearly depicts the strong Tropical P band under the ITCZ movement during the year, and the highly positive Subtropical E-P values (Figure 7.2). The noisiness

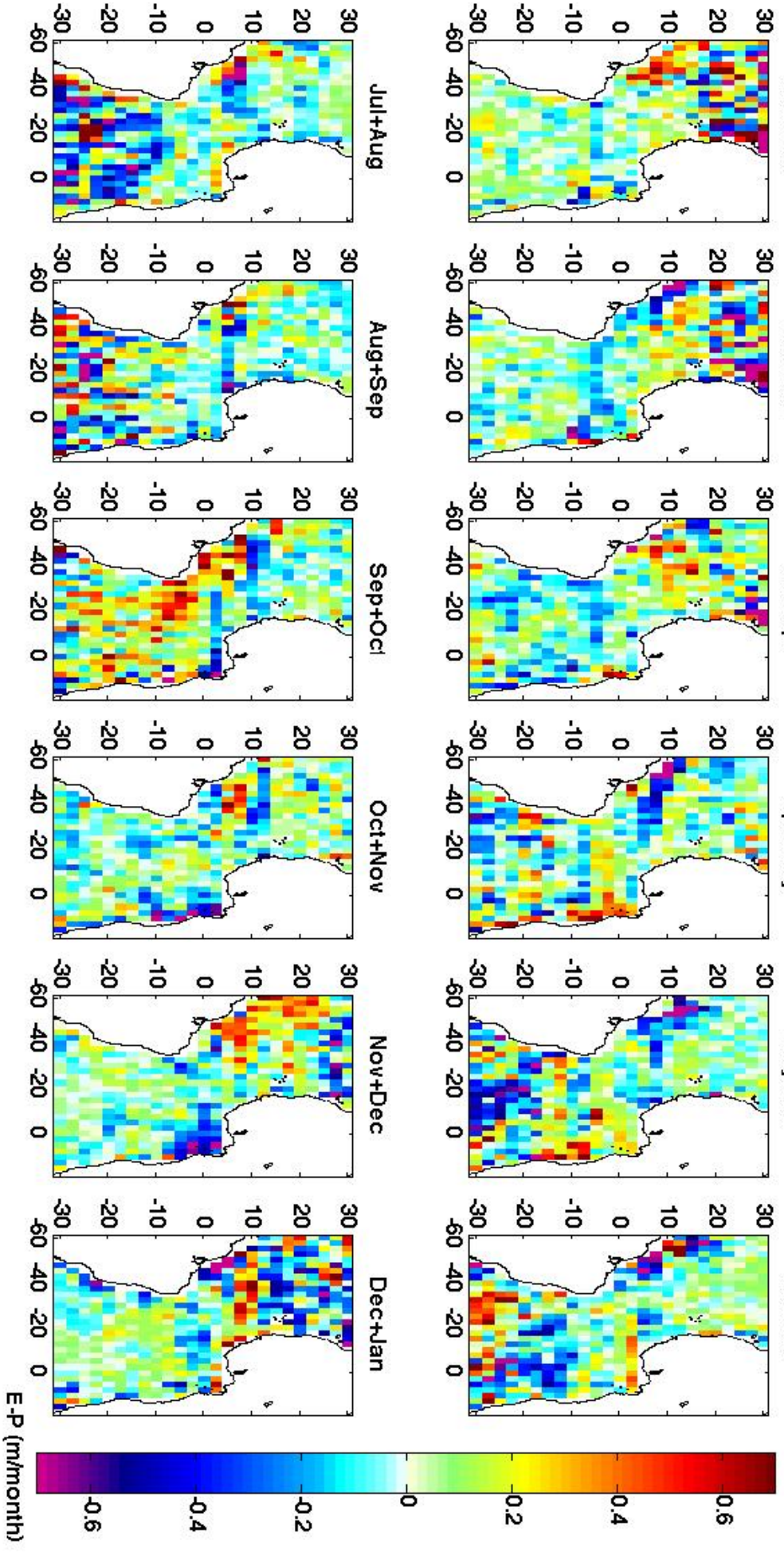

Figure 7.1: Monthly fields of E-P from SMOS as averages every 2 months for 2010, in 2.5° x 2.5° spatial resolution.

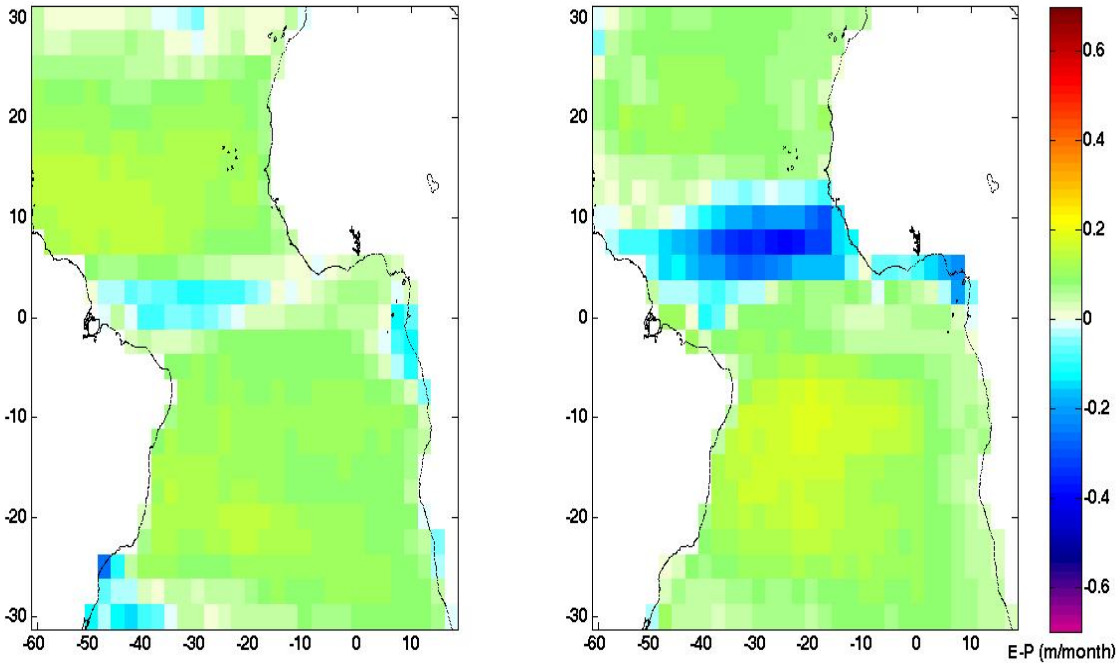

Figure 7.2: Monthly mean E-P fields from OAFlux-GPCP as averages every 2 months for i) January and February (left) and ii) July and August (right) in 2010, in 2.5° x 2.5° spatial resolution.

of SMOS E-P makes it difficult to discern those same patterns, and the magnitude of the SMOS E-P field generally shows large discrepancies from the OAFlux-GPCP E-P values.

Sensitivity to the MLD and SMOS SSS fields To gain a better understanding of the observed noise on the monthly SMOS E-P maps, the analysis considers next the different component fields used in the reconstruction. For this, the impact is assessed of averaging every 2 months the monthly climatological MLD and the SMOS SSS fields used as replacement for the MLS. Figures 7.4 and 7.5 show examples of month-to-month differences of MLD and SMOS SSS, respectively, for selected months, in order to examine whether the variability in the two variables may have an impact on SMOS E-P. Note that the reconstructed SMOS E-P depends on the monthly MLD and SMOS SSS fields (and not the month-to-month difference) and that month-to-month differences are shown here only as a measure of the variability (and reliability) of these fields. Overall, although their monthly fields are generally smooth (see for instance, Chapter 3, Figure 3.15 for MLD, and Figure 3.6, top panel for SMOS SSS), the month-to-month difference fields of MLD and SMOS SSS show marked patterns of variability. Large monthly MLD variations occur in the Subtropics, particularly in the S. Atlantic, while as expected, significant monthly SSS changes are seen along the Tropics. These month-to-month variations of MLD and MLS, and in turn, the combination of their averaged distributions every 2 months in Equation 7.3, will contribute to the observed lack of coherent features of SMOS E-P fields and explain, at least partly, the aforementioned differences with OAFlux-GPCP.

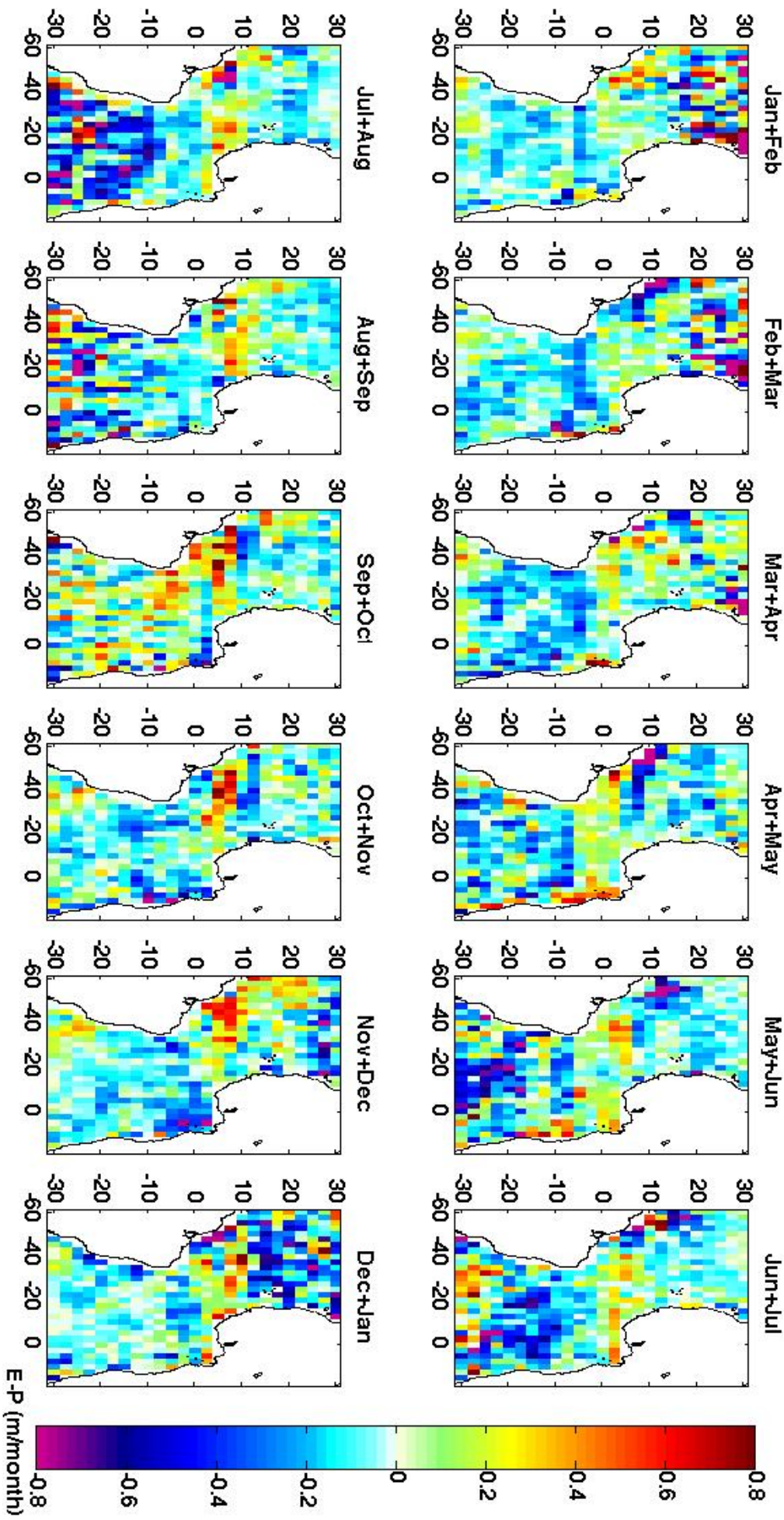

Figure 7.3: Differences of SMOS minus OAFlux-GPCP monthly E-P fields for 2010 in 2.5° x 2.5° spatial resolution.

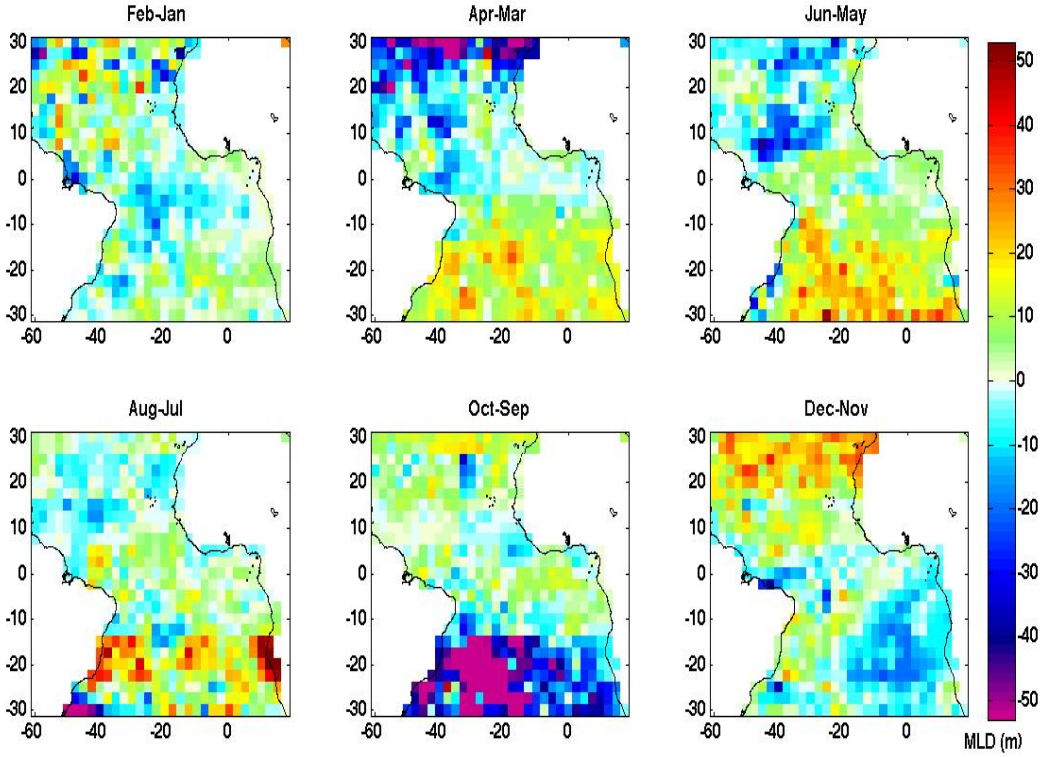

Figure 7.4: Month-to-month differences of Ifremer climatological MLD based on a fixed density threshold criterion, for February-January, April-March, June-May, August-July, October-September and December-November (from top left to bottom right), in 2.5° x 2.5° spatial resolution.

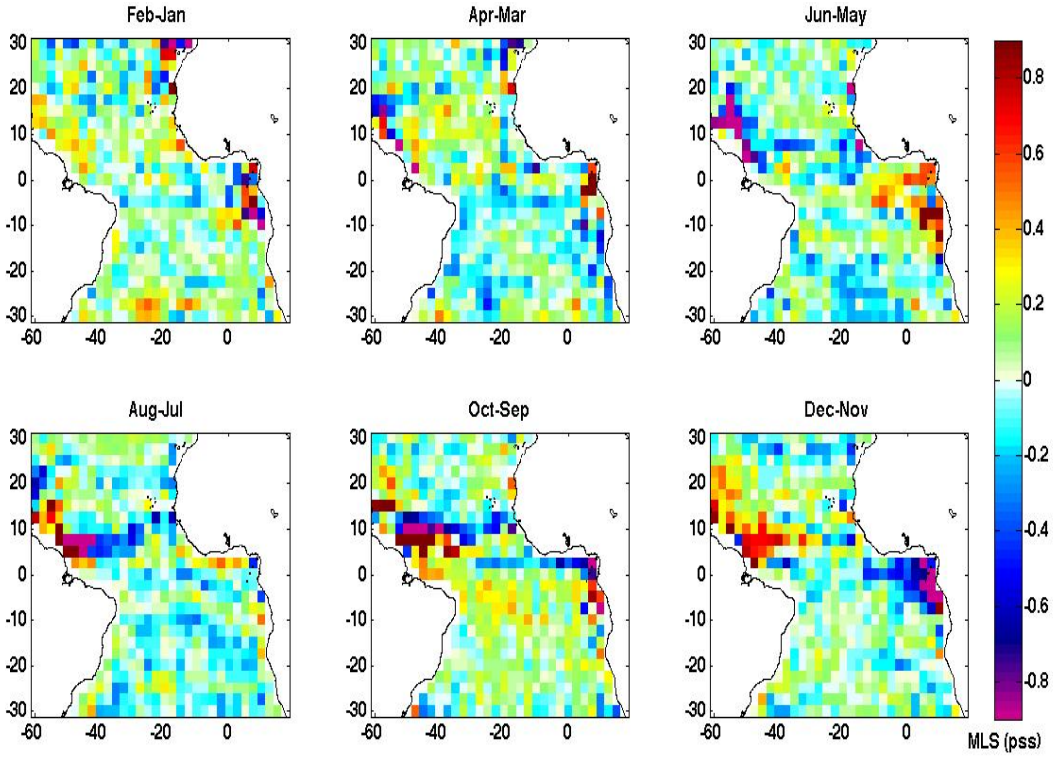

Figure 7.5: Month-to-month differences of SMOS SSS used as MLS for February-January, April-March, June-May, August-July, October-September and December-November (from top left to bottom right) in 2010, in 2.5° x 2.5° spatial resolution. The SMOS uncertainty in the region of interest is ∼0.31 pss.

Overall, the monthly MLD differences (Figure 7.4) range between -27 m and 22 m, but can reach up to -53 m and 32 m towards the Subtropics, and even exceed these values in few grid cells (Note that the slightly larger spatial resolution presented here as compared to the original 2° x 2° resolution does not modify the results). The largest MLD variations occur during winter time in each Hemisphere, when the MLD deepens (i.e. increases), particularly in the S. Subtropical Atlantic. However, the limited number of profiles per grid cell and the large areas in the S.H. with no observations at all (See Chapter 3, Figure 3.14), indicate large uncertainties in the MLD data, particularly over the S. Subtropical basin, that likely contribute to a great extent to the observed noise in the SMOS E-P fields.

As regards the monthly variations of SMOS SSS, Figure 7.5, displaying them for 2010, provides an insight into both the monthly derivatives of SSS used to reconstruct E-P (i.e. first right-hand side term in Equation 7.3), as well as in the sensitivity of averaging SSS every 2 months to form the MLS fields. The largest SSS changes of up to ±0.9 pss (99% quantiles) occur along the Tropics, towards the north-western basin and close to the major Amazon/Orinoco and Congo/Niger rivers, where they can reach up to 4-5 pss in few grid cells during the year (See Chapters 4 and 5, which focus on the strong seasonal SSS variability in these regions). In contrast, the rest of the Atlantic basin is characterized by small SSS variations that do not generally exceed ±0.2 pss.

7.3.2 Monthly zonal averages of SMOS E-P fields in 2010

Next, the analysis examines whether SMOS can depict the zonally averaged distribution of E-P across the width of the "open" oceanic Atlantic basin 30°N-30°S, excluding data from the two river-influenced regions. Figure 7.6 shows the zonal averages (left) and st. dev. (right) of SMOS and OAFlux-GPCP E-P for Jul-Aug (top) and Nov-Dec (bottom) in 2010, providing an insight into their boreal summer and winter variations during the year. Similar patterns are also observed for 2011 and 2012 (plots not shown). SMOS generally fails to capture the zonally averaged seasonal E-P patterns seen in OAFlux-GPCP (Figure 7.6, left plots). In boreal summer (Aug-Jul), there is a E-P minimum around 7.5°N in both datasets, however SMOS shows a different magnitude compared to OAFlux-GPCP, given also the much larger st. dev. of the former in that location (Figure 7.6, top). Overall, the st. dev. of SMOS E-P increases during winter in both Hemispheres, particularly for the S. Subtropical Atlantic (Figure 7.6, right plots), which as seen previously, is likely due to the large MLD uncertainties. In boreal winter (Dec-Nov), SMOS shows a similar magnitude of the local Tropical E-P minimum, but slightly displayed southward compared to OAFlux-GPCP (Figure 7.6, bottom, left).

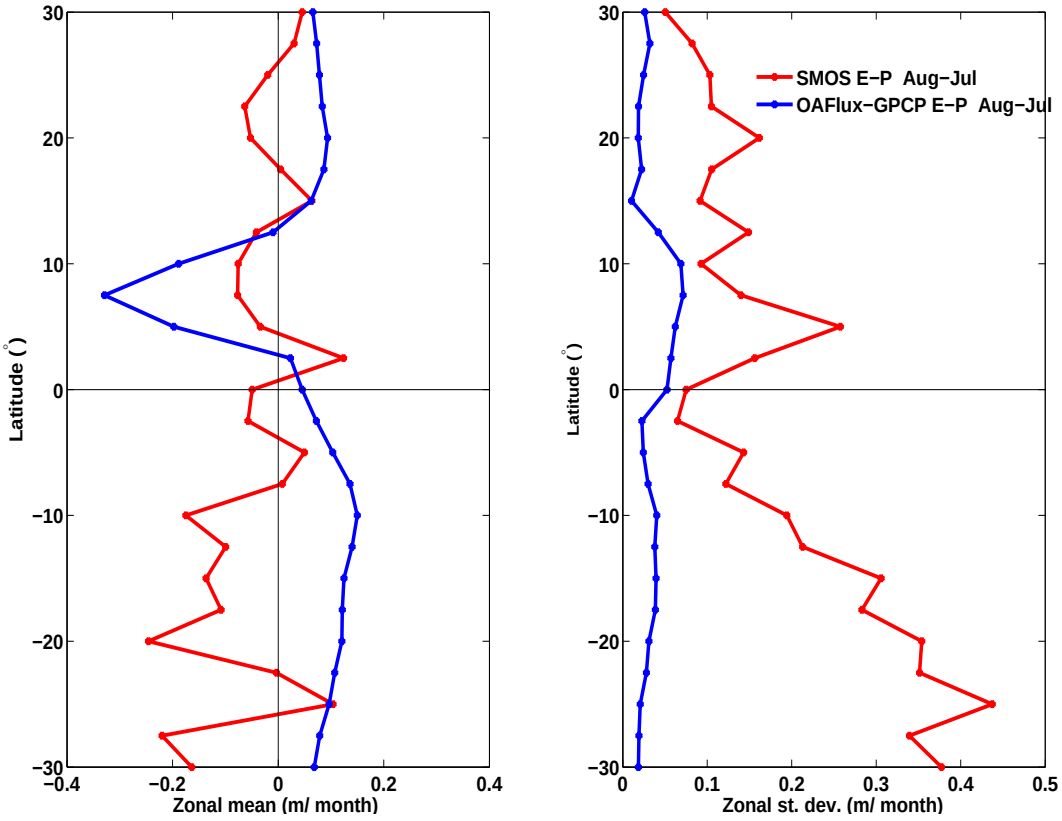

(a) Aug-Jul

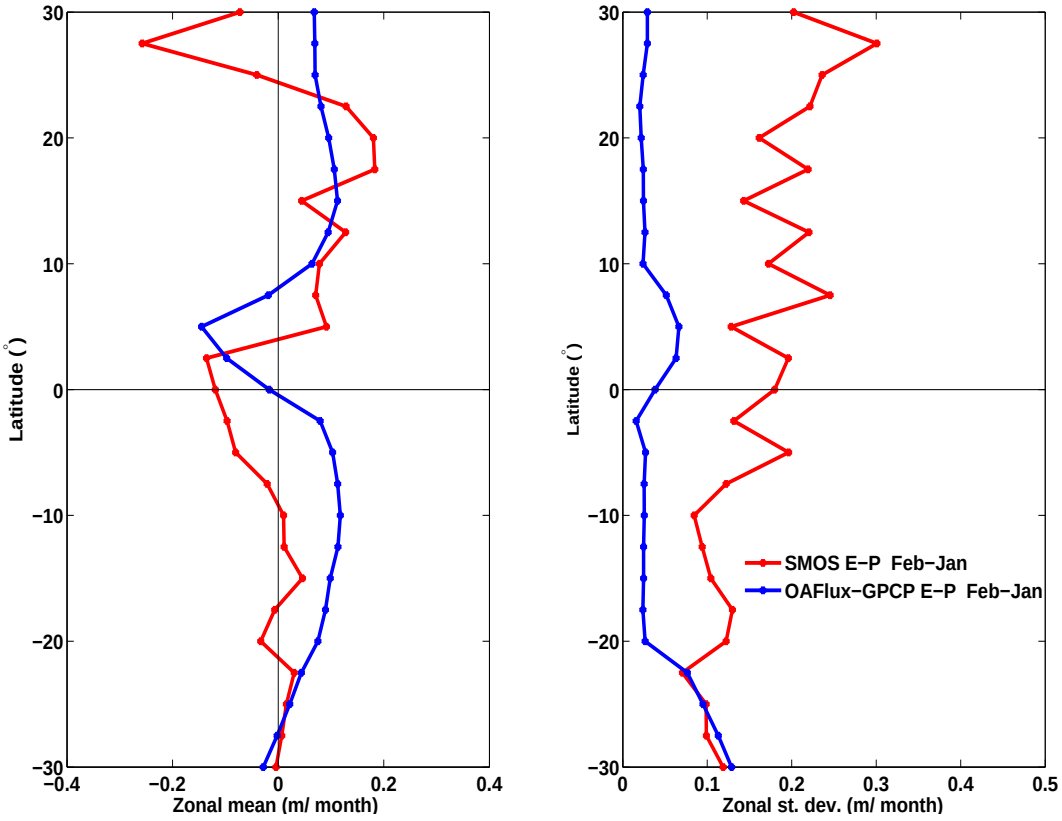

(b) Dec-Nov

Figure 7.6: Monthly zonal averages (left) and st. dev. (right) of SMOS (red) and OAFlux-GPCP (blue) E-P fields for a) Aug-Jul and b) Dec-Nov 2010 over the "open" oceanic basin. The zonal mean at a given latitude is taken across the basin width.

Given the localized capability of SMOS to display some of the E-P patterns, the rest of chapter focuses on the examination of zonal E-P extrema in small subregions over the "open" ocean in the E-dominated Subtropics (Section 7.4) and P-dominated Tropics (Section 7.5), respectively. It is worth noting that selection of different subregions from those presented below as examples, did not alter or improve noticeably the overall conclusions, both for the N. and S. Subtropics and Equatorial Atlantic, as well as across the whole "open" oceanic basin width and/or only towards its centre (i.e. excluding longitudes close to the coasts), (see for instance, Figure 7.1 for 2010).

7.4 SMOS E-P in E-dominated Subtropical Atlantic regimes

The objective of this section is to explore whether SMOS can capture the excess of E over P in two "open" ocean, E-dominated subregions of the N. and S. Subtropical Atlantic. For this, their zonally averaged E-P maxima are examined on monthly and seasonal time scales.

N. Subtropical Atlantic subregion Figure 7.7 shows the monthly (Figure 7.7, a) and seasonal (Figure 7.7, b) maxima of zonal E-P means from SMOS (red) and OAFlux-GPCP (blue) over the N. Subtropical Atlantic region 15°-25°N during the period 2010-2012. The top panels in each case display the latitude of their occurrence, while the bottom panels show their magnitude. In general, although SMOS does not display exactly the same position of zonal E-P maxima indicated from OAFlux-GPCP, it still seems to capture some of their latitudinal variation in time (Figure 7.7, a and b, top panels), and show satisfactory agreement in magnitude over most of the 3 years (Figure 7.7, a and b, bottom panels).

S. Subtropical Atlantic subregion In turn, focusing on a S. Subtropical Atlantic region between 17.5°-27.5°S, 20°W-0°E, Figure 7.8 displays the location (top panels) and magnitude (bottom panels) of the monthly (Figure 7.8, a) and seasonal (Figure 7.8, b) zonal E-P maxima, respectively, from SMOS (red) and OAFlux-GPCP (blue) over the years 2010-2012. On a monthly basis, SMOS indicates large and rapid changes in the latitudinal position of the maxima that are not seen in OAFlux-GPCP (Figure 7.8, a, top). On seasonal time scales, SMOS E-P maxima are found at the same location with the OAFlux-GPCP maxima in boreal spring and autumn, and within 1-2 grid cells (2.5°-5°) during boreal winter (Figure 7.8, b, top). In contrast, in all boreal summers, SMOS suggests a more southward position by 10° relative to OAFlux-GPCP.

As regards the magnitude of zonal E-P maxima in the S. Subtropical regime, OAFlux-GPCP suggests a very constant monthly and seasonal value of ∼0.1 m/-month throughout the period 2010-2012 (Figure 7.8, a and b, bottom panels).

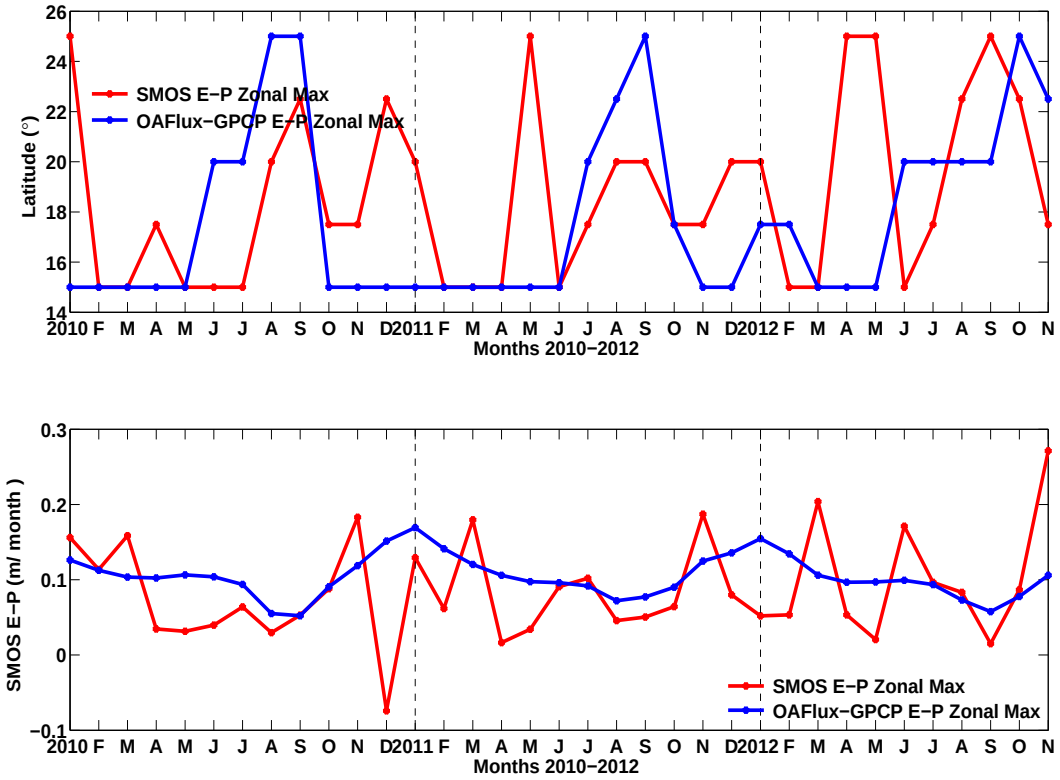

(a) Monthly zonal E-P maxima

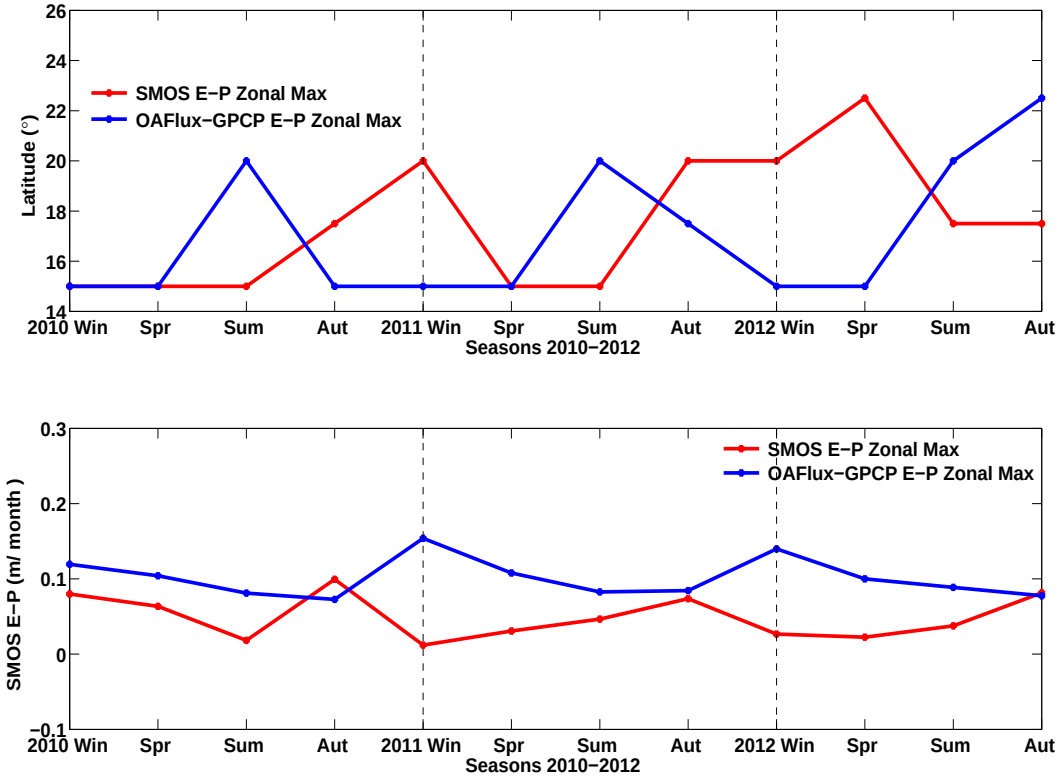

(b) Seasonal zonal E-P maxima

Figure 7.7: a) Monthly and b) seasonal maxima of zonally averaged E-P fields across the basin width in the N. Subtropical Atlantic region 15°-25°N for 2010-2012 from SMOS (red) and OAFlux-GPCP (blue), in terms of their location (top) and magnitude (bottom).

In contrast, SMOS shows a large seasonal variability of the magnitude, being in best agreement with OAFlux-GPCP in autumn of all 3 years, when the smallest differences of only 0.02-0.03 m/month are observed, and secondarily in winters 2011-2012 and summer 2012 (Figure 7.8, b, bottom).

7.5 Can SMOS display the ITCZ in the Tropical Atlantic?

Next, the analysis focuses on the zonally averaged E-P over a P-dominated region along the Tropical Atlantic, aiming to examine whether the band of maximum P under the ITCZ can be detected from SMOS. For this, the interest is on the E-P minima along the Equatorial "open" oceanic basin between 0°-10°N. Slightly different regions were also examined, but the definition of their boundaries does not lead to any pronounced differences in the conclusions presented here. The top two panels in Figure 7.9 show the monthly zonal E-P minima from SMOS and OAFlux-GPCP, in terms of their location and magnitude in 2010-2012, respectively. The bottom panels (Figure 7.9, b) display them on a seasonal basis, in order to potentially enable a more clear identification of the ITCZ migration during the 3 years. In general, SMOS manages to capture most of the latitudinal ITCZ movement both on monthly and seasonal time scales. It also displays successfully the magnitude of the monthly E-P minima as indicated by OAFlux-GPCP over most of the 3 years.

More specifically, the monthly SMOS E-P minima show a latitudinal shift by ∼10° over the year, with good repeatability. This broadly matches what is seen in OAFlux-GPCP albeit with a slight temporal offset (∼2 months) (Figure 7.9, a, top). In autumn, the strong P patterns associated with the ITCZ appear in SMOS as minima located at a more northward position than for OAFlux-GPCP, around 10°N between Sep-Nov in all 3 years. The same holds true on a seasonal basis, although the two datasets almost never (except for winter 2011) indicate exactly the same location of P patterns because of the temporal shift (Figure 7.9, b, top). Interestingly, SMOS captures noticeably well the magnitude of zonal E-P minima, particularly their monthly values over most of the 3-year period (Figure 7.9, a, bottom). On a seasonal basis, the agreement is less striking, as the seasonal values are dominated by the large discrepancies (of the order of 0.1-0.2 m/month) seen in summer for all 3 years (Figure 7.9, b, bottom).

7.6 Discussion and Conclusions

Salinity changes reflect a complex balance between atmospheric and oceanic processes occurring on multiple temporal and spatial scales. Depending on the region, oceanic processes can have a much smaller contribution, allowing the potential use

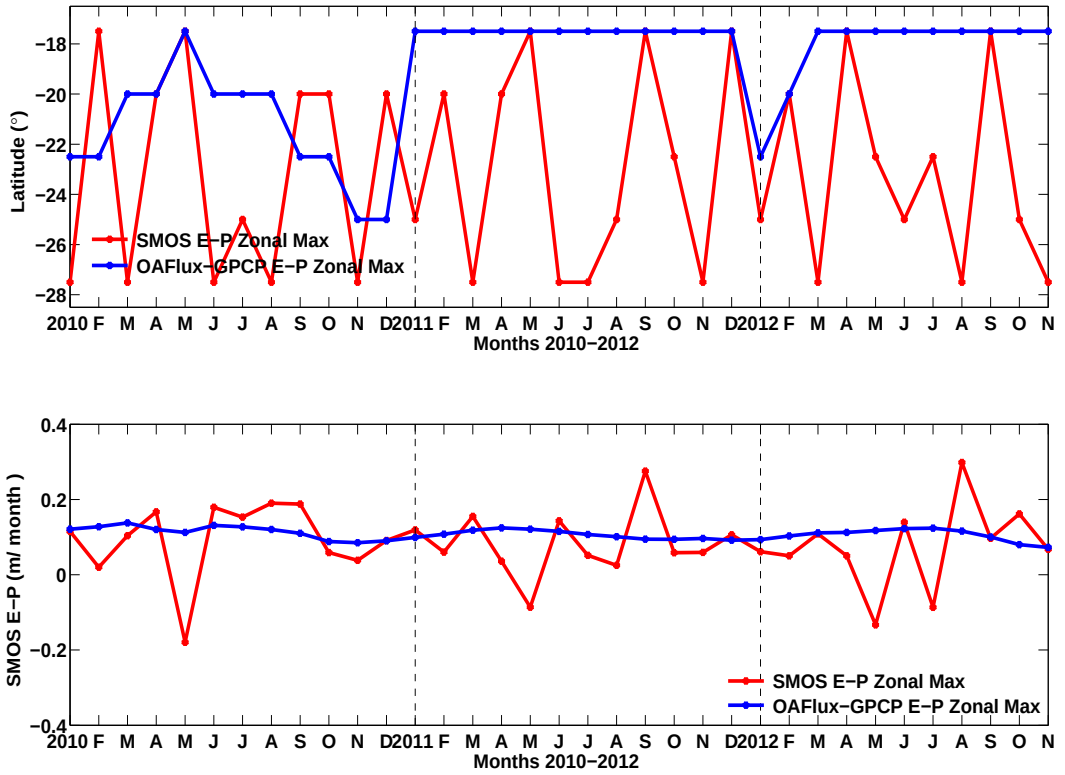

(a) Monthly zonal E-P maxima

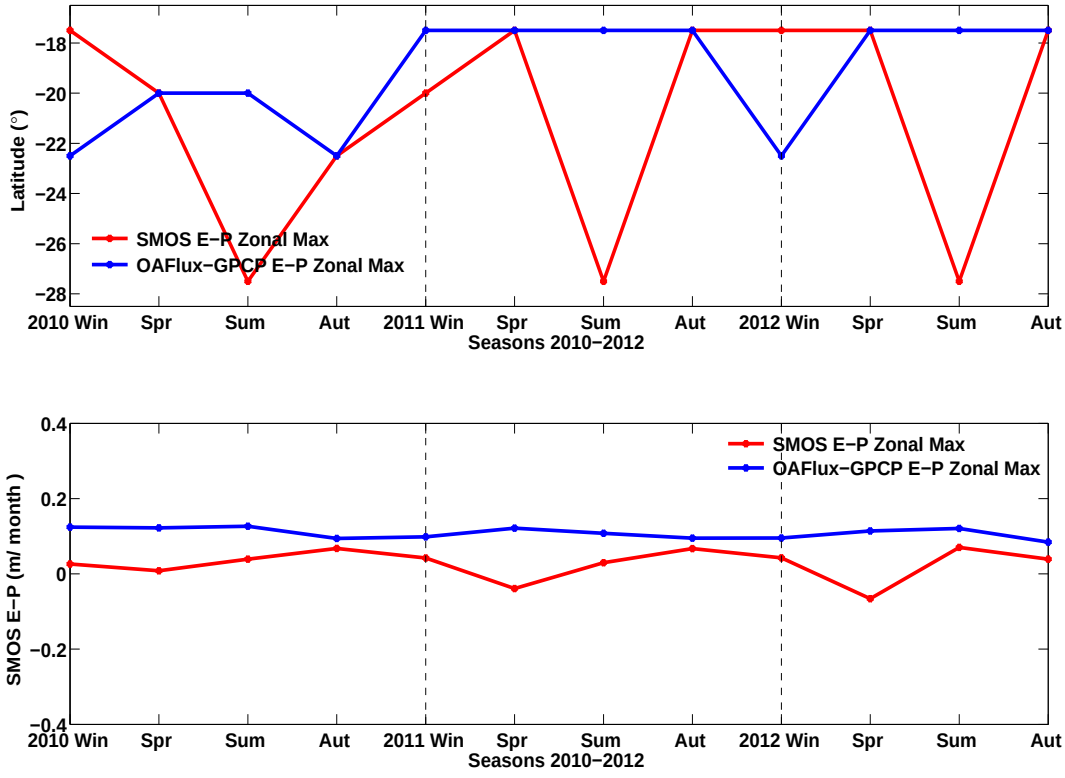

(b) Seasonal zonal E-P maxima

Figure 7.8: a) Monthly and b) seasonal maxima of zonally averaged E-P across the basin width in the S. Subtropical Atlantic region 17.5°-27.5°S, 20°W-0°E for 2010-2012 from SMOS (red) and OAFlux-GPCP (blue), in terms of their location (top) and magnitude (bottom).

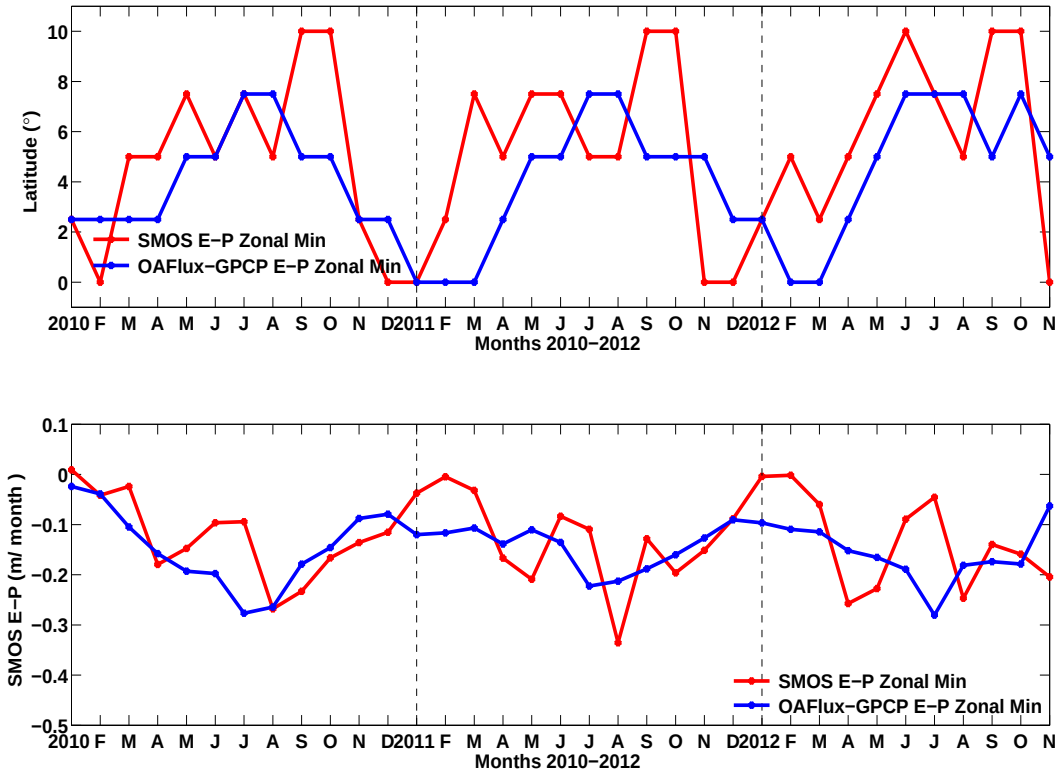

(a) Monthly zonal E-P minima

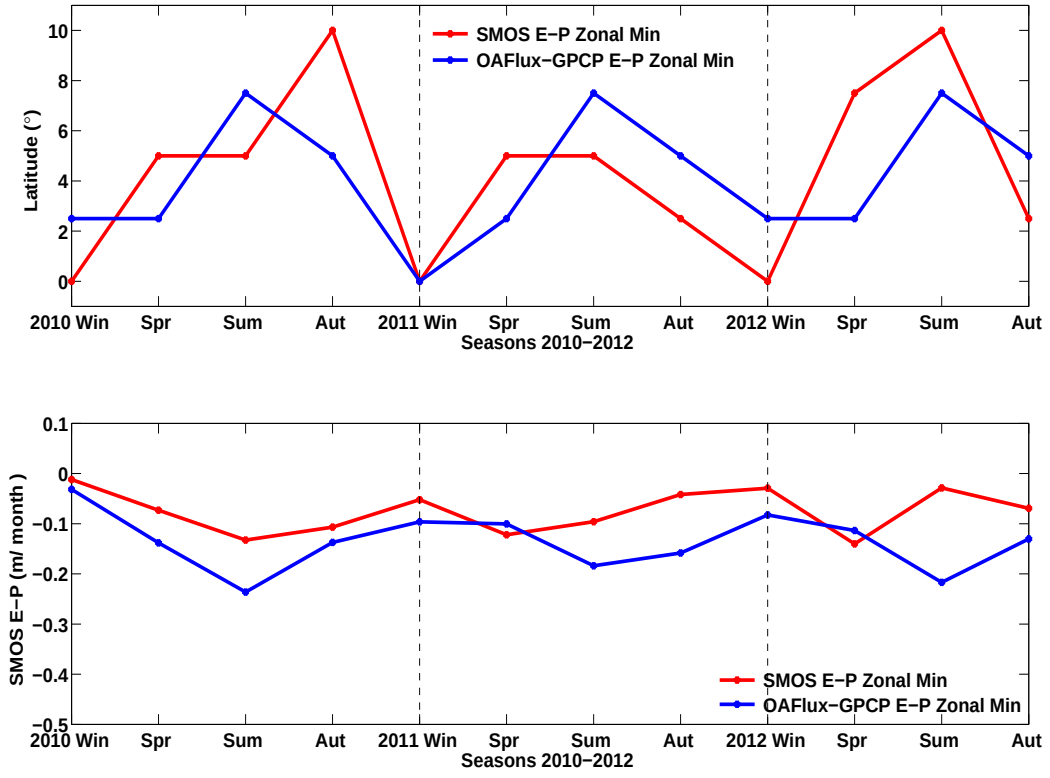

(b) Seasonal zonal E-P minima

Figure 7.9: a) Monthly and b) seasonal zonal E-P minima across the basin width in the Tropical Atlantic region 0°-10°N for 2010-2012 from SMOS (red) and OAFlux-GPCP (blue), in terms of their location (top) and magnitude (bottom).

of salinity variations as a proxy to estimate E-P. This chapter presents the first attempt to reconstruct E-P fields from SMOS observations to explore the relation of

satellite-derived SSS with E-P and the other processes in the Tropical/Subtropical Atlantic basin. The aim is to assess to what extent SMOS can capture the main E-P characteristics over the E-dominated Subtropics and P-dominated Tropics, respectively.

Overall, the monthly E-P fields estimated from SMOS are noisy, displaying only locally and indistinctly some of the E-P patterns in the Atlantic basin. Largest discrepancies with the OAFlux-GPCP E-P fields are observed in winter season in each hemisphere, when the climatological MLD deepens and shows the strongest month-to-month variations, particularly in the S. Subtropical Atlantic. Averaged zonally across the width of the "open" oceanic basin (excluding the western and eastern riverine subregions), SMOS E-P still indicates a poor correspondence with OAFlux-GPCP, both in magnitude and in latitudinal dependence.

Aiming to examine whether the band of maximum P under the ITCZ can be detected from SMOS, next the analysis considered the location and magnitude of zonal E-P minima averaged over the Tropical Atlantic subregion 0°-10°N. In general, SMOS E-P manages to capture most of the latitudinal ITCZ movement both on monthly and seasonal time scales, showing a latitudinal shift by $\sim$10° over the year with good repeatability. This broadly agrees with OAFlux-GPCP, albeit with a slight temporal offset ($\sim$2 months). Interestingly, SMOS captures noticeably well the monthly magnitude of zonal E-P minima over most of period 2010-2012, while on a seasonal basis, the agreement is less striking, primarily due to the large discrepancies in summer for all 3 years.

In turn, looking at whether the zonal E-P maxima from SMOS can capture the excess of E over P in two Subtropical regimes in the N. (15°-25°N) and S. (17.5°-27.5°S, 20°W-0°E) Subtropical Atlantic, respectively, suggests a weaker correspondence with OAFlux-GPCP E-P compared to the P-dominated regime. Nevertheless, in the N. Subtropical Atlantic, although SMOS does not display exactly the same position of zonal E-P maxima from OAFlux-GPCP, it still seems to capture some of their latitudinal variation in time, and satisfactory display their magnitude over most of the 3 years. In the S. Subtropical Atlantic, the seasonal SMOS E-P maxima occur at the same location with OAFlux-GPCP in boreal spring and autumn, and within 1-2 grid cells (2.5°-5°) in winter, while further southwards by 10° in all summers. SMOS shows a large seasonal variability of the E-P magnitude, being in best agreement with OAFlux-GPCP in autumn of all 3 years with differences of only 0.02-0.03 m/month, and secondarily in winters 2011-2012 and summer 2012. The different consistency of SMOS E-P with OAFlux-GPCP between the two Subtropical regimes is, at least partly, explained by the significant uncertainties in the MLD climatology, particularly in the S.H..

This better agreement of SMOS E-P with OAFlux-GPCP in the Tropical Atlantic compared to the Subtropical latitudes may be partly explained by the relationship of the E-P and MLD terms relative to dS/dt in the Equation 7.2. Given

that the MLD is generally deeper, i.e. larger MLD values, in the Subtropical Atlantic, where the strongest month-to-month variations are also observed, indicates a smaller contribution of the E-P term to dS/dt compared to the Tropics. In turn, a shallower MLD suggests that the E-P values have a larger effect on the salinity changes in the Equation 7.2, explaining further the better consistency of the derived SMOS E-P field in the Tropical Atlantic. Here it should be noted that reconstruction of SMOS E-P fields using different MLD datasets based on different determination criteria, and/or a fixed value of MLD for the Tropics and Subtropics, respectively, was also tested (plots not shown), and did not lead to any noticeable improvement to the observed noise.

On the other hand, the weaker link of SMOS SSS variations with E-P in the Subtropical regimes compared to the Tropical band likely suggests a more complex relation between them in regions characterized by E excess. The spatio-temporal shift seen in both P- and E-dominated regions potentially implies the joint contribution of freshwater fluxes and oceanic processes to SSS changes, particularly of horizontal advection. The findings of this work come in accordance with numerous other studies. *Reul et al.* (2013), based on SMOS 10-day fields, suggest a good agreement of negative SSS anomalies with strong positive P anomalies at a fixed point, or with negative E-P anomalies averaged in monthly bins over the northern Tropical Atlantic for 2010. *Bingham et al.* (2011), using in situ salinity observations, including Argo and World Ocean Database (WOD) data, and NCEP E-P estimates, find the seasonal cycles of near-surface salinity and freshwater fluxes to compare reasonably well, but with differences in amplitude and phase-relationship shifts, pointing to the importance of advection in the seasonal salt balance in this region (e.g. *Foltz et al.*, 2004; *Foltz and McPhaden*, 2008).

More recently, *Yu* (2014), using Aquarius SSS, Argo subsurface salinity, TRMM P, OAFlux E and wind stress, together with satellite-derived mean dynamic topography and sea surface height observations, points to the different relationship of the Tropical Pacific salinity minimum with E-P and mean Ekman advection between the western, central and eastern part of the basin. These two processes compete against each other in governing the SSS seasonal variability under the ITCZ. The observed Tropical Pacific low-salinity convergence zone (LSCZ), although owns its source to the ITCZ P, its generation and maintenance are dominated by wind-driven Ekman dynamics and not the surface freshwater flux. *Hasson et al.*, 2014, combined SMOS LOCEAN with TSG and Argo ISAS as well as DRAKKAR simulation model SSS outputs to analyze the 2010-2011 La Niña signature in the western Tropical Pacific. They find a bipolar SSS anomaly between the equatorial band and southwards, which is associated with both horizontal advection and surface forcing, primarily P, as the latter is strongly modulated during ENSO in the region. These two processes, together with subsurface forcing also control the S. Pacific Sea Surface Salinity maximum (*Hasson et al.*, 2013), in ratios similar to the ones observed for the N. Atlantic Salinity Maximum (*Qu et al.*, 2011).

Yu (2011) suggests that freshwater fluxes together with oceanic dynamics explain about 40% of the seasonal MLS variability over the global ocean, given uncertainties in the data and unresolved low-order salinity dynamics. On the other hand, *Vinogradova and Ponte* (2013) find a strong linear link between ECCO modelled salinity variations and E-P at annual and shorter time scales, only in regions with less than 0.2 pss monthly salinity changes and thus away from the equator and towards the borders of the Atlantic basin examined here, i.e. at ∼30°N and ∼30°S. Exceptions with E-P variations in the Tropics to be stronger than the oceanic processes may occur, such as towards the north-eastern Tropical Atlantic (see *Yu*, 2011, Figures 9 and 7), however, averaging zonally the E-P across the whole ("open") oceanic basin may impact both on its latitudinal location and magnitude. Thus, given the observed spatio-temporal shift, this explains to a great extent the poor correspondence in the monthly and annual zonal averages between SMOS and OAFlux-GPCP E-P across most latitudes of the basin.

The temporal lag between SMOS and OAFlux-GPCP E-P may also reflect a potential 2-3 month lag between the variable and its time derivative, as proposed by *Vinogradova and Ponte*, 2013. Likewise, they suggest that a potential MLD lag of ∼1 month to adapt to changes due to freshwater forcing, possibly decreases the amplitude of salinity variations relative to freshwater fluxes and introduces a phase shift between them, which comes in agreement with what is observed in this work. The monthly to seasonal time scales examined here are likely too coarse, in case this phase shift actually occurs within a month. Thus, in addition to uncertainties in its definition from the interpolated climatology, averaging the MLD every 2 months potentially contributes significantly to the noise in the reconstructed SMOS E-P fields. Examination of SMOS E-P on a finer temporal resolution, e.g. 10 days, would likely improve the correspondence of SSS variations with E-P by capturing, for instance, strong P events and thus, large E-P variations, however, at the cost of increasing the SMOS uncertainty. Consequently, it would not necessarily decrease the observed noise. Similarly, the chosen 2.5° x 2.5° spatial resolution of GPCP in order to avoid interpolation is likely too coarse to accurately recover most of the E-P variability on these short time scales. In accordance, weaker correlations between salinity variations and freshwater fluxes are found on larger than ∼100 km scales based on the ECCO model (*Vinogradova and Ponte*, 2013).

In addition to issues concerning the sensitivity to the spatio-temporal scales, use of satellite SSS observations corresponding to the first 1 cm of the ocean surface as representative of the MLS, may further affect the derived relationship between salinity variations and E-P, given also the necessary assumptions for the mixing depth of freshwater fluxes on monthly time scales. The better ability of SMOS to detect the Tropical E-P minima potentially leaves implications for the haline skin layer effect (e.g. *Zhang and Zhang*, 2012) on the SMOS measurements over E-dominated regions. Moreover, uncertainties and errors in all datasets, including the SMOS uncertainty of ∼0.3 pss over the Tropical/Subtropical Atlantic (See

Chapter 3, Section 3.2.3; *Reul and Tenerelli*, 2011; *Hernandez et al.*, 2014) and residual RFI effects likely contribute significantly to the noisy SMOS E-P fields, although the relaxation to the climatology of the CATDS-CECOS V02 SSS product for 2011-2012 would be expected to smooth out some of this noise. The same also applies for the observed discrepancies of SMOS E-P with OAFlux-GPCP, which are often considered here as the "reference" field, although they have their individual weaknesses and uncertainties and may not adequately represent the E-P field. Error estimates for OAFlux E are not currently available (to the author's knowledge), but they are expected to be noticeable, as the E field is derived from other variables (See discussion in Chapter 3; Section 3.3). The uncertainty of the GPCP v2.2 P data is estimated to be about 0.25 m/year in the Tropical/Subtropical Atlantic basin, increasing up to ∼0.45-0.6 m/year in the Tropical ITCZ band, slightly north of the equator (plot not shown), and thus noticeably large relative to the expected E-P signal (See, for instance, Figures 7.1 and 7.2). Similarly, the MLD uncertainty is generally considered to be equal to a few meters (*Berger et al.*, 2014), i.e. around 10 m (e.g. *Ren and Riser*, 2009). However the limited number of profiles per grid cell in the region of interest which are used to form the present MLD climatology (See Chapter 3, Figure 3.14), potentially indicates a much larger uncertainty, which is expected to also increase more during winter due to the even smaller number of observations, and thus, further degrading the quality of the results. Finally, differentiating SSS to reconstruct E-P from SMOS potentially increases further the observed noise in the SMOS E-P fields.

To conclude, in contrast to the preceding Chapters, this Chapter is a more exploratory analysis, which aimed at determining whether there is any relationship between SSS variations from SMOS and E-P, while neglecting the other terms of the salt budget equation. This simple balance does seem to hold for limited regions and times when the SMOS reconstructed E-P field is compared with OAFlux-GPCP (which itself contains large uncertainties). On monthly to seasonal time scales, the reconstruction of E-P from SMOS cannot work in regions where large SSS variations occur, i.e. in proximity to large river outflows or where the ocean circulation (horizontal and vertical advection and mixing) are dominant drivers of SSS changes. Given the major role of advection in most of the basin, further analysis and accounting for the influence of horizontal advection, is required to reveal where and when during the year a simple relationship between them may hold in both E-dominated and P-dominated regimes. Nevertheless, while highlighting the difficulties, the results presented here do provide some encouragement for the SSS-based E-P reconstruction. A more comprehensive understanding of the link of satellite SSS variations with E-P in the salt budget would contribute to the potential of assimilating satellite SSS observations into ocean models, and helping to constrain the E-P estimates and the global hydrological cycle (e.g. *Lagerloef et al.*, 2010).

Chapter 8

Conclusions

8.1 Overview of the achievements

Taking advantage of the availability of spatially dense sea surface salinity (SSS) measurements from space through the ESA SMOS mission, the rationale of this work was to characterize the SSS distribution and variability on short (seasonal to interannual) time scales, and investigate the role of surface freshwater fluxes, i.e. Evaporation minus Precipitation (E-P) and river outflow (R). Given its major influence on the Meridional Overturning Circulation (MOC) and the density-driven Thermohaline Circulation (THC), the focus is on the Tropical/Subtropical Atlantic basin 30°N-30°S, which encompasses two dynamically different atmospheric regimes, i.e. the E-dominated Subtropics and the P-dominated Tropics.

The general objectives of this PhD project, stated in Chapter 1, have been broadly met. The first part of the analysis carried out an examination of the Tropical Atlantic SSS seasonal variability in 2010, in conjunction with the Intertropical Convergence Zone (ITCZ) movement and the influence of the major Amazon/Orinoco and the Congo/Niger river systems on either side of the basin (Chapter 4 and *Tzortzi et al.*, 2013). Thereafter, the growing satellite SSS data record enabled a first analysis of the interannual variability of the SSS seasonal cycle relative to the influence of E, P, E-P and R variability in the Tropical Atlantic basin as a whole, and in the two river-dominated regions, over the first 3 years of SMOS (Chapter 5). The next step was to quantify the dominant spatial and temporal scales of SSS variability from SMOS over the Tropical/Subtropical Atlantic basin (Chapter 6). Finally, focusing on the surface freshwater forcing term of the salt budget equation, an exploratory analysis was undertaken for the estimation of E-P from satellite SSS variations, with the aim of defining whether and where SMOS can detect the main characteristics of the E-P distribution (Chapter 7).

The main achievements of this thesis are:

- The analysis of SMOS data provides new insights into the Tropical/Subtropical Atlantic SSS variability and its spatial and temporal scales on sub-annual to interannual time scales. It may also offer the potential to detect some of the main E-P characteristics in limited regions over monthly to seasonal time scales.

- Two west/east poles of strong SSS variations dominate the Tropical Atlantic variability close to the major Amazon/Orinoco and Congo/Niger river systems, with pronounced, out-of-phase SSS seasonal cycles that compensate each other on interannual time scales. The analysis points to the sensitivity of the Tropical Atlantic salinity budget and thus, of the larger-scale Atlantic circulation and variability, on the two river-influenced poles.

- P and R are the primary controlling drivers of SSS variability (E plays a minor role), competing with each other for their dominance on SSS variations in the two poles, which display varying spatial scales, but long persistence in time (sub-annually to interannually).

- On sub-annual to interannual time scales, the spatial scales of SSS in the Tropical/Subtropical Atlantic are anisotropic, i.e. up to ∼2660 km in the zonal (W-E), and ∼1300 km in the meridional (N-S) direction. The removal of the seasonal cycle decreases them substantially, i.e. by 40% in the zonal and 60% in the meridional direction, reaching ∼1660 km and ∼500 km, respectively.

- Coherent SSS variations persist up to ∼3-4 months over most of the Tropical/Subtropical Atlantic basin, and up to ∼2-3 months for the SSS anomalies.

- Spatially homogeneous SSS changes show the longest, overall, zonal length scales along two Tropical bands on either side of the equator, spanning over the whole basin width, and persisting on sub-annual to interannual time scales. Analysis of SSS anomalies indicates the seasonal ITCZ influence may act to mainly enhance the zonal spatial scales.

- The longest meridional length scales occur in the S. Subtropical, and secondarily western N. Subtropical Atlantic, in addition to the equatorward branches of the Subtropical Gyres and along the Boundary Currents for the SSS anomalies.

- Analyses suggest that advection may play an essential role in determining the spatio-temporal scales of SSS over most of the Atlantic basin. The reconstructed monthly E-P fields from SMOS are very noisy and show any correspondence with the OAFlux-GPCP estimates only in limited regions (e.g. in the ITCZ dominated band), and after much spatial averaging.

- At basin-wide scales, SMOS E-P minima manage to capture most of the latitudinal ITCZ movement both on monthly and seasonal time scales, albeit

with a slight temporal offset (∼2 months) compared to OAFlux-GPCP. They also display noticeably well the E-P magnitude, particularly their monthly values over most of the 3-year period.

- A potentially weaker or more complex link of SMOS SSS variations with E-P seems to hold in E-dominated regions. Nevertheless, SMOS still manages to capture some of the latitudinal variation of zonal E-P maxima in time and their magnitude, particularly in the S. and N. Subtropical Atlantic, respectively.

In this final Chapter, the main conclusions of the thesis are summarised and discussed (Section 8.2). The last section (Section 8.3) presents recommendations for expanding and taking forward the present analysis, as well as suggested directions for future research on the subject and the region of interest.

8.2 The main outcomes of the research

Seasonal SSS variability in the Tropical Atlantic

Chapter 4 presented the first satellite-based analysis of the Tropical Atlantic (20°N-20°S) SSS variability on seasonal time scales, using the first full year, 2010, of SMOS measurements from the Ifremer CATDS L3 products. This work is published in *Tzortzi et al.*, 2013. Over an annual cycle, SMOS reveals two "poles" of strong SSS seasonal variability in proximity to the outflows from the major Amazon/Orinoco and Congo/Niger river systems on either side of the basin. SSS at the two poles shows an amplitude of up to 6.5 pss, and out-of-phase by 6 months seasonal cycles, that largely compensate each other. This was the first time that this West-East compensation was observed. A much smaller SSS range (0.08 pss) is observed over the Tropical Atlantic basin 20°N-20°S as a whole. The dominant processes controlling the SSS variability were investigated using GPCPv2.2 P, OAFlux E, annual ORE-HYBAM and climatological river flow data from Dai and Trenberth. For the western pole (Amazon/Orinoco), SSS varies in phase with P and lags R by 1-2 months, while E variability is generally of minor importance. A more complex relationship between SSS and the surface forcing terms holds for the eastern pole (Congo/Niger), likely indicating the significant role of advection and mixing (*Yu*, 2011).

Interannual variability of Tropical Atlantic SSS seasonal cycle

Extending the same method to the following two years of complete SMOS data (2011-2012) in Chapter 5, offers a first analysis of the interannual variability of the Tropical Atlantic SSS from space. During the 3-year period, the seasonal cycle of SSS over the whole Tropical Atlantic basin was relatively constant, with a small amplitude increase from 0.08 pss in 2010 to 0.15 pss in 2012. The location

of SSS minima is closely linked to that of P maxima throughout the examined period, displaced northward in summer in accordance with the ITCZ location. Close to the major river systems, the strong local variations of SSS seen in 2010 continue to be apparent the next two years. The SSS annual range of 6 pss/6.5 pss in the western/eastern pole in 2010 is similar to the balance of ∼7 pss in both subregions in 2012, but is noticeably disrupted in 2011, with values of ∼7.6 pss/5.2 pss, respectively. Nevertheless, the western and eastern poles exhibit the same pronounced, out-of-phase seasonal cycles of SSS throughout the period 2010-2012, and the W-E seasonal compensation holds on interannual time-scales.

Given the dominance of seasonal variations in SSS over the Tropical Atlantic, the analysis considered deviations during the years 2010-2012 in each subregion from the 3-year SMOS and longer-term WOA09 climatological SSS mean cycle, respectively. Year-to-year variations of the SSS seasonal cycle in both poles are primarily due to the strong interannual variability of their SSS minima, as opposed to the generally constant maxima over the 3 years. The eastern pole shows a larger seasonal and interannual SSS variability, which is also apparent when compared with the two climatological cycles. Inter-comparison of the SMOS and WOA09 climatologies suggests large differences in both subregions, particularly the western pole. This could originate from the different depth of measurements, the spatio-temporal sparsity of WOA09 observations which hinders a satisfactory representation of the SSS variability, and/or the inability of long-term climatology of capturing the potential impact of major events during the examined years (e.g. El Niño/La Niña).

Investigation of the interannual phase-relationships between the seasonal cycles of SSS and the surface forcing terms of E, P and R, points to P and R as the primary drivers, which compete with each other to control the SSS variability in both poles throughout the period 2010-2012. Similarly to SSS, P and R display strong seasonal cycles. In contrast, E has small variability (both seasonally and interannually), and therefore, does not play an important role on the Tropical Atlantic SSS variability. In both subregions, R appears to lag P by a few months, potentially due to water storage, as suggested by *Chen et al.* (2010). Interannual variations in the phase-relationship between P and R may be also influenced by the ENSO phases, although the short time period examined here hinders any firm conclusions. Nevertheless, the observed lag of maximum Amazon/Orinoco discharge in 2012 relative to the maximum P rates seen in the previous two years, comes in accordance with the study of *Satyamurty et al.* (2013), who attribute the maximum runoff of the Amazon river in 2012 to the 2011 La Niña conditions. In turn, the lag of SSS minima relative to R maxima indicates the delay in the freshwater reaching the river mouth and then being advected by the surface currents. Variations in advection and mixing processes, and potential residual conditions from the previous year (*Grodsky et al.*, 2014a), may contribute further to the interannual SSS variability in the two subregions, while over the eastern pole, equatorial and

coastal upwelling may also have an impact. Nevertheless, the strong link of SSS to P and R (and thus P over land) in both poles over the 3 years likely suggests the secondary role of the other processes in SSS variations, while demonstrating clearly that salinity can serve as a natural indicator of the water cycle.

Regional SSS variations in the two river-influenced poles seem to play a key role on the sensitivity of the Tropical Atlantic salinity budget. Their exclusion from the analysis results in a weaker SSS seasonal cycle over the rest of the Tropical Atlantic basin, while the amplification of SSS variability if either pole is excluded from the full regional mean in all 3 years, particularly the eastern pole. If variations in the amplitude or phasing of the salinity variability in either pole occur, they may have consequences for the higher latitude circulation. This emphasizes the need to better understand the SSS variability in the two poles, and the potential link of these river-influenced regions to the larger-scale Atlantic circulation and variability.

Spatial and temporal characteristic scales of SSS in the Tropical/ Subtropical Atlantic

Another essential objective towards a better understanding and description of SSS variability is the determination of its spatio-temporal scales. This was addressed in Chapter 6 over the Tropical/Subtropical Atlantic basin 30°N-30°S, who presented for the first time a satellite-based examination of the SSS characteristic scales. The aim was to identify regions with spatially homogeneous SSS variations on sub-annual to interannual time scales. Similarly, the analysis examined temporal decorrelation lengths of SSS over the first 3 complete years (2010-2012) of SMOS data, to describe how quickly SSS changes evolve in the different regimes of the basin, pointing out regions where coherent SSS variations persist in time. Given that the correlation of a variable can arise both from itself and the factors that influence it (e.g. *Dale and Fortin*, 2009), the outcomes of this analysis also offer a more comprehensive interpretation of the different processes that control and are influenced by SSS in the region of interest.

SMOS reveals different SSS characteristic scales at different latitudes and longitudes over the Tropical/Subtropical Atlantic basin. On sub-annual to interannual time scales, the spatial decorrelation lengths of SSS are anisotropic, i.e. up to ∼2660 km in the zonal (W-E) and ∼1300 km in the meridional (N-S) direction. The removal of the seasonal cycle reveals substantially reduced spatial scales for the SSS anomalies, i.e. by ∼40% in the W-E and ∼60% in the N-S direction, reaching ∼1660 km and ∼500 km, respectively. Consistent SSS changes generally persist up to ∼3-4 months over most of the basin, while up to ∼2-3 months for the SSS anomalies. There is indirect evidence of advection playing potentially a crucial role in determining the spatio-temporal characteristic scales of SSS, both in the P- and E-dominated regions. Combined with the seasonal ITCZ migration, advection by the zonal surface currents may lead to the observed longest, overall,

zonal spatial SSS scales along two Tropical bands on either side of the equator, particularly north of it. Persisting on sub-annual to interannual time scales, coherent SSS changes along these bands span over the whole basin width. The removal of the seasonal cycle indicates the ITCZ influence in mainly acting to enhance both the zonal spatial and temporal decorrelation length scales of SSS, as homogeneous SSS anomalies continue to occur over long distances along the two Tropical bands, but are less persistent in time by ∼1 month. This is consistent with previous studies that emphasize the primary impact of anomalous Ekman advection (e.g. *Mignot and Frankignoul*, 2003) and geostrophic components (e.g. *Mignot*, 2004) in generating the interannual SSS changes.

In contrast, at the equator, there are noticeably shorter zonal spatial SSS scales, but with a long persistence in time (up to generally ∼2-3 months), regardless of the inclusion of seasonal cycle or not. Equatorial SSS anomalies display longer meridional spatial scales than northwards/southwards. This may indicate salt exchanges between the boundaries of the equatorial currents, and/or their interaction with equatorial upwelling, but these other processes have not been explored in this work. Close to the Amazon plume and the northern Gulf of Guinea, the dynamic, integrated effect of large freshwater input (due to the ITCZ-driven P and river discharge) with the regional ocean circulation probably prohibit homogeneous SSS variations to occur over large distances, i.e. up to only ∼600 km in the W-E and ∼300 km in the N-S direction. In contrast, the Orinoco region and the rest of Gulf of Guinea, dominated by the two aforementioned basin-wide bands, show longer zonal, as well as long meridional spatial scales (over ∼700 km) along the coasts of the latter region. SSS variations generally persist up to ∼3 months in the two river-influenced regions, and up to ∼4 months close to the Amazon and Congo river mouths, likely pointing to the amplitude of their seasonal cycle and the relatively constant influence of freshwater discharge over such long periods. Excluding the effect of seasonality, decreases the spatial scales of SSS anomalies, which however, have a longer persistence in time by up to ∼1 month close to the river mouths.

Towards the centres of the E-dominated Subtropics and in proximity to the SSS maximum regions, there are coherent SSS changes over long spatial and temporal scales of up to ∼3-4 months, in agreement with the expected small SSS variations there due to weak advection and mixing processes (e.g. *Vinogradova and Ponte*, 2013). However, along the branches of the Subtropical Gyres and the Boundary Currents, SSS variations show only long meridional spatial scales, particularly in the S.H.. SSS anomaly changes show a longer persistence in time along the southern and northern branches of the N. and S. Subtropical Gyres, respectively, which may indicate the expected slower equatorward flow of the Gyres. In contrast, along the coasts where the Boundary Currents flow, SSS changes persist by

∼1 month less on interannual, compared to sub-annual, time scales. At basin-wide scales, the temporal decorrelation length scales of SSS anomalies display an opposite latitudinal pattern relative to those for SSS over most of the basin.

Estimation of E-P field from SMOS SSS changes in the Tropical/ Subtropical Atlantic

Finally, Chapter 7 presented an exploratory analysis of the salt budget from satellite SSS, by attempting to reconstruct for the first time the E-P field from SMOS measurements. For this, the analysis explored the relationship between satellite SSS variations and E-P over the Tropical/ Subtropical Atlantic basin 30°N-30°S for the period 2010-2012, with a focus on where SMOS can detect the main characteristics of the E-P distribution.

Overall, the monthly E-P fields estimated from SMOS are noisy, displaying only locally and indistinctly some of the E-P patterns in the Atlantic basin. Largest discrepancies when compared to OAFlux-GPCP E-P are observed in winter season in each hemisphere, when the climatological MLD deepens and shows the strongest month-to-month variations, particularly in the S. Subtropical Atlantic. The large uncertainties in the MLD climatology, due to the limited number of observations and large areas with no data at all, especially in the S.H., are likely to contribute significantly to the noise in the reconstructed SMOS E-P fields. On basin-wide scales and away from the riverine influence, the correspondence between SMOS and OAFlux-GPCP still remains poor both in magnitude and in latitudinal dependence. However, one should bear in mind the impact of averaging zonally in introducing discrepancies in both the latitudinal position and magnitude, as pointed out by *Yu*, 2011.

Nevertheless, looking at the zonal E-P minima over a Tropical subregion (0°-10°N), SMOS E-P manages, in general, to capture most of the latitudinal ITCZ movement both on monthly and seasonal time scales, but with a slight temporal offset (∼2 months) compared to OAFlux-GPCP. Interestingly, SMOS E-P also captures noticeably well their magnitude, particularly their monthly values over most of period 2010-2012. The fairly long zonal spatial scales of homogeneous SSS variations along the Tropical band north of the equator, persisting on sub-annual to interannual time scales (as shown in Chapter 6), are likely to contribute to this better consistency of SMOS E-P with OAFlux-GPCP in the P-dominated regime. Their agreement in terms of magnitude is less striking on seasonal time scales, primarily due to the large discrepancies seen in all summers. This likely indicates the larger contribution of oceanic processes during this season, as for instance, of horizontal advection along the North Equatorial Counter Current (NECC) which shows strong variations in boreal summer (e.g. *Yu*, 2011), and of equatorial upwelling, primarily occurring during this season (e.g. *Keenlyside and Latif*, 2007).

In turn, examining whether the zonal E-P maxima from SMOS can capture the excess of E over P in two Subtropical regimes in the N. (15°-25°N) and S. (17.5°-27.5°S, 20°W-0°E) Subtropical Atlantic, respectively, suggests a weaker or potentially more complex link of SMOS SSS variations with E-P in E-dominated regions. Nevertheless, in the N. Subtropical Atlantic, although SMOS E-P does not display exactly the same position of zonal E-P maxima from OAFlux-GPCP, it still seems to capture some of their latitudinal variation in time, and satisfactorily display similar magnitude over most of the 3 years. In the S. Subtropical Atlantic, the seasonal SMOS E-P maxima occur at the same location with OAFlux-GPCP in boreal spring and autumn, and within 1-2 grid cells (2.5°-5°) in winter, while lying further southwards by 10° in all summers. Showing a large seasonal variability of the magnitude, SMOS is in best agreement with OAFlux-GPCP in autumn of all 3 years, with differences of only 0.02-0.03 m/month, and secondarily in winters 2011-2012 and summer 2012.

The observed spatio-temporal shift in the zonally averaged extrema in both P- and E-dominated regions likely implies the joint contribution of freshwater fluxes and oceanic processes to SSS changes, particularly of horizontal advection. In accordance with the findings presented here, *Reul et al.* (2013) using SMOS 10-day fields and satellite OSCAR (Ocean Surface Current Analysis Real Time, www.oscar.noaa.gov) surface currents, suggest a good agreement of negative SSS anomalies with strong positive P anomalies at a fixed point, or with negative E-P anomalies averaged in monthly bins over the northern Tropical Atlantic for 2010. *Bingham et al.* (2011), using in situ salinity observations, including Argo and World Ocean Database (WOD) data, and NCEP E-P estimates, find the seasonal cycles of near-surface salinity and freshwater fluxes to compare reasonably well, but with differences in amplitude and phase-relationship shifts. They also point to the importance of advection in the seasonal salinity balance in this region (e.g. *Foltz et al.*, 2004; *Foltz and McPhaden*, 2008). *Yu* (2011), based also on an observational analysis of the mixed layer salinity (MLS) budget, suggests that freshwater fluxes together with oceanic dynamics explain about 40% of the seasonal MLS variability over the global ocean, given uncertainties in the data and unresolved low-order salinity dynamics. On the other hand, a potential 2-3 month lag between the variable and its time derivative, as well as a potential delay of the MLD to adapt to freshwater changes introducing a phase shift between salinity variations and E-P (*Vinogradova and Ponte*, 2013), could all contribute to the observed shift and explain, at least partly, the noise in the SMOS E-P fields.

The monthly to seasonal time scales examined here are likely too coarse, as this MLD phase shift may actually occur within a month. Similarly, the coarse 2.5° x 2.5° spatial resolution imposed by the resolution of GPCP, hinders further the accurate detection of E-P variability on these short time scales. This is supported also by the weaker correlations found between salinity variations and freshwater fluxes on larger than ∼100 km scales based on ECCO model outputs (*Vinogradova*

and Ponte, 2013). Finally, the usage of satellite SSS observations corresponding to the first 1 cm of the ocean surface as representative of the MLS, the associated assumptions for the mixing depth of freshwater fluxes at monthly time scales, and uncertainties and errors in all datasets (including the OAFlux-GPCP which is often used here as a "reference" field), all introduce significant uncertainties in the SMOS-derived E-P. Thus, the reconstructed E-P field from SMOS do capture, but only locally, some of the main E-P characteristics on monthly to seasonal time scales. As expected, the approach does not work in regions of strong river influence and where the oceanic circulation (horizontal and vertical advection and mixing) are dominant drivers of the SSS changes.

To conclude, during this PhD, significant new results were obtained, thanks to the innovative exploitation of SMOS SSS data. The scientific understanding was improved with regard to many aspects of the SSS variability over the Tropical/-Subtropical Atlantic basin, on sub-annual to interannual time scales. The novel synthesis of SMOS SSS with satellite precipitation and in situ observations enables a new approach to examine the variability in the Tropical freshwater fluxes, and its potential impacts on the Atlantic ocean circulation. Arguing in support of the exploitation of satellite SSS observations from SMOS (and Aquarius/SAC-D), the achievements of this thesis demonstrate clearly the advantage of the improved spatio-temporal coverage of satellites in offering the potential for a more detailed depiction of the SSS variability in dynamic regions, such as close to major river systems, where in situ measurements remain very constrained. This is the first time (to the author's knowledge), that the combined influence of the Congo and Niger rivers on SSS variations in the Gulf of Guinea was examined, while pointing to the potentially significant link of these river-influenced regions on the Tropical Atlantic salt transport and budget. Improved knowledge of regional SSS variations in the Amazon/Orinoco and Congo/Niger plumes will contribute to many oceanographic fields, including biogeochemistry, ocean and atmospheric climate studies, while highlighting also the potential socio-economic impact of this new information for the large populations living along the Atlantic coasts. Moreover, an important outcome of this work is the first satellite-based description of the spatio-temporal scales of SSS variations in the Tropical/Subtropical Atlantic. Together with the potential of reconstructing some of the main E-P characteristics from satellite SSS observations, such information will be of great value for the potential assimilation of satellite SSS measurements into models to help constrain the uncertain E-P field, in addition to benefiting a wide range of oceanographic, freshwater budget and modelling studies. Finally, this research, by revealing the strong link of SSS variations with P and R seasonal cycles as well as the better consistency of the reconstructed SMOS E-P field to capture features of the ITCZ-driven Tropical P patterns, further demonstrates how SSS serves as a natural indicator of the water cycle.

8.3 Recommendations for future research

This final section presents recommendations on how the research in this thesis can be expanded in the future to provide further insights into the objectives addressed here. In addition, proposals are made for new research directions towards an improved description of the SSS field and its variability, and the further exploitation of satellite SSS observations.

Further analysis of the developing data record from SMOS, supplemented by Aquarius/ SAC-D and Argo float data (which provide useful complementary information on surface salinity but do not attain the spatio-temporal sampling possible from satellites), will improve our understanding on the SSS distribution and variability. Better knowledge of the interannual variations of the SSS seasonal cycle in the two Tropical Atlantic river-influenced poles will reveal whether their seasonal compensation continues to hold at multi-annual time-scales (Chapter 5). Equally important, a longer satellite-derived SSS record will supply new information to understand the impact of the El Niño/La Niña phases on SSS variations in the two poles and over the Tropical/Subtropical Atlantic basin as a whole. This research could be also supported by correlations between an ENSO index with SSS and the surface forcing terms, given that changes in P and zonal currents are the main mechanisms for the ENSO signatures in SSS (e.g. *Singh et al.*, 2011).

Accounting for variations in the spatial extent of the river plumes (see e.g. *Foltz and McPhaden*, 2008; *Grodsky et al.*, 2014a for the Amazon/Orinoco, and e.g. *Denamiel et al.*, 2013 for the Congo River) by performing a seasonal determination of the boundaries of the two poles would refine the estimation of area-weighted means of the examined variables, i.e. SSS, E, P, and E-P, offering potentially a clearer view of their phase-relationships. This, in conjunction with examination of the role of horizontal advection, by using for instance surface current velocities from OSCAR (Ocean Surface Current Analysis Real Time) or model outputs, would supply essential information on the advection processes and export freshwater pathways of each pole into the basin during the year. Identification of coherent spatio-temporal features between SSS and organic matter from satellite ocean colour data (e.g. *Reul et al.*, 2013) would also contribute to the study of the river plume pathways.

The complexity of year-to-year variations in each pole is also suggested by potential interconnections between them due to atmospheric and oceanic processes, such as through advection by the NECC, where fresh anomalies from the Amazon/Orinoco region may propagate up to the westernmost part of Gulf of Guinea (e.g. *Coles et al.*, 2013). Therefore, monitoring the freshwater advection pathways of the Amazon/Orinoco and Congo/Niger river systems along the surface currents may unveil any potential freshwater transport across the Atlantic basin via the Equatorial currents, and salt exchanges between the two poles. Consequently,

this would point out whether and how sub-annual to interannual variations in one plume may influence the variability of the other, while enriching our knowledge on the link of these regions to the larger-scale Atlantic circulation and variability.

Comparison of the outcomes of this analysis on the seasonal and interannual variability of the Tropical Atlantic SSS with Aquarius and near-surface in situ SSS datasets (e.g. *Reverdin et al.*, 2012) to check whether the same behaviour of SSS in the two poles is revealed, would be beneficial. This would also provide information on the performance of SMOS in proximity to the coast and the river plumes, where its uncertainty increases (*Reul et al.*, 2012b). In turn, it would indicate whether adjustment of the CATDS-CECOS version V02 data to the WOA01 climatology (i.e. the years 2011-2012) may excessively smooth some characteristics of the SSS variability in these dynamic river-influenced regions. On the other hand, performing a similar analysis with model outputs would allow the examination of the influence of more terms, such as advection and mixing processes on the SSS variability in each pole. Among others, that would also point to the relative role, for instance, of small-scale variability which becomes important in regions of strong stratification (ITCZ, rivers), and to the penetration depth of these fresh SSS signals close to the plumes.

Examination of the characteristic scales of SSS variations in time and space (Chapter 6) on a finer spatio-temporal resolution is essential in order to capture shorter mesoscale processes of SSS, that occur faster in time, with decorrelation lengths of less that 2 months. Establishment of the SMOS uncertainty relative to the observed length scales, and determination of the signal to noise ratio, is fundamental to distinguish the "real" signal from any measurements' noise. This would also help significantly in defining the potential of satellite SSS observations for assimilation into ocean models. Comparison of the characteristic SSS scales from different SMOS products (i.e. Ifremer, LOCEAN, ESA) and Aquarius fields would contribute towards this objective.

Equally important, a vital next step of this analysis (Chapter 6), which was not performed in this PhD due to the limited time, is the examination of cross-correlations between SSS and the freshwater terms, i.e. E-P, E, P, R, and horizontal advection. This will offer a clearer picture of how SSS changes in time and space relative to variations in the surface forcing terms, and where and when each controlling mechanism plays the dominant role on SSS variations over the different regimes of the Tropical/Subtropical Atlantic basin. In addition, new insights into potential interconnections among regions, such as between the two riverine poles mentioned above that likely influence further the spatio-temporal length scales of SSS, may be revealed, while contributing to a better interpretation of the observed patterns.

Improved refinement of the characteristic scales of SSS and identification of the most appropriate satellite SSS product will also benefit significantly the reconstruction of E-P field from SMOS (Chapter 7), and accordingly from Aquarius, by clarifying further fundamental aspects of the salt budget. These include, among others, the relation of satellite SSS variations with E-P and whether the observed SSS signals are due to accumulated or regional P, while helping to separate the role of freshwater fluxes from advection. Estimation of the SMOS E-P field on smaller time scales, e.g. 10 days, may improve the correspondence of SSS changes with E-P by capturing, for instance, strong P events and thus, large E-P variations. In turn, looking at shorter-term SSS variations occurring within a month would enable the avoidance of averaging the MLD and MLS fields every 2 months, and thus the ability to define more precisely any possible time lag, resulting potentially in more consistent E-P patterns. However, care should be taken with regard to the trade-off between a finer temporal resolution (e.g. 10 days) and the cost of increasing the uncertainty of satellite SSS measurements. As above, better determination of the SMOS uncertainty in terms of the characteristic spatio-temporal SSS scales will help to address these issues. Equally important, examination of the law of error propagation, i.e. accounting for uncertainties in each of the different terms considered for the reconstruction of SMOS E-P field, is essential for its refinement.

Inclusion of the role of horizontal advection term in the salinity budget would likely contribute to improved E-P fields from SMOS. This would offer new insights into the link of satellite SSS variations with E-P, and where and when during the year a linear relationship between them may hold over the P- and E-dominated regimes (including the SPURS regions). Similarly, accounting for the riverine freshwater input by performing, for instance, area-weighted means of SMOS E-P and including the R term, may enhance the ability of SMOS to capture the expected E-P patterns. Given that differentiation increases noise, inferring E-P from SMOS by integrating in time over the mixed layer depth and applying a smoothing filter to the noisy SMOS fields may also contribute to obtaining a clearer depiction of the E-P distribution from SMOS over the Atlantic Ocean, and then over other basins.

The long meridional spatial SSS scales along the coasts revealed from SMOS in this work (Chapter 6), such as near S. Africa where the Benguela Current flows, point to the possibility of using satellite SSS in synergy with other satellite (e.g. SST, SSH, ocean colour) and in situ measurements, to reveal new aspects of monitoring the Boundary Currents. Indeed, while writing this chapter, a first attempt has been published for the Gulf Stream in the N.W. Atlantic ($\sim$30°-50°N) using SMOS data, suggesting that satellite SSS serves as a better proxy to constrain the estimates of the surface density field (*Reul et al.*, 2014). In synergy with SSH and SST fields, remotely-sensed SSS can contribute to more clearly determine baroclinic instabilities that influence the surface dynamic topography without modifying the surface density. In turn, an interesting aspect is the synergy of satellite SSS and

gravity measurements from the GRACE mission to potentially examine the salt transport associated with these water masses.

Of high importance for many oceanographic and climate studies, improved knowledge of the Boundary Currents' characteristics will offer new information on the mesoscale features dominating them, the strong ocean-atmosphere interactions along them, and the salt transport pathways over the different branches of the Meridional Overturning Circulation and their variability. For instance, a better understanding of the Boundary Currents around Africa may provide new information on the transport of salty (and warm) water from the Indo-Pacific into the Atlantic basin through the Agulhas retroflection and leakage. Reaching up to the Gulf of Guinea through the Benguela and regional currents, new insights would be gained into the regional salt budget and the coastal upwelling processes, which further influence the SSS variability along the Atlantic coasts.

Finally, capturing the eddy fluxes is also essential elsewhere, such as in the N. Subtropical Atlantic, where eddies likely account for over ∼50% of the annual E-P balance (*Gordon and Giulivi*, 2014). Thus, given their potential important role on the uncertain E-P fields, improved monitoring of the mesoscale features would provide new information on their role in compensating the air-sea flux of freshwater (and heat), improving the E-P evaluation. For this, it would be also interesting to test the application of a newly developed algorithm for detecting SST fronts and the calculation of a frontal index (*Lekouara*, 2013) on satellite SSS images.

Prioritizing the above suggestions for future research is quite difficult, since they are in general strongly interrelated between them. Nevertheless, two main directions could be proposed: improving our knowledge on the Tropical/Subtropical Atlantic salinity budget and variability and its relation to the Atlantic MOC strength, and exploring the potential benefits of satellite SSS to data assimilation procedures and optimally interpolated products. As regards the former, examination of the salt transport and exchanges along the ocean currents, such as the Equatorial and Boundary Currents in the region of interest, is essential to understand any potential connectivity between the two river-influenced poles on either side of the basin and their role to the larger-scale Atlantic circulation. In turn, this would enable the examination of any salt transport from the Tropical/Subtropical Atlantic towards the higher latitudes and dense water formation regions, and from the Indo-Pacific into the Atlantic basin, providing a much wider understanding of the Atlantic salinity variability and the relative influence of the different controlling mechanisms in the region. Equally important, accessing the impact of satellite SSS observations to improve predictions and ocean state estimates is a very timely and important field of research, and many recent studies dealing with this issue suggest promising outcomes (*Vernieres et al.*, 2014; *Hackert et al.*, 2014; *Vinogradova et al.*, 2014; *Köhl et al.*, 2014). Thus, improved description of the characteristic length scales of SSS variations in time and space represents a vital

step to understand how (e.g. directly or indirectly), where and when satellite SSS measurements can be used to benefit data assimilation and optimal interpolation procedures.

To conclude, all the above clearly demonstrate the various research pathways opened up through this PhD work as well as the numerous possibilities of using satellite SSS measurements for future research applications. A new era for physical oceanography has just started with the first satellite salinity missions of SMOS and Aquarius, emphasizing the necessity of continuing the remotely-sensed SSS measurements from satellites to the future.

Appendix A

Comparison of SSS annual range in 2010 from CATDS SMOS versions V01 and V02

The two versions V01 and V02 of CATDS SMOS data are compared for their common period May-December 2010. V02 gives in general more data close to the coast, therefore, it is initially filtered to match the grid cells of V01 for consistency. Figure A.1 shows the annual range of SSS calculated for the period May-December 2010 from the two different versions. It reaches up to 5.66 pss in V01 and 6.09 pss in V02, indicating in general a good agreement between them, given all the uncertainties associated with SMOS data processing and the different corrections applied in each version. Moreover, defining the two poles according to the criterion that SSS range is greater than 1.5 pss, the two datasets give roughly the same grid cells in each subregion (Figure A.1, left panel and Figure A.2). Small differences are particularly observed south of the Gulf of Guinea where V01 has a few more grid cells.

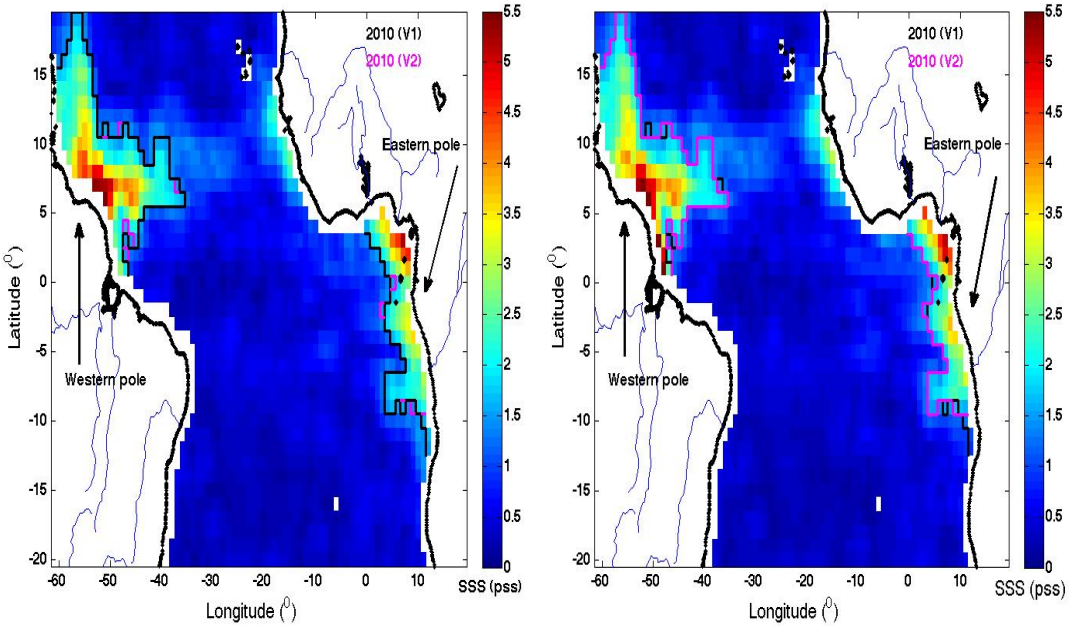

(a) Version V01 (b) Version V02

Figure A.1: SSS annual range in 2010 based on a) V01 and b) V02 for the common period May-December. Black (V01) and magenta (V02) solid lines in both figures indicate the boundaries of the two subregions defined according to the condition that the seasonal range in SSS is greater than 1.5 pss.

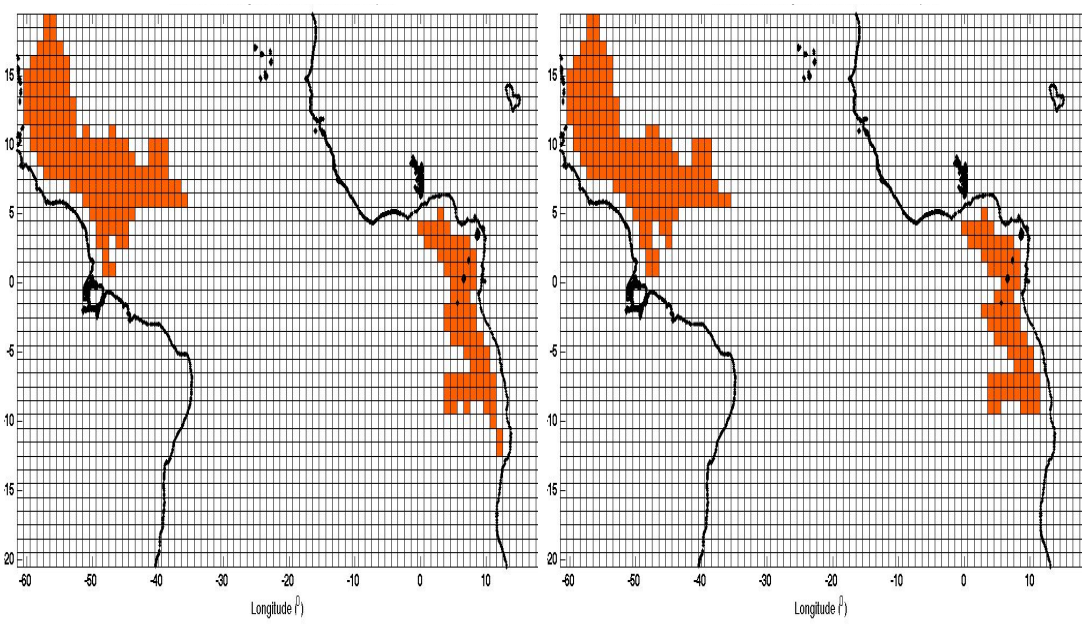

(a) Version V01 (b) Version V02

Figure A.2: Grids at the two subregions based on the criterion that the SSS range is greater than 1.5 pss at the common period May-December 2010 from a) V01 and b) V02.

Appendix B

[Tzortzi et al., 2013 GRL paper]

GEOPHYSICAL RESEARCH LETTERS, VOL. 40, 2143–2147, doi:10.1002/grl.50225, 2013

Tropical Atlantic salinity variability: New insights from SMOS

E. Tzortzi,[1,2] S. A. Josey,[1] M. Srokosz,[1] and C. Gommenginger[1]

Received 20 December 2012; revised 1 February 2013; accepted 5 February 2013; published 26 May 2013.

[1] Observations from the SMOS satellite are used to reveal new aspects of Tropical Atlantic sea surface salinity (SSS) variability. Over an annual cycle, the variability is dominated by eastern and western basin SSS "poles," with seasonal ranges up to 6.5 pss (practical salinity scale), that vary out of phase by 6 months and largely compensate each other. A much smaller SSS range (0.08 pss) is observed for the region as a whole. The dominant processes controlling SSS variability are investigated using GPCPv2.2 precipitation (P), OAFlux evaporation (E), and Dai and Trenberth river flow (R) data sets. For the western pole, SSS varies in phase with P and lags R by 1–2 months; a more complex relationship holds for the eastern pole. The synthesis of novel satellite SSS data with E, P, and R enables a new approach to determining variability in Tropical freshwater fluxes and its potential impacts on the Atlantic ocean circulation.
Citation: Tzortzi, E., S. A. Josey, M. Srokosz, and C. Gommenginger (2013), Tropical Atlantic salinity variability: New insights from SMOS, *Geophys. Res. Lett., 40*, 2143–2147, doi:10.1002/grl.50225.

1. Introduction

[2] Sea surface salinity (SSS) is a natural indicator of changes in the hydrological cycle [*IPCC*, 2007; *Bindoff et al*., 2007; *Yu*, 2011]. Salinity variations in recent decades [*Curry et al*., 2003; *Terray et al*., 2012; *Durack et al*., 2012] have been linked to the Atlantic meridional overturning circulation (MOC) strength and variability [*Thorpe et al*., 2001; *Häkkinen*, 2002; *Vellinga and Wu*, 2004; *Wang et al*., 2010]. The Tropical Atlantic is potentially important for the strength of the MOC via its influence on the salinity of waters advected to dense water formation regions [*Vellinga et al*., 2002; *Pardaens et al*., 2008]. However, a historical lack of in situ observations has prevented a reliable depiction of SSS variability in this region [*Delcroix et al*., 2005; *Reverdin et al*., 2007; *Gordon and Giulivi*, 2008].

[3] The recent advent of L-band satellite SSS measurements from the European Space Agency Soil Moisture and Ocean Salinity (SMOS) mission, launched in November 2009, provides a new opportunity to determine Tropical Atlantic SSS variability. The SMOS and more recent Aquarius/SACD salinity missions have started to provide new insights into SSS-related processes, for example, the eastern Pacific fresh pool [*Alory et al*., 2012], hurricanes [*Reul et al*., 2012a; *Grodsky et al*., 2012], and Tropical Instability Waves [*Lee et al*., 2012; *Lagerloef et al*., 2012].

[1]National Oceanography Centre Southampton, Southampton, UK.
[2]School of Ocean and Earth Science, University of Southampton, Southampton, UK.

Corresponding author: E. Tzortzi, Room 164/25, National Oceanography Centre, European Way, Southampton SO14 3ZH, UK. (E.Tzortzi@noc.soton.ac.uk)

0094-8276/13/10.1002/grl.50225

[4] We present here the first analysis of SSS variability at seasonal time scales in the Tropical Atlantic using data from SMOS. The salinity balance in this region is expected to be influenced by variations in precipitation and evaporation associated with the north-south movement of the Inter-Tropical Convergence Zone (ITCZ) and outflow from two of the largest global river systems: the Amazon/Orinoco and Niger/Congo. We use SMOS SSS observations in combination with the latest version of the GPCP precipitation (P), the OAFlux evaporation (E), and the Dai and Trenberth river flow (R) data sets to determine SSS changes throughout the annual cycle and investigate the key processes that control this variability.

[5] Previous analyses based on ship data are heavily limited by the concentration of data along a few narrow shipping routes and near-complete lack of information in between (see, e.g., Figure 1 of *Dessier and Donguy*, [1994]). Such analyses provide some indication of the influence of river outflow on salinity but are necessarily climatological in nature and only provide a "very crude picture of the SSS field" [*Dessier and Donguy*, 1994]. SMOS offers a major step forward as, for the first time, it is possible to quantify salinity variability using spatially complete fields for individual years rather than relying on heavily interpolated climatological data sets with significant sampling issues. The data sets that we employ are described in section 2, and our novel results are presented in section 3. This is followed by a discussion of their significance and conclusions in section 4.

2. Data Sets

[6] For this study, we use research SMOS SSS level 3 monthly mean products (V01) for the first complete year (2010) at 1.0° × 1.0° spatial resolution from the French Centre Aval de Traitement des Donnees SMOS (CATDS) [*Reul et al*., 2011]. The uncertainty of SMOS SSS in individual 1.0° grid cells in the Tropics has been estimated to be around 0.3 pss (practical salinity scale) [*Reul et al*., 2012b]. Monthly P fields for the same period have been taken from the latest satellite-gauge product of the Global Precipitation Climatology Project (GPCP), version 2.2 [*Huffman and Bolvin*, 2012] released in August 2012, at 2.5° × 2.5° resolution. Monthly E fields are acquired from the Objectively Analyzed air-sea Fluxes (OAFlux) hybrid data set [*Yu and Weller*, 2007; *Yu et al*., 2008], which has a 1.0° × 1.0° spatial resolution and is a combination of satellite and reanalysis data. Finally, time series of monthly river flow rates at the farthest downstream station for the Amazon, Orinoco, Congo, and Niger rivers are obtained from the Dai and Trenberth Global River Flow Dataset [*Dai and Trenberth*, 2002; *Dai et al*., 2009]. These are used to form climatological means for the common period of January 1941 to December 1992 when data are available for all four rivers. In addition, we have used data for 2010 from

the ORE-HYBAM network stations (www.ore-hybam.org) for the Amazon and Orinoco rivers. Note that data from this source are not available for the Niger so we are not able to include them in our eastern subregion analysis.

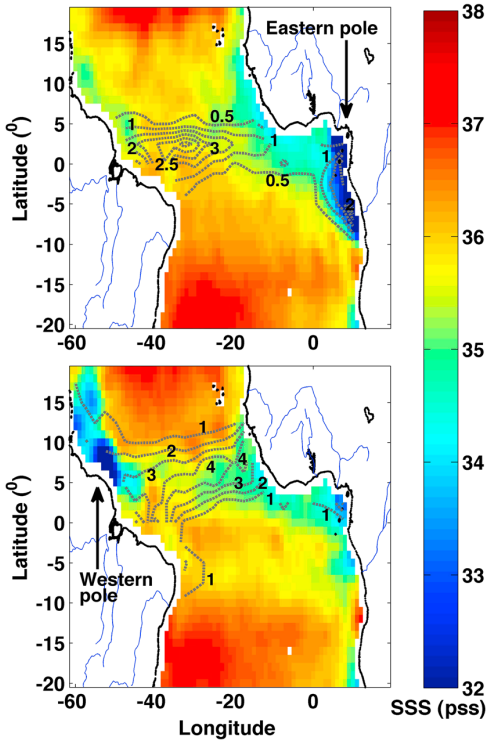

Figure 1. SMOS SSS mean (pss) in the Tropical Atlantic for (top) January and (bottom) July 2010, with GPCP P mean contours (m/year) overlaid. Note that P contours for January are shown every 0.5 m/year, while those for July are every 1 m/year (to avoid overcrowding of contour lines).

3. Results

3.1. SSS Variability in the Tropical Atlantic from SMOS

[7] Monthly mean fields of SSS from SMOS in the Tropical Atlantic are shown in Figure 1 for January and July 2010. SSS displays its highest values at the northern and southern extremes of this region throughout the year, reaching up to ~37.4 pss. In contrast, in the equatorial band, SSS is reduced, varying around 34.5–35.0 pss, and the location of this band is displaced northward in July relative to January. This is consistent with the northward displacement of the ITCZ and hence the zone of maximum P in boreal summer, as shown by the contours in Figure 1.

[8] By combining SMOS data with the latest version of the GPCP satellite precipitation data set and evaporation from OAFlux, we are able to carry out an observation-based comparison of these terms for individual months in 2010 (zonal means for January and July are shown in Figure 2, where the average at a given latitude is taken across the width of the basin). There is a clear alignment between the SSS minimum and the maximum (minimum) in P (E-P), indicating that at basin wide scales the position of the salinity minimum is tied to the precipitation maximum (the variation in E is relatively small across the Tropics). This is the first time that such an analysis has been possible using satellite data alone for the two principal fields (SSS and P) and demonstrates the ability of remote sensing for tracking variability in these key components of the Tropical freshwater budget.

[9] In addition, the SMOS data reveal the presence of seasonally dependent SSS minima (referred to hereafter as "poles") on opposite sides of the basin located north/south of the equator in the western/eastern basin (see Figure 1). These poles are close to the outflows of the major river systems, and previous analyses of climatological ship observation-based data sets suggest that outflow plays a significant role in their generation [*Dessier and Donguy*, 1994]. In the western Tropical Atlantic pole, the fresh signal is stronger in July (SSS as low as 29.7 pss) than January (SSS minimum ~35.0 pss). In contrast, the eastern Tropical Atlantic pole in the Gulf of Guinea has its lowest salinity in January (SSS ~28.8 pss) and is more saline in July (minimum 33.5 pss).

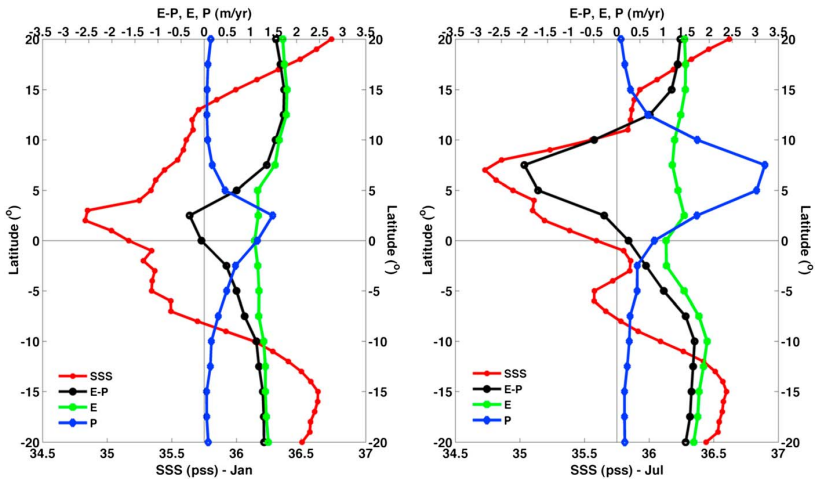

Figure 2. Tropical Atlantic zonal mean values for (red) SSS, (green) E, (blue) P, and (black) E-P for (left panel) January 2010 and (right panel) July 2010. The zonal mean at a given latitude is taken across the width of the basin.

[10] The two salinity poles are clearly evident in Figure 3, which shows the seasonal range of SSS in 2010 (i.e., the difference between the maximum and minimum monthly mean values in each grid cell). The magnitude of the range in each pole is similar, up to 6.5 (6) pss in the eastern (western) Tropical Atlantic. In contrast, the SSS seasonal range typically lies between 0.1 and 1.5 pss for the rest of the region.

[11] We have quantified the area-weighted mean SSS for subregions that encompass the two poles defined according to the criterion that the seasonal range in SSS exceeds 1.5 pss (different choices for this threshold have been considered and do not significantly modify our conclusions). These subregions are indicated by the areas outlined in black in Figure 3. The seasonal cycle of SSS for these two subregions, and the region from 20°N–20°S as a whole, is shown in Figure 4. SSS is typically fresher in the eastern subregion and has a slightly larger seasonal variability (here by ~0.35 pss) compared to the western subregion. The subregions are characterized by out-of-phase seasonal cycles and tend to compensate as the mean SSS for the whole region shows little seasonal variation. The seasonal range for the eastern subregion is 1.92 pss, for the western subregion is 1.57 pss, and for the region as a whole is 0.08 pss.

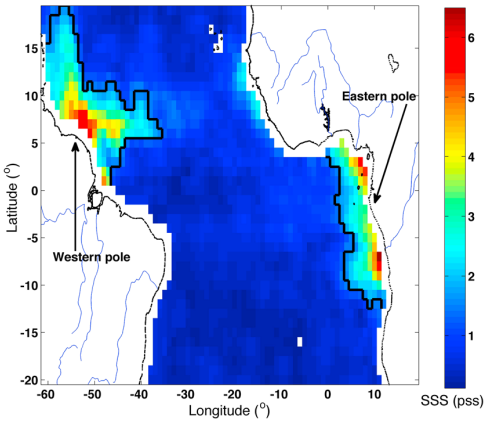

Figure 3. SMOS SSS range (maximum minus minimum during the year) in the Tropical Atlantic 20°N–20°S for 2010. The solid black lines indicate the boundaries of the western and eastern subregions defined according to the condition that the seasonal range in SSS is greater than 1.5 pss.

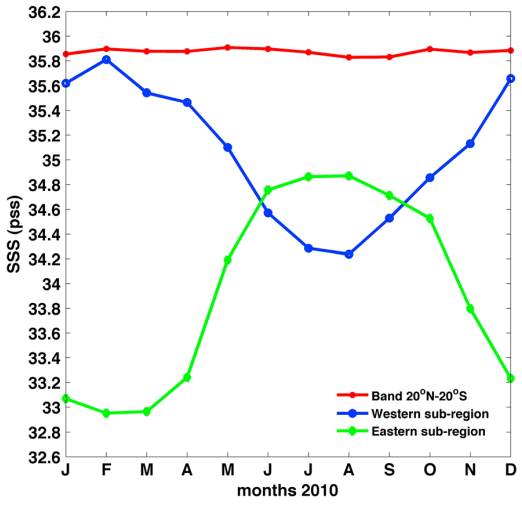

Figure 4. Area-weighted mean of SMOS SSS (pss) over (red) the whole region 20°N–20°S, (blue) the western subregion, and (green) the eastern subregion in 2010.

3.2. Relationship of SSS Variability to E, P, and R

[12] We now examine the extent to which the strong seasonal variability in SSS revealed by SMOS in the eastern and western subregions may be linked to variations in surface freshwater forcing due to evaporation, precipitation, and runoff. For this analysis, we focus on the phase relationships between the seasonal cycles of the different terms. This is supported by estimates of the relative magnitudes of the E, P, and R seasonal ranges (obtained by integrating over the relevant subregions in the case of E and P). The seasonal cycles of SSS, E-P, E, P, and R in each subregion are shown in Figure 5. In addition to climatological R, Figure 5 includes river discharge for 2010 obtained from the ORE-HYBAM network stations for the Amazon and Orinoco rivers in the western subregion.

[13] In the western subregion, strong seasonal cycles are evident in SSS, P, E-P, and R. SSS varies in phase with P, and lags R by about 1 month. To show the phase relationships more clearly, vertical lines on the figure indicate the months of maximum (February) and minimum (August) SSS. These coincide with the minimum and maximum months of the P cycle and lag the minimum (maximum) in R by 2 (1) months. In contrast to the other terms, E is relatively constant throughout the year and is thus unlikely to play a significant role in the strong SSS variability observed by SMOS. Consequently, the E-P seasonal cycle closely follows the variation found for P alone. The amplitudes of the E-P and R seasonal cycles are similar in magnitude implying a roughly equal contribution of variability in the air-sea freshwater flux (dominated by P) and the river outflow, R, to the seasonal variability in SSS. Caveats that need to be borne in mind here are that the R data are climatological in nature and that mixing and advective processes have been ignored. Note that the ORE-HYBAM data for R in 2010 show the same maximum and minimum months as the climatological data, indicating that our phase relationship conclusions drawn above are not affected by the use of climatological data for R. The amplitude of the cycle is larger than the climatological range, indicating a potentially more significant role for R in this particular year relative to the long-term mean.

[14] Seasonal cycles in all terms are observed in the eastern subregion as E now has a clearer seasonal variation than in the western subregion, although its amplitude remains smaller than P. The clear in-phase relationship betweeen SSS and P observed in the western subregion is no longer evident. The maximum in SSS falls within a prolonged 4 month period, July–September, in which P is at a minimum. However, the SSS minimum in February occurs at a time when P is close to the average for the year as a whole, and at this time, P exhibits strong intermonth variability. The intermonth variability may reflect limitations with the satellite data set as the eastern subregion is more coastally confined than the western subregion and the accuracy of the GPCPv2.2 precipiation retrievals are potentially influenced by the proximity of land.

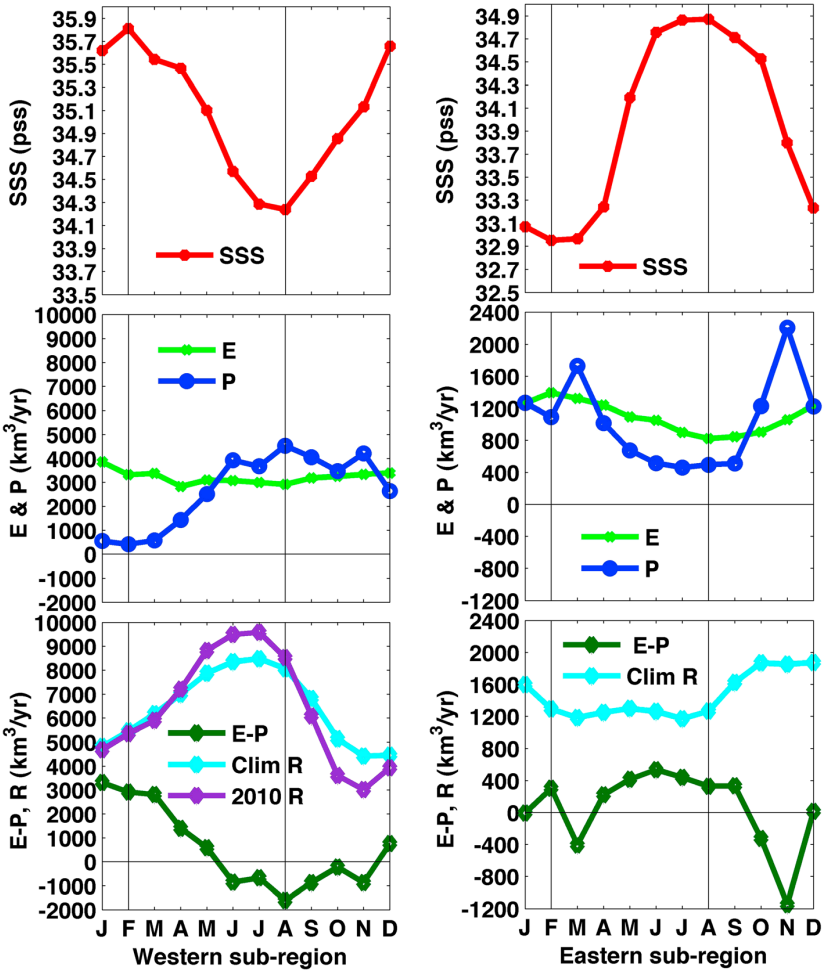

Figure 5. Seasonal cycles for 2010 of (red) area-weighted mean SMOS SSS and (light green) integrated OAFlux E, (blue) GPCP P, and (dark green) OAFLUX-GPCP E-P for the western subregion (left panel) and the eastern subregion (right panel). Also shown are the sum of the long-term climatological means of riverine flow rates (R, cyan lines) for the period 1941–1992 for the (bottom left panel) Amazon and Orinoco in the western subregion and (bottom right panel) Congo and Niger in the eastern subregion. Finally, ORE-HYBAM monthly river dicharge data for 2010 for the Amazon and Orinoco in the western subregion are shown in purple.

The relationship between SSS and R in the eastern subregion is also unclear as both the SSS maximum and minimum months have similar values for R (although there is some consistency as the SSS maximum falls at the end of a prolonged period, March–July, of low river outflow). The difference in strength of the SSS-R phase relationship between the two subregions may arise from the considerably lower outflow rates in the Congo/Niger river system (about 1500 km^3 $year^{-1}$) compared to the Amazon/Orinoco (about 7000 km^3 $year^{-1}$) that are likely to result in a weaker impact on SSS.

[15] In summary, the western subregion shows a clear relationship between SSS, P, and R with in-phase agreement between SSS and P and a 1–2 month lag of SSS with respect to R. The relationships in the eastern subregion are not well defined, and this may reflect a weaker R signal. In both cases, a more detailed treatment of the budgets, which takes into account advection and mixing, is required to make further progress.

4. Summary and Conclusions

[16] Analyses of ocean surface salinity variability to date have been severely limited by the lack of data as they have relied primarily on irregular, spatially inhomogeneous measurements from ships [e.g., *Dessier and Donguy*, 1994]. With the advent of spatially dense salinity measurements from space through the SMOS and Aquarius/SACD satellites, it is now possible to characterize sea surface salinity (SSS) variability in more detail to investigate the processes that drive it. We presented here the first satellite-based analysis of SSS variability at seasonal time scales in the Tropical Atlantic using the first full year, 2010, of SMOS measurements. Our results show that, in the Tropical Atlantic at least, the SMOS SSS data from CATDS are of sufficient quality to provide valuable scientific insight into processes governing SSS variability.

[17] The Tropical Atlantic has a relatively constant salinity throughout the year during 2010 varying by just 0.08 pss when averaged over the region as a whole. However, strong local variations are evident at two poles on opposite sides of the basin that are close to the outflows from the Amazon/Orinoco and Congo/Niger river systems. The SMOS measurements reveal large amplitude seasonal cycles up to 6.5 pss at these two sites that are out of phase by 6 months and compensate each other in their influence on the whole region's mean salinity. The relationships between these seasonal cycles and the surface forcing terms—E, P, and R—were investigated. For the western pole, SSS varies in phase with P, while it lags R by 1–2 months (E has little seasonal variability). In contrast, it is difficult to establish a clear relationship between SSS and the surface forcing terms for the eastern pole, and this may indicate a significant role for advection and mixing [*Yu*, 2011]. We plan to undertake a more detailed treatment of the budgets that takes into account advection and mixing in future research.

[18] Further analysis of the developing data record from SMOS, supplemented by Aquarius/SACD and Argo float data (which provide useful complementary information on surface salinity but do not achieve the spatial and temporal sampling possible using satellites), will reveal whether the seasonal compensation between the two poles continues to hold at multiannual time scales. The amplitude of the seasonal cycle in SSS for the full region doubles to about 0.16 pss if either pole is excluded from the full regional mean, indicating the sensitivity of the Tropical Atlantic salinity budget to their influence. Variations in the amplitude or phasing of the salinity variability in either pole thus have the potential to significantly modify Tropical Atlantic SSS with consequences for higher-latitude Atlantic circulation through modified surface layer density [*Vellinga and Wu*, 2004]. Such variations may be expected as result of natural variability (e.g., through the influence of El Niño) and anthropogenic climate change. To conclude, the novel results presented here clearly demonstrate (1) the potential of harnessing satellite-based SSS and P observations to develop our understanding of controls on ocean surface salinity and (2) their value in monitoring salinity variability over Tropical regions that have the potential to influence the larger-scale ocean circulation.

[19] **Acknowledgments.** We are grateful to our two reviewers for their helpful comments and for pointing us to the river discharge data for 2010 from ORE-HYBAM. We would also like to thank the Ocean Salinity Expertise Center (CECOS) and Centre Aval de Traitement des Donnees SMOS (CATDS; http://www.catds.fr/) for the availability of the SMOS SSS L3 product used in this work. The river flow data have been obtained from www.cgd.ucar.edu/cas/catalog/surface/dai-runoff/index.html and www.ore-hybam.org, the OAFlux data from http://oaflux.whoi.edu/data.html, and the GPCP data from http://precip.gsfc.nasa.gov/gpcp_v2.2_data.html.

References

Alory, G., C. Maes, T. Delcroix, N. Reul, and S. Illig (2012), Seasonal dynamics of sea surface salinity off Panama: The far eastern Pacific fresh pool, *J. Geophys. Res.*, *117*, C04028, doi:10.1029/2011JC007802.

Bindoff, N. L., et al. (2007), Observations: Oceanic climate change and sea level, in *Climate Change 2007: The Physical Science Basis: Contribution of Working Group I to the Fourth Assessment Report of the Intergovernmental Panel on Climate Change*, edited by S. Solomon et al., pp. 385–432, Cambridge University Press, New York.

Curry, R., R. R. Dickson, and I. Yashayaev (2003), A change in the fresh water balance of the Atlantic over the past four decades, *Nature*, *426* (6968), 826–829.

Dai, A., and K. E. Trenberth (2002), Estimates of freshwater discharge from continents: Latitudinal and seasonal variations, *J. Hydrometeorol.*, *3*, 660–687.

Dai, A., T. Qian, K. E. Trenberth, and J. D. Milliman (2009), Changes in continental freshwater discharge from 1948 to 2004, *J. Climate*, *22*, 2773–2792.

Delcroix, T., M. McPhaden, A. Dessier, and Y. Gouriou (2005), Time and space scales for sea surface salinity in the Tropical oceans, *Deep Sea Res., Part I*, *52*, 787–813.

Dessier, A., and J. R. Donguy (1994), The sea surface salinity in the tropical Atlantic between 10° S and 30° N - Seasonal and interannual variations (1977–1989), *Deep Sea Res., Part I*, *41*, 81–100, doi:10.1016/0967-0637(94)90027-2.

Durack, P. J., S. E. Wijffels, and R. J. Matear (2012), Ocean salinities reveal strong global water cycle intensification during 1950 to 2000, *Science*, *336*, 455–458, doi:10.1126/science.1212222.

Gordon, A. L., and C. F. Giulivi (2008), Sea surface salinity trends over fifty years within the subtropical North Atlantic, *Oceanography*, *21*(1a), 20–29.

Grodsky, S. A., N. Reul, G. Lagerloef, G. Reverdin, J. A. Carton, B. Chapron, Y. Quilfen, V. A. Kudryavtsev, and H.-Y. Kao (2012), Haline hurricane wake in the Amazon/Orinoco plume: AQUARIUS/SACD and SMOS observations, *Geophys. Res. Lett.*, *39*, doi:10.1029/2012GL053335.

Häkkinen, S. (2002), Surface salinity in the northern North Atlantic, *J. Geophys. Res.*, *107* (C12), 8003, doi:10.1029/2001JC00081.

Huffman, G. J., and D. T. Bolvin (2012), GPCP Version 2.2 Combined Precipitation Data Set Documentation, Laboratory for Atmospheres, NASA, 27 August 2012, ftp://precip.gsfc.nasa.gov/pub/gpcp-v2.2/doc/V2.2_doc.pdf.

Intergovernmental Panel on Climate Change (IPCC) (2007), *Climate Change: The Physical Science Basis*, edited by S. Solomon, D. Qin, M. Manning, Z. Chen, M. Marquis, K. B. Avery, M. Tignor, and H. L. Miller, Cambridge University Press, Cambridge, UK.

Lagerloef, G., F. Wentz, S. Yueh, H-Y. Kao, G. C. Johnson, and J. M. Lyman (2012), Aquarius satellite mission provides new, detailed view of sea surface salinity, *Bull. Am. Meteorol. Soc.*, *93* (7), S70–S71, doi:10.1175/2012BAMSStateoftheClimate.1.

Lee, T., G. Lagerloef, M. M. Gierach, H.-Y. Kao, S. Yueh, and K. Dohan (2012), Aquarius reveals salinity structure of Tropical instability waves, *Geophys. Res. Lett.*, *39*, L12610, doi:10.1029/2012GL052232.

Pardaens, A., M. Vellinga, P. Wu, and B. Ingleby (2008), Large-scale Atlantic salinity changes over the last half-century: A model–observation comparison, *J. Climate*, *21*, 1698–1720.

Reul, N., and Ifremer CATDS-CECOS Team (2011), SMOS L3 SSS Research Products: Product User Manual Reprocessed Year 2010, IFREMER, Plouzané, France.

Reul, N., J. Tenerelli, B. Chapron, D. Vandemark, Y. Quilfen, and Y. Kerr (2012a), SMOS satellite L-band radiometer. A new capability for ocean surface remote sensing in hurricanes, *J. Geophys. Res. Oceans*, *117*, C02006, doi:10.1029/2011JC007474.

Reul, N., J. Tenerelli, J. Boutin, B. Chapron, F. Paul, E. Brion, F. Gaillard, and O. Archer (2012b), Overview of the first SMOS sea surface salinity products. Part I: Quality assessment for the second half of 2010, *IEEE Trans. Geosci. Remote Sens.*, *50*, 1636–1647, doi:10.1109/TGRS.2012.2188408.

Reverdin, G., E. Kesterane, C. Frankignoul, and T. Delcroix (2007), Sea surface salinity in the Atlantic Ocean (30°S-50°N), *Prog. Oceanogr.*, *73*, 311–340, doi:10.1026/j.pocean.2006.11.004.

Terray, L., L. Corre, S. Cravatte, T. Delcroix, G. Reverdin, and A. Ribes (2012), Near-surface salinity as nature's rain gauge to detect human influence on the Tropical water cycle, *J. Climate*, *25*, 958–977.

Thorpe, R. B., J. M. Gregory, T. C. Johns, R. A. Wood, and J. F. B. Mitchell (2001), Mechanisms determining the Atlantic thermohaline circulation response to greenhouse gas forcing in a non-flux-adjusted coupled climate model, *J. Climate*, *14*, 3102–3116.

Vellinga, M., R. A. Wood, and J. M. Gregory (2002), Processes governing the recovery of a perturbed thermohaline circulation HadCM3, *J. Climate*, *15*, 764–780.

Vellinga, M., and P. Wu (2004), Low-latitude fresh water influence on centennial variability of the thermohaline circulation, *J. Climate*, *17*, 4498–4511.

Wang, C., S. Dong, and E. Munoz (2010), Seawater density variations in the North Atlantic and the Atlantic meridional overturning circulation, *Clim. Dyn.*, *34*, 953–968.

Yu, L., and R. Weller (2007), Objectively analyzed air–sea heat fluxes for the global ice-free oceans (1981–2005), *Bull. Am. Meteorol. Soc.*, *88*, 527–539.

Yu, L., X. Jin, and R. A. Weller (2008), Multidecade Global Flux Datasets from the Objectively Analyzed Air-sea Fluxes (OAFlux) Project: Latent and Sensible Heat Fluxes, Ocean Evaporation, and Related Surface Meteorological Variables, Technical Report OAFlux Project Technical Report (OA2008-01), Woods Hole Oceanographic Institution, http://oaflux.whoi.edu/publications.html.

Yu, L. (2011), A global relationship between the ocean water cycle and near-surface salinity, *J. Geophys. Res.*, *116*, C10025, doi:10.1029/2010JC006937.

References

Adler, R., G. Huffman, A. Chang, R. Ferraro, P.-P. Xie, J. Janowiak, B. Rudolf, U. Schneider, S. Curtis, D. Bolvin, A. Gruber, J. Susskind, P. Arkin, and E. Nelkin (2003), The version-2 global precipitation climatology project (GPCP) monthly precipitation analysis (1979-present), *Journal of Hydrometeorology*, *4*, 1147–1167.

Allen, M. R., and W. J. Ingram (2002), Constraints on future changes in climate and the hydrologic cycle., *Nature*, *419*(6903), 224–32, doi:10.1038/nature01092.

Alory, G., C. Maes, T. Delcroix, N. Reul, and S. Illig (2012), Seasonal dynamics of sea surface salinity off Panama: The far Eastern Pacific Fresh Pool, *Journal of Geophysical Research*, *117*(C4), C04,028, doi:10.1029/2011JC007802.

Anderson, J. E., and S. C. Riser (2012), Near-Surface Variability of Temperature and Salinity : Observations from Profiling Floats, in *Aquarius/SACD Science Team Meeting*, Buenos Aires, Argentina.

Antonov, J. I. (2002), Steric sea level variations during 19571994: Importance of salinity, *Journal of Geophysical Research*, *107*(C12), 8013, doi:10.1029/2001JC000964.

Antonov, J. I., D. Seidov, T. P. Boyer, R. Locarnini, A. Mishonov, H. E. Garcia, O. Baranova, M. Zweng, and D. Johnson (2010), *World Ocean Atlas 2009 Volume 2 : Salinity*, vol. 2, 184 pp., S. Levitus Ed. NOAA Atlas NESDIS 69, U.S. Gov. Printing Office, Washington, D.C.

Balaguru, K., P. Chang, R. Saravanan, L. R. Leung, Z. Xu, M. Li, and J.-S. Hsieh (2012), Ocean barrier layers effect on tropical cyclone intensification, *109*(36), 14,343–14,347, doi:10.1073/pnas.1201364109.

Ballabrera-Poy, J., R. Murtugudde, and A. J. Busalacchi (2002), On the potential impact of sea surface salinity observations on ENSO predictions, *Journal of Geophysical Research*, *107*(C12), 8007, doi:10.1029/2001JC000834.

Banks, C. J., C. P. Gommenginger, M. A. Srokosz, and H. M. Snaith (2012), Validating SMOS Ocean Surface Salinity in the Atlantic With Argo and Operational Ocean Model Data, *IEEE Transactions on Geoscience and Remote Sensing*, *50*(5), 1688–1702, doi:10.1109/TGRS.2011.2167340.

Batteen, M. L., C. A. Collins, C. R. Gunderson, and C. S. Nelson (1995), The effect of salinity on density in the California Current system, *Journal of Geophysical Research*, *100*(C5), 8733, doi:10.1029/95JC00424.

Berger, H., A. M. Treguier, N. Perenne, and C. Talandier (2014), Dynamical contribution to sea surface salinity variations in the eastern Gulf of Guinea based on numerical modelling, *Climate Dynamics*, *43*(11), 3105–3122, doi: 10.1007/s00382-014-2195-4.

Bindoff, N., J. Willebrand, V. Artale, A. Cazenave, J. Gregory, S. Gulev, K. Hanawa, C. L. Quéré, S. Levitus, Y. Nojiri, C. Shum, L. Talley, and A. Unnikrishnan (2007), Observations: oceanic climate change and sea level, in *Climate Change 2007: The Physical Science Basis. Contribution of Working Group I to the Fourth Assessment Report of the Intergovernmental Panel on Climate Change*, Solomon, S. Qin, S. Manning, M. Chen, Z. Marquis, M. Averyt, K.B. Tignor, M. Miller, H.L. (eds.), Cambridge University Press, Cambridge, United Kingdom and New York, NY, USA.

Bingham, F. M., G. R. Foltz, and M. J. McPhaden (2010), Seasonal cycles of surface layer salinity in the Pacific Ocean, *Ocean Science*, *6*(3), 775–787, doi: 10.5194/os-6-775-2010.

Bingham, F. M., G. R. Foltz, and M. J. McPhaden (2011), Characteristics of the seasonal cycle of surface layer salinity in the global ocean, *Ocean Science Discussions*, *8*(6), 2377–2415, doi:10.5194/osd-8-2377-2011.

Bourlès, B., R. Lumpkin, M. J. McPhaden, F. Hernandez, P. Nobre, E. Campos, L. Yu, S. Planton, A. Busalacchi, A. D. Moura, J. Servain, and J. Trotte (2008), The Pirata Program: History, Accomplishments, and Future Directions, *Bulletin of the American Meteorological Society*, *89*(8), 1111–1125, doi: 10.1175/2008BAMS2462.1.

Boutin, J., and N. Martin (2006), ARGO Upper Salinity Measurements: Perspectives for L-Band Radiometers Calibration and Retrieved Sea Surface Salinity Validation, *IEEE Geoscience and Remote Sensing Letters*, *3*(2), 202–206, doi: 10.1109/LGRS.2005.861930.

Boutin, J., and N. Martin (2014), Sea surface salinity under rain cells: SMOS satellite and in situ drifters observations, *Journal of Geophysical Research: Oceans*, pp. 5533–5545, doi:10.1002/2014JC010070.Received.

Boutin, J., P. Waldteufel, N. Martin, G. Caudal, and E. Dinnat (2004), Surface Salinity Retrieved from SMOS Measurements over the Global Ocean: Imprecisions Due to Sea Surface Roughness and Temperature Uncertainties, *Journal of Atmospheric and Oceanic Technology*, *21*(9), 1432–1447, doi:10.1175/1520-0426(2004)021⟨1432:SSRFSM⟩2.0.CO;2.

Boutin, J., N. Martin, X. Yin, J. Font, N. Reul, and P. Spurgeon (2012), First Assessment of SMOS Data Over Open Ocean: Part IISea Surface Salinity, *IEEE Transactions on Geoscience and Remote Sensing*, *50*(5), 1662–1675, doi: 10.1109/TGRS.2012.2184546.

Boutin, J., N. Martin, G. Reverdin, X. Yin, and F. Gaillard (2013), Sea surface freshening inferred from SMOS and ARGO salinity: impact of rain, *Ocean Science*, *9*(1), 183–192, doi:10.5194/os-9-183-2013.

Boyer, T., S. Levitus, J. Antonov, R. Locarnini, A. Mishonov, H. Garcia, and S. a. Josey (2007), Changes in freshwater content in the North Atlantic Ocean 1955-2006, *Geophysical Research Letters*, *34*(16), doi:10.1029/2007GL030126.

Boyer, T. P., and S. Levitus (2002), Harmonic analysis of climatological sea surface salinity, *Journal of Geophysical Research*, *107*(C12), 8006, doi:10.1029/ 2001JC000829.

Boyer, T. P., S. Levitus, J. I. Antonov, R. Locarnini, and H. E. Garcia (2005), Linear trends in salinity for the World Ocean, 19551998, *Geophysical Research Letters*, *32*(1), L01,604, doi:10.1029/2004GL021791.

Brandt, P., M. Araujo, B. Bourlès, M. Dengler, W. E. Johns, C. F. Lumpkin, M. J. Mcphaden, P. Nobre, and L. Terray (2013), Tropical Atlantic Climate Experiment (TACE), in *CLIVAR Exchanges*, vol. 18, pp. 6–11, International CLIVAR Project Office.

Breugem, W.-P., W. Hazeleger, and R. J. Haarsma (2007), Mechanisms of Northern Tropical Atlantic Variability and Response to CO 2 Doubling, *Journal of Climate*, *20*(11), 2691–2705, doi:10.1175/JCLI4137.1.

Breugem, W.-P., P. Chang, C. J. Jang, J. Mignot, and W. Hazeleger (2008), Barrier layers and tropical Atlantic SST biases in coupled GCMs, *Tellus A*, *60*(5), 885–897, doi:10.1111/j.1600-0870.2008.00343.x.

Carton, J. (1991), Effect of Seasonal Surface Freshwater Flux on Sea Surface Temperature in the Tropical Atlantic Ocean, *Journal of Geophysical Research: Oceans*, *96*, 12,593–12,598.

Carton, J., and Z. Zhou (1997), Annual cycle of sea surface temperature in the tropical Atlantic Ocean, *Journal of Geophysical Research*, *102*(C13), 27,813–27,824.

Carval, T., B. Keeley, Y. Takatsuki, T. Yoshida, S. Loch, C. Schmid, R. Goldsmith, A. Wong, R. McCreadie, and A. Thresher (2006), Argo Data Management: Users Manual, *Tech. rep.*, Ifremer, Brest, France.

Chen, J. L., C. R. Wilson, and B. D. Tapley (2010), The 2009 exceptional Amazon flood and interannual terrestrial water storage change observed by GRACE, *Water Resources Research*, *46*(12), doi:10.1029/2010WR009383.

Coles, V. J. V., M. M. T. Brooks, J. Hopkins, M. R. Stukel, P. L. Yager, and R. R. Hood (2013), The pathways and properties of the Amazon River Plume in the tropical North Atlantic Ocean, *Journal of Geophysical Research: Oceans*, *118*(12), 6894–6913, doi:10.1002/2013JC008981.

Cooley, S. R., V. J. Coles, a. Subramaniam, and P. L. Yager (2007), Seasonal variations in the Amazon plume-related atmospheric carbon sink, *Global Biogeochemical Cycles*, *21*(3), n/a–n/a, doi:10.1029/2006GB002831.

Cronin, M. F., and M. J. McPhaden (1999), Diurnal cycle of rainfall and surface salinity in the Western Pacific Warm Pool, *Geophysical Research Letters*, *26*(23), 3465–3468, doi:10.1029/1999GL010504.

Cubasch, U., G. Meehl, and G. Boer (2001), Projections of future climate change, in *Climate Change 2001: The Scientific Basis. Contribution of Working Group I to the Third Assessment Report of the Intergovernmental Panel on Climate Change*, edited by C. I. J. Houghton, J. T., Y. Ding, D. J. Griggs, M. Noguer, P. van der Linden, X. Dai, K. Maskell, chap. 9, pp. 525–582, Cambridge University Press, Cambridge, United Kingdom.

Curry, R., and C. Mauritzen (2005), Dilution of the northern North Atlantic Ocean in recent decades., *Science (New York, N.Y.)*, *308*(5729), 1772–4, doi:10.1126/science.1109477.

Curry, R., B. Dickson, and I. Yashayaev (2003), A change in the freshwater balance of the Atlantic Ocean over the past four decades., *Nature*, *426*(6968), 826–9, doi:10.1038/nature02206.

Da-Allada, C. Y., G. Alory, Y. du Penhoat, E. Kestenare, F. Durand, and N. M. Hounkonnou (2013), Seasonal mixed-layer salinity balance in the tropical Atlantic Ocean: Mean state and seasonal cycle, *Journal of Geophysical Research: Oceans*, *118*(1), 332–345, doi:10.1029/2012JC008357.

Dai, A., and K. Trenberth (2002), Estimates of freshwater discharge from continents: Latitudinal and seasonal variations, *Journal of hydrometeorology*, pp. 660–687, doi:http://dx.doi.org/10.1175/1525-7541(2002)003⟨0660:EOFDFC⟩2.0.CO;2.

Dai, A., T. Qian, K. E. Trenberth, and J. D. Milliman (2009), Changes in Continental Freshwater Discharge from 1948 to 2004, *Journal of Climate*, *22*(10), 2773–2792, doi:10.1175/2008JCLI2592.1.

Dale, M. R. T., and M.-J. Fortin (2009), Spatial autocorrelation and statistical tests: Some solutions, *Journal of Agricultural, Biological, and Environmental Statistics*, *14*(2), 188–206, doi:10.1198/jabes.2009.0012.

Dauphinee, T. (1980), Introduction to the Special Issue on the Practical Salinity Scale 1978, *IEEE Journal of Oceanic Engineering*, *OE-5*(1), 1–2.

de Boyer Montégut, C., G. Madec, A. S. Fischer, A. Lazar, and D. Iudicone (2004), Mixed layer depth over the global ocean: An examination of profile data and a profile-based climatology, *Journal of Geophysical Research*, *109*(C12), C12,003, doi:10.1029/2004JC002378.

de Boyer Montégut, C. C., J. Mignot, A. Lazar, and S. Cravatte (2007), Control of salinity on the mixed layer depth in the world ocean: 2. Tropical areas, *Journal of Geophysical Research*, *112*(C10), C10,010, doi:10.1029/2006JC003954.

Delcroix, T., and C. Hénin (1991), Seasonal and interannual variations of sea surface salinity in the tropical Pacific Ocean, *Journal of Geophysical Research*, *96*(C12), 22,135, doi:10.1029/91JC02124.

Delcroix, T., and M. McPhaden (2002), Interannual sea surface salinity and temperature changes in the western Pacific warm pool during 19922000, *Journal of Geophysical Research*, *107*(C12), 8002, doi:10.1029/2001JC000862.

Delcroix, T., M. J. McPhaden, A. Dessier, and Y. Gouriou (2005), Time and space scales for sea surface salinity in the tropical oceans, *Deep Sea Research Part I: Oceanographic Research Papers*, *52*(5), 787–813, doi:10.1016/j.dsr.2004.11.012.

Delcroix, T., S. Cravatte, and M. J. McPhaden (2007), Decadal variations and trends in tropical Pacific sea surface salinity since 1970, *Journal of Geophysical Research*, *112*(C3), C03,012, doi:10.1029/2006JC003801.

Denamiel, C., W. P. Budgell, and R. Toumi (2013), The Congo River plume: Impact of the forcing on the far-field and near-field dynamics, *Journal of Geophysical Research: Oceans*, *118*(2), 964–989, doi:10.1002/jgrc.20062.

Dessier, A., and J. R. Donguy (1994), The sea surface salinity in the tropical Atlantic between 10S and 30Nseasonal and interannual variations (19771989), *Deep Sea Research Part I: Oceanographic Research Papers*, *41*(1), 81–100, doi:10.1016/0967-0637(94)90027-2.

Dickson, R., B. Rudels, S. Dye, M. Karcher, J. Meincke, and I. Yashayaev (2007), Current estimates of freshwater flux through Arctic and subarctic seas, *Progress in Oceanography*, *73*(3-4), 210–230, doi:10.1016/j.pocean.2006.12.003.

Dinnat, E. P., J. Boutin, G. Caudal, and J. Etcheto (2003), Issues concerning the sea emissivity modeling at L band for retrieving surface salinity, *Radio Science*, *38*(4), doi:10.1029/2002RS002637.

Doney, S. C., D. M. Glover, M. S. J., and M. Fuentes (2003), Mesoscale variability of Sea-viewing Wide Field-of-view Sensor (SeaWiFS) satellite ocean color: Global patterns and spatial scales, *Journal of Geophysical Research*, *108*(C2), 3024, doi:10.1029/2001JC000843.

Donguy, J.-R., and G. Meyers (1996), Mean annual variation of transport of major currents in the tropical Pacific Ocean, *Deep Sea Research Part I: Oceanographic Research Papers*, *43*(7), 1105–1122, doi:10.1016/0967-0637(96)00047-7.

Donohoe, A., J. Marshall, D. Ferreira, K. Armour, and D. McGee (2014), The Interannual Variability of Tropical Precipitation and Interhemispheric Energy Transport, *Journal of Climate*, *27*(9), 3377–3392, doi:10.1175/JCLI-D-13-00499.1.

Durack, P. J., and S. E. Wijffels (2010), Fifty-Year Trends in Global Ocean Salinities and Their Relationship to Broad-Scale Warming, *Journal of Climate*, *23*(16), 4342–4362, doi:10.1175/2010JCLI3377.1.

Durack, P. J., S. E. Wijffels, and R. J. Matear (2012), Ocean salinities reveal strong global water cycle intensification during 1950 to 2000., *Science (New York, N.Y.)*, *336*(6080), 455–8, doi:10.1126/science.1212222.

Durand, F., and L. Gourdeau (2002), Assimilation of sea surface salinity in a tropical Oceanic General Circulation Model (OGCM): A twin experiment approach, *Journal of Geophysical Research*, *107*(C12), 8004, doi:10.1029/2001JC000849.

Durand, F., G. Alory, R. Dussin, and N. Reul (2013), SMOS reveals the signature of Indian Ocean Dipole events, *Ocean Dynamics*, (October), doi:10.1007/s10236-013-0660-y.

Eden, C. (2007), Eddy length scales in the North Atlantic Ocean, *Journal of Geophysical Research*, *112*(C6), C06,004, doi:10.1029/2006JC003901.

Emile-Geay, J. (2003), Warren revisited: Atmospheric freshwater fluxes and Why is no deep water formed in the North Pacific, *Journal of Geophysical Research*, *108*(C6), 3178, doi:10.1029/2001JC001058.

Fairall, C., E. Bradley, and J. Hare (2003), Bulk parameterization of air-sea fluxes: Updates and verification for the COARE algorithm, *Journal of . . .*, *16*, 571–591.

Fairall, C., B. Barnier, D. Berry, M. Bourassa, E. Bradley, C. Clayson, G. de Leeuw, W. Drennan, S. Gille, S. Gulev, E. Kent, W. McGillis, G. Quartly, V. Ryabinin, S. Smith, R. Weller, M. Yelland, and H.-M. Zhang (2010), Observations to Quantify Air-Sea Fluxes and Their Role in Climate Variability and Predictability, in *Proceedings of OceanObs09: Sustained Ocean Observations and Information for Society, Vol. 2.*, edited by D. Hall, J., Harrison, D.E. and Stammer, 6, pp. 299–313, European Space Agency, Noordwijk, The Netherlands, doi:10.5270/OceanObs09.cwp.27.

Ffield, A. (2007), Amazon and Orinoco River Plumes and NBC Rings: Bystanders or Participants in Hurricane Events?, *Journal of Climate*, *20*(2), 316–333, doi:10.1175/JCLI3985.1.

Foltz, G. R., and M. J. McPhaden (2008), Seasonal mixed layer salinity balance of the tropical North Atlantic Ocean, *Journal of Geophysical Research*, *113*(C2), C02,013, doi:10.1029/2007JC004178.

Foltz, G. R., S. A. Grodsky, and J. A. Carton (2004), Seasonal salt budget of the northwestern tropical Atlantic Ocean along 38W, *Journal of Geophysical Research*, *109*(C3), C03,052, doi:10.1029/2003JC002111.

Foltz, G. R., M. J. McPhaden, and R. Lumpkin (2012), A Strong Atlantic Meridional Mode Event in 2009: The Role of Mixed Layer Dynamics, *Journal of Climate*, *25*(1), 363–380, doi:10.1175/JCLI-D-11-00150.1.

Font, J., J. Boutin, and N. Reul (2010a), SMOS: Objectives and approach for ocean salinity observations, in *Proc. ESA Living Planet Symposium*, 1, Bergen, Norway.

Font, J., A. Camps, A. Borges, M. Martin-Neira, J. Boutin, N. Reul, Y. H. Kerr, A. Hahne, and S. Mecklenburg (2010b), SMOS: The Challenging Sea Surface Salinity Measurement From Space, *Proceedings of the IEEE*, *98*(5), 649–665, doi:10.1109/JPROC.2009.2033096.

Font, J., J. Boutin, N. Reul, P. Spurgeon, J. Ballabrera-Poy, A. Chuprin, C. Gabarró, J. Gourrion, S. Guimbard, C. Hénocq, S. Lavender, N. Martin, J. Martínez, M. McCulloch, I. Meirold-Mautner, C. Mugerin, F. Petitcolin, M. Portabella, R. Sabia, M. Talone, J. Tenerelli, A. Turiel, J.-L. Vergely, P. Waldteufel, X. Yin, S. Zine, and S. Delwart (2013), SMOS first data analysis for sea surface salinity determination, *International Journal of Remote Sensing*, *34*(9-10), 3654–3670, doi:10.1080/01431161.2012.716541.

Foster, R. a., A. Subramaniam, and J. P. Zehr (2009), Distribution and activity of diazotrophs in the Eastern Equatorial Atlantic., *Environmental microbiology*, *11*(4), 741–50, doi:10.1111/j.1462-2920.2008.01796.x.

Gabarró, C., J. Font, A. Camps, M. Vall-Llossera, and A. Julià (2004), A new empirical model of sea surface microwave emissivity for salinity remote sensing, *Geophysical Research Letters*, *31*(1), L01,309, doi:10.1029/2003GL018964.

Giannini, A., Y. Kushnir, and M. Cane (2000), Interannual variability of Caribbean rainfall, ENSO, and the Atlantic ocean, *Journal of Climate*, *13*, 297–311.

Giannini, A., R. Saravanan, and P. Chang (2003), Ocean Forcing of Sahel Rainfall on Interannual to Interdecadal Time Scales, *Science*, *302*, 1027–1030, doi:10.1016/S1364-8152(03)00114-2.

Giannini, A., R. Saravanan, and P. Chang (2005), Dynamics of the boreal summer African monsoon in the NSIPP1 atmospheric model, *Climate Dynamics*, *25*(5), 517–535, doi:10.1007/s00382-005-0056-x.

Gordon, A., and C. Giulivi (2008), Sea Surface Salinity Trends over fifty years within the subtropical North Atlantic, *Oceanography*, *21*(1a), 20–29.

Gordon, A., and C. Giulivi (2014), Ocean eddy freshwater flux convergence into the North Atlantic subtropics, *Journal of Geophysical Research: Oceans*, *119*, 3327–3335, doi:10.1002/2013JC009596.

Gould, J., D. Roemmich, S. Wijffels, H. Freeland, M. Ignaszewsky, X. Jianping, S. Pouliquen, Y. Desaubies, U. Send, K. Radhakrishnan, K. Takeuchi, K. Kim, M. Danchenkov, P. Sutton, B. King, B. Owens, and S. Riser (2004), Argo profiling floats bring new era of in situ ocean observations, *Eos, Transactions American Geophysical Union*, *85*(19), 185, doi:10.1029/2004EO190002.

Gouriou, Y., and T. Delcroix (2002), Seasonal and ENSO variations of sea surface salinity and temperature in the South Pacific Convergence Zone during 19762000, *Journal of Geophysical Research*, *107*(C12), 3185, doi:10.1029/2001JC000830.

Grist, J., and S. Josey (2003), Inverse analysis adjustment of the SOC air-sea flux climatology using ocean heat transport constraints, *Journal of Climate*, *16*, 3274–3295.

Grist, J., R. Marsh, and S. Josey (2009), On the Relationship between the North Atlantic Meridional Overturning Circulation and the Surface-Forced Overturning Streamfunction, *Journal of Climate*, *22*(19), 4989–5002, doi:10.1175/2009JCLI2574.1.

Grodsky, S. A., N. Reul, G. Lagerloef, G. Reverdin, J. a. Carton, B. Chapron, Y. Quilfen, V. N. Kudryavtsev, and H.-Y. Kao (2012), Haline hurricane wake in the Amazon/Orinoco plume: AQUARIUS/SACD and SMOS observations, *Geophysical Research Letters*, *39*(20), doi:10.1029/2012GL053335.

Grodsky, S. A., G. Reverdin, J. A. Carton, and V. J. Coles (2014a), Year-to-year salinity changes in the Amazon plume: Contrasting 2011 and 2012 Aquarius/SACD and SMOS satellite data, *Remote Sensing of Environment*, *140*, 14–22, doi:10.1016/j.rse.2013.08.033.

Grodsky, S. A., J. A. Carton, and F. O. Bryan (2014b), A curious local surface salinity maximum in the northwestern tropical Atlantic, *Journal of Geophysical Research: Oceans*, *119*(1), 484–495, doi:10.1002/2013JC009450.

Grunseich, G., B. Subrahmanyam, and B. Wang (2013), The Madden-Julian oscillation detected in Aquarius salinity observations, *Geophysical Research Letters*, *40*(20), 5461–5466, doi:10.1002/2013GL058173.

Hackert, E., A. J. Busalacchi, and J. Ballabrera-Poy (2014), Impact of Aquarius sea surface salinity observations on coupled forecasts for the tropical Indo-Pacific Ocean, *Journal of Geophysical Research: Oceans*, *119*, 4045–4067, doi:10.1002/2013JC009697.Received.

Häkkinen, S. (2002), Surface salinity variability in the northern North Atlantic during recent decades, *Journal of Geophysical Research*, *107*(C12), 8003, doi: 10.1029/2001JC000812.

Hanawa, K., and L. D. Talley (2001), *Ocean Circulation and Climate - Observing and Modelling the Global Ocean*, *International Geophysics*, vol. 77, 373–386 pp., Elsevier, doi:10.1016/S0074-6142(01)80129-7.

Hasson, A., T. Delcroix, and J. Boutin (2013), Formation and variability of the South Pacific Sea Surface Salinity maximum in recent decades, *Journal of Geophysical Research: Oceans*, *118*(10), 5109–5116, doi:10.1002/jgrc.20367.

Hasson, A., T. Delcroix, and J. Boutin (2014), Analyzing the 20102011 La Ni˜na signature in the tropical Pacific sea surface salinity using in situ data, SMOS observations, and a numerical simulation, *Journal of Geophysical Research: Oceans*, pp. 3855–3867, doi:10.1002/2013JC009388.Received.

Held, I., and B. Soden (2006), Robust responses of the hydrological cycle to global warming, *Journal of Climate*, *19*, 5686–5699.

Hellweger, F., and A. Gordon (2002), Tracing Amazon river water into the Caribbean Sea, *Journal of Marine Research*, *60*(4), 537–549, doi:10.1357/002224002762324202.

Helm, K. P., N. L. Bindoff, and J. A. Church (2010), Changes in the global hydrological-cycle inferred from ocean salinity, *Geophysical Research Letters*, *37*(18), doi:10.1029/2010GL044222.

Hénin, C., Y. du Penhoat, and M. Ioualalen (1998), Observations of sea surface salinity in the western Pacific fresh pool: Large-scale changes in 19921995, *Journal of Geophysical Research*, *103*(C4), 7523, doi:10.1029/97JC01773.

Henocq, C., J. Boutin, G. Reverdin, F. Petitcolin, S. Arnault, and P. Lattes (2010), Vertical Variability of Near-Surface Salinity in the Tropics: Consequences for L-Band Radiometer Calibration and Validation, *Journal of Atmospheric and Oceanic Technology*, *27*(1), 192–209, doi:10.1175/2009JTECHO670.1.

Hernandez, O., J. Boutin, N. Kolodziejczyk, G. Reverdin, N. Martin, F. Gaillard, N. Reul, and J. L. Vergely (2014), SMOS salinity in the subtropical North Atlantic salinity maximum: 1. Comparison with Aquarius and in situ salinity, *Journal of Geophysical Research: Oceans*, *119*, 2121–2128, doi:10.1002/jgrc.20224.

Holte, J., and L. Talley (2009), A New Algorithm for Finding Mixed Layer Depths with Applications to Argo Data and Subantarctic Mode Water Formation*, *Journal of Atmospheric and Oceanic Technology*, *26*(9), 1920–1939, doi:10.1175/2009JTECHO543.1.

Hu, C., E. T. Montgomery, R. W. Schmitt, and F. E. Muller-Karger (2004), The dispersal of the Amazon and Orinoco River water in the tropical Atlantic and Caribbean Sea: Observation from space and S-PALACE floats, *Deep Sea Research Part II: Topical Studies in Oceanography*, *51*(10-11), 1151–1171, doi: 10.1016/j.dsr2.2004.04.001.

Huffman, G., and D. Bolvin (2013), GPCP Version 2 Combined Precipitation Data Set Documentation, *Tech. Rep. March 2013*, NASA Goddard Space Flight Center, Mesoscale Atmospheric Processes Laboratory and Science Systems and Applications, Inc.

Intergovernmental Panel on Climate Change (IPCC) 2007 (2007), *Fourth Assessment Report: Climate Change 2007: The AR4 Synthesis Report*, Geneva, Switzerland: IPCC.

Intergovernmental Panel on Climate Change (IPCC) 2013 (2013), *Fifth Assessment Report: Climate Change 2013: The AR5 Synthesis Report*, Geneva, Switzerland: IPCC.

Johnson, E. S., G. S. E. Lagerloef, J. Gunn, and F. Bonjean (2002), Surface salinity advection in the tropical oceans compared with atmospheric freshwater forcing: A trial balance, *Journal of Geophysical Research*, *107*(C12), 8014, doi: 10.1029/2001JC001122.

Johnson, G. C. (2006), Generation and Initial Evolution of a Mode Water θ S Anomaly*, *Journal of Physical Oceanography*, *36*(4), 739–751, doi:10.1175/JPO2895.1.

Johnson, J., and M. Zhang (1999), Theoretical study of the small slope approximation for ocean polarimetric thermal emission, *IEEE Transactions on Geoscience and Remote Sensing*, *37*(5), 2305–2316, doi:10.1109/36.789627.

Josey, S. A., and R. Marsh (2005), Surface freshwater flux variability and recent freshening of the North Atlantic in the eastern subpolar gyre, *Journal of Geophysical Research*, *110*(C5), C05,008, doi:10.1029/2004JC002521.

Kalnay, E., M. Kanamitsu, R. Kistler, W. Collins, D. Deaven, L. Gandin, M. Iredell, S. Saha, G. White, J. Woollen, Y. Zhu, A. Leetmaa, R. Reynolds, M. Chelliah, W. Ebisuzaki, W. Higgins, J. Janowiak, K. C. Mo, C. Ropelewski, J. Wang, R. Jenne, and D. Joseph (1996), The NCEP/NCAR 40-Year Reanalysis Project, *Bulletin of the American Meteorological Society*, *77*(3), 437–471, doi:10.1175/1520-0477(1996)077⟨0437:TNYRP⟩2.0.CO;2.

Keenlyside, N. S., and M. Latif (2007), Understanding Equatorial Atlantic Interannual Variability, *Journal of Climate*, *20*(1), 131–142, doi:10.1175/JCLI3992.1.

Kerr, Y., J.-P. Waldteufel, J. Boutin, M.-J. Escorihuela, J. Font, N. Reul, C. Gruhier, S. E. Juglea, M. R. Drinkwater, A. Hahne, M. Martin-Neira, and

S. Mecklenburg (2010), The SMOS mission: New tool for monitoring key elements of the global water cycle, *Proceedings of the IEEE*, *98*(5), 666–687.

Kistler, R., W. Collins, S. Saha, G. White, J. Woollen, M. Chelliah, W. Ebisuzaki, M. Kanamitsu, V. Kousky, H. van den Dool, R. Jenne, and M. Fiorino (2001), The NCEP-NCAR 50-year reanalysis: Monthly means CD-ROM and documentation, *Bulletin of the American Meteorological Society*, *82*(February 2001), 247–268.

Klein, L., and C. Swift (1977), An improved model for the dielectric constant of sea water at microwave frequencies, *IEEE Transactions on Antennas and Propagation*, *AP-25*(1), 104–111.

Köhl, A., M. S. Martins, and D. Stammer (2014), Impact of assimilating surface salinity from SMOS on ocean circulation estimates, *Journal of Geophysical Research: Oceans*, *119*, 5449–5464, doi:10.1002/2014JC010040.Received.

Kuragano, T., and M. Kamachi (2000), Global statistical space-time scales of oceanic variability estimated from the TOPEX/POSEIDON altimeter data, *Journal of Geophysical Research*, *105*(C1), 955, doi:10.1029/1999JC900247.

Kushnir, Y., W. Robinson, P. Chang, and A. W. Robertson (2006), The Physical Basis for Predicting Atlantic Sector Seasonal-to-Interannual Climate Variability, *Journal of Climate*, *19*(Lorenz 1963), 5949–5970.

Lagerloef, G., and J. Font (2010), SMOS and Aquarius/SAC-D Missions: The Era of Spaceborne Salinity Measurements is About to Begin, in *Oceanography from Space*, edited by V. Barale, J. Gower, and L. Alberotanza, chap. 3, pp. 35–58, Springer Netherlands, Dordrecht, doi:10.1007/978-90-481-8681-5.

Lagerloef, G., F. R. Colomb, D. L. Vine, F. Wentz, S. Yueh, C. Ruf, J. Lilly, J. Gunn, Y. Chao, A. DeCharon, G. Feldman, and C. Swift (2008), The Aquarius/SAC-D Mission: Designed to Meet the Salinity Remote-Sensing Challenge, *Oceanography*, *21*(1), 68–81.

Lagerloef, G., R. Schmitt, J. Schanze, and H.-Y. Kao (2010), The Ocean and the Global Water Cycle, *Oceanography*, *23*(4), 82–93, doi:10.5670/oceanog.2010.07.

Laraque, A., G. Mahé, D. Orange, and B. Marieu (2001), Spatiotemporal variations in hydrological regimes within Central Africa during the XXth century, *Journal of Hydrology*, *245*(1996), 104–117.

Lass, H., M. Schmidt, V. Mohrholz, and G. Nausch (2000), Hydrographic and current measurements in the area of the Angola-Benguela front, *Journal of Physical Oceanography*, *30*(1987), 2589–2609.

Latif, M., and A. Grötzner (2000), The equatorial Atlantic oscillation and its response to ENSO, *Climate Dynamics*, *16*, 213–218.

Lee, T., G. Lagerloef, M. M. Gierach, H.-Y. Kao, S. Yueh, and K. Dohan (2012), Aquarius reveals salinity structure of tropical instability waves, *Geophysical Research Letters*, *39*(12), doi:10.1029/2012GL052232.

Lekouara, M. (2013), Exploring frontogenesis processes in new satellite sea surface temperature data sets, Ph.D. thesis, School of Ocean and Earth Science, Faculty of Natural and Environmental Sciences, University of Southampton.

Lentz, S. (1995), Seasonal variations in the horizontal structure of the Amazon Plume inferred from historical hydrographic data, *Journal of Geophysical Research*, *100*, 2391–2400.

Lentz, S. J., and R. Limeburner (1995), The Amazon River Plume during AMASSEDS: Spatial characteristics and salinity variability, *Journal of Geophysical Research*, *100*(C2), 2355, doi:10.1029/94JC01411.

Levitus, S. (1982), *Climatological Atlas of the World Ocean*, 173 pp., NOAA Professional Paper No. 13, U.S. Gov. Printing Office.

Lewis, E. L., and R. G. Perkin (1978), Salinity: Its definition and calculation, *Journal of Geophysical Research*, *83*(C1), 466, doi:10.1029/JC083iC01p00466.

Loukos, H., F. Vivier, P. P. Murphy, D. E. Harrison, and C. Le Quéré (2000), Interannual variability of equatorial Pacific CO 2 fluxes estimated from temperature and salinity data, *Geophysical Research Letters*, *27*(12), 1735–1738, doi:10.1029/1999GL011013.

Lukas, R., and E. Lindstrom (1991), The mixed layer of the western equatorial Pacific Ocean, *Journal of Geophysical Research*, *96*(S01), 3343, doi:10.1029/90JC01951.

Maes, C. (1998), Estimating the influence of salinity on sea level anomaly in the ocean, *Geophysical Research Letters*, *25*(19), 3551–3554, doi:10.1029/98GL02758.

Manabe, S., and R. Stouffer (1995), Simulation of abrupt climate change induced by freshwater input to the North Atlantic Ocean, *Nature*, *378*, 165–167.

Marengo, J. A., J. Tomasella, L. M. Alves, W. R. Soares, and D. A. Rodriguez (2011), The drought of 2010 in the context of historical droughts in the Amazon region, *Geophysical Research Letters*, *38*(12), doi:10.1029/2011GL047436.

Martín-Neira, M., S. Ribó, and A. J. Martín-Polegre (2002), Polarimetric mode of MIRAS, *IEEE Transactions on Geoscience and Remote Sensing*, *40*(8), 1755–1768.

Materia, S., S. Gualdi, A. Navarra, and L. Terray (2012), The effect of Congo River freshwater discharge on Eastern Equatorial Atlantic climate variability, *Climate Dynamics*, *39*(9-10), 2109–2125, doi:10.1007/s00382-012-1514-x.

Mecklenburg, S., M. Drusch, Y. H. Kerr, S. Member, J. Font, M. Martín-neira, S. Delwart, G. Buenadicha, N. Reul, E. Daganzo-eusebio, R. Oliva, and R. Crapolicchio (2012), ESA's Soil Moisture and Ocean Salinity Mission : Mission Performance and Operations, *IEEE Transactions on Geoscience and Remote Sensing*, *50*(5), 1354–1366.

Meehl, G., T. Stocker, W. Collins, P. Friedlingstein, A. Gaye, J. Gregory, A. Kitoh, R. Knutti, J. Murphy, A. Noda, S. Raper, I. Watterson, A. Weaver, and Z.-C. Zhao (2007), Global climate projections, in *Climate Change 2007: The Physical Science Basis. Contribution of Working Group I to the Fourth Assessment Report of the Intergovernmental Panel on Climate Change*, edited by M. T. [Solomon, S., D. Qin, M. Manning, Z. Chen, M. Marquis, K.B. Averyt and H. M. (eds.), chap. 10, Cambridge University Press, Cambridge, United Kingdom and New York, NY, USA.

Menezes, V. V., H. E. Phillips, A. Schiller, C. M. Domingues, and N. L. Bindoff (2013), Salinity dominance on the Indian Ocean Eastern Gyral current, *Geophysical Research Letters*, *40*(21), 5716–5721, doi:10.1002/2013GL057887.

Mignot, J. (2004), Interannual to interdecadal variability of sea surface salinity in the Atlantic and its link to the atmosphere in a coupled model, *Journal of Geophysical Research*, *109*(C4), C04,005, doi:10.1029/2003JC002005.

Mignot, J., and C. Frankignoul (2003), On the interannual variability of surface salinity in the Atlantic, *Climate dynamics*, *20*(May 2002), 555–565, doi:10.1007/s00382-002-0294-0.

Mignot, J., a. Lazar, and M. Lacarra (2012), On the formation of barrier layers and associated vertical temperature inversions: A focus on the northwestern tropical Atlantic, *Journal of Geophysical Research*, *117*(C2), C02,010, doi:10.1029/2011JC007435.

Molinari, R. L., and J. F. Festa (2000), Effect of subjective choices on the objective analysis of sea surface temperature data in the tropical Atlantic and Pacific oceans, *Oceanologica Acta*, *23*, 3–14, doi:10.1016/S0399-1784(00)00108-0.

Muller-Karger, F., C. McClain, and P. Richardson (1988), The dispersal of the Amazon's water, *Nature*, *333*, 56–58.

Nikiema, O., J.-L. Devenon, and M. Baklouti (2007), Numerical modeling of the amazon river plume, *Continental Shelf Research*, *27*(7), 873 – 899, doi:http://dx.doi.org/10.1016/j.csr.2006.12.004.

Pardaens, A., M. Vellinga, P. Wu, and B. Ingleby (2008), Large-Scale Atlantic Salinity Changes over the Last Half-Century: A ModelObservation Comparison, *Journal of Climate*, *21*(8), 1698–1720, doi:10.1175/2007JCLI1988.1.

Philander, S. (2001), *Atlantic Ocean equatorial currents*, 188–191 pp., Princeton University, Academic Press, Princeton, NJ, USA, doi:10.1006/rwos.2001.0361.

Pierce, D. W., P. J. Gleckler, T. P. Barnett, B. D. Santer, and P. J. Durack (2012), The fingerprint of human-induced changes in the ocean's salinity and temperature fields, *Geophysical Research Letters*, *39*(21), n/a–n/a, doi:10.1029/2012GL053389.

Polo, I., B. Rodríguez-Fonseca, T. Losada, and J. García-Serrano (2008), Tropical Atlantic Variability Modes (19792002). Part I: Time-Evolving SST Modes Related to West African Rainfall, *Journal of Climate*, *21*(24), 6457–6475, doi:10.1175/2008JCLI2607.1.

Potter, R. a., and M. S. Lozier (2004), On the warming and salinification of the Mediterranean outflow waters in the North Atlantic, *Geophysical Research Letters*, *31*(1), L01,202, doi:10.1029/2003GL018161.

Qu, T., S. Gao, and I. Fukumori (2011), What governs the North Atlantic salinity maximum in a global GCM?, *Geophysical Research Letters*, *38*(7), doi:10.1029/2011GL046757.

Qu, T., Y. T. Song, and C. Maes (2014), Sea surface salinity and barrier layer variability in the equatorial Pacific as seen from Aquarius and Argo, *Journal of Geophysical Research: Oceans*, *119*(1), 15–29, doi:10.1002/2013JC009375.

Quartly, G. D., T. H. Guymer, and K. G. Birch (2002), Back to basics: Measuring rainfall at sea: Part 10 In situ sensors, *Weather*, *57*(9), 315–320, doi:10.1256/00431650260283488.

Quartly, G. D., E. A. Kyte, M. A. Srokosz, and M. N. Tsimplis (2007), An intercomparison of global oceanic precipitation climatologies, *Journal of Geophysical Research*, *112*(D10), D10,121, doi:10.1029/2006JD007810.

Ren, L., and S. C. Riser (2009), Seasonal salt budget in the northeast Pacific Ocean, *Journal of Geophysical Research*, *114*(C12), C12,004, doi:10.1029/2009JC005307.

Ren, L., K. Speer, and E. P. Chassignet (2011), The mixed layer salinity budget and sea ice in the Southern Ocean, *Journal of Geophysical Research*, *116*(C8), C08,031, doi:10.1029/2010JC006634.

Reul, N., and Ifremer CATDS-CECOS Team (2011), SMOS Level 3 SSS Research products - Product User Manual Reprocessed Year 2010, *Tech. Rep. 1*, IFREMER, Plouzané, France.

Reul, N., and Ifremer CATDS-CECOS Team (2012), SMOS Level 3 SSS Research products - Product User Manual Reprocessed Years 2010-2012, *Tech. Rep. 2*, IFREMER, Plouzané, France.

Reul, N., and J. Tenerelli (2011), SMOS Level 3 SSS Research products - Product Validation Document- Reprocessed Year 2010, *Tech. Rep. 1.*

Reul, N., J. Tenerelli, B. Chapron, D. Vandemark, Y. Quilfen, and Y. Kerr (2012a), SMOS satellite L-band radiometer: A new capability for ocean surface remote sensing in hurricanes, *Journal of Geophysical Research*, *117*(C2), C02,006, doi: 10.1029/2011JC007474.

Reul, N., J. Tenerelli, J. Boutin, B. Chapron, F. Paul, E. Brion, F. Gaillard, and O. Archer (2012b), Overview of the First SMOS Sea Surface Salinity Products. Part I: Quality Assessment for the Second Half of 2010, *IEEE Transactions on Geoscience and Remote Sensing*, *50*(5), 1636–1647, doi:10.1109/TGRS.2012.2188408.

Reul, N., S. Fournier, J. Boutin, O. Hernandez, C. Maes, B. Chapron, G. Alory, Y. Quilfen, J. Tenerelli, S. Morisset, Y. Kerr, S. Mecklenburg, and S. Delwart (2013), Sea Surface Salinity Observations from Space with the SMOS Satellite: A New Means to Monitor the Marine Branch of the Water Cycle, *Surveys in Geophysics*, doi:10.1007/s10712-013-9244-0.

Reul, N., B. Chapron, T. Lee, C. Donlon, J. Boutin, and G. Alory (2014), Sea surface salinity structure of the meandering Gulf Stream revealed by SMOS sensor, *Geophysical Research Letters*, *41*(9), 3141–3148, doi:10.1002/2014GL059215.

Reverdin, G., E. Kestenare, C. Frankignoul, and T. Delcroix (2007), Surface salinity in the Atlantic Ocean (30S-50N), *Progress in Oceanography*, *73*(3-4), 311–340, doi:10.1016/j.pocean.2006.11.004.

Reverdin, G., S. Morisset, J. Boutin, and N. Martin (2012), Rain-induced variability of near sea-surface T and S from drifter data, *Journal of Geophysical Research*, *117*(C2), C02,032, doi:10.1029/2011JC007549.

Robinson, I. (2004), *Measuring the Oceans from Space: The Principles and Methods of Satellite Oceanography*, Springer Praxis Books / Geophysical Sciences, Chichester, United Kingdom.

Robinson, I. (2010), *Discovering the Ocean from Space: The unique applications of satellite oceanography*, Springer Praxis Books, Springer.

Roemmich, D., G. Johnson, S. Riser, R. Davis, J. Gilson, W. B. Owens, S. Garzoli, C. Schmid, and M. Ignaszewski (2009), The Argo Program: Observing the Global Oceans with Profiling Floats, *Oceanography*, *22*(2), 34–43, doi: 10.5670/oceanog.2009.36.

Romanou, A., W. B. Rossow, and S. H. Chou (2006), Decorrelation scales of high-resolution turbulent fluxes at the ocean surface and a method to fill in gaps in satellite data products, *Journal of Climate*, *19*(2002), 3378–3393, doi: 10.1175/JCLI3773.1.

Romanova, V., A. Köhl, and D. Stammer (2011), Seasonal cycle of near-surface freshwater budget in the western tropical Atlantic, *Journal of Geophysical Research*, *116*(July), C07,009, doi:10.1029/2010JC006650.

Salisbury, J., D. Vandemark, J. Campbell, C. Hunt, D. Wisser, N. Reul, and B. Chapron (2011), Spatial and temporal coherence between Amazon River discharge, salinity, and light absorption by colored organic carbon in western tropical Atlantic surface waters, *Journal of Geophysical Research*, *116*(Figure 1), C00H02, doi:10.1029/2011JC006989.

Sapiano, M. R. P., and P. A. Arkin (2009), An Intercomparison and Validation of High-Resolution Satellite Precipitation Estimates with 3-Hourly Gauge Data, *Journal of Hydrometeorology*, *10*(1), 149–166, doi:10.1175/2008JHM1052.1.

Satyamurty, P., C. P. W. da Costa, A. O. Manzi, and L. A. Candido (2013), A quick look at the 2012 record flood in the Amazon Basin, *Geophysical Research Letters*, *40*(7), 1396–1401, doi:10.1002/grl.50245.

Schanze, J. J., R. W. Schmitt, and L. L. Yu (2010), The global oceanic freshwater cycle: A state-of-the-art quantification, *Journal of Marine Research*, *68*(3), 569–595, doi:10.1357/002224010794657164.

Schlax, M., D. Chelton, and M. Freilich (2001), Sampling errors in wind fields constructed from single and tandem scatterometer datasets, *J. Atmos. Oceanic Tech.*, *18*, 1014–1036.

Schmitt, R. (2008), Salinity and the Global Water Cycle, *Oceanography*, *21*(1), 12–19.

Schmitt, R. W. (1995), The ocean component of the global water cycle Global Water Reservoirs and Fluxes, *Reviews of Goephysics, Supplement*, (95), 1395–1409.

Signorini, S. R., R. G. Murtugudde, C. McClain, J. R. Christian, J. Picaut, and A. J. Busalacchi (1999), Biological and physical signatures in the tropical and subtropical Atlantic, *104*, 18,367–18,382.

Singh, A., T. Delcroix, and S. Cravatte (2011), Contrasting the flavors of El Niño-Southern Oscillation using sea surface salinity observations, *Journal of Geophysical Research*, *116*(C6), C06,016, doi:10.1029/2010JC006862.

Sohn, B., E. Smith, F. Robertson, and S.-C. Park (2004), Derived Over-Ocean Water Vapor Transports from Satellite-Retrieved E-P Datasets, *Journal of Climate*, *17*, 1352–1365.

SPURS Workshop Report (2010), Salinity Processes in the Upper-Ocean Regional Study (SPURS), *Tech. Rep. January*, Jet Propulsion Laboratory, California Institute of Technology, NASA.

Stark, S., R. Wood, and H. Banks (2006), Reevaluating the causes of observed changes in Indian Ocean water masses, *Journal of climate*, *19*(McCartney 1977), 4075–4086.

Stewart, R. (2007), *Introduction to physical oceanography*, September, Department of Oceanography, Texas A & M University, Texas.

Stockdale, T., M. Balmaseda, and A. Vidard (2006), Tropical Atlantic SST prediction with coupled ocean-atmosphere GCMs, *Journal of climate*, *19*, 6047–6061.

Stott, P. A., R. T. Sutton, and D. M. Smith (2008), Detection and attribution of Atlantic salinity changes, *Geophysical Research Letters*, *35*(21), L21,702, doi: 10.1029/2008GL035874.

Strub, T. P., V. Combes, F. A. Shillington, and O. Pizarro (2013), Currents and processes along the eastern boundaries, in *Ocean Circulation and Climate: A 21st Century Perspective*, vol. 103, chap. 14, Academic press.

Talley, L. D. (2008), Freshwater transport estimates and the global overturning circulation: Shallow, deep and throughflow components, *Progress in Oceanography*, *78*(4), 257–303, doi:10.1016/j.pocean.2008.05.001.

Taylor, P. (2000), Intercomparison and validation of oceanatmosphere energy flux fields, *Joint WCRP/SCOR Working Group on AirSea Fluxes Final Rep., WCRP-112, WMO/TD- No. 1036*, (June).

Terray, L., L. Corre, S. Cravatte, T. Delcroix, G. Reverdin, and A. Ribes (2012), Near-Surface Salinity as Natures Rain Gauge to Detect Human Influence on the Tropical Water Cycle, *Journal of Climate*, *25*(3), 958–977, doi:10.1175/ JCLI-D-10-05025.1.

Thorpe, R., J. Gregory, T. Johns, R. A. Wood, and J. Mitchell (2001), Mechanisms Determining the Atlantic Thermohaline Circulation Response to Greenhouse Gas Forcing in a Non-Flux-Adjusted Coupled Climate Model, *Journal of Climate*, *14*, 3102–3116.

Tomczak, M., and S. Godfrey (2003), The Atlantic Ocean, in *Regional Oceanography: An introduction*, vol. 2, 2nd ed. ed., chap. 14, pp. 229–252, Daya Publishing House, Delhi, India.

Tzortzi, E., S. A. Josey, M. Srokosz, and C. Gommenginger (2013), Tropical Atlantic salinity variability: New insights from SMOS, *Geophysical Research Letters*, *40*(10), 2143–2147, doi:10.1002/grl.50225.

US CLIVAR Group (2007), U . S . CLIVAR : Climate Variability and Predictability, *Tech. rep.*, U.S. CLIVAR Office, Washington, D.C.

Van den Dool, H., P. Peng, A. Johansson, M. Chelliah, A. Shabbar, and S. Saha (2006), Seasonal-to-decadal predictability and prediction of North American climate- The Atlantic Influence, *Journal of Climate*, *19*, 6005–6024.

Vangriesheim, A., C. Pierre, A. Aminot, N. Metzl, F. Baurand, and J.-C. Caprais (2009), The influence of Congo River discharges in the surface and deep layers of the Gulf of Guinea, *Deep Sea Research Part II: Topical Studies in Oceanography*, *56*(23), 2183–2196, doi:10.1016/j.dsr2.2009.04.002.

Vellinga, M., and P. Wu (2004), Low-latitude freshwater influence on centennial variability of the Atlantic thermohaline circulation, *Journal of Climate*, *17*, 4498–4511.

Vellinga, M., R. a. Wood, and J. M. Gregory (2002), Processes governing the recovery of a perturbed thermohaline circulation in HadCM3, *Journal of Climate*, *15*(7), 764–780, doi:10.1175/1520-0442(2002)015⟨0764:PGTROA⟩2.0.CO;2.

Vernieres, G., R. Kovach, C. Keppenne, S. Akella, L. Brucker, and E. Dinnat (2014), The impact of the assimilation of Aquarius sea surface salinity data in the GEOS ocean data assimilation system, *Journal of Geophysical Research: Oceans*, *119*, 6974–6987, doi:10.1002/2014JC010006.Received.

Vialard, J. (2002), A modeling study of salinity variability and its effects in the tropical Pacific Ocean during the 19931999 period, *Journal of Geophysical Research*, *107*(C12), 8005, doi:10.1029/2000JC000758.

Vialard, J., and P. Delecluse (1998), An OGCM Study for the TOGA Decade. Part I: Role of Salinity in the Physics of the Western Pacific Fresh Pool, *Journal of Physical Oceanography*, *28*(6), 1071–1088, doi:10.1175/1520-0485(1998)028⟨1071:AOSFTT⟩2.0.CO;2.

Vinogradova, N., R. M. Ponte, I. Fukumori, and O. Wang (2014), Estimating satellite salinity errors for assimilation of Aquarius and SMOS data into climate models, *Journal of Geophysical Research: Oceans*, *119*, 4732–4744, doi:10.1002/2014JC009906.Received.

Vinogradova, N. T., and R. M. Ponte (2012), Assessing Temporal Aliasing in Satellite-Based Surface Salinity Measurements, *Journal of Atmospheric and Oceanic Technology*, *29*(9), 1391–1400, doi:10.1175/JTECH-D-11-00055.1.

Vinogradova, N. T., and R. M. Ponte (2013), Clarifying the link between surface salinity and freshwater fluxes on monthly to interannual time scales, *Journal of Geophysical Research: Oceans*, *118*(6), 3190–3201, doi:10.1002/jgrc.20200.

Vizy, E. K., and K. H. Cook (2010), Influence of the Amazon/Orinoco Plume on the summertime Atlantic climate, *Journal of Geophysical Research*, *115*(D21), D21,112, doi:10.1029/2010JD014049.

von Storch, H., and F. Zwiers (2001), *Statistical Analysis in Climate Research*, Cambridge University Press.

Wang, B., J.-Y. Moon, K. Kikuchi, J.-Y. Lee, and S.-Y. Yim (2011), Tropical ISO and Extratropical Extreme Weather during the 2009-2011 ENSO Cycle, in *Science and Technology Infusion Climate Bulletin, 36th NOAA Annual Climate Diagnostics and Prediction Workshop*, October, NOAA's National Weather Service, Fort Worth, Texas.

Wang, C., S. Dong, and E. Munoz (2010), Seawater density variations in the North Atlantic and the Atlantic meridional overturning circulation, *Climate Dynamics*, *34*(7-8), 953–968, doi:10.1007/s00382-009-0560-5.

Wijesekera, H. W., and M. C. Gregg (1996), Surface layer response to weak winds, westerly bursts, and rain squalls in the western Pacific warm pool, *Journal of Geophysical Research*, *101*(C1), 977, doi:10.1029/95JC02553.

Wijffels, S. E. (2001), Ocean transport of fresh water, in *Ocean Circulation and Climate*, vol. 77, chap. 6.2, pp. 475–488, Academic Press, doi:10.1016/S0074-6142(01)80135-2.

Wijffels, S. E., R. W. Schmitt, H. L. Bryden, and A. Stigebrandt (1992), Transport of Freshwater by the Oceans, *Journal of Physical Oceanography*, *22*(2), 155–162, doi:10.1175/1520-0485(1992)022⟨0155:TOFBTO⟩2.0.CO;2.

Wisser, D., B. M. Fekete, C. J. Vörösmarty, and a. H. Schumann (2010), Reconstructing 20th century global hydrography: a contribution to the Global Terrestrial Network- Hydrology (GTN-H), *Hydrology and Earth System Sciences*, *14*(1), 1–24, doi:10.5194/hess-14-1-2010.

Worthington, L. V. (1981), The Water Masses of the World Ocean : of a Fine-Scale Census, in *Evolution of Physical Oceanography*, edited by B. Warren and C. Wunsch, pp. 42–69, MIT Press, Cambridge, MA.

Wu, P., R. Wood, and P. Stott (2004), Does the recent freshening trend in the North Atlantic indicate a weakening thermohaline circulation?, *Geophysical Research Letters*, *31*(2), L02,301, doi:10.1029/2003GL018584.

Wu, P., R. Wood, and P. Stott (2005), Human influence on increasing Arctic river discharges, *Geophysical Research Letters*, *32*(2), L02,703, doi:10.1029/2004GL021570.

Yashayaev, I., and A. Clarke (2008), Evolution of North Atlantic Water Masses Inferred from Labrador Sea Salinity Series, *Oceanography*, *21*(1), 30–45.

Yin, X., J. Boutin, and P. Spurgeon (2012), First Assessment of SMOS Data Over Open Ocean: Part IPacific Ocean, *IEEE Transactions on Geoscience and Remote Sensing*, *50*(5), 1648–1661, doi:10.1109/TGRS.2012.2188407.

Yin, X., J. Boutin, N. Martin, P. Spurgeon, J.-l. Vergely, and F. Gaillard (2013), Errors in SMOS Sea Surface Salinity and their dependency on a priori wind speed, *Remote Sensing of Environment*, doi:10.1016/j.rse.2013.09.008.

Yoo, J.-M., and J. Carton (1990), Annual and Interannual Variation of the Freshwater Budge in the Tropical Atlantic Ocean and the Caribbean Sea, *Journal of Physical Oceanography*, *20*, 831–845.

Yu, L. (2010), On Sea Surface Salinity Skin Effect Induced by Evaporation and Implications for Remote Sensing of Ocean Salinity, *Journal of Physical Oceanography*, *40*(1), 85–102, doi:10.1175/2009JPO4168.1.

Yu, L. (2011), A global relationship between the ocean water cycle and near-surface salinity, *Journal of Geophysical Research*, *116*(C10), C10,025, doi:10.1029/2010JC006937.

Yu, L. (2014), Coherent evidence from Aquarius and Argo for the existence of a shallow low-salinity convergence zone beneath the Pacific ITCZ, *Journal of Geophysical Research: Oceans*, *119*, 7625–7644, doi:10.1002/jgrc.20224.

Yu, L., and R. a. Weller (2007), Objectively Analyzed AirSea Heat Fluxes for the Global Ice-Free Oceans (1981-2005), *Bulletin of the American Meteorological Society*, *88*(4), 527–539, doi:10.1175/BAMS-88-4-527.

Yu, L., X. Jin, and R. A. Weller (2008), Multidecade Global Flux Datasets from the Objectively Analyzed Air-sea Fluxes (OAFlux) Project : Latent and Sensible Heat Fluxes , Ocean Evaporation , and Related Surface Meteorological Variables, *Tech. Rep. January*, Woods Hole Oceanographic Institution.

Zebiak, S. (1993), Air-sea interaction in the equatorial Atlantic region, *Journal of Climate*, *6*, 1567–1586.

Zeng, N., J.-H. Yoon, J. A. Marengo, A. Subramaniam, C. A. Nobre, A. Mariotti, and J. D. Neelin (2008), Causes and impacts of the 2005 Amazon drought, *Environmental Research Letters*, *3*(1), doi:10.1088/1748-9326/3/1/014002.

Zhang, R., T. L. Delworth, and I. M. Held (2007), Can the Atlantic Ocean drive the observed multidecadal variability in Northern Hemisphere mean temperature?, *Geophysical Research Letters*, *34*(2), L02,709, doi:10.1029/2006GL028683.

Zhang, Y., and X. Zhang (2012), Ocean haline skin layer and turbulent surface convections, *Journal of Geophysical Research*, *117*(C4), C04,017, doi:10.1029/2011JC007464.